ARIADNE

DESIGN, CONSTRUCTION AND OPERATION OF A LIQUID ARGON TIME PROJECTION CHAMBER WITH NOVEL OPTICAL READOUT

Thesis submitted in accordance with the requirements of the University of Liverpool for the degree of Doctor in Philosophy by Adam Roberts.

March, 2020

Abstract

Liquid Argon time projection chambers are poised to be a crucial tool to push the frontiers of physics. Two-phase Liquid Argon TPCs offer the potential for excellent signal-to-noise at modest cost, even on the kiloton scale. Worldwide R&D activities are ongoing, searching for ways of improving detector performance.

The ARIADNE detector is exploring novel readout technologies for two-phase Liquid Argon TPCs. ARIADNE is a one ton detector, designed to characterise optical readout techniques and assess their suitability as a potential alternative to more commonly used charge readout approaches. The construction of the detector including Geant4 and COMSOL electric field simulations that informed the design are detailed.

Starting from readout using EMCCD cameras, the development and characterisation of a range of camera technologies has been studied. The performance of optical readout using EMCCD cameras was tested using the CERN T9 testbeam. Excellent x, y resolution was achieved. Limitations in z dimension reconstruction in high pileup environments motivated the development of a novel camera technology. A camera, based on the Timepix 3 ASIC, provides many benefits in the context of optical TPCs, with full x, y, z, E readout now made possible using a single camera. The camera was initially tested using a 100 mbar CF4 gas demonstrator TPC. Excellent 3D reconstruction of events was possible, even given the higher drift velocity seen in gas TPCs. Calorimetry studies found clear energy peaks, corresponding to the Americium-241 alpha source placed inside the TPC. Moreover, the Bragg peak of stopping alpha tracks was seen and measured.

The camera based on Timepix 3 was also tested using ARIADNE. Once again, excellent 3D reconstruction was possible. The slower drift velocity of electrons in Liquid Argon gave a z position resolution on the millimeter scale. Synchronisation of the camera with an external PMT was tested successfully. Measurements of electron lifetime were taken using the camera. Preliminary studies provided a rough energy calibration, allowing a single stopping muon candidate to be characterised.

Preliminary testing using a large 1m $\times$ 1m field of view are promising in terms of sensitivity. Extrapolation of the results in order to image a volume similar to the DUNE detector is discussed.

Acknowledgements

First and foremost, my greatest thanks go to Dr Konstantinos Mavrokoridis. The opportunity to work at the Liverpool Liquid Argon laboratory has been especially rewarding. Under his supervision I have been exposed to a wide variety of experimental physics and I have benefited greatly from his experience and knowledge. Together we have experienced the ups and downs of experimental physics. Special thanks must also go to my close colleagues Jared Vann, Barney Philippou and Krishanu Majumdar for their friendship throughout my studies.

I would like to thank Christos Touramanis for his supervision. His deep knowledge of Physics always allowed for stimulating conversation. I am grateful to Sam Powel and Ashley Greenall for their help navigating the often mystifying nature of electronics. An enormous thank you must go to Tony Smith, his knowledge and experience has warded off a great many complications. I deeply enjoyed our stimulating conversations.

A special thank you must go to Kevin Mccormick, Daniel Hollywood, Mark Whitley and all of the University of Liverpool workshop staff for their continued support. My experience of experimental physics would certainly not have been the same without their unwavering willingness to help in any way possible.

I would like to thank Vinícius Franco, William Turner, Twiglet Anthony, Heather McKenzie Wark, Tabitha Leonie Odell Halewood-leagas and all of my friends who I have met throughout my time at the University of Liverpool. Together we have shared many experiences, which were assuredly enriching.

A special thank you must go to Samantha Thomas for her enduring support throughout my studies and especially whilst writing this Thesis.

This work would never have been possible without the unconditional encouragement provided by my family.

Contents

Foreword and structure of this thesis

1 Introduction **1**

1.1 The frontiers of physics 1

1.1.1 Neutrino oscillations 2

1.1.2 Nucleon decay 3

1.1.3 Supernovae 5

1.1.4 Dark matter searches using Liquid Argon 5

2 The Liquid Argon time projection chamber **7**

2.1 Liquid Argon as a detector target 7

2.2 Interactions of particles with matter 9

2.2.1 Relativistic charged particles 9

2.2.2 Multiple Coulomb scattering (MCS) 10

2.3 Ionisation 12

2.3.1 Recombination 12

2.4 Scintillation 17

2.4.1 Quenching of scintillation light by impurities 21

2.5 Electron transport 24

2.5.1 Electron drift velocity 25

2.5.2 Electron diffusion 27

2.5.3 Electron attachment to impurities 33

2.6 Single phase readout 37

2.7 Dual-phase readout 38

2.7.1 Extraction of electrons from liquid to gas 38

2.7.2 MicroPattern gaseous detectors (MPGDs) 48

3 Optical readout **50**
3.0.1 THGEM Light production 51
3.0.2 Light collection 56

4 The ARIADNE detector **58**
4.1 Detection principle 58
4.2 Cryostat 61
4.2.1 Top flange 61
4.2.2 Cryostat body 63
4.3 Beam window 63
4.4 Field cage 64
4.4.1 Resistor chain PCBs 70
4.5 High voltage feedthroughs 72
4.5.1 General high voltage considerations 72
4.5.2 ARIADNE Cathode and HV feedthrough 73
4.5.3 20 kV feedthrough 76
4.6 THGEM 77
4.7 Glass sheet / wavelength shifting 79
4.8 EMCCD Cameras 81
4.9 PMTs and light collection 84
4.10 Liquid Argon purification and recirculation 87
4.10.1 Liquid argon Purification cartridge 87
4.10.2 Liquid argon Recirculation 90
4.11 Cryogenics 94
4.12 Detector monitoring and slow control 97

5 The ARIADNE detector exposed to the CERN T9 beamline **99**
5.1 Beamline simulation 99
5.2 Beamline deployment 102

6 Development of Timepix 3 based camera readout **110**
6.1 The Timepix3 ASIC 110
6.1.1 Detecting optical photons using Timepix 3 112
6.2 DAQ and readout 115
6.3 Image intensifiers 117
6.3.1 Photocathode 118
6.3.2 Microchannel plates (MCPs) 118

6.3.3 Phosphor screen and relay optics 120
6.3.4 Photonis Cricket 120

7 Performance of optical TPX3 readout in 100 mbar CF4 gas 122
7.0.1 Intensifier configuration 122
7.0.2 Detector setup 123
7.0.3 Results 127
7.0.4 THGEM Bias scan 132
7.0.5 Calorimetry 134
7.0.6 Discussion 136

8 Performance of optical TPX3 readout in Liquid Argon 139
8.1 Gallery 141
8.2 Measurement of THGEM light production 147
8.3 Measuring electron lifetime 149
8.4 Energy deposition of throughgoing MIPs 152
8.5 Position resolution 158
8.5.1 x, y direction 158
8.5.2 z direction 161
8.6 Discussion 161

9 Future developments 164
9.1 Technological advances 164
9.1.1 Timepix 4 164
9.1.2 Image intensifier developments 165
9.1.3 Direct VUV imaging 166
9.2 Imaging larger areas 170

10 Conclusion 173

Appendices 192

A Determination of D_T 193

Foreword and structure of this thesis

In Chapter 1 we review a theoretical motivation for Liquid Argon Time projection chambers. We take a wide look at the many different sectors of physics which are proposing the use of Liquid Argon TPCs as a tool for discovery. In Chapter 2, operational aspects of Liquid Argon TPCs are discussed. We will discuss what aspects make Argon an excellent detector target. We will discuss the operational principle of a LArTPC, paying close attention to electron transport processes. Particular attention is paid to dual-phase operation. In Chapter 3, optical readout of a dual phase LArTPC is introduced. The mechanisms through which a THGEM can be used to produce light are explained. The expected light output of a THGEM as a function of potential difference is presented.

In Chapter 4, the ARIADNE detector is introduced. We discuss key design aspects of the experiment, from Cryostat manufacture through to detector monitoring and slow control. Where relevant, Geant4 and COMSOL electric field simulations are presented. In Chapter 5, operation of the ARIADNE detector at the CERN T9 Beamline is presented. We discuss the performance of EMCCD cameras and lessons learned.

In Chapter 6, the development of a novel Timepix3 based camera technology is outlined. The operational aspects of the camera are explained in detail. In Chapter 7, the camera is characterised using a 100 millibar gas TPC. We take a look at 3D event reconstruction capabilities, as well as basic calorimetric performance. In Chapter 8, the Timepix3 based camera is installed onto the ARIADNE detector. Performance of the camera for readout of a dual phase LArTPC is studied in detail.

In Chapter 9, a selection of opportunities future improvements are discussed. An outlook towards the readout of large detectors is provided.

The ARIADNE program is proudly supported by the European Research Council Grant No. 677927 and the University of Liverpool.

Chapter 1

Introduction

1.1 The frontiers of physics

The liquid Argon time projection chamber is poised to be a crucial tool for next generation tests of theoretical physics. The DUNE collaboration [1] is proposing the use of 40 kiloton scale LArTPCs. This experiment will, for the first time using a single experiment, provide comprehensive precision measurements of the parameters that govern neutrino oscillations. A discussion of the theoretical context of neutrino oscillations and the potential reach of the DUNE experiment will be presented in Section 1.1.1.

The aim of the ARIADNE experiment [2] is to both reduce the technological hurdle posed by the construction of these large scale detectors, as well as to explore novel technologies which may enhance detector performance. In this section we will review several large LArTPCs that are proposed and discuss the scientific reach of each.

The DUNE experiment has a rich physics program, extending far beyond neutrino oscillations. The large active volume of the 40 kiloton scale LArTPCs that are proposed by DUNE offer immense volumes of nucleons, making them well suited for nucleon decay searches. Nucleon decay is discussed in 1.1.2.

The physics of supernovae is not well constrained by experimental data. Precision measurement of the neutrino flux during the core collapse of a star would allow tighter constraints to be placed on theoretical models and provide a better understanding of supernovae. Once again, the large active volume of proposed kiloton scale LArTPCs makes them a world-class neutrino observatory. Supernovae physics is discussed in 1.1.3.

The search for dark matter, in many different forms, has branches across the wide breath of particle physics, from the high energy frontiers of the LHC to ultra low energy probes such as LIGO, an experiment where some hints of dark matter may have already been seen [3]. The liquid Argon TPC has been proposed for several dark matter detection experiments. The search for dark matter using Liquid Argon TPCs will be discussed in 1.1.4.

This thesis could never do justice to the varied and exciting work ongoing within each of these different sectors. For a more detailed and comprehensive review, the reader is referred elsewhere [4, 5].

1.1.1 Neutrino oscillations

Experimental evidence points towards the existence of three flavours of neutrino; electron ($\nu_e/\bar{\nu}_e$), muon ($\nu_\mu/\bar{\nu}_\mu$) and tau ($\nu_\tau/\bar{\nu}_\tau$). Further evidence has confirmed both that neutrinos have mass and that neutrinos, after traveling some distance, are able to transition fluidly between the three flavours. This transition between neutrino flavours is the so called flavour neutrino oscillation, or neutrino mixing. One of the main physics goals of the DUNE experiment is the measurement of all of the parameters that define this rate of neutrino mixing.

In terms of a field theory, we can express the neutrino field as a superposition of all possible neutrino flavour fields. As mentioned earlier, experimental evidence points to the existence of three flavours, although theoretical models present no such constraint. Considering three neutrino flavours, the rate of neutrino mixing can be expressed as

$$\begin{pmatrix} \nu_e \\ \nu_\mu \\ \nu_\tau \end{pmatrix} = \underbrace{\begin{pmatrix} U_{e1} & U_{e2} & U_{e3} \\ U_{\mu 1} & U_{\mu 2} & U_{\mu 3} \\ U_{\tau 1} & U_{\tau 2} & U_{\tau 3} \end{pmatrix}}_{\text{PMNS Matrix}} \begin{pmatrix} \nu_1 \\ \nu_2 \\ \nu_3 \end{pmatrix} \tag{1.1}$$

where ν_e, ν_μ and ν_τ are the neutrino flavour eigenstate fields and ν_1, ν_2 and ν_3 are the neutrino mass eigenstate fields. The Pontecorvo-Maki-Nakagawa-Sakata matrix, or PMNS matrix for short, defines the relative mixing between the neutrino flavours. Given that all experimental data can be described using three neutrino flavours, we have made the assumption that the PMNS matrix is a 3×3 matrix. The PMNS matrix may also be expressed

as the product of three flavor mixing matrices

$$U_{\text{PMNS}} = \begin{pmatrix} 1 & 0 & 0 \\ 0 & c_{23} & s_{23} \\ 0 & -s_{23} & c_{23} \end{pmatrix} \begin{pmatrix} c_{13} & 0 & e^{-i\delta_{\text{CP}}} s_{13} \\ 0 & 1 & 0 \\ -e^{i\delta_{\text{CP}}} s_{13} & 0 & c_{13} \end{pmatrix} \begin{pmatrix} c_{12} & s_{12} & 0 \\ -s_{12} & c_{12} & 0 \\ 0 & 0 & 1 \end{pmatrix} \tag{1.2}$$

We see that the PMNS matrix is completely defined by three mixing angles and a CP-violating phase. The CP-violating phase, δ_{CP}, depends on whether the neutrinos are Dirac or Majorana. A Majorana fermion is its own anti-particle whereas a Dirac fermion has a distinct anti-particle, which has opposite lepton charge. Since at any point in space we must be able to measure at least one of the flavours (the neutrino cannot simply vanish), the PMNS matrix must be unitary. Current experimental data constrains the existence of at least three neutrino flavours (e, μ, τ), which each must have a mass less than 1 eV. Additionally, the mass of each neutrino flavour must be distinct. It is currently undetermined whether neutrinos are Dirac or Majorana fermions.

A comprehensive measurement of the PMNS matrix will settle several key remaining questions about the nature of the neutrino. Some parameters of this matrix have been measured, with varying degrees of accuracy, by several generations of experiments [6–10]. However, the combination of measurements from different detector technologies has proven to be a challenge, as each experiment has its own unique set of systematic uncertainties. Reconciling these systematic uncertainties into a coherent picture is not trivial. The DUNE experiment is designed to provide precision measurements of multiple parameters of the PMNS matrix. Measurements provided by the DUNE experiment will help settle remaining open questions in the neutrino sector. Precision measurement of δ_{CP} can determine if neutrinos are Dirac or Majorana in nature, and could explain the origin of matter-antimatter asymmetry in the universe.

1.1.2 Nucleon decay

Grand unified theories (GUTs) [11] propose that the strong, weak and electromagnetic forces may all be explained within the context of a larger, unifying, theory. Different GUTs each predict different mechanisms by which

different nucleons may decay, and make predictions about the expected lifetime of the nucleon states. By searching for nucleon decays, or by setting constraints on their lifetime by their absence, constraints can be set on allowable GUTs. These constraints, if strict enough, may be incompatible with certain theoretical models, ruling them out. An interesting specific example is proton decay. In the standard model, proton decay is forbidden. Hence, experimental observation of proton decay would be a clear sign of physics beyond the standard model. Certain GUT models require proton decay. For example, the Georgi–Glashow model requires that the proton decays into a positron and neutral pion [12]. The neutral pion then decays to two gammas. The half life for this decay is approximately 10^{34} years.

A natural byproduct of a 40-kiloton scale LArTPC is a large number of nucleons contained within the detector. It is expected that the DUNE experiment will extend the nucleon decay lifetime limits by an order of magnitude beyond the current limits, set by Super-K, in several channels [1, 12]. Other decay channels, however, remain better suited to large water Cherenkov detectors due to differences in detector efficiencies. The searches performed by the DUNE experiment are expected to be complimentary to those that are proposed by Hyper-Kamiokande. A LArTPC has good efficiency for detecting charged particles in the final state. Neutron decays are not detected with good efficiency in a LArTPC due to the lack of charged particles in the final state, thus producing no ionisation. Of particular interest are nucleon decays which have a charged Kaon in the final state. Charged Kaons can be detected with high efficiency in a LArTPC, since the high Kaon mass results in a large ionisation yield. The relatively short lifetime of the Kaon means that the decay products can also be detected in the LArTPC, in total producing an event with a very unique signature. The DUNE experiment expects to have world leading sensitivity to the following proton decays

Decay channel	Current best limits ($\times 10^{33}$ years)	DUNE projected limits ($\times 10^{33}$ years)
$p \to \mu^+ + K^0$	1.6 [13]	10-11 [1]
$p \to \bar{\nu} + K^+$	5.9 [14]	12-13 [1]

In summary, the DUNE detector should be able to present either direct evidence for proton decay, or world leading constraints on the proton decay lifetime. In the case that a signal of proton decay were to be ob-

served in DUNE, it would be important for the signal to also be observed in Hyper-Kamiokande, given the different detection technologies. Complimentary searches using multiple detection techniques can only be beneficial.

1.1.3 Supernovae

The neutrino flux that emanates from the core of a collapsing star gives a unique insight into the physics that is ongoing during the supernovae. Observation of such a supernovae using the next generation of 40-kiloton scale detectors would help to constrain the physical processes that are occurring during core collapse. Both the flavour content and the flux of the neutrinos which are emitted from a supernova vary over time through the different stages of core collapse. Accurate measurement of these parameters throughout the process of a supernovae will provide much needed constraints for theoretical models [12].

The large number of neutrinos produced in supernovae present several unique experimental opportunities. The quantity of neutrinos produced is so large that neutrino-neutrino coherent scattering is expected to be a measurable effect. Supernovae present the only experimental opportunity to measure this effect. The large distance traveled by supernova neutrinos before reaching earth also provides an uniquely long baseline for time-of-flight measurements. These time-of-flight measurements provide a way to search for Lorentz and CPT-violating effects in neutrinos. These effects are quantised using standard model extension parameters (SMEs) [15]. For a supernova comparable to SN1987, at a distance of 50 kpc, Figure 1.1 summarises the projected improvements to the SME parameters that could be provided by DUNE.

1.1.4 Dark matter searches using Liquid Argon

Several experiments have proposed the use of Liquid Argon TPCs for dark matter detection attempts. DarkSide-20k [16] is a proposed 20 Tonne Two-Phase LAr TPC for direct dark matter detection. ArDM [17–19] is a ton-scale Liquid Argon TPC for direct dark matter searches whilst WArP [20] has a sensitive mass of 140 kg Argon.

Many of these dark matter searches using LArTPCs feature similar detector configurations; A sensitive volume which is surrounded by a large

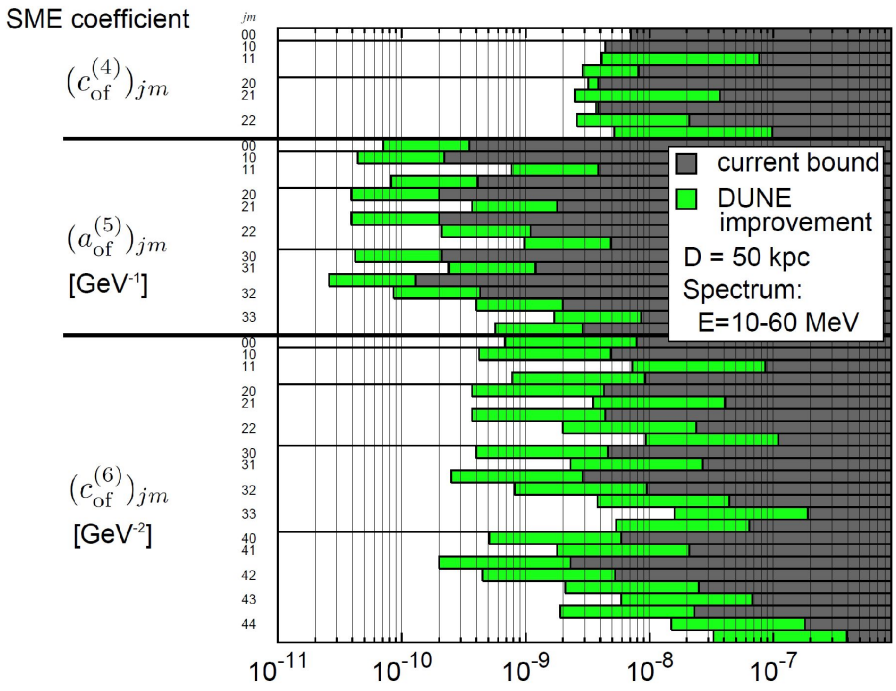

Figure 1.1: DUNE projected sensitivity to standard model extension parameters for a supernova comparable to SN1987 at a distance of 50 kpc. Reproduced from [1].

shielding/veto volume. This shielding volume helps to reduce background signals and, when used as a veto, allows very high signal efficiencies by allowing rejection of those events which originated in the shielding volume, but were also detected in the sensitive volume. A veto volume allows efficient selection of those events which originated in the sensitive volume and are fully contained. The challenge of using Liquid Argon for dark matter searches is radiopurity. Most commercially available Argon has been both produced and stored on the earths surface and thus, has been subject to a continuous flux of cosmic rays. This cosmic ray flux can result in the production of the radioactive ^{39}Ar isotope [12], which presents an unacceptable background signal for dark matter searches. Therefore, extra care is required to produce Liquid Argon exclusively from ^{40}Ar, which is stable. A detector filled of pure ^{40}Ar makes an excellent dark matter target [21]. The nuclear properties of Liquid Argon are highly complimentary to Liquid Xenon [22], which is another popular target for direct dark matter detection attempts. LUX-ZEPLIN (LZ) [23] is a two-phase Liquid Xenon (LXe) direct dark matter detection experiment which will feature a sensitive volume of 7 tonnes LXe.

Chapter 2

The Liquid Argon time projection chamber

2.1 Liquid Argon as a detector target

As described by Carlo Rubbia in 1977 [24], several properties make Liquid Argon a good target for particle detection. Liquid Argon is dense, encouraging interactions. Liquid Argon has high electron mobility and does not capture drifting electrons. Both of these features allow for efficient drift over long distances. Crucially, Liquid Argon is cheap. The realisation of future experiments with sensitive volumes in the region of 40 kiloton is sensitively dependent on the cost of the chosen target material. The favorable electron transport characteristics of Liquid Argon are only true for highly pure Liquid Argon. Small levels of impurities can destroy these important characteristics. Purification of Liquid Argon remains a considerable challenge for current Liquid Argon TPC based experiments. Liquid Argon produces copious amounts of scintillation light (few tens of thousands of photons per MeV [25]) and is transparent to this scintillation light, allowing for efficient detection.

However, Liquid Argon has some considerable drawbacks. The cryogenic nature of Liquid Argon requires the construction and use of cryostats, which become costly for large experiments. The requirement that detector components should be able to operate for long periods of times in cryogenic conditions gives rise to engineering challenges. The most abundant, and therefore cheapest, form of Argon is ^{40}Ar. When exposed to cosmic rays, ^{39}Ar may be produced [26]. ^{39}Ar is radioactive, making its presence largely

unsuitable for certain experiments such as direct dark matter detection. Removal of ^{39}Ar is possible but expensive, meaning that Xenon has often been preferred for liquid noble TPC direct dark matter detection experiments. The DarkSide-20k experiment is a direct dark matter detection experiment, which is proposing the use of purified liquid Argon [16] as a target.

General properties

Property	Value	Notes
Atomic number	18	
Atomic weight	39.948	
Normal boiling point	87 Kelvin	
Liquid density	1.396 g/cm^3	
Heat of vaporization	161 kJ/kg	
Heat capacity	1.117 kJ/kg/K	
Thermal conductivity	0.1256 W/m/k	
Viscosity	270 μ Pascal-s	
Expansion ratio	847	
Electron drift velocity	1.6 mm/μs	At 0.5 kV/cm, 87 K
Ion drift velocity	8E-6 mm/μs!	At 0.5 kV/cm, 87 K
Dielectric constant	1.5	
Peak scintillation wavelength	128 nm	
Ionisation W-value	23.6 eV	
MIP energy loss	2.12 MeV/cm	

Notable Isotopes of Argon

Isotope	Abundance	Radioactivity
^{40}Ar	99.6%	Stable
^{39}Ar	Produced by cosmic flux	β^-(565keV), half life = 269 y
^{38}Ar	0.06%	Stable
^{37}Ar	0.03%	Stable

2.2 Interactions of particles with matter

2.2.1 Relativistic charged particles

A complete review of the interactions of particles with matter is given in [5]. Here we will instead discuss aspects that are directly relevant in the context of a Liquid Argon TPC. When a charged particle traverses through Liquid Argon, a mixture of ionisation and excitation is produced, generally by successive single collisions with electrons of the Argon atoms. The energy loss of the charged particle is often quoted as dE/dX. The "Bethe equation" is the most widely used theoretical model to predict energy loss for relativistic heavy charged particles. This model predicts, with accuracy within a few percent, the mean energy loss for particles in the region $0.1 \leqslant \beta\gamma \leqslant 1000$ for most materials with Z > 10. The "Bethe equation" is as follows:

$$\langle -\frac{dE}{dX} \rangle = Kz^2 \frac{Z}{A} \frac{1}{\beta^2} \left[\frac{1}{2} \ln \frac{2m_e c^2 \beta^2 \gamma^2 W_{\max}}{I^2} - \beta^2 - \frac{\delta(\beta\gamma)}{2} \right] \tag{2.1}$$

where $\langle -dE/dX \rangle$ is the mean energy loss. $K = 4\pi N_A {r_e}^2 m_e c^2$, where N_A is Avogadro's number, r_e is the classical electron radius, m_e is the electron mass and c is the speed of light. ze is the charge of the incident particle. Z is the absorber atomic number. $W_{\max}$ is the maximum kinetic energy transfer in a single collision with a single electron and I is the mean excitation energy. $\delta(\beta\gamma)$ is the density-effect correction [27].

Let us consider the case of many cosmic muons passing through a LArTPC. The distribution of energy lost by these muons can be approximately described using a Landau distribution. This distribution has a peak at the so called 'most probable value' followed by an extensive tail out to higher energies. This long tail is the result of the rarer collision processes. It is this tail that means $\langle -dE/dX \rangle$ must be used with caution. The mean of the energy loss distribution is heavily weighted by this tail, the tail which is formed from rare processes that may not well represented, even with modest number of events. It is for this reason that the most probable value of a Landau fit is instead generally a more robust measure of energy loss. The peak of the most probably energy loss is formed much more reliably by the abundant lower energy collisions.

Occasionally, it is possible that a very large momentum transfer occurs to a single electron. This single electron gains so much kinetic energy that it

itself can become ionising and produce an observable track in the detector. This track is known as a delta ray (δ-ray) and can be seen as small branches from tracks which are otherwise expected to be only ionising.

Event reconstruction and analysis techniques can often exacerbate the difficulties with using the mean energy loss as a tool for particle identification. In order for the mean energy loss to represent a reliable measure, the analysis method must be able to reliably reconstruct the additional energy loss contained within δ-rays, and reliably associate this energy loss to the parent track.

2.2.2 Multiple Coulomb scattering (MCS)

As well as losing energy, particles are also scattered during their traversal of matter. The distribution of scattering angles is expected to be mostly Gaussian but once again a large tail may exist as a result of rarer scattering events that can produce large angles, for example nuclear recoils. The standard deviation of the scattering distribution is predicted by Lynch & Dahl [28] as:

$$\theta_0 = \frac{13.6 \text{ MeV}}{\beta c p} z \sqrt{\frac{x}{X_0}} \left[1 + 0.038 \ln(\frac{x}{X_0}) \right] \tag{2.2}$$

Where p is the particle momentum, βc is the particle velocity and z is the charge number of the incoming particle. x/X_0 is the thickness of the scattering medium with units of radiation lengths.

Energy reconstruction of particles in the LArTPC is perhaps better known using energy loss, or dE/dX. Measurements of multiple coulomb scattering however give an additional handle on the momenta of a particle in a TPC and are undoubtedly useful. Both ICARUS and Microboone have recently been exploring this concept [29, 30].

Multiple Coulomb scattering (MCS) should be considered as a complimentary handle on particle momentum compared to dE/dX. Reconstruction of particle momenta through either dE/dX or MCS can excel under different circumstances. In the case that Liquid Argon purity is poor, ionisation electrons may be lost during the drift. In the case of an analysis which solely uses dE/dX, care must be taken to ensure that either the Liquid argon purity is so great that electron capture by impurities is not an issue or that accurate purity corrections are performed. Using MCS to determine particle

momenta is generally insensitive to purity effects since, even if a track has extreme variations in relative intensity throughout it's length by impurity attachment, this will have little effect on the resolved track position. On the other hand, in the case of a TPC which has high field non-uniformities, accurate measurement of MCS may be a challenge. Drift field non-uniformities will distort the reconstructed position of the track in the TPC and lead to unreliable MCS measurements. In this case, momentum measurement via dE/dX may be more reliable. In any real TPC, there is most likely a combination of both purity effects and drift field non-uniformities and so complimentary MCS and dE/dX momentum measurements should be considered.

2.3 Ionisation

As a charged particle traverses Liqud Argon, Argon atoms may be ionised. The energy required to liberate an electron from an Argon atom is known as the W-value. The W-value for Liquid Argon has been measured as $23.6^{+0.5}_{-0.3}$ eV [31]. For reference, the W-value for gas Argon has been measured as 26.3±0.2 eV [32].

We can use the W-value to predict the number of electrons that will be liberated by an ionising particle in the LArTPC. Naturally, the number of liberated electrons is not exact, but is according to a roughly Gaussian distribution. The standard deviation of this distribution is predicted according to $\sqrt{FN}$, where F is the so called Fano-factor and N is the mean number of created electron-ion pairs. The Fano-factor has been calculated to be in the range 0.107-0.116 for Liquid Argon [33].

We can predict that, for a minimum ionising particle (MIP) with $dE/dX =$ 2.12 MeV/cm, the mean ionisation yield is 89800 electron-ion pairs per centimeter with a standard deviation of 9880. The Fano factor places a limit on the energy resolution that is possible in an ionisation detector. If we assume that $F = 0.11$, the limiting energy resolution is given as roughly $0.33\sqrt{N}$, where N is the number of electron-ion pairs. If we consider a 1 cm segment of a MIP-like track, this limiting resolution is around 11%.

In practice, detector effects mean that this limiting resolution imposed by the Fano-factor is never realised. Of all of the electron-ion pairs that are initially created by an ionising event, a large fraction are lost almost immediately to recombination. Even more electrons are lost by attachment to impurities during drift. Both of these effects degrade energy resolution.

2.3.1 Recombination

The effect of electron recombination in Liquid Argon is often quoted as a recombination factor, R. If we let the initial number of liberated electron-ion pairs equal Q_0 then R is defined as $Q = Q_0 R$, where Q is the number of electron-ion pairs which survive recombination. The rate of recombination is generally assumed to be a function of ionisation density as well as the applied electric field, $\vec{E}$. In the limit of no electric field, all ionised charge is expected to eventually recombine ($\lim_{\vec{E}\to 0} R = 0$). Conversely, in the limit of infinite electric field, all charge is expected to survive recombination

($\lim_{\vec{E}\to\infty} R = 1$). The dependence of the rate of recombination on the ionisation charge density is often parameterised using dE/dX. However, since ionisation charge density is not strictly proportional to dE/dX, this dependence should be considered as an approximation. In other words, the true recombination rate is expected to vary depending on the type of ionising particle, rather than simply dE/dX.

The ICARUS collaboration, and later the ArgoNeuT collaboration, have both performed detailed studies of the rate of recombination in Liquid Argon [34, 35]. These studies represent the most in-depth understanding of recombination theory in Liquid Argon. The most important results from both of these studies will be highlighted in the following discussion.

It is also worth noting that recombination and light production by scintillation in Liquid Argon are closely related. We will see later that, as an end result of the recombination process, scintillation light is produced. Thus, as recombination is reduced, total scintillation output is also reduced.

Many theories of electron recombination have been proposed in the literature. The earliest models, the so called geminate theory [36], suggest that each ion and electron pair should be considered independently. After ionisation, the ion and electron both move under the effects of diffusion, their mutual coulomb attraction and the forces applied by external electric fields. The germinate model predicts that if recombination does happen, the electron recombines with the exact ion from which it originated. This recombination of the electron with its parent ion is known as initial recombination. In order for this model to be realistic, it is obvious that the electron must remain close to the ion from which it originated. If the electron escapes to a distance far from the initial ion, there is no reason to expect for it to recombine with the parent ion, and not another available ion nearby. Electrons, once ionised, have a large amount of kinetic energy. Their high kinetic energy means that electrons are not immediately able to recombine, but must first thermalise. The process of thermalisation happens very quickly, on the order of nanoseconds [37, 38]. During this time, calculations and simulations showed that the electrons will travel a mean thermalisation distance of roughly 2.6 μm [38]. This thermalisation distance is much further than the reasonable range of the attractive coloumb force between the parent ion and the ionised electron (The average interatomic spacing is approximately 4Å [39]). Thus, these considerations suggest that direct recombination with

the parent ion is unlikely. A critical test showed that, in Liquid Argon, data does not agree well with germinate theory [40].

The elimination of germinate theory thus leads to the conclusion that ionised electrons are instead mostly effected by the collective forces from the total ion cloud around an ionising track. Columnar theory [41] predicts that an ionising track creates a dense column of ions and electrons around the core of the track. The core of the column is formed by the relatively immobile ions and the periphery of the column is formed by a cylindrical cloud of electrons. According to this model, the ions and electrons are to drift away from the central core of the column as a result of diffusion and as the result of any applied electric field. The predictions of columnar theory, according to Jaffe's model, can be expressed using a form of Birk's law:

$$R_{\text{Jaffe}} = \frac{1}{1 + q_0 F(\vec{E} \sin \phi)} \tag{2.3}$$

where q_0 is the initial ionisation density, $\vec{E}$ is the applied electric field, at an angle ϕ relative to the ionisation column. F is a function which parameterises the diffusion of electrons and ions, dependent on the diffusion and mobility coefficients in the Liquid Argon. A recent modification of Jaffe's theory is the so called 'modified columnar theory' proposed by Kramers [42]. This model incorporates more realistic model of electron diffusion which has a strong effect on the predictions of the model at low ionisation densities. A shared limitation of both Jaffe's and Kramers' model is the assumption that electrons and ions have equal drift velocities and that their mobility is independent of the applied electric field. Both of these assumptions are demonstrably false.

Thomas and Imel proposed a new model which reworks the assumptions made by both Jaffe and Kramers [43]. This model instead assumes that ions are immobile and there is zero diffusion. This model replaces the columnar structure of the ionised charge cloud with a uniformly distributed box geometry. This model is therefore commonly known as the box model. This model predicts that:

$$R_{\text{Box}} = \frac{1}{\xi} \ln(1 + \xi), \qquad \text{where } \xi = \frac{N_0}{4a^2 \mu \vec{E}} \tag{2.4}$$

where $N_0/4a^2$ represents the charge density inside a microscopic box of side

length a. μ is the electron mobility and $\vec{E}$ is the applied electric field.

A limitation of both the columnar and box theories is that they all assume that the electron drift velocity is linearly proportional to the applied electric field. In the case of Liquid Argon, this assumption is incorrect above ≈ 0.2 kV/cm [44], far below the nominal drift field of most experiments. Additionally, the box model includes no dependence on the track angle relative to the electric field direction. Although these limitation are fundamental, both models are still able to provide reasonable agreement with experimental data, albeit in limited regimes.

Electron recombination in Liquid Argon is still an active area of research. We have discussed the two most widespread theories, the box model and the modified columnar model. These models each only provide reasonable agreement with experimental data over a subset of electric field values. So far, the most accepted model appears to be an approximate solution to Equation 2.4, given by a form of Birk's law:

$$R_{\text{Box}} = \frac{1}{1 + k_e/\xi} \tag{2.5}$$

where k_e is left as a constant, to be determined by fitting to experimental data. The ICARUS collaboration found that an additional scaling factor, A, substantially improves the fit of the model to the data and so we finally reach

$$R_{\text{Box}} = \frac{A}{1 + k_e/\xi} \tag{2.6}$$

where both A and k_e are determined by fitting. Looking back at Equation 2.4, ξ is seen to be a function of the initial ionised charge density, electron mobility and applied electric field. Given that relatively little data exists about the ionisation charge density as a function of energy for many particle types, an approximation is generally made that the ionisation charge density is proportional to dE/dX. Thus, the term $N_0/4a^2$ can be re-expressed as $k\ dE/dX$. We now reach a final expression for electron recombination as a function of dE/dX and electric field $\vec{E}$, parameters which are easily measured in a LArTPC:

$$R_{\text{Box}} = \frac{A}{1 + k_q \frac{dE/dX}{\vec{E}}} \tag{2.7}$$

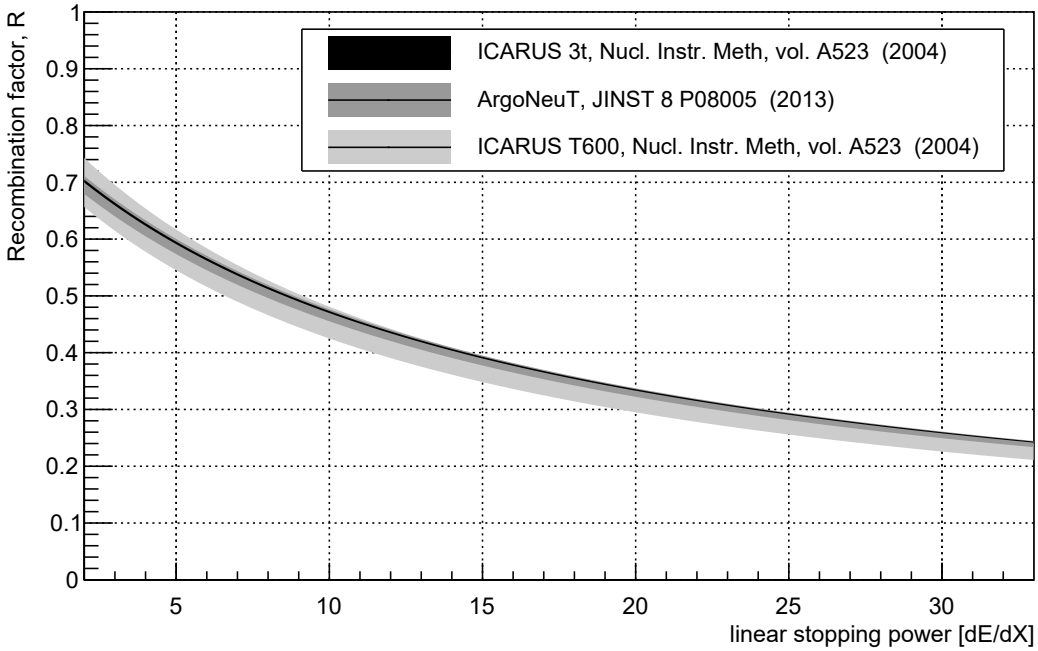

Figure 2.1: Experimental measurements of the recombination factor as a function of stopping power. The best model constraints are provided by ICARUS T600 [34]. The functional form of the model is described in Equation 2.7. The model of valid for drift fields between 0.1-1.0 kV/cm, which provides comprehensive coverage across most drift fields typically used in most experiments. This model is valid for protons and muons with dE/dX in the range 1.5 to 30 MeV/(g/cm^2).

According to ICARUS [34], the experimental values for the parameters A and k_q are given by $A = 0.800 \pm 0.003$ and $k_q = 0.0486 \pm 0.0006$ (kV/cm)(g/cm^2)/MeV. These values are valid for electric fields between 0.1 and 1.0 kV/cm and for dE/dX between 1.5 to 30 MeV/(g/cm^2). These values have been independently verified by the ArgoNeuT collaboration [35] who found that $A = 0.793 \pm 0.018$ and $k_q = 0.049 \pm 0.002$ (kV/cm)(g/cm^2)/MeV. The predictions of Equation 2.7 are plotted as a function of dE/dX in Figure 2.1 for a fixed electric field of 0.5 kV/cm. The predictions are plotted for three different versions of the parameters A and B, from the results of three different detectors. The tightest predictions are from the ICARUS T600 detector. The fit parameters from ICARUS 3t and ArgoNeuT are constant with the parameters found by ICARUS T600 but both have relatively larger uncertainties.

2.4 Scintillation

When charged particles interact with Liquid Argon, a mixture of both ionisation and excitation of Argon atoms occurs. Both the ionisation and excitation phenomena can eventually lead to the emission of scintillation light. In the case of Argon excitation, an excited Ar^* state is produced. The de-excitation process for Ar^*, and other noble gasses, is more involved than a direct de-excitation with the emission of a photon. Argon, like other noble gasses, has a full outer shell. This full outer shell means that covalent bonding is minimal between neighbouring Argon atoms, when in the ground state. However, when an Argon atom is excited, the electron leaves behind a hole in the valence shell, meaning that covalent bonding may now be possible. Figure 2.3 plots the potential curves for excited Argon atoms as a function of nuclear separation. We see that the potential for excited Ar^* states features a dip in potential if an excited Ar^* state moves closer to a ground state Ar atom, forming a covalent bond. The resulting molecule, formed from a ground state Ar Atom and an excited Ar^* atom, is known as an excimer. This excimer state may be expressed as $(ArAr)^*$. The emission spectrum of Argon is defined by all the possible ways by which this excimer can decay back into the ground state.

In Argon, there are two possible excimer states than can be formed, seen as the red and blue potentials on Figure 2.3. The difference between these two states is related to the spin of the excited electron. Since Argon has a closed shell structure, in the ground state all electrons are paired, $\uparrow\downarrow$. When one of these electrons is excited, the spin of the excited electron may stay paired with the ground state electron, giving for example spin-$\uparrow$ in the ground state and spin-$\downarrow$ in the excited state. In the case that the spins remain coupled in this way, the excited state is known as the singlet excited state. It is also possible that the spin of the excited electron can decouple from the spin of the ground state electron. In this case we could have, for example, spin-$\uparrow$ in the ground state and also spin-$\uparrow$ in the excited state. A state in which the spin of the excited electron aligns with the spin of the ground state electron is known as the triplet excited state. On Figure 2.3, we see the singlet state as ${}^1\Sigma_u^+$ (red line) and the triplet state as ${}^3\Sigma_u^+$ (blue line). The decay of both the singlet and triplet states to the ground state ${}^1\Sigma_g^+$ (black line) is mediated by the emission of a VUV photon. The wavelength

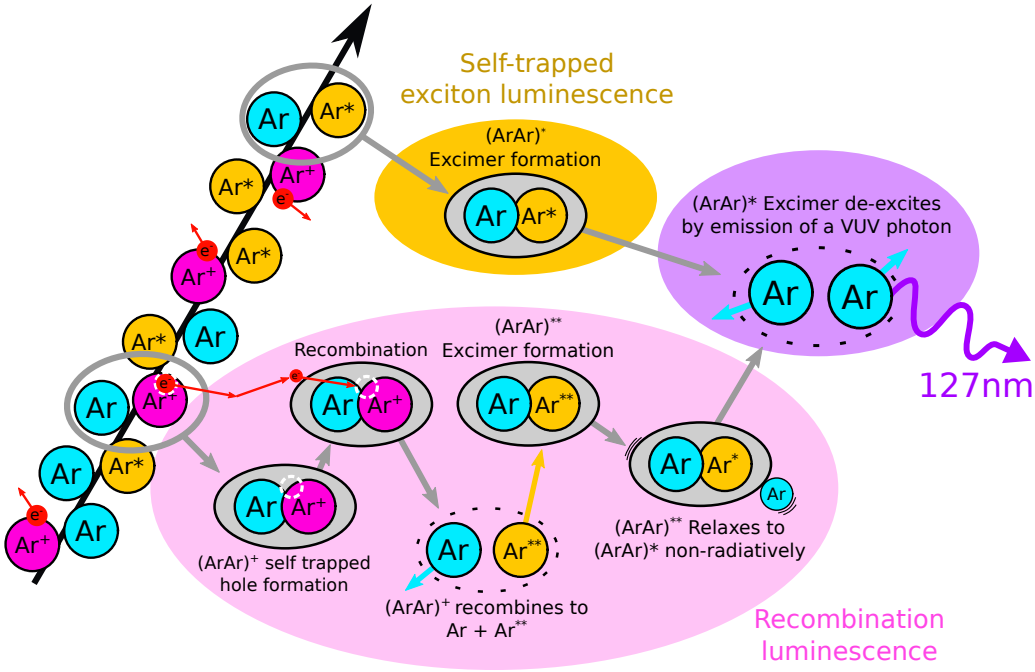

Figure 2.2: Scintillation mechanisms of Liquid Argon.

of this photon is determined by the potential difference between the excited state and the ground state. Since we see that the dip in the potential of the $(ArAr)^*$ eximer is relatively broad, the photon emitted during the transition to the ground state has a spread range of wavelengths. This spread is drawn on Figure 2.3 as ΔE. For this reason, the scintillation spectrum of Argon, as well as other noble gasses/liquids is characterised by continuous emission features, rather than the mono-energetic emission spectra that are typical of direct de-excitation. The emission spectrum of Argon is dominated by a peak at 126.8 nm $\pm$ 7.8 nm (FWHM) [45].

The triplet excimer state features a change of spin for the excited electron. Therefore, in order to decay, the excited electron must reverse this spin change. This results in the triplet decay having a much longer timescale than the singlet excimer state, which needs no such spin transition. For Liquid Argon, the singlet state is characterised by a decay time constant of 6 ns whilst the triplet state is characterised by a decay time constant of around 1500 ns, for theoretically pure liquid [46]. Due to the large difference in decay time constants, the singlet state is often referred to as the fast component and the triplet state as the slow component.

Figure 2.3 is also useful to understand why Argon is transparent to its own scintillation light. The nuclear separation distance between two ground

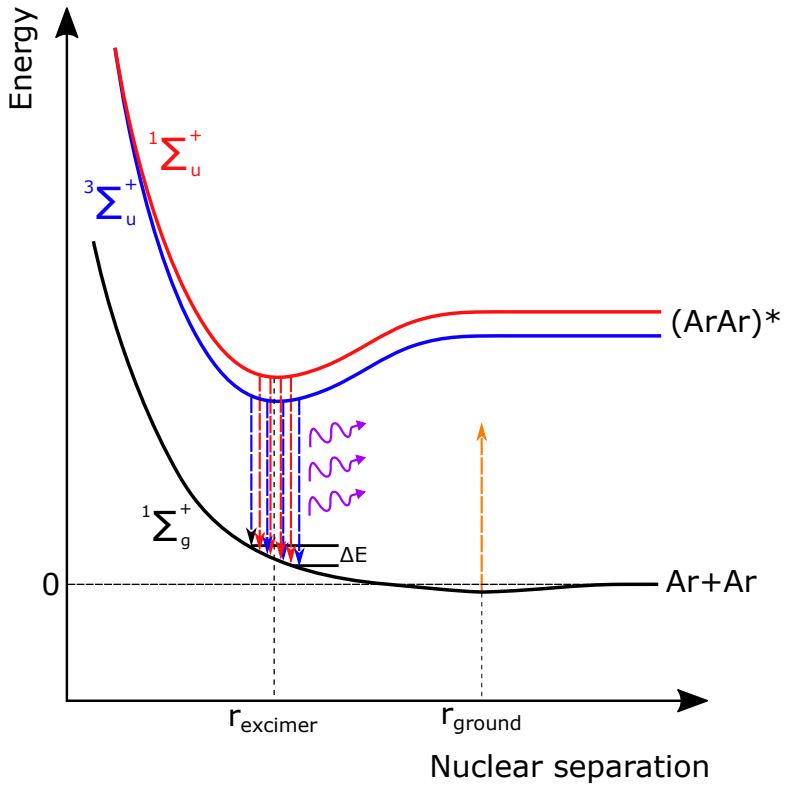

Figure 2.3: Scintillation process for Argon and other noble gasses/liquids. See [47] for a theoretical discussion of the shapes of the $^3\Sigma_u^+$ and $^1\Sigma_u^+$ potentials. The ground state nuclear separation is approximately 4Å [40]. In the excimer state, the nuclear separation is reduced to approximately 2.4Å [48]. The minimum potential in the excimer state is approximately 10.5 eV. When at the excimer nuclear separation, the ground state potential is approximately 1 eV. A VUV photon is emitted when the excimer decays, with a wavelength centered around 126.8 nm (9.8 eV).

state Argon atoms is much larger than that of Argon excimers, labeled on Figure 2.3 as r_{ground} and $r_{excimer}$ respectively. The difference in potential between both the $^3\Sigma_u^+$ and $^1\Sigma_u^+$ states to the ground state $^1\Sigma_g^+$ at $r_{excimer}$ is much smaller than at r_{ground}. Thus, it can be seen that the energy carried by the decay of the excimer is not sufficient to excite two ground state Argon atoms back to an $(ArAr)^*$ excimer (orange arrow).

Now that we understand how $(ArAr)^*$ excimers produce scintillation light in Argon, we must consider the possible ways that $(ArAr)^*$ eximers can be produced. The most straightforward method is the excitation of Argon atoms by charged particle passage. These excited Ar^* atoms immediately go on to form the $(ArAr)^*$ eximers, then decay to produce scintillation light. However, charged particle passage through Argon can also cause ionisation. The ionisation process creates Argon ions, Ar^+ and free electrons. Analogous to the formation of the $(ArAr)^*$ excimers, the newly created hole of the Ar^+ ion makes it is energetically favourable to form a bond with a nearby ground state Argon atom [49]. The resulting molecule, $(ArAr)^+$, contains what is known as a self-trapped hole. If an electron is able to re-combine with this trapped hole, the two neutral Argon atoms can be reformed. Once an electron is recombined with the self-trapped hole, it is no longer energetically favourable for the $(ArAr)^+$ molecule to exist. Thus, the two Argon atoms rapidly repel each other and disassociate. When the $(ArAr)^+$ molecule dissociates to re-form the two neutral Argon atoms, one of these atoms is produced in a highly excited state, Ar^{**}. Once again, it is energetically favourable for this highly excited Ar^{**} atom to associate with a nearby Argon atom, forming the $(ArAr)^{**}$ molecule. This $(ArAr)^{**}$ molecule undergoes a dissociation to lower excited Ar^* state plus a ground state Argon atom [50, 51], possibly by a phonon induced radiationless transition [52]. Little or no experimental data is available on this process of dissociation and the mechanism is not well understood. The remaining Ar^* is able to, as before, form an $(ArAr)^*$ excimer and finally dissociate to ground state Ar + Ar by the emission of a VUV photon. Figure 2.2 illustrates these scintillation processes.

Although Argon predominantly scintillates at 126.8 nm, a modest quantity of photons are also generated in the near-infrared (NIR), peaking at 970 nm [45, 53, 54]. The electroluminescence yield of the NIR component of Argon has been measured elsewhere to be approximately six times less than

the VUV component [54]. The detection of these NIR photons may be more straightforward than detection of the VUV component, since wavelength shifting can be avoided.

2.4.1 Quenching of scintillation light by impurities

We saw in Section 2.4 that, in Argon, scintillation light production is the result of radiative de-excitation of the $(\mathrm{ArAr})^*$ excimer. The emission of the VUV photon from either the singlet or triplet excimer state takes some time, characterised by the time constants of each process. In the case of the singlet, the time constant is τ_1 = 2-6 ns. For the triplet state, the time constant is $\tau_2 \approx 1500$ ns for perfectly pure liquid Argon.

For the excimer state to radiatively decay with the emission of a VUV photon, the excimer state must exist long enough for the process to occur. In other words, if some other process causes the excimer to de-excite non-radiatively, the emission of a VUV photon no longer occurs. It is possible that, in the presence of impurities, other processes can cause the non-radiative de-excitation of the excimer. Of particular significance is the collisional de-excitaiton of the excimer to ground state. In the presence of impurities, $(\mathrm{ArAr})^*$ can undergo a two-body collision, $(\mathrm{ArAr})^* + X \rightarrow 2\,\mathrm{Ar} + X$, where X is the impurity atom/molecule. This collisional de-excitaiton process is non-radiative, and thus the excimer no longer produces a VUV photon. This reduction in scintillation light production is known as quenching.

Given the longer decay time constant of the triplet state, it is intuitive that the triplet state is more sensitive to the presence of impurities than the singlet state. Simply put, the triplet state exists for a longer time and therefore has an increased time window to collide with impurity atoms/molecules and be de-excited collisionally. For the impurity concentrations typical in LArTPCs, the very short decay time of the singlet state makes it relatively insensitive to impurity concentration. Many studies have been performed in the literature to quantify the quenching of Argon scintillation by different impurities, X. Particular interest has been paid to those impurities which are typically found in commercial Liquid and gas Argon. High purity commercial Liquid Argon typically contains trace quantities of Oxygen, Water, Carbon monoxide, Hydrogen and other hydrocarbons, each at the $\leqslant$ 1 ppm level. Liquid Argon also typically contains trace Nitrogen at a higher level, typically $\leqslant$ 3 ppm. Carbon Dioxide is present a lower level, typ-

ically $\leqslant 0.5$ ppm. The effects of Oxygen and Nitrogen are well represented in the literature for liquid Argon [55–57]. Figure 2.4 plots the quenching factor for Oxygen and Nitrogen as a function of impurity concentration. The effects of Carbon monoxide and Hydrogen appear to have not been studied, despite their typical presence in N6.0 liquid Argon. Of all the hydrocarbons, only Methane appears to have been studied in any detail [58], yet was shown to have a substantial quenching effect, reaching a quenching factor of roughly 0.8 at only 0.1 ppm impurity. This quenching effect of Methane appears to be the strongest of all of the tested impurities. Given that commercial liquid Argon typically contains 1 ppm of trade hydrocarbons, it would seem that purification/filtration of Methane should be given some consideration.

The quenching effect of H_2O, and CO_2 have been measured in gas Argon [55] and show quenching effects similar to that of O_2. Nitrogen is consistently seen to quench scintillation light at a slower rate than other impurities. Both H_2O and O_2 are extensively purified in Liquid Argon TPCs for reasons other than scintillation light production (See Section 2.5.3). The removal of H_2O and O_2 is typically so effective that they should have essentially zero impact on scintillation light production. Filtration of Nitrogen and other proven quenchers is typically not performed. Perhaps an improvement of scintillation light production may be possible if the filtration of Nitrogen, and possibly Methane and other unknown hydrocarbons, is considered.

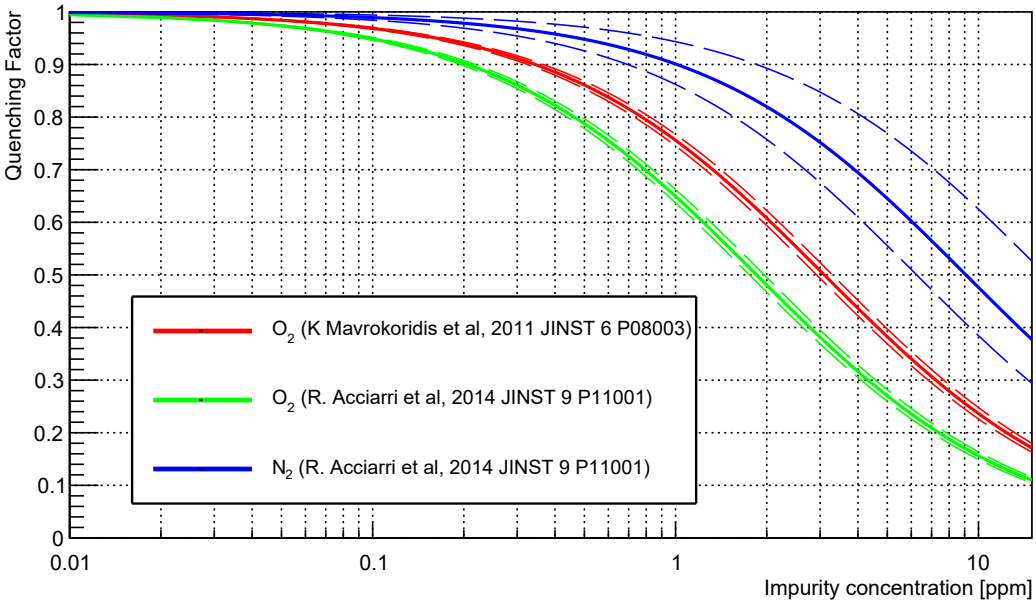

Figure 2.4: Relative quenching effects of O_2 and N_2. Oxygen is consistently seen to quench light production for any concentration greater than 0.1 ppb.

2.5 Electron transport

In order to operate as a TPC, the ionised charge must be collected. An externally applied electric field induces the net motion of the ionised electrons, typically directing them towards a readout device. This net motion of electrons in the Liquid Argon is called drift. As we saw in Section 2.3.1, the fraction of electrons that survive recombination, and thus are detectable, is dependent on the magnitude of the electric field. For a MIP, at 0.5 kV/cm, the recombination factor is approximately 0.7. This means that approximately 70 % of electrons are available for detection, whilst 30 % recombine. The nature of a TPC is that the z dimension (the direction along the drift) is not explicitly detected. The z position is instead inferred, assuming a known drift velocity of the electrons in the TPC. This assumption of course requires that the drift velocity be known precisely for best possible resolution in z.

In general, the collective motion of a charge cloud in Liquid Argon can be described by the combination of several effects. First, there may be a net motion of the charge cloud as the result of an applied electric field. Secondly, over time, the charge cloud can diffuse and grow in space. Finally, the total number of electrons in the charge cloud can change. Attachment of the electrons to electronegative impurities causes the net reduction in the number of electrons. At very high electric fields, ionisation could cause an increase in the net number of electrons in the charge cloud. Ionisation is not present at the drift fields typical used and so in general the net number of electrons in the charge cloud tends only to decrease during the drift. These collective effects may be described using Fick's equation [59, 60]. Let $\boldsymbol{n}$ describe the development of the charge cloud in (x, y, z, t). The drift field is applied in the $+z$ direction. Under these circumstances, Fick's equation can be expressed as:

$$\frac{\partial \boldsymbol{n}}{\partial t} = D_L \frac{\partial^2 \boldsymbol{n}}{\partial z^2} + D_T \left(\frac{\partial^2 \boldsymbol{n}}{\partial x^2} + \frac{\partial^2 \boldsymbol{n}}{\partial y^2} \right) - v \frac{\partial^2 \boldsymbol{n}}{\partial z} - \lambda v \boldsymbol{n} \tag{2.8}$$

The coefficients D_L and D_T parameterise the rate of diffusion in the longitudinal and transverse planes, respectively. The negative sign in front of the $-v\partial^2 \boldsymbol{n}/\partial z$ term is explained by the fact that electrons drift in the opposite direction of the drift field. In other words, the net motion of electrons is backwards along the field lines of the drift field. Since we assumed the

drift field was applied in the $+z$ direction, the net motion of the charge cloud is in the $-z$ direction. λ parameterises the loss or gain of electrons by impurity attachment or ionisation. As mentioned earlier, λ almost exclusively describes losses by attachment to impurities. The general solution to Equation 2.8 is given by:

$$\boldsymbol{n} = \frac{n_0}{4\pi D_T t\sqrt{4\pi D_L t}} \underbrace{\exp\left(-\frac{(z-vt)^2}{4D_L t}\right)}_{\substack{\text{Longitudinal}\\ \text{diffusion}}} \underbrace{\exp\left(\frac{x^2+y^2}{4D_T t}\right)}_{\substack{\text{Transverse}\\ \text{diffusion}}} \underbrace{\exp\left(-\lambda v t\right)}_{\substack{\text{Impurity}\\ \text{attachment}}} \quad (2.9)$$

where n_0 is the number of electrons at $(x, y, z) = (0, 0, 0)$ at $t = 0$. This solution neatly decomposes into three distinct exponentials. Models for both longitudinal and transverse diffusion are discussed in Section 2.5.2. Models for the drift velocity, v, are discussed in Section 2.5.1. Finally, a discussion of λ, the attachment of electrons to impurities, is given in Section 2.5.3.

2.5.1 Electron drift velocity

In 2000, W. Walkowiak studied the drift velocity of electrons in Liquid Argon over a large range of drift fields (0.5 kV/cm - 12.6 kV/cm) [61]. Given that 0.5 kV/cm is the nominal operating field of many experiments, the lower limit of the work performed by W. Walkowiak was not ideal. In 2004, the ICARUS collaboration performed a study, extending the measurements of electron drift velocity to a range more suitable to LArTPCs (0.056 kV/cm - 1 kV/cm) [62]. This study found results that were in good agreement with the model proposed by W. Walkowiak, in the range that Walkowiak originally proposed. Below to 0.5 kV/cm the measured drift velocities began to diverge from the predictions of the model. Considering the lower limit that W. Walkowiak proposed of 0.5 kV/cm, this is perhaps unsurprising. The ICARUS study did not propose any new function to describe their experimental data. A good fit to their data was possible by fitting of the empirical function proposed by W. Walkowiak, although the fit parameters were not published.

Electron mobility is defined as $\mu = v_d/E$ where v_d is the electron drift velocity and E is the electric field. This relationship implies that, if E is very well known, a theoretical model for μ should translate well to a theoretical model of v_d. In 2016, a study was performed of both electron diffusion

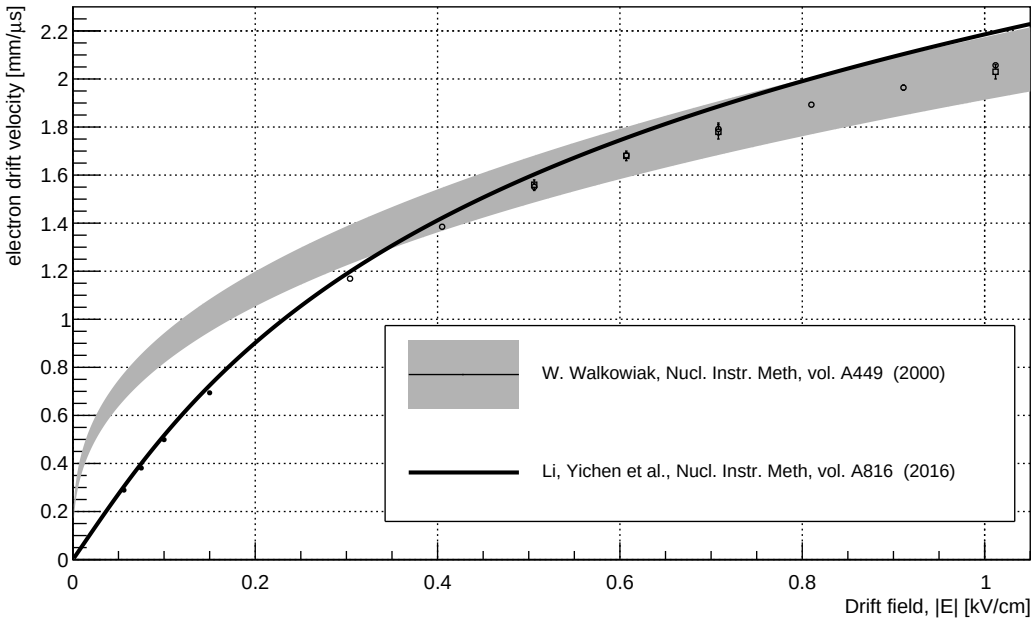

Figure 2.5: Comparison between theoretical electron drift velocity models. The model of W. Walkowiak [61] was first proposed in 2000, focused towards very large drift fields, greater than 0.5 kV/cm. Later, in 2016, Yichen et al proposed a new model [62] which better describes experimental data across the working range of most liquid Argon TPCs.

and electron drift velocity in Liquid Argon [44], which performed a series expansion of electron drift velocity. The study also performed a global fit of a large selection of the world's data for electron mobility in LAr. The model presented in the paper is a parameterisation of μ, the electron mobility, but we will recast it as a parameterisation of v_d using $\mu = v_d/E$. We have

$$v_d = \frac{a_0 E + a_1 E^2 + a_2 E^{5/2} + a_3 E^{7/2}}{1 + (a_1/a_0)E + a_4 E^2 + a_5 E^3} \left(\frac{T}{T_0}\right)^{-3/2} \tag{2.10}$$

where E is the drift field in units of kV/cm and v_d is the drift velocity in cm/s. The reference temperature, T_0 was fixed at 89 K in this model. The values of a_0 through a_5 are given in [44] as $a_0 = 551.6$, $a_1 = 7953.7$, $a_2 = 4440.43$, $a_3 = 4.29$, $a_4 = 43.63$ and $a_5 = 0.2053$.

Figure 2.5 plots this model as a function of drift field. Also overlaid onto figure 2.5 are the experimental data, published by ICARUS in 2004. The original model proposed by W. Walkowiak is seen with a 1σ error band. Figure 2.5 clearly demonstrates the tension between the model of W. Walkowiak and experimental data below 0.5 kV/cm.

2.5.2 Electron diffusion

Throughout the process of drifting, a charge cloud will diffuse in both longitudinal and transverse planes. The parameter D_L describes the diffusion in the longitudinal plane, the drift direction, and the parameter D_T describes the diffusion in the transverse plane, perpendicular to the drift. Both transverse and longitudinal diffusion is Gaussian in space, with standard deviations given by

$$\sigma_T = \sqrt{2D_T t} \tag{2.11}$$

$$\sigma_L = \sqrt{2D_L t} \tag{2.12}$$

The most successful parameterisation of D_T and D_L is proposed in [44], and can be written as

$$D_L = \left(\frac{a_0 + a_1 E + a_2 E^{3/2} + a_3 E^{5/2}}{1 + (a_1/a_0)E + a_4 E^2 + a_5 E^3}\right)\left(\frac{b_0 + b_1 E + b_2 E^2}{1 + (b_1/b_0)E + b_3 E^2}\right)\left(\frac{T}{T_1}\right)\left(\frac{T}{T_0}\right)^{-3/2} \tag{2.13}$$

where we have two reference temperatures, T_0 and T_1. This is an artifact from the methodology used to produce this parameterisation. First, a global fit was performed on electron mobility, μ. For this global fit, a reference temperature of $T_0 = 89$ K is used. Next, a secondary parameterisation was developed for the effective longitudinal electron energy, ϵ_L. For this parameterisation, the more suitable reference temperature was $T_1 = 87$ K. Thus, when determining $D_L = \mu\epsilon_L/e$, two reference temperatures are introduced.

The parameterisation for D_T is not given directly, but D_L and D_T are related according to

$$D_T = \frac{D_L}{1 + \frac{E}{\mu}\frac{\partial \mu}{\partial E}} \tag{2.14}$$

The derivation of D_T, although relatively straightforward, is protracted. The result can be found in Appendix A.

We can see from Equation 2.13 that both D_L and D_T are dependent on both the temperature of the Liquid Argon and the applied drift field. The Longitudinal diffusion coefficient, D_L, is plotted in Figure 2.6 as a function of drift field for three different temperatures, 87 Kelvin, 85 Kelvin

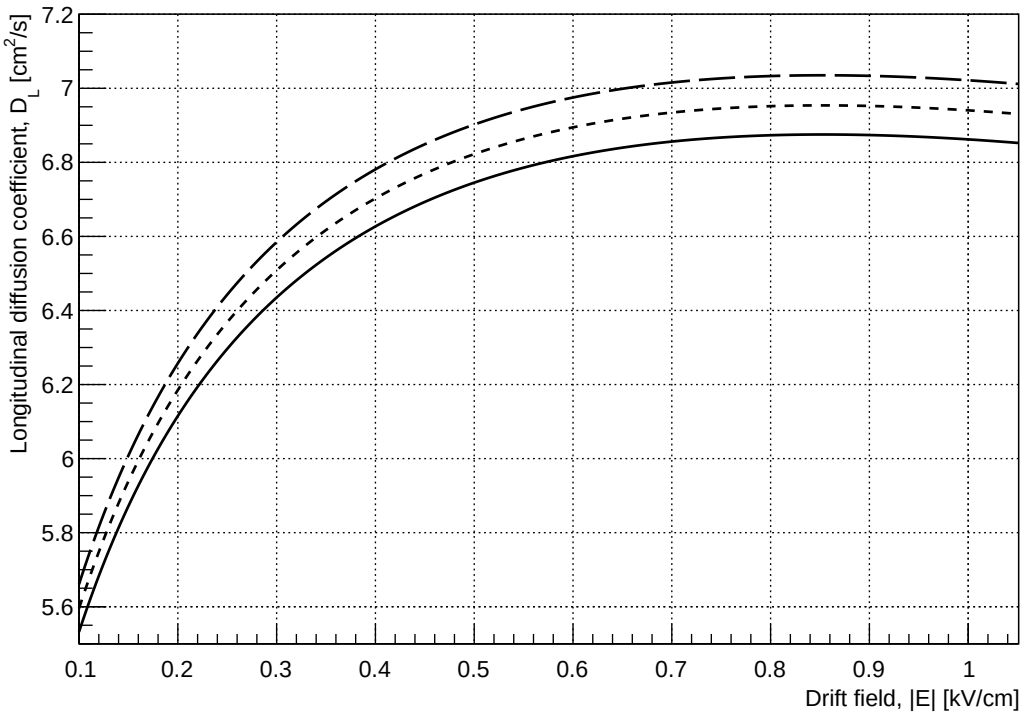

Figure 2.6: Predictions of the model shown in Equation 2.13 of the longitudinal diffusion coefficient for three temperatures, 87 Kelvin (long dashed line), 85 Kelvin (dashed line) and 83 Kelvin (solid line).

and 83 Kelvin. The transverse diffusion coefficient, D_T, is plotted in Figure 2.7, again as a function of drift field for the same three temperatures.

As we saw from Equations 2.11 and 2.12, the diffusion coefficients are related to the standard deviation of the physical diffusion of the charge cloud that can be expected after a drift of time t. Given that detector dimensions are more easily understood in terms of drift length, rather than drift time, we will take the liberty to recast these formulae as a function of drift length, using $v_d = d/t$. Since we already introduced a modern, accurate, parameterisation for v_d in Section 2.5.1, this transformation is trivial. Thus, we can now present plots of transverse and longitudinal diffusion as a function of drift length. Figure 2.8 plots the standard deviation of the transverse diffusion as a function of drift length for a liquid Argon temperature of 87 Kelvin. This plot shows three curves, for three different drift fields, 0.25 kV/cm, 0.5 kV/cm and 1 kV/cm. We see that the total transverse diffusion is mostly sensitive to drift length, with only a subtle dependence on drift field, at least for values of drift fields greater than 0.25 kV/cm. Below 0.25 kV/cm, a significant increase in transverse diffusion starts to becomes

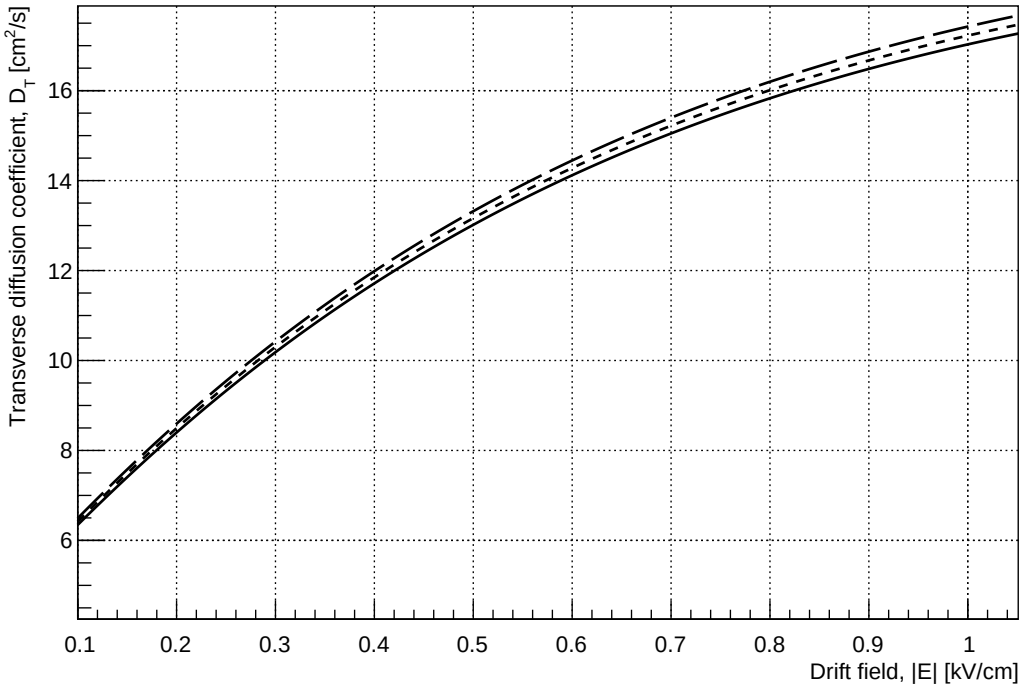

Figure 2.7: Predictions of the model shown in Equation 2.14 of the transverse diffusion coefficient for three temperatures, 87 Kelvin (long dashed line), 85 Kelvin (dashed line) and 83 Kelvin (solid line).

visible.

We can also plot longitudinal diffusion as a function of liquid Argon temperature, for a fixed drift field. Figure 2.9 plots the standard deviation of longitudinal diffusion for three temperatures, 87 Kelvin, 85 Kelvin and 83 Kelvin. The difference between the three curves is subtle yet highlights an important point that Liquid Argon temperature must be well understood in a detector. Any temperature gradients in the Liquid Argon causes a gradient in drift velocity throughout the detector volume.

Finally, we will consider the transverse diffusion that we can expect in the ARIADNE detector. We will constrain the detector length to 80 cm, and fix the Liquid Argon temperature to 87 Kelvin. Figure 2.10 plots the theoretical standard deviation transverse diffusion in the ARIADNE detector as a function of drift field. We can see that above about 0.2 kV/cm, the transverse diffusion is large insensitive to drift field (note the small range on the y-axis). At the nominal drift field of 0.5 kV/cm, the predicted transverse diffusion for a track drifted from the cathode is predicted as between 1.1 mm and 1.15 mm.

Now we must consider longitudinal diffusion, along the direction of the

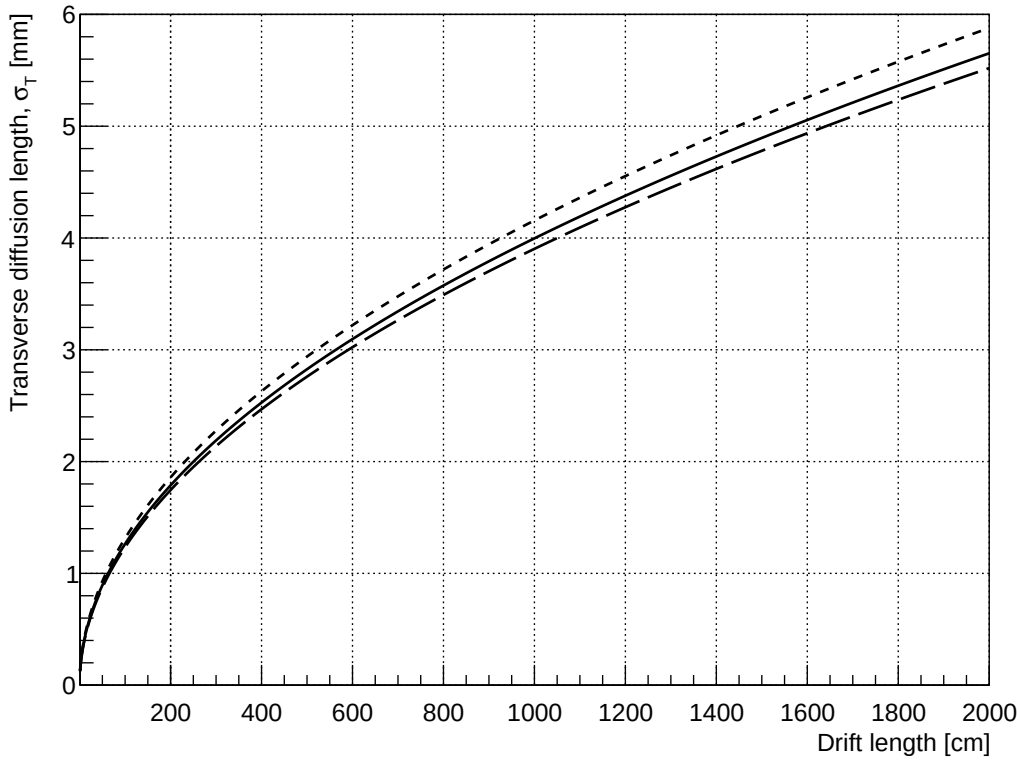

Figure 2.8: Predictions of the standard deviation of transverse diffusion, in mm, as a function of drift length for three different drift fields: 0.25 kV/cm (long dashed line), 0.5 kV/cm (dashed line) and 1 kV/cm (solid line).

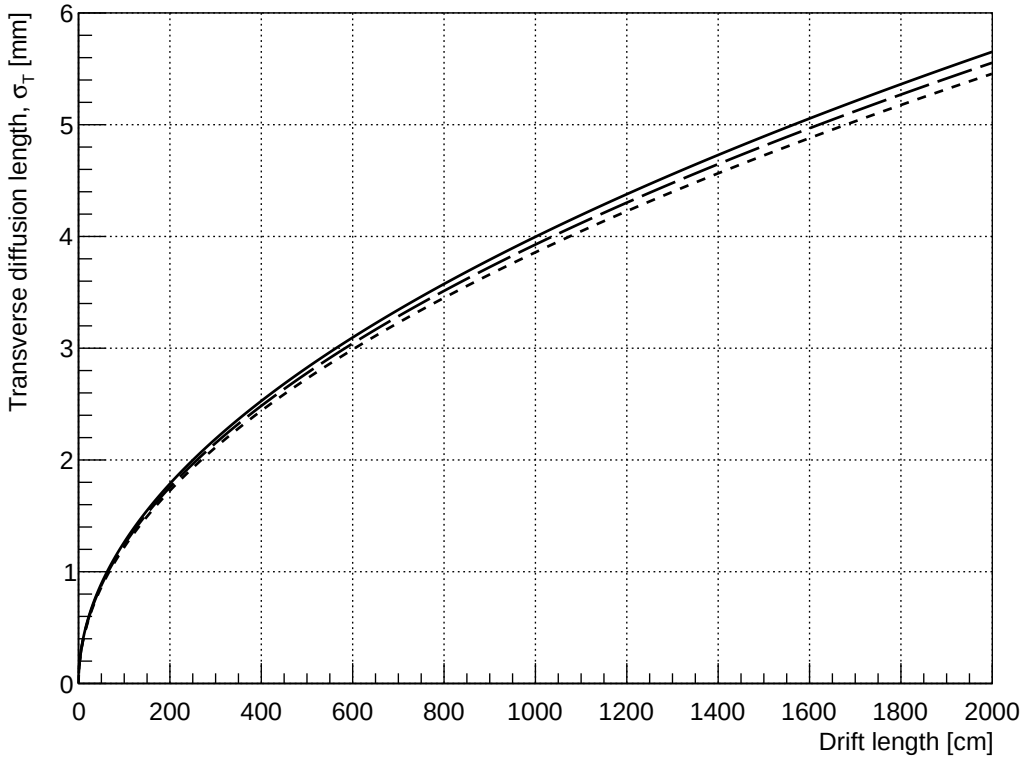

Figure 2.9: Predictions of the standard deviation of transverse diffusion, in mm, as a function of drift length for three different Liquid Argon temperatures: 87 Kelvin (dashed line), 85 Kelvin (long dashed line) and 83 Kelvin (solid line).

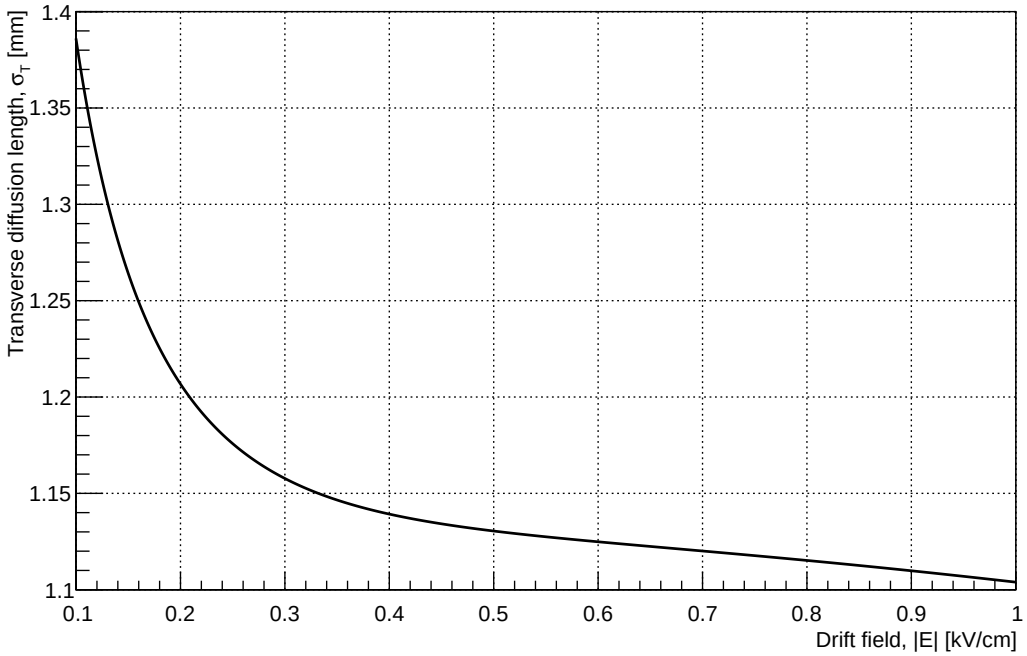

Figure 2.10: Predicted transverse diffusion for the ARIADNE detector as a function of drift field. This prediction is for electrons which have drifted the full length of the ARIADNE TPC, 80 cm. Only very modest improvements in transverse diffusion are seen across a wide range of drift fields, from 0.1 kV/cm, up to 1 kV/cm. Very little improvement in transverse diffusion is predicted when increasing the drift field above the nominal operating field of 0.5 kV/cm.

drift. In the case of a TPC, it does not make much sense to discuss this diffusion in terms of physical distance, but rather time. We will adopt the notation proposed in [44] and talk about 'diffusion time'. The spread of the charge cloud in the transverse plane adds a timing component to the arrival of the charge signal at a readout device. For most typical detector dimensions we can consider this time to be approximately Gaussian. This diffusion time is given as

$$\sigma_L \approx \sqrt{\frac{2dD_L}{v^3}} \tag{2.15}$$

where d is the drift distance and v is the drift velocity. D_L is the longitudinal diffusion coefficient. σ_L has units of time and represents the degradation of timing resolution of a charge cloud due to diffusion during the drift. Figure 2.11 plots the standard deviation diffusion time as a function of drift length for three different drift fields, 0.25 kV/cm, 0.5 kV/cm and 1 kV/cm. We see that the diffusion time responds considerably to increasing drift field. Thus, when considering readout electronics for any realistic detector, care must be taken that the shaping time of the readout electronics are compatible with the expected diffusion time for the range of drift fields over which the detector will be operated. The fact that longitudinal diffusion time is more sensitive to drift field than transverse diffusion is not surprising if we compare Figures 2.6 and 2.7. The longitudinal diffusion coefficient is seen to plateau after around 0.4 kV/cm, whereas the transverse diffusion coefficient is seen to be always steadily rising.

2.5.3 Electron attachment to impurities

There are several mechanisms by which the purity of a Liquid Argon may be disturbed. The initial Argon used to fill the detector generally contains trace amounts of Oxygen (1 ppm), Water (1 ppm), Nitrogen (3 ppm), Hydrogen (1 ppm), Carbon Monoxide (1 ppm), Carbon Dioxide (0.5 ppm) and Hydrocarbons (1 ppm total). Trace quantities of air may also be present in the detector volume, either through incomplete purging of the detector volume before filling, or introduced over time through leaks. Air contamination mainly introduces additional Nitrogen and Oxygen impurities but trace additions of Water, Carbon dioxide and methane are possible depending on climate. Outgassing of detector components can also introduce further im-

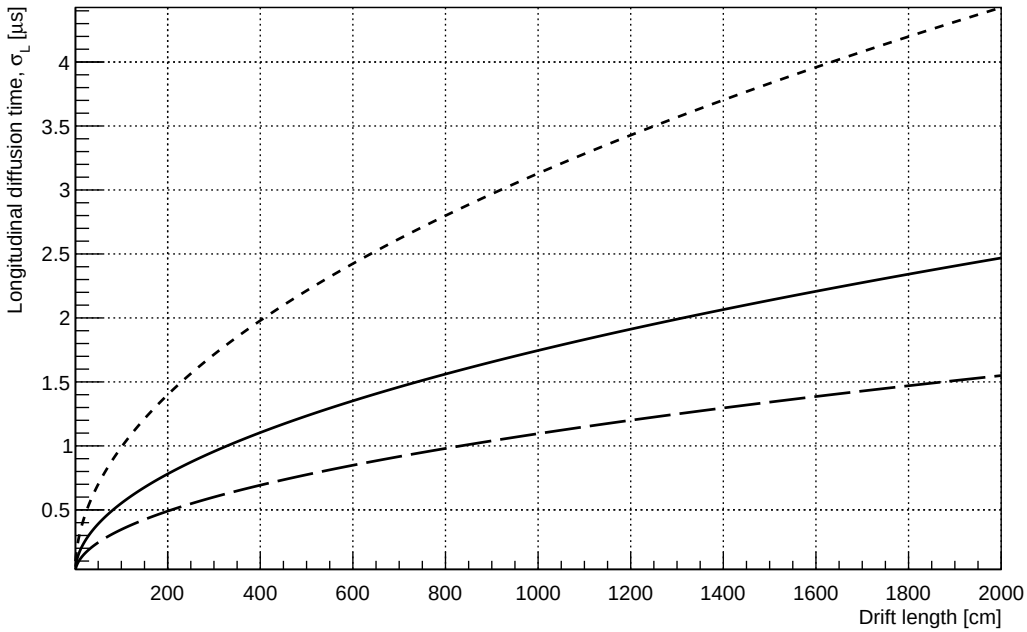

Figure 2.11: Predictions of Longitudinal diffusion time, as a function of drift length for three different drift fields: 0.25 kV/cm (dashed line), 0.5 kV/cm (solid line) and 1 kV/cm (long dashed line). When compared to transverse diffusion, changes in drift field have a large effect on longitudinal diffusion.

purities. This outgassing component can sometimes be especially insidious since outgassing products can contain impurities which are difficult to purify using standard filtration systems. Since the exact composition of outgassing components is difficult to predict, re-circulation and purification systems are typically not designed to filter them.

In Liquid Argon the main process by which impurities can capture electrons is by the so called three-body attachment. The stable capture of an electron by impurities through this process requires several conditions to be met. First, the impurity must make an initial capture of the electron, forming an excited ion state. This excited ion state is formed with sufficient energy to eject the electron and so a third atom/molecule must be present to stabilise the capture. This third atom/molecule allows the excited ion to de-excite collisionally, forming a stable ion state. The total rate by which electrons are captured by impurities is thus defined by the rate of two distinct processes; The rate at which the impurities can capture electrons and the rate at which the newly formed excited ions can de-excite to a stable ion. In the case of a LArTPC, this third body is almost exclusively an Ar atom.

The rate by which electronegative impurities capture electrons is defined by a rate constant, k. Since the cross section of the electron capture process is dependent on the kinetic energy of the drifting electron, k is a function of the drift field. The rate of electron loss in the TPC is related to k according the following differential equation

$$\frac{\partial N}{\partial t} = -kN \tag{2.16}$$

Although it would seem that a theoretical framework exists for predicting k for various impurities in Liquid Argon [63], all of the currently available information is the result of direct experimental measurements of k for various impurities. As a result, k is only known for a certain subset of impurities. Equation 2.16 has the solution

$$N = N_0 e^{-kt} \tag{2.17}$$

where, if we now define the electron lifetime as $\tau = 1/k$, we have

$$N = N_0 e^{-t/\tau} \tag{2.18}$$

Electron lifetime is the probably the most commonly used parameter to quantify the effect of impurities in a LArTPC.

Summarising results from [64], at 0.5 kV/cm; The attachment rate of Oxygen is almost an order of magnitude higher than Nitrous oxide. Again at 0.5 kV/cm, the rate constant for carbon dioxide is more than an order of magnitude lower than that of Oxygen [65]. The attachment rate of Sulfur hexafluoride is very high, almost three orders of magnitude more than Oxygen but this molecule is rare in commercial LAr, although may be present in air at the ppt level [66]. Given that Oxygen makes up 20% of air, a leak in a detector would cause more electrons to be lost by attachment to Oxygen, even given the high attachment rate of Sulfur hexafluoride, due to its exceptionally low trace presence in air. Nitrogen is assumed to not affect drifting electrons, probably due to having no electronegativity [67]. Water is known to attach to drifting electrons, [68] at a rate comparable to oxygen. It has been suggested that water is the only significant contaminant that is introduced by outgassing of materials [69]. It does not appear that the attachment rate is known for any of Hydrogen, Carbon Monoxide or other

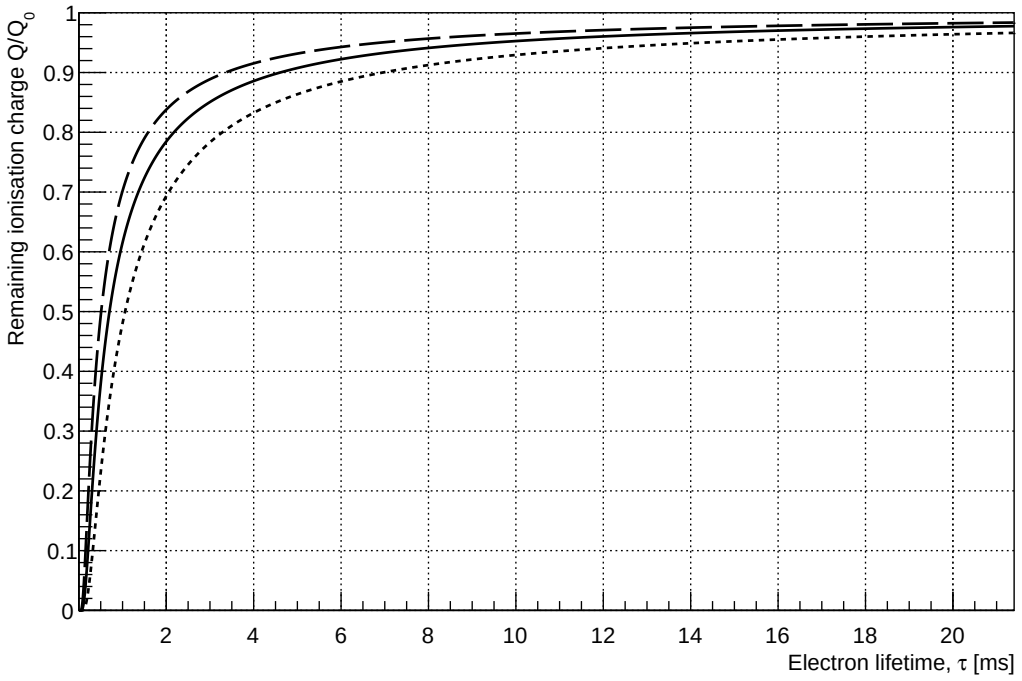

Figure 2.12: Predictions of electron losses to attachment to impurities as a function of electron lifetime, for the drift length of the ARIADNE detector. Results are plotted for three drift fields, 0.25 kV/cm (dashed line), 0.5 kV/cm (solid line) and 1 kV/cm (long dashed line). At low electron lifetimes, increasing the drift field can have a substantial effect on electron losses to impurities. Electron lifetimes in the range of 3-10 ms are somewhat typical for well purified Liquid Argon.

hydrocarbon impurities.

We saw from Equation 2.18 that the number of electrons lost to impurities is given by $\exp(-t/\tau)$, where τ is the electron lifetime. The exponential nature of the loss makes retaining 100% of the ionisation signal practically impossible. If we consider ARIADNE, with 80 cm drift length, we can quantify the effect of electron lifetime and the effect of impurities on drifting electrons. Plotted in Figure 2.12 is the ratio of initial ionised charge that survives a 80 cm drift, Q/Q_0, as a function of electron lifetime, for three drift fields, 0.25 kV/cm, 0.5 kV/cm and 1 kV/cm. The upper limit of electron lifetime on this plot is fixed at 21.4 ms, the highest known lifetime that has been achieved [70]. At low electron lifetimes ($\tau < 1$ ms), an increase in drift field can have a substantial effect on the loss of electrons to impurities. Methods for the purification of Liquid Argon are discussed in Section 4.10.

2.6 Single phase readout

Given the nature of this Thesis, single phase readout will be discussed only in passing to provide a more complete context of Liquid Argon detector technologies. Single phase detectors rely on placing charge readout devices in the Liquid Argon phase. Thus, the signal that is created in the liquid phase is readout in the Liquid phase. There is some freedom in which approach is used to readout the charge signal, for example pixel based or strip (wire) based readout. By far the most common approach has been strip (wire) based, although pixel based readout has been explored recently [71]. We will focus here on strip (wire) based readout.

In order to reconstruct an event in a LArTPC with a strip based readout approach, two (or more) readout planes are required. With a single wire, there is ambiguity about where along the wire the signal was received from. To combat this ambiguity, another plane of wires, rotated at an angle relative to the first, can be used to constrain the position on the wire where the signal originates from. Several parameters are tunable when designing such a wire based readout approach including the spacing between wires and the relative angle between both wires planes. A popular approach is to use three wires planes, arranged roughly 30-40 degrees relative to one another. The use of three wire planes over two provides improved reconstruction capability and reduced possibility of ambiguities.

In order to maximise signal collection efficiency, two wire planes can be biased to a positive voltage. When an electron cloud passes by these wires, it is deflected around them. The signal on this wire is caused by induction, rather than collection. The final plane of wires performs charge collection. Thus, there are two induction planes and one collection plane.

Single phase readout has a very successful history, with almost all of the historically famous detectors being readout in this way. Well known examples include ICARUS [72], MicroBooNE [73], SBND [74] and Single-Phase ProtoDUNE [75].

2.7 Dual-phase readout

Dual-phase TPCs were proposed as a way to exploit developments in micropattern gas detectors (MPGDs). As their name would suggest, MPGDs generally perform best in a gas phase. Severely reduced performance is however still possible in the liquid phase. To take full advantage of a MPGD, the electron signal in the Liquid argon must be transferred from the liquid phase to the gas phase, by a process known as electron extraction.

2.7.1 Extraction of electrons from liquid to gas

The emission of electrons from the liquid to gas phase has been well studied [76]. The process is known to have two components in time. The first emission component, which is very fast, $\mathcal{O}(ns)$, is the combination of several processes, all of which happen on a fast timescale. In order for an electron to cross the Liquid/gas interface it must have sufficient kinetic energy, perpendicular to the interface. This condition gives rise to an electric field dependence of the electron extraction efficiency. At higher electric fields, the electrons are more energetic and are therefore more likely to meet the emission condition. The extraction of electrons which meet the emission condition is very fast, $\mathcal{O}(ns)$. It is possible that, on the first attempt, the electrons do not meet the emission condition, perhaps due to a collision with an Argon atom very close to the interface, resulting in the electron having insufficient kinetic energy perpendicular to the interface to be extracted. In case the electrons do not meet the emission condition, they will be reflected off the interface. Following this reflection, the electrons are again accelerated towards the boundary by the electric field. Depending on the collisions experienced between the electrons and the Argon atoms near the interface, it may take several repeated attempts before the electrons meet the emission condition and are extracted. These repeated reflections occur very quickly, $\mathcal{O}(ns)$. The fast component of electron emission is the sum of those electrons which are directly emitted over the potential barrier on the first attempt, as well as those electrons which reflect off the potential barrier but eventually, after one or several reflections, meet the emission criteria and are extracted into the gas phase.

Each reflection at the boundary causes the electrons to lose a small fraction of their kinetic energy. If, after many collisions, the electrons still

never meet the emission criteria, they may lose enough energy as to become trapped at the boundary. The electrons will continue to reflect off the boundary, with energy provided by the electric field. The slow component of electron emission results from these electrons which fail to cross the potential barrier, even after repeated attempts. These 'cold' electrons are eventually emitted by thermionic emission. The electrons are 'heated' by the applied electric field across the boundary. The probability, and thus the rate, of electron emission across the boundary depends on the magnitude of the applied electric field.

Experimental data for the emission time constant for electrons as a function of electric field in Liquid Argon is quite limited. [77] presents the most comprehensive dataset in the range 0.1 - 0.5 kV/cm. Extension of measurements beyond this range were more recently performed [76], extending the measured range up to 1.71 kV/cm. Although some measurements appear to extend the tested range up to 4 kV/cm [78], the test procedure was not sensitive to the emission time constant. Several models have been proposed to describe the emission time as a function of electric field. The first, and most simple model, predicts that

$$\tau = \frac{\lambda_1}{\mu E} \exp\left(\frac{V_0}{k_B T}\right) \tag{2.19}$$

where λ_1 is the electron mean free path in the Liquid, μ is the electron mobility, E is the electric field in the extraction region, V_0 is the potential barrier at the liquid/gas interface, k_B is Boltzmann's constant and T is the liquid Argon temperature. When attempting to fit this model to experimental data, μ is often treated as a constant as a function of E. Although we now know this to not be true, this assumption was typical at the time when this model was proposed [76] and [77]. This assumption allows us describe the model in terms of a single free parameter, A, as

$$\tau = \frac{A}{E} \tag{2.20}$$

The result of such a fit to experimental data can be seen in Figure 2.13. Although perhaps reasonable at higher fields, the tension is clear. Thus, we can probably conclude that either that the model is not appropriate or that the assumption that μ is a constant is invalid. Given that, in Section 2.5.1,

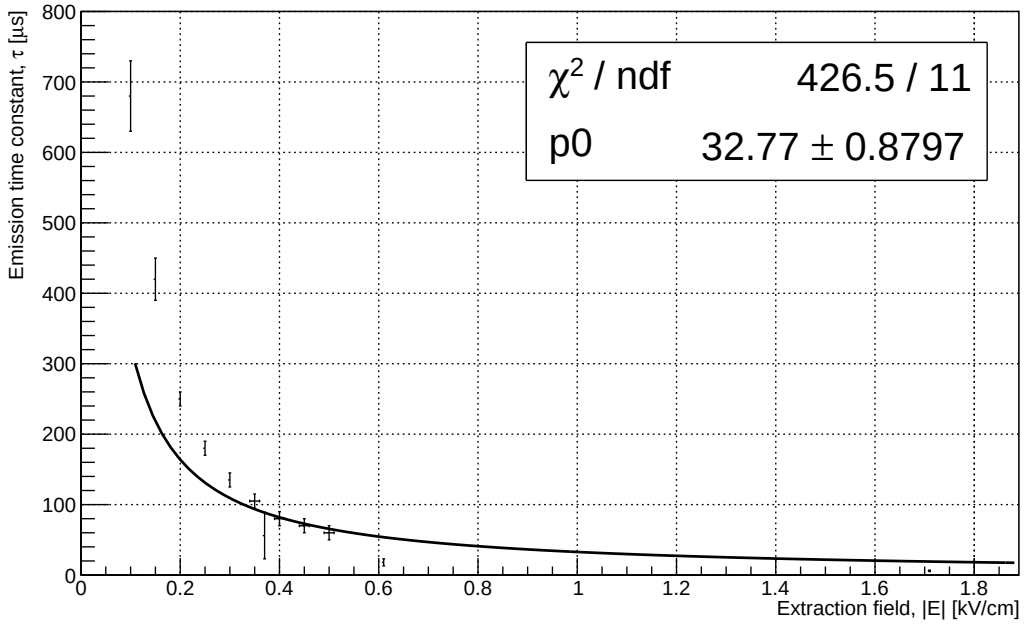

Figure 2.13: Predictions of extraction region emission time constant as a function of extraction field, according to Equation 2.21.

we already presented a model for μ as a function of E, it is unsurprising that the assumption of constant μ is flawed. We can try, using the $\mu(T, E)$ model that was not available to the authors at the time of their publication, to improve the assumption of constant μ. The model will be

$$\tau = \frac{A}{\frac{a_0 E + a_1 E^2 + a_2 E^{5/2} + a_3 E^{7/2}}{1 + (a_1/a_0) E + a_4 E^2 + a_5 E^3} \left(\frac{T}{T_0}\right)^{-3/2}} \tag{2.21}$$

where we assume that the Liquid Argon temperature is 87 K at the interface for simplicity. The result of this fit is even worse than of the fixed μ assumption. We can probably conclude that neither of these models is appropriate.

One limitation of the models presented in Equations 2.20 and 2.21 is that the potential at the Liquid/Gas interface is assumed to be constant. In fact, we can expect this potential to vary as a function of electric field, according to the Schottky effect. The Schottky effect serves to lower the potential barrier, increasing the rate of thermionic emission. We can express the Schottky effect corrected emission lifetime as

$$\tau = \frac{\lambda}{\mu E} \exp\left(-\frac{V_0 + \Delta V}{k_B T}\right) \tag{2.22}$$

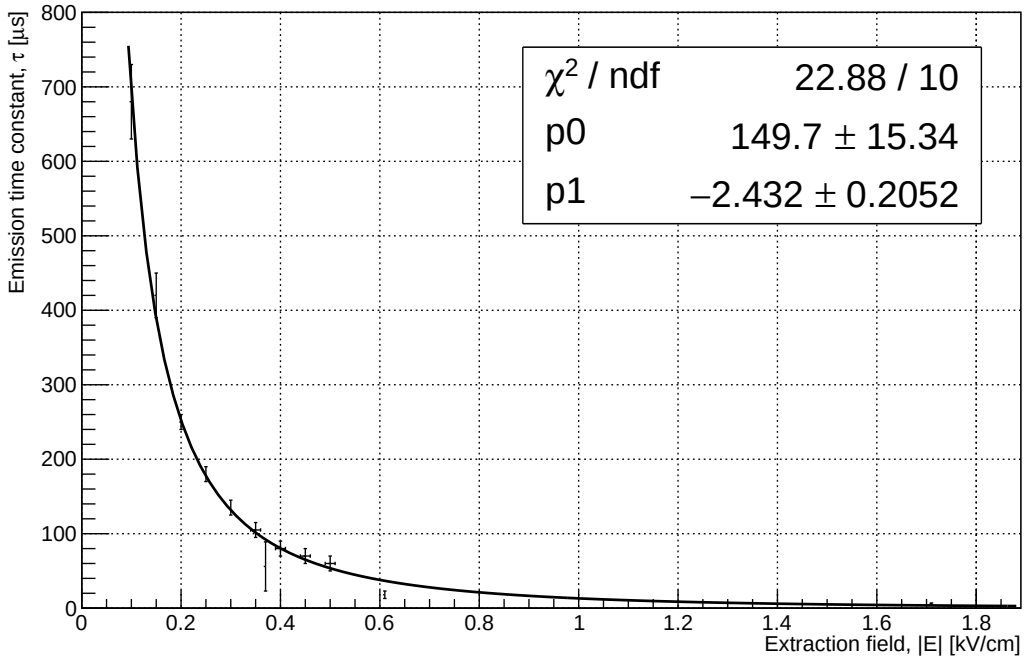

Figure 2.14: Predictions of the extraction region emission time constant as a function of extraction field, according to Equation 2.24. The additional of a Schottki correction factor provides a large improvement in the perceived fit of the model.

where ΔV is the perturbation in the potential barrier due to the Schottky effect, given by

$$\Delta V = e\sqrt{\frac{\varepsilon_L - 1}{\varepsilon_L + 1}\frac{eE}{4\pi\varepsilon_0}} \tag{2.23}$$

Where e is the electron charge, ε_L is the dielectric constant of Liquid Argon (1.503 ± 0.003) and ε_0 is the permittivity of free space. We can again consider this model in the case of constant μ or parametric $\mu(T, E)$. In the case of fixed μ, we can express Equation 2.22 as a function of the form

$$\tau = \frac{A}{E}\exp\left(B\sqrt{E}\right) \tag{2.24}$$

where A parameterises $\lambda/\mu\exp\left(-V_0/k_BT\right)$ and B parameterises all of the constant terms in $\Delta V/k_BT$. The results of the fit can be seen in Figure 2.14. The Schottky effect corrected model clearly represents a significant improvement. This may be considered good evidence for the presence of the Schottky effect on the Liquid/gas interface in LAr.

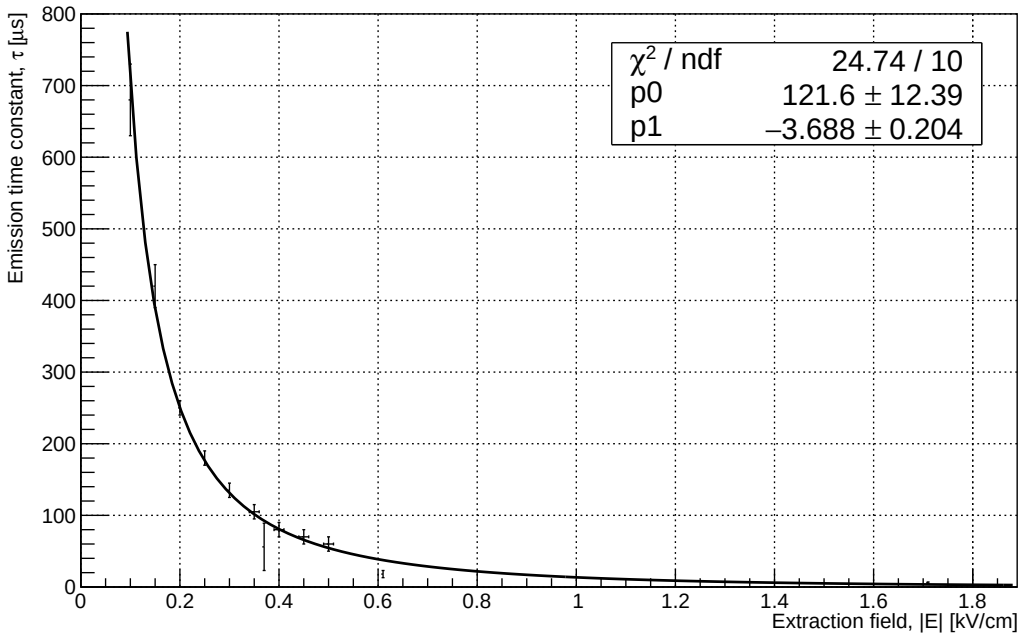

Figure 2.15: Predictions of the extraction region emission time constant as a function of extraction field, according to Equation 2.25, which additionally includes the model of parametric electron mobility. The perceived fit of the model is similar to that of Figure 2.15, but an incompatibility of fit parameters is apparent.

Since the model of parametric $\mu(T, E)$ was only developed in 2015, the Authors of both [76] and [77] could not have developed a model of electron extraction using this knowledge. We can attempt to extend the model of Equation 2.22 to include the effects of parametric $\mu(T, E)$. The new model may be expressed as

$$\tau = \frac{A}{\frac{a_0 E + a_1 E^2 + a_2 E^{5/2} + a_3 E^{7/2}}{1 + (a_1/a_0) E + a_4 E^2 + a_5 E^3} \left(\frac{T}{T_0}\right)^{-3/2}} \exp\left(B\sqrt{E}\right) \tag{2.25}$$

The results of this fit are shown in Figure 2.15. No significant difference is seen between a fit using parametric μ or constant μ, at least in terms of χ^2. What does start to become apparent between these two models however is some tension in the fit parameters. The model with parametric $\mu(T, E)$ prefers a significantly higher value for the constant B, so different from the model of constant μ as to be incompatible. Let's take a closer look at what is defined by the parameter B. The parameter B, in both models, is defined

as

$$B = \frac{e\sqrt{\frac{\varepsilon_L - 1}{\varepsilon_L + 1}\frac{e}{4\pi\varepsilon_0}}}{k_B T} \tag{2.26}$$

Given that every term in this expression is known, we can compare the prediction of this value from the fit to what is expected based on known values of the constants. We can calculate the parameter B, in Liquid Argon, should be given as

$$B = \frac{e\sqrt{\frac{1.505 - 1}{1.505 + 1}\frac{e}{4\pi\varepsilon_0}}}{k_B T} = 0.717\sqrt{\text{cm/kV}} \tag{2.27}$$

Neither model does a good job at describing this constant. We can again most likely conclude that these models are nonphysical, even if they qualitatively do a good job of describing the shape of the data.

An extension to the extraction model, proposed in [76], is that an additional term must be included to factor in electrons which, once extracted, collide with a gas Argon atom and rebound back into the liquid phase, becoming trapped once again. This additional term serves to extend the emission lifetime. This term is introduced through an additional factor of C/x, giving the new model a $A/x^2 \exp(B\sqrt{E})$ dependence. The result of fitting this function to the data, again with a constant μ approximation, is shown in Figure 2.16. This new model is makes a much more physical prediction of the parameter B, which is now compatible with the expected value. In fact, we can argue that the parameter B should not even be a parameter at all. If we fix B to 0.717 $\sqrt{\text{cm/kV}}$, the model still does an acceptable job of describing the experimental data.

Of course, we must now interpret this discussion in view of the operation of a LArTPC. Results from [78] are often quoted, potentially inaccurately, that an extraction field of 3 - 4 kV/cm provides 100 % extraction efficiency. Whilst this may have been true for the experimental setup of [78], caution must be used when extrapolating this value to other detectors. We have already seen in this section that electron emission in the extraction region occurs over a characteristic timescale. The collection efficiency should more realistically described as the fraction of electrons which have been emitted within the integration time of the detector readout device. Integrating for

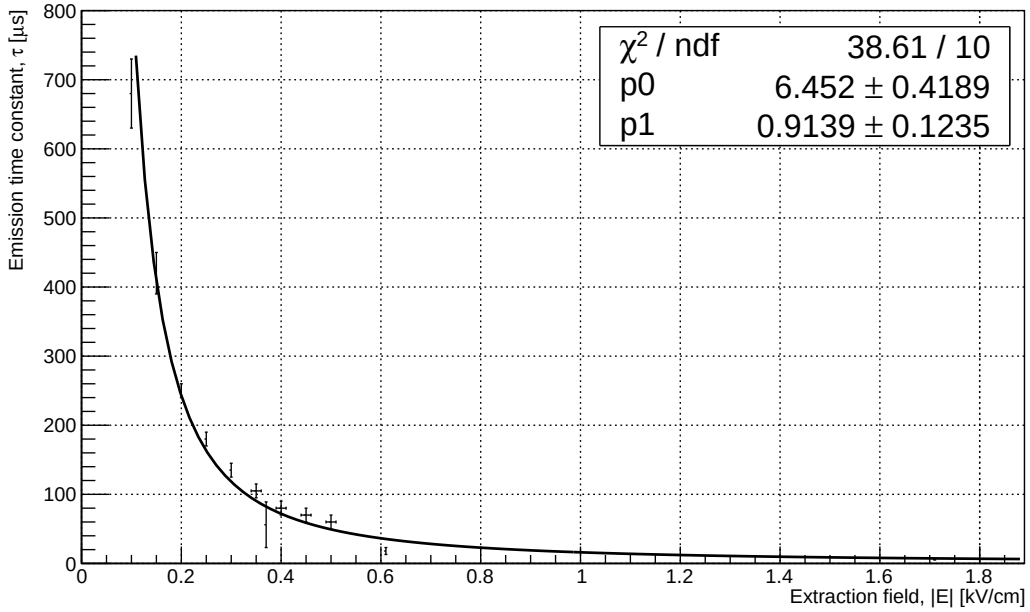

Figure 2.16: Predictions of electron exaction emission time as a function of extraction field, according to Equation 2.26. This model incorporates the possible of extracted electrons being reflected back into the Liquid phase. This model makes physically reasonable predictions of the fit parameters.

a longer time will improve apparent extraction efficiency and visa versa. Thus, the results presented in [78] are only strictly true for shaping times comparable with the setup of [78], which was roughly 400 μs.

In some sense, the battle is not about ensuring 100 % extraction efficiency, but instead ensuring that the timing characteristics of the slowly emitted electrons in the extraction region do not negatively impact the timing resolution of the detector. We saw earlier, in Section 2.5.2, that longitudinal electron diffusion during the drift serves to add a so called 'diffusion time' to the charge signal. We will assume a diffusion time of $\sigma_L = 1$ μs, which should be roughly accurate for ARIADNE. Given that this diffusion time sets a fundamental limit of detector timing performance before the extraction region, it would be desirable that the emission timing effects of the extraction region do not significant degrade this value further. We can for example require that close to 100 % of the slowly extracted electrons should be extracted within 1 μs. The emission of slow electrons proceeds exponentially, according to $Q/Q_0 = \exp(-t/\tau)$, where τ is the emission time constant. If we assume that most electrons are extracted after 5 time constants (99.3% extracted), we can imply a requirement of $\tau \ < 0.2$ μs.

Fortunately, it appears this problem is avoided by considering the ratio of electrons which are extracted by fast processes versus slow processes. We earlier discussed that only those electrons which are emitted by a slow process have a characteristic time constant. The fast emitted electrons are all extracted in $\mathcal{O}(ns)$. In order to be emitted via a fast process, the longitudinal kinetic energy of the electron must be greater than the potential barrier at the Liquid/gas interface. Thus, increasing the extraction field is doubly effective at increasing the fraction of electrons which are emitted by fast processes. Both the longitudinal kinetic energy of the electron is increased, and the potential barrier V is reduced by the Schottky effect. If we plot the potential barrier and the mean longitudinal electron energy versus the electric field, we can qualitatively observe this effect. Figure 2.17, which uses V_0 =0.065 eV [78], plots the average longitudinal electron energy versus liquid/gas interface potential barrier. We can see that, close to roughly 3 kV/cm extraction field, the average longitudinal energy of the electrons becomes greater than the potential barrier. For electric fields close to and greater than this value, the majority of electrons are likely emitted through fast processes. Experimental results [78] show a similar threshold, where electron extraction was found to be dominated by the fast components above extraction fields of 2.5-3 kV/cm.

The conclusion of this discussion is that acceptable performance of the extraction region should be realised for extraction fields greater than roughly 3 kV/cm in the Liquid, both in terms of electron extraction efficiency and timing resolution, with almost all electrons being extracted by fast processes, on the order of nanoseconds. For extraction fields much below 3 kV/cm in the Liquid, the performance of the extraction region becomes non-trivial. Extraction efficiency is reduced and a slow component of electron emission may become present which can degrade detector timing resolution.

We will now discuss how the height of the liquid Argon level within the extraction region effects performance. Given that Liquid argon and gas argon have different dielectric constants, as the Liquid level is varied, the effective extraction field across the Liquid phase will too vary. Modeling the extraction region as a parallel plate capacitor with two dielectrics, the electric field in the Liquid phase is given by

$$E_{\text{Liquid}} = \frac{V}{\varepsilon_L(D-d)+d} \tag{2.28}$$

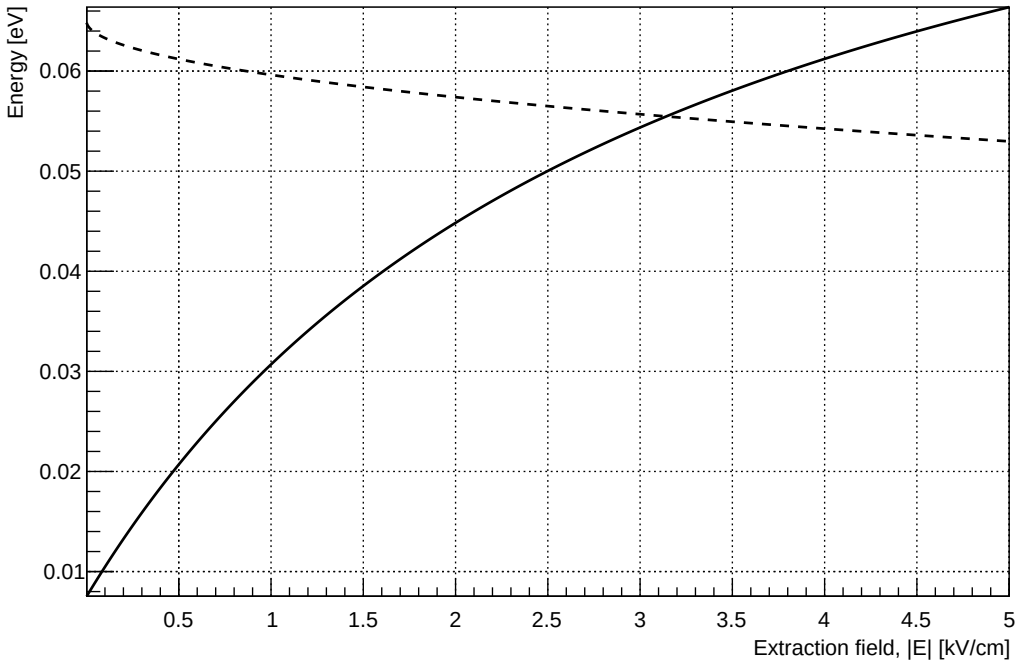

Figure 2.17: Predictions of Liquid/Gas interface potential compared to the mean longitudinal kinetic energy of drifting electrons. The interface potential (dashed line) is seen to decrease with increasing extraction field, due to the Schottki effect. The electron mean longitudinal kinetic energy overcomes the predicted interface potential near 3 kV/cm.

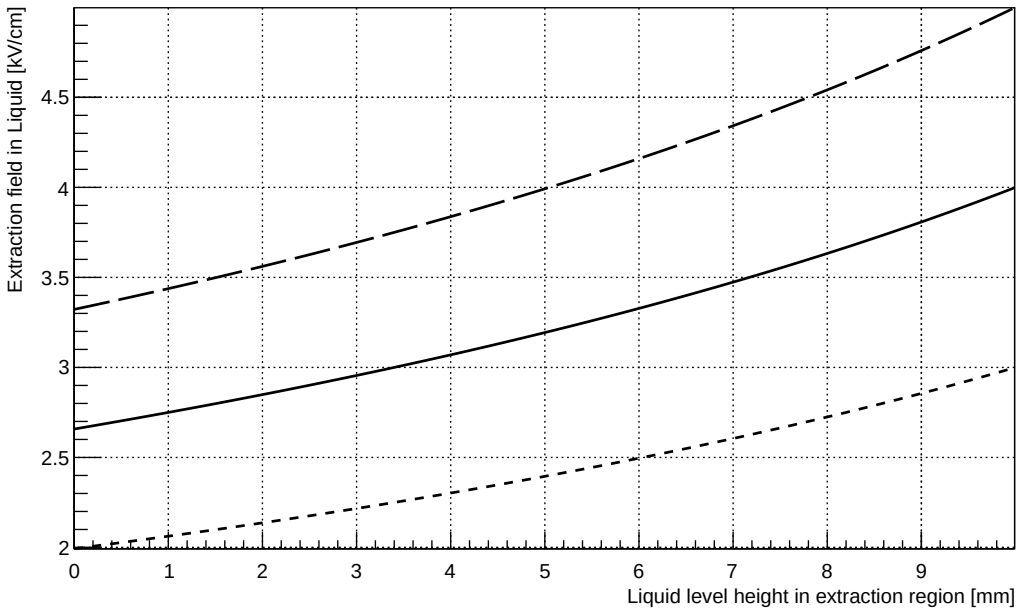

Figure 2.18: Extraction field on the Liquid/Gas Argon interface as a function of Liquid level above the lower grid in the extraction region. Three different potential differences are applied across the extraction region; 5 kV (long dashed line), 4 kV (solid line) and 3 kV(dashed line). It is seen that extraction efficiency should increased with higher liquid levels within the extraction region.

where V is the potential difference across the extraction region, ε_L is the dielectric constant of Liquid Argon, D is the total width of the extraction region and d is the height of the liquid level, above to the bottom of the extraction region. We will consider here a 10 mm wide extraction region, which is a somewhat typical dimension. The dependence of the liquid Argon level on the effective extraction field are shown in Figure 2.18 for several potential differences across the extraction region. Thus, the sensitivity of the detector to the liquid Argon level is dependent on the absolute bias that is applied across the extraction region. At a potential difference of 4 kV, full extraction region performance should be realised for all liquid Argon levels greater than $\approx$ 3mm. A higher potential difference, closer to 5 kV across the extraction region, should guarantee full performance for all liquid Argon levels in the extraction region. In reality, the potential difference across an extraction region is often a balance between extraction efficiency and electrical stability.

Figure 2.18 is also useful for discussing tolerances when considering the construction of a real-world extraction region. The ARIADNE extraction

grid was measured after assembly to be flat within 200 μm. If we consider the case of a nominal extraction region bias of 4 kV, and a nominal liquid level height of 5 mm; The theoretical extraction field on the surface of the liquid will be 3.194 kV/cm. A sagging of the extraction grid mesh of 200 μm increases the effective extraction field on the surface of the liquid to 3.272 kV/cm, a variation of 2%. In practice, the ability to accurately control both the height and flatness of the liquid level within the extraction region is likely to be the limiting factor on extraction field uniformity.

2.7.2 MicroPattern gaseous detectors (MPGDs)

The crucial benefit of a two-phase detector is the ability to take advantage of MPGDs, operating in the gas phase. In recent years the trend has been towards the use of Thick Gaseous Electron Multipliers (THGEMs) [79, 80]. THGEMs have their origins in the original gas electron multipliers (GEMs) [81].

The general operating principle of the THGEM and the GEM are very similar. The device is formed of an insulating bulk material which has a conductive plating/coating on both the top and bottom surfaces. The device additionally contains a dense array of through holes. In the case of the THGEM these holes are typically created by drilling. In the case of a GEM, the holes are produced by chemical etching. By applying a potential difference across the bulk, a large electric field is created in each hole. A more recent nomenclature has been introduced for THGEMs which have large (x, y) dimensions. These larger THGEMs are often called Large electron multipliers (LEMs). The terms THGEM and LEM are, in general, interchangeable. This thesis will use both THGEM and LEM interchangeably, respecting the nomenclature most used in the domain which is being discussed.

One curious but noteworthy development in recent years has been efforts to produce micropattern gas detectors that can be operated while submerged in liquid Xenon or liquid Argon. Liquid hole Multipliers (LHMs) [82, 83] take advantage of a trapped vapor bubble in each hole of the device. This trapped bubble allows for large gains and light production while allowing the device to be submerged in liquid. Such a device would remove the burden of the extraction region in a dual-phase TPC yet still provide the advantages of signal gain provided by a MPGD.

Charge readout of a two-phase TPC is generally performed using a segmented anode. This segmented anode is placed a couple of millimeters above the LEM. The separation between the LEM and the anode must be held with a modest tolerance ($\pm$ 5 %) to ensure a uniform electric field between the LEM and the readout anode. Any deviations in this transfer field could lead to deviations of the electron trajectory during transfer and introduce uncertainties into event reconstruction. The anode currently proposed for readout of a two-phase DUNE module is formed of many orthogonal strips, with a strip to strip pitch of 3.125 mm [84]. These strips provide two distinct views of the collected charge signal, and thus the event in the detector. The strip geometry is constructed in such a way as to ensure that the collected charge is shared evenly between both views. An intricate and elegant strip geometry is used to minimise the strip length, and hence the strip capacitance. Since strip capacitance is eventually related to the electronic noise that can be expected, lowest possible strip capacitance is preferred. The currently proposed anode design has an estimated electronic noise of roughly 1000 electrons for the 2-m strip length.

Chapter 3

Optical readout

The most noteworthy aspect of the ARIADNE detector is the readout approach. As discussed earlier, typically, dual-phase TPCs are readout by collecting charge on a segmented anode above the THGEM/LEM. The ARIADNE detector instead exploits light that is produced during the electron transfer process in the THGEM. The optical readout principle is shown in Figure 3.1 in the simplest form. In general, a camera, placed at a modest distance from the THGEM, collects the photons which are produced in the THGEM holes. The distance between the camera and the THGEM is constrained by the field of view of the imaging lens, the sensor size of the camera and the desired (x, y) detector area to be covered by a single camera. A wider field of view allows more detector area to be covered, at the cost of (x, y) resolution. Multiple cameras may be tiled together to cover almost arbitrarily large detector areas.

Optical TPCs are not a new concept. Many direct dark matter detection experiments already work using the optical readout principle. Recent examples include LZ [23] and DarkSide [16]. The reason that this readout principle has not seen more widespread use for the larger LArTPCs of neutrino oscillation physics is perhaps related to cost of scaling the approach used by many dark matter experiments. These experiments, to achieve best possible detection thresholds, generally use densely packed arrays of photodetectors, very close to the location of light production. Scaling such a geometry to a large, several meters by several meters detector, can become prohibitively expensive. ARIADNE has been developing new methods and technologies which allow for a single photodetector to cover a larger detector area. Thus, the cost of optical readout can be greatly reduced and the

readout approach becomes highly scalable. Additionally, the high resolution of commercially available photodetectors, such as EMCCD and CCD cameras, enables excellent x, y resolution. ARIADNE has found that the optical readout devices can be placed far (>1 m) from the point of light production, while still retaining good detection thresholds. This allows the optical readout device to even be installed outside of the detector cryostat. This has significant benefits in terms of maintenance, calibration and future upgradability of an experiment. No longer does the sensitive cryogenic volume of the detector need to be disturbed for access to the readout device.

3.0.1 THGEM Light production

In low electric fields, electrons do not gain sufficient kinetic energy to ionise Argon atoms. Instead, electron collisions with gas Argon atoms can only cause excitation. Scintillation light is produced as the excited Argon atoms de-excite, as earlier described in Section 2.4. As the electric field increases, the electrons may gain enough kinetic energy to ionise Argon atoms, thus releasing more electrons. These newly liberated electrons can, in turn, go on to produce more ionisation. The resulting electron avalanche is known as a Townsend discharge.

These two processes combine to give the THGEM a light output that is linear, or proportional, at lower electric fields. Once in the Townsend regime, exponential increasing light production occurs with increasing THGEM bias. Although operation in the Townsend regime produces a large light signal, there are some downsides. An unavoidable consequence of the production of electrons by ionisation, is the production of ions. In Liquid Argon, the mobility of ions is much much less than that of electrons [85], with drift velocities as low as 1 cm/s in a typical 0.5 kV/cm drift field. Given this extremely slow drift velocity. Thus, these ions slowly drift backwards through the TPC volume, remaining in the detector volume for extremely long periods of time. These ions may even accumulate to levels which can cause issues with detector performance. If enough ions accumulate in the TPC volume, their presence can distort the drift field and alter the path of drifting electrons. This effect is known as space charge.

Figure 3.2 shows the cross sections for excitation, ionisation and elastic scattering of electrons on Argon atoms as a function of electron energy. At very low energies, the dominant process is elastic scattering. This process

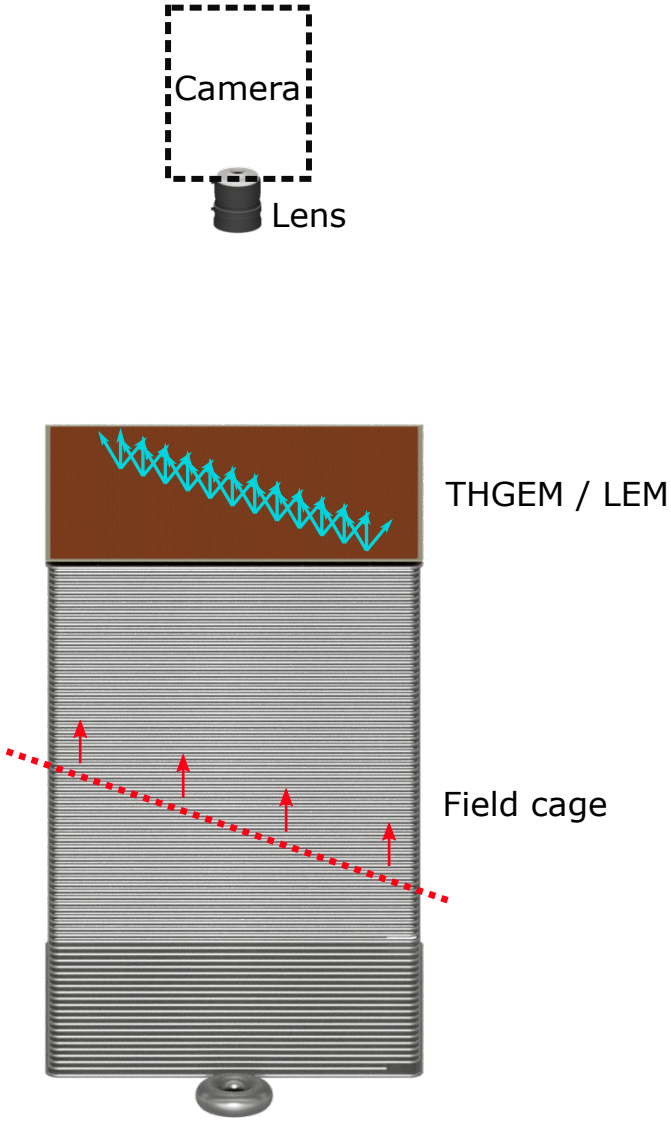

Figure 3.1: Optical Readout Principle. Light produced in the THGEM holes is captured using a camera. The choice of camera is flexible depending on the needs of an experiment. The choice of lens determines the field of view and resolution of the readout. A narrow field of view provides higher resolution but requires more cameras to cover the same THGEM area. The camera can be mounted outside of the TPC volume to provide easy access for calibration, maintenance and future upgrade.

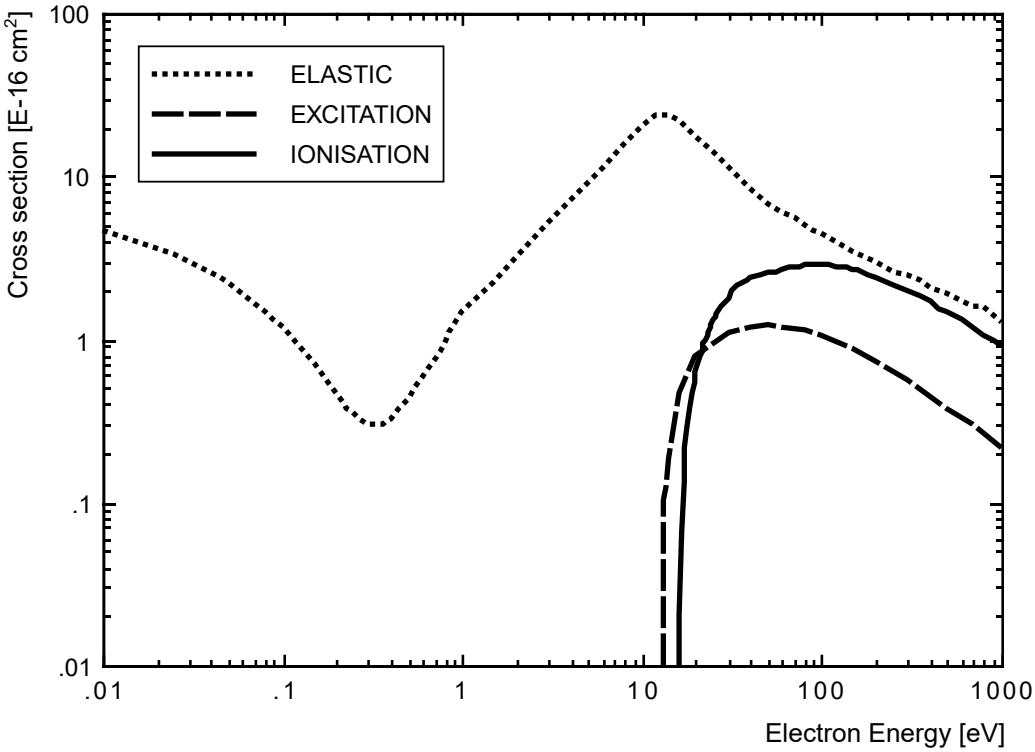

Figure 3.2: Electron-Argon cross sections for Elastic and inelastic scattering plus ionisation. At very low kinetic energies, only elastic scattering is present. Above 12.9 eV, excitation becomes possible. This enables the production of scintillation light. A small region between 12.9 eV and 15.7 eV exists, where light production is increased but no ionisation can occur. Above 15.7 eV, the Townsend avalanche regime begins.

has been suggested to lead to the production of small, broadband, light production by neutral bremsstrahlung [86, 87]. For the purposes of this discussion we will ignore light production by neutral bremsstrahlung as it is not a dominant contribution in the VUV. From Figure 3.2, we can see that the threshold for excitation is lower than that of ionisation (12.9 eV compared to 15.7 eV). Thus, electrons with energies in this range will produce light only by excitation processes and no ions will be produced. This is known as electroluminescence. Once electrons gain an energy above the ionisation threshold, the Townsend regime begins.

Figure 3.2 describes the relative cross sections of the different processes as a function of electron energy. For our purposes, it is more useful to consider the rate of these processes as a function of electric field. Thus, we will be able to predict the relative rates of the different processes as a function of electric field applied across the holes of a THGEM.

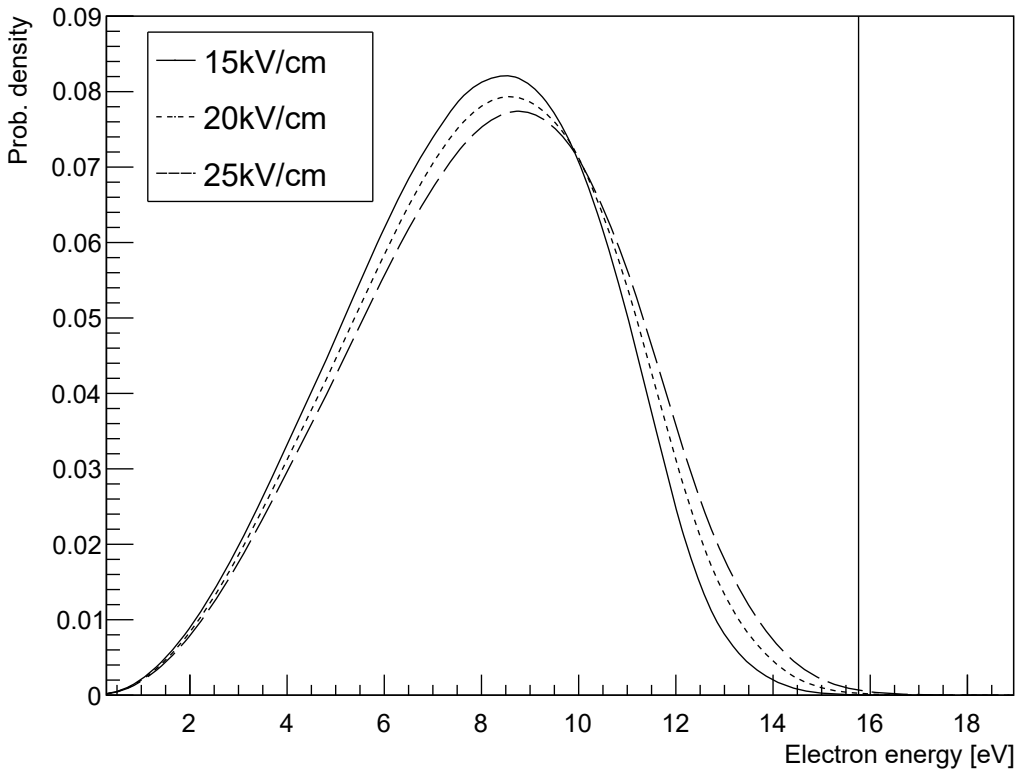

Figure 3.3: Electron kinetic energy distributions in three different linear electric fields. Only the extreme tail of the distributions are seem to be above the ionisation threshold, drawn as a solid black line at 15.7 eV.

Magboltz 11.7 [88] was used to calculate the energy distributions of electrons as a function of electric field in Argon gas at 1013 mbar and 88 Kelvin. Figure 3.3 plots the result of the calculations. A solid line is drawn at the ionisation threshold. It is clear that only the extreme tail of the highly energetic electrons are responsible for ionisation.

We will define the gain of a THGEM as the mean number of electrons leaving the THGEM per incident electron. Garfield [89] was used to simulate the expected THGEM gain as a function of potential difference. The simulations found that the charge gain produced by the ARIADNE THGEM may be somewhat less than what is typically expected from two-phase THGEM operation. This reduction in gain can probably be ascribed to the fact that the ARIADNE detector does not have a traditional anode for reading out the THGEM charge. Normally, an additional transfer field would exist in the region between the THGEM and the readout anode. This additional transfer field creates a more uniform field distribution near the exit of the THGEM hole, which can only be beneficial in terms of avalanche development. To

verify this, further simulations were performed, including the effect of this transfer field. Once this transfer field was included, the simulated gain of the THGEM recovered to more commonly accepted values. Figure 3.4 plots the simulated trajectories of electrons in the ARIADNE THGEM, which has no readout anode and no transfer field. The electrons are collected on the top plane of the THGEM. Figure 3.4 also plots the trajectories of electrons in the case of an anode installed above the THGEM, including a modest transfer field.

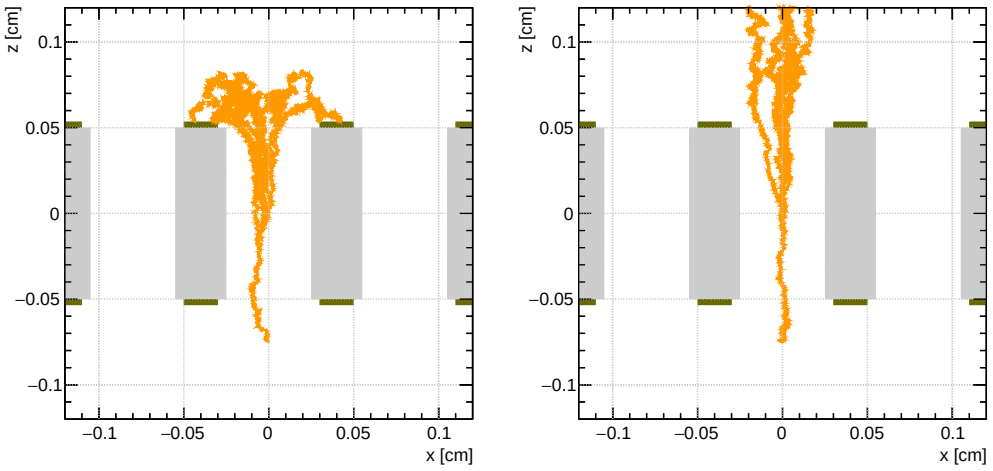

(a) (b)

Figure 3.4: Simulated electron avalanches using Garfield. a) Without dedicated readout anode and transfer field. This is the THGEM configuration in the ARIADNE detector. b) With dedicated transfer field and charge collection anode above the THGEM. This setup is typical in dual-phase charge readout detectors.

Using Garfield, we can calculate the number of excitation and ionisation processes that occur as a function of applied bias across the THGEM. Figure 3.5 plots the results of the simulation. The results of the simulation agree with the qualitatively understood model of a proportional regime of light production at low biases, followed by the onset of an exponentially enhanced number of excitations once ionisation is possible. No such linear regime is seen in the distribution of mean number of ionisations as a function of THGEM bias, which is well described by a single exponential.

We can propose a theoretical model to describe the rate of excitation, and light production. The model is defined by a linear component, $Ax + B$,

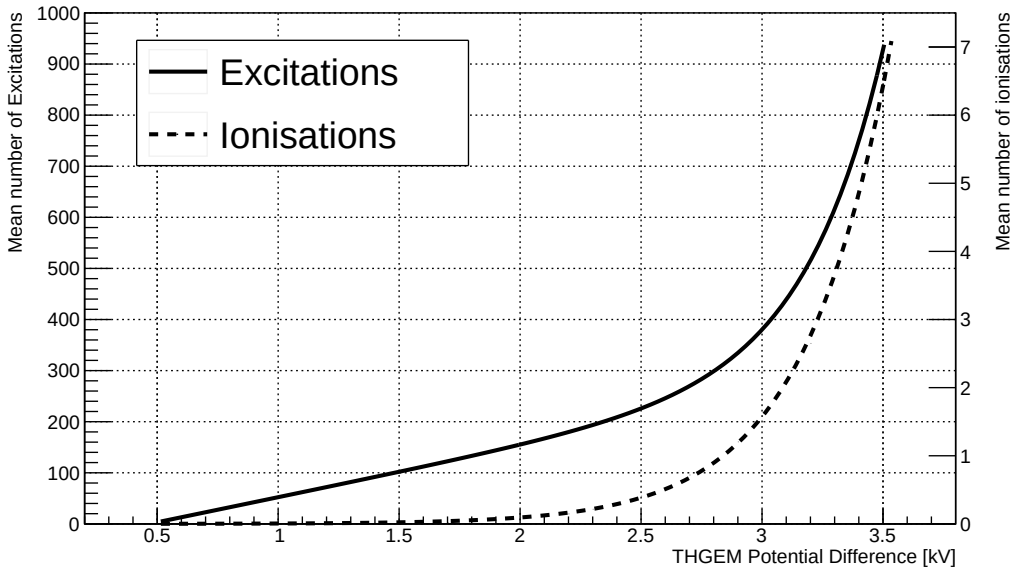

Figure 3.5: Mean number of ionisations and excitations during the passage of a single electron through a THGEM hole. Simulation performed at 1100 mbar and 88 Kelvin. The proportional linear regime of electroluminescence is well represented in the mean number of excitations at lower THGEM fields.

plus an exponentially enhanced component, $Cx\exp(Dx)$, where x is the bias across the THGEM. We can write the model as

$$N_\gamma = Ax(1 + B\exp(Cx)) + D \tag{3.1}$$

where N_γ is the number of number of photons produced. x is the THGEM bias, and A,B,C and D are constants to be found from the fit. This model is in excellent agreement with the rate of excitation found using the Garfield simulations. Later, in Section 8.2, this model will be compared against experimental data taken from ARIADNE.

3.0.2 Light collection

Once generated in the THGEM, the photons must be detected. The VUV (126.8 nm) wavelength of dominant electroluminescent component of Argon makes direct detection difficult. ARIADNE uses a wavelength shifting plate, coated with TPB, to wavelength shift these VUV photons to visible wavelengths. After this step, the photons can be detected using more conventional lenses and camera technologies. The reference design of ARI-

ADNE uses four EMCCD cameras, each with a Spacecom VF50095M 50mm focal length lens. The lens is installed at a distance of 1 m from the THGEM plane. The VF50095M lens is a 'high speed' lens, with n f-number of 0.95. The f-number of lens is defined as

$$\text{f-number} = f/D \tag{3.2}$$

where f is the focal length of the lens and D is the lens diameter. Thus, a lower f-number translates to a larger aperture/diameter for the same focal length. This larger aperture should increase the solid angle of the lens and improve light collection. At a distance of 1 mm from the THGEM plane, and with an aperture of 53 mm, the lens will have a solid angle of approximately 0.002 Steradian. This translates to an expected light collection efficiency of 0.016%.

The reference design of ARIADNE uses four Andor iXon Ultra 888 EMCCD cameras (see Section 4.8), which have a sensor size of 13.3 mm × 13.3 mm. The sensor has 1024 × 1024 pixels. When coupled with a 50mm focal length lens, the resulting angle of view is approximately 15 degrees in both width and height. Since the THGEM plane is 1 m away from the lens, the field of view is slightly larger than 26 cm × 26 cm per camera. The 1024 × 1024 pixels of the camera provide a nominal resolution of 260 μm × 260 μm per pixel. At this resolution, individual holes of the THGEM, which have 500 μm diameter, can be seen. Typically, the cameras are operated in 4 × 4 binning, producing a nominal resolution of slightly less than 1 mm per pixel.

Chapter 4

The ARIADNE detector

4.1 Detection principle

A general view of the ARIADNE detector can be seen in Figure 4.1. The detection principle of the ARIADNE detector is illustrated in Figure 4.2. Electrons are produced in the active volume during the passage of charged particles. These electrons drift to the extraction region with a nominal 0.5 kV/cm drift field. The electrons are extracted into the gas phase using a nominal 2 kV/cm extraction field. Once in the gas phase, the electrons enter the holes of the THGEM, where light production occurs by electroluminescence. This light is predominantly produced at 128 nm and is wavelength shifted using TPB, coated on the underside of a borosilicate glass sheet 2 mm above the THGEM. The light that is re-emitted from the TPB, at 430 nm, is detected using four Andor EMCCD cameras. Since the cameras are mounted outside of the cryogenic volume, they can be easily changed or upgraded.

Four Hamamatsu R5912-02MOD PMTs are installed underneath the TPC to provide detection of S1 light and auxiliary S2 light collection.

The design of ARIADNE was such that results from the detector should be easy to interpret in the context of any future two-phase LArTPC designs. The tiling of many 50 $\times$ 50 cm large electron multipliers (LEMs) is common to many two-phase experiments and so this dimension was chosen for the ARIADNE THGEM. The drift length of the TPC is mostly constrained by logistics. The 80 cm drift length gives the detector a total height that may still be easily manipulated using the locally available cranes.

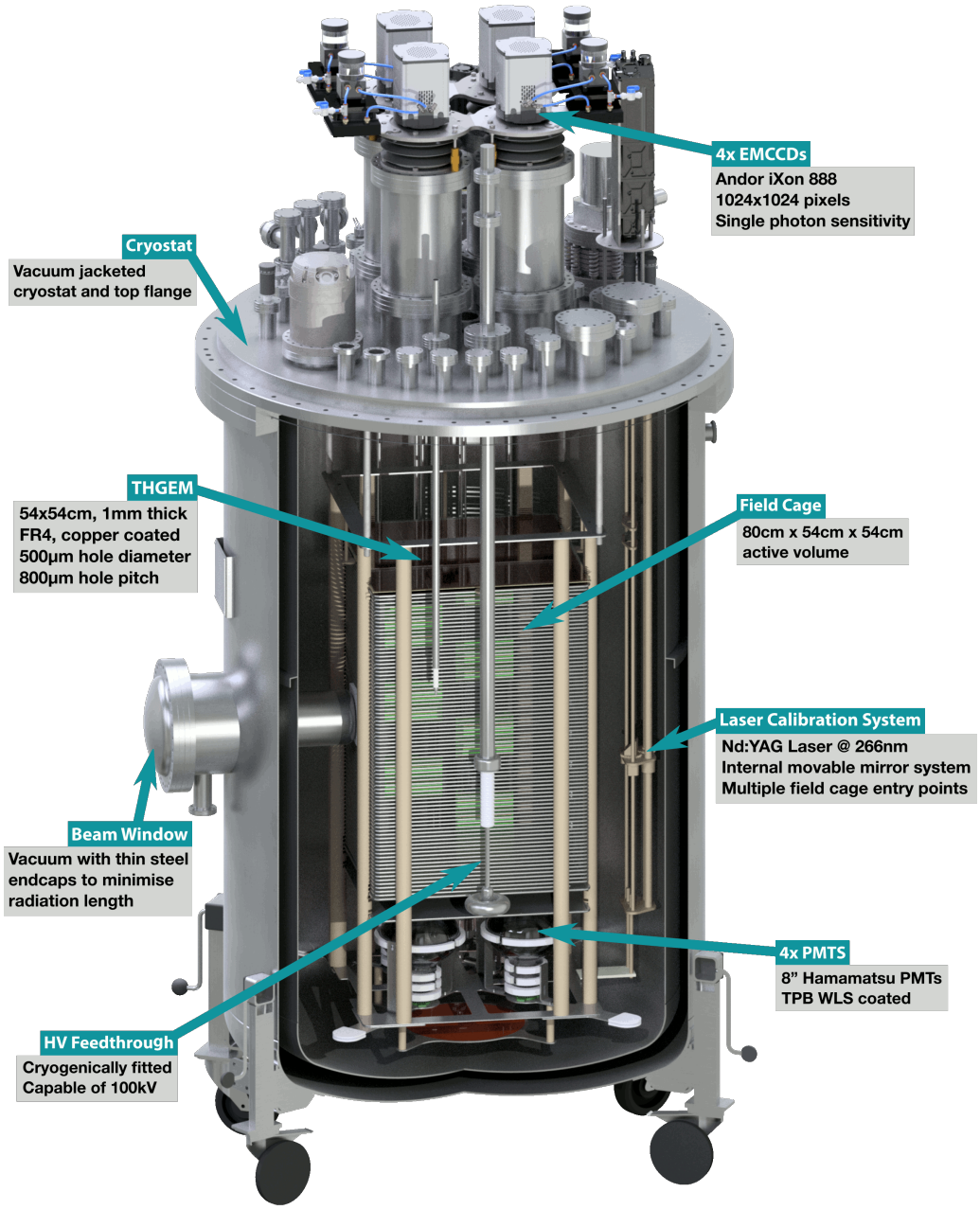

Figure 4.1: The ARIADNE detector.

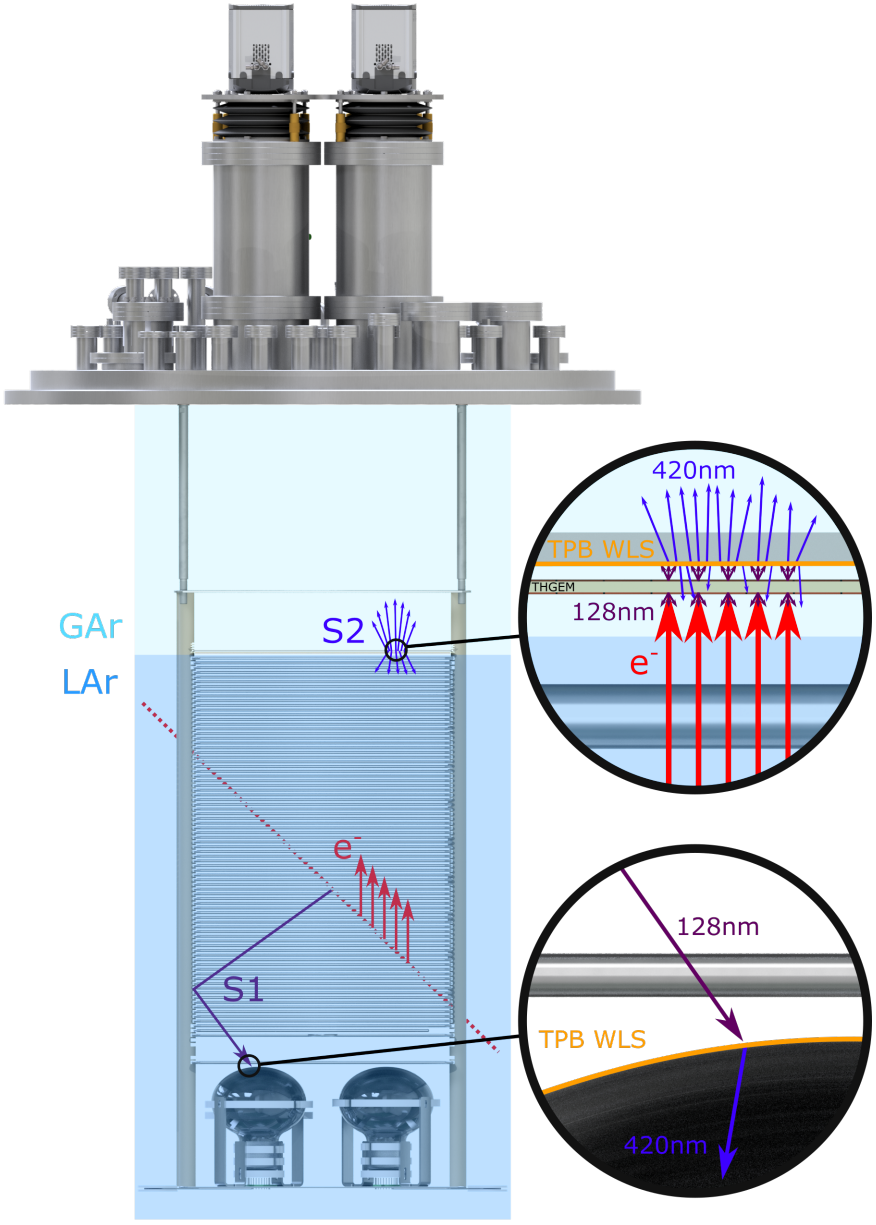

Figure 4.2: ARIADNE detection principle. An ionising particle creates free electrons in the Liquid Argon. These free electrons are drifted to the surface of the Liquid, and extracted into the gas phase. The electrons enter the holes of a THGEM, where they are accelerated. This process produces light as gas argon Atoms are excited by collisions with the accelerated electrons then de-excite. The light produced at 128 nm is wavelength shifted using TPB, coated on the underside of a glass sheet. The 420 nm light, re-emitted from the TPB, is detected using externally mounted cameras.

4.2 Cryostat

The ARIADNE cryostat is composed of two parts; a separable flange and body. Both the cryostat flange and body have integral vacuum jackets to minimise the total heat input into the detector volume. The cryostat was manufactured by Wessington cryogenics, Tyne & Wear, UK. Figure 4.3 shows several photographs taken during manufacture of the cryostat. The internal diameter of the cryostat is 1.07 meters and the internal height is 1.8 meters. The cryostat has a maximum rated capacity of 1530 litres when 95% full and a maximum service pressure of 4 bar(g).

4.2.1 Top flange

The top flange of the cryostat contains a wide selection of feedthroughs for detector instrumentation. Four central DN200 flanges provide mounting points for the cameras. The large diameter of these central feedthroughs allow the cameras to have a wide field of view without being obscured. Two DN160CF feedthroughs are provided in the top flange. A leybold Turbovac 350i turbomolecular vacuum pump is directly attached to one of these flanges. This direct attachment to the flange provides efficient pumping of the detector volume. The detector volume is typically pumped to better than 1E-5 mbar before filling with Liquid Argon. This evacuation of the cryostat helps to reduce outgassing of materials within the detector, reducing the volume of impurities that must be handled by the liquid argon recirculation and purification system.

Mounted to the second DN160CF feedthrough is a Cryomech AL300 Gifford-McMahon Cryorefrigerator unit. During operation, the ARIADNE detector works as a closed loop. Thus, the heat loads of the cryostat must be offset by this cold head. The cold head has a cooling capacity of 266 W when at 80 K, reducing to 166 W at 50 K. This cooling capacity was found to be sufficient for the head loads experienced by the cryostat, although a cryocooler with increased cooling power may have been desirable. The operation of the cryocooler is discussed in more detail in Section 4.11. A DN75CF feedthrough provides a mounting point for the cathode high voltage feedthrough. This feedthrough is axially aligned with the toroid of the TPC cathode, inside the cryostat. A large selection of auxiliary DN40CF feedthroughs provide access for detector instrumentation such as thermo-

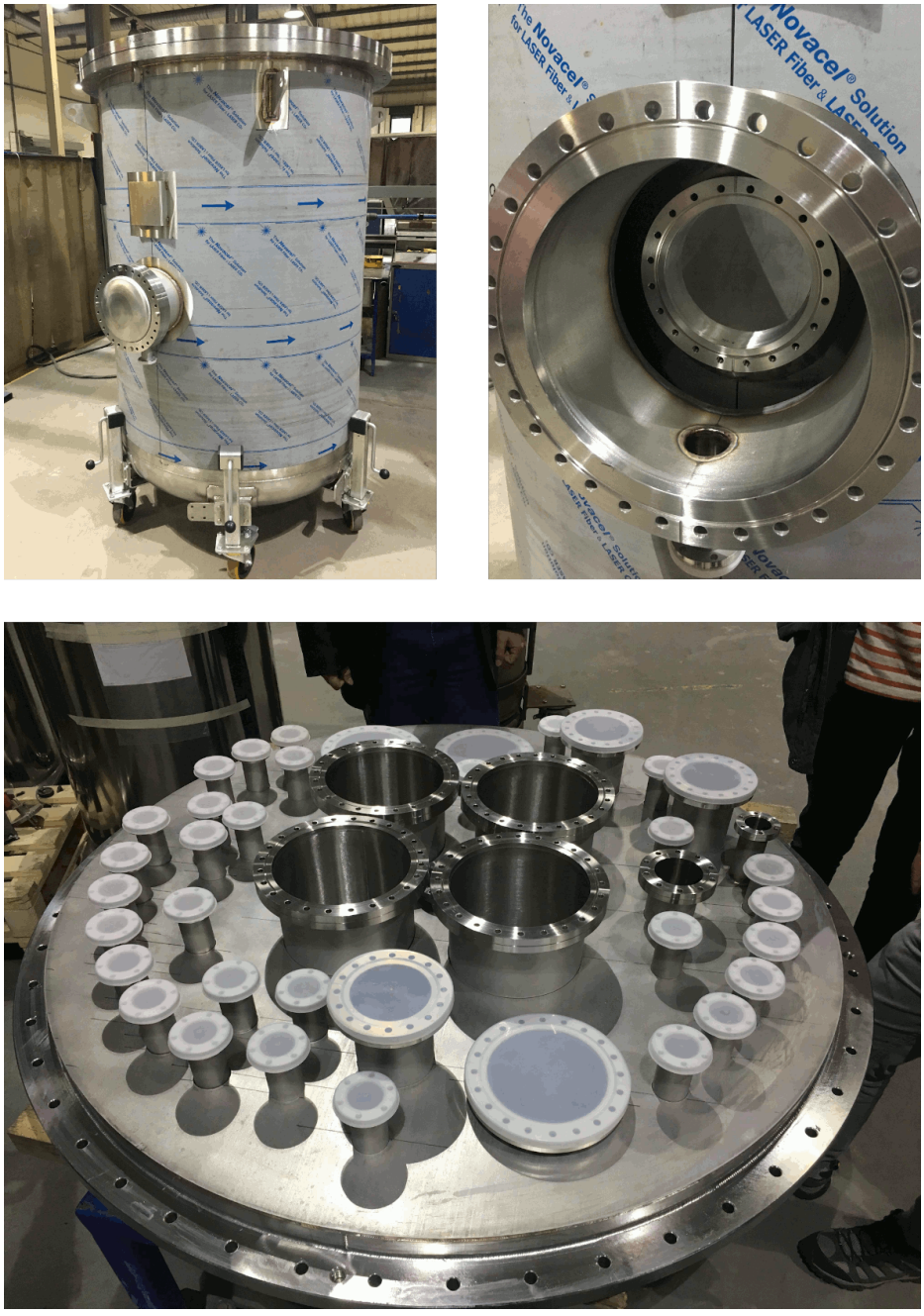

Figure 4.3: Photographs taken during cryostat manufacture at Wessington cryogenics, Tyne & Wear, UK.

couples, cryogenic filling lines and pressure sensors.

4.2.2 Cryostat body

The cryostat body is vacuum jacket insulated vessel. The jacket of the cryostat is fitted with multi-layer superinsulation. Six height-adjustable wheels allow the height of the cryostat to be adjusted. This feature was particularly useful during beamline operation where the height of the beam window could be aligned with the height of the beamline. The inner wall of the cryostat is fitted with a stiffening ring, which was necessary to allow the cryostat volume to be pumped to UHV. Four lifting eyes allow the detector to be lifted from the cryostat body. The cryostat was designed with an indium groove to allow a vacuum tight seal to be created between the flange and the main vessel. Typically during operation the vessel was instead sealed using a Viton A gasket. This gasket is reusable, reducing the need for expensive indium wire. In principle, Viton may allow the permeation of small quantities of water through the bulk material. During operation the detector is generally kept at a slight overpressure to minimise the change of contamination through any microscopic leaks. It is expected that this overpressure should result in a negligible rate of water permeation through the Viton gasket.

4.3 Beam window

Two coaxial conflat flanges are integrated into the vacuum jacket of the cryostat, providing mounting points for the beam window and beam plug assemblies. The beam transport assembly is composed of two parts, an external beam window and an internal beam plug. The beam window forms the interface between the air side of the detector and the vacuum jacket of the cryostat. The beam plug forms the interface between the cryostat and the liquid argon in the detector volume. Figure 4.4 shows a cross section of the complete beam window assembly, when installed on the cryostat. The design goals of the beam window are relatively simple; minimise the total radiation length for thoroughgoing particles. The outer beam window, the interface between the air side and the cryostat, is formed from 0.9 mm thick stainless steel dished end. The shape of this window provides

increased strength against the pressure forces between the air side and the vacuum jacket of the cryostat. The internal section of the beam window is integrated into the vacuum jacket of the cryostat. Thus, once particles pass through the beam window, they travel in vacuum space. The particles travel in vacuum space until they reach the end of the beam plug, which is at a distance of approximately 2 cm from the active area of the TPC. The exit of the beam plug is placed as close as possible to the field case, whilst however ensuring that the local electric field does not exceed 40 kV/cm. The geometry of the beam plug and the distance from the field cage was optimised using COMSOL simulations. The results of the simulation are shown in Figure 4.5. One final element is used to further reduce the radiation length of the assembly. A Ultra-high-molecular-weight polyethylene (UHMWPE) element is mounted onto the field cage. This element displaces the uninstrumented LAr that would be present between the end of the beam plug and the active region of the TPC. Since UHMWPE has a much longer characteristic radiation length than LAr (50 cm compared to 14 cm), this component further reduces the total radiation length of the system. The total material budget of the final beam window design is 0.21 X_0. This is more than an order of magnitude improved compared to an unmodified ARIADNE cryostat, which would have roughly 2.3 X_0.

4.4 Field cage

The field cage is supported by eight PEEK 450G rods. Rectangular slots are milled into the support rods every 1 cm, each supporting a field cage ring. Additional varieties of slots are milled at the top and bottom of the rods, providing mounting points for the glass wavelength shifting plate, the THGEM, and the PMT protection grid. The back side of one of the eight rods is milled flat and has tapped holes for mounting an insulating PEEK 450G tube. This tube serves as a cable conduit, guaranteeing separation between the PMT signal and HV cables from the field cage. The grounded shield of these coaxial cables may otherwise present a discharge route for the field cage.

The field cage provides a uniform drift field between the cathode and the extraction region of the TPC. ARIADNE employs a typical field cage design, formed from a series of field shaping elements, each connected by a

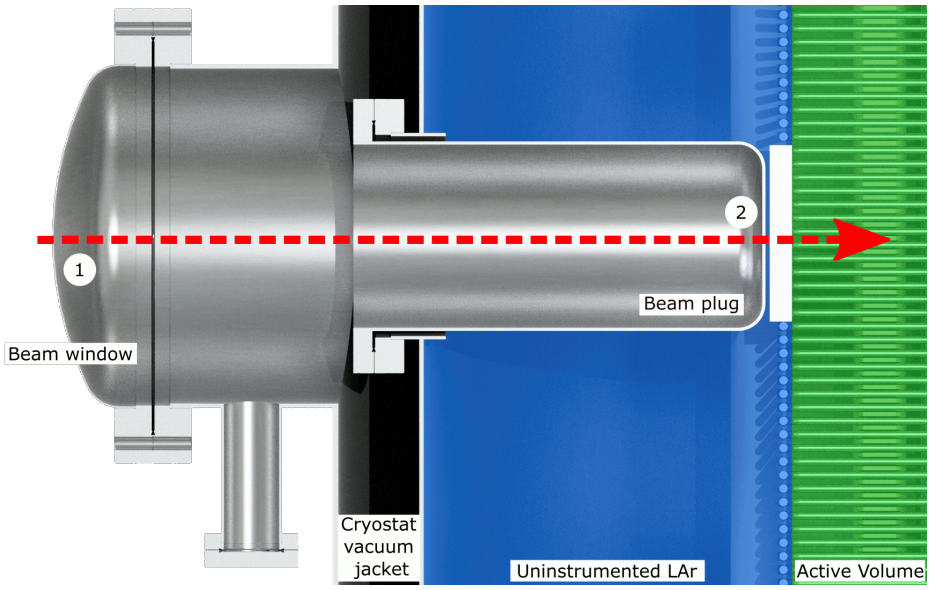

Figure 4.4: ARIADNE beam window design. An external beam window creates the interface between the air side of the detector and the vacuum jacket of the detector. Particles travel through the vacuum jacket of the cryostat, through the beam plug, which extends into the uninstrumented LAr. Once near the field cage, the particles exit the beam plug and enter the active region of the detector.

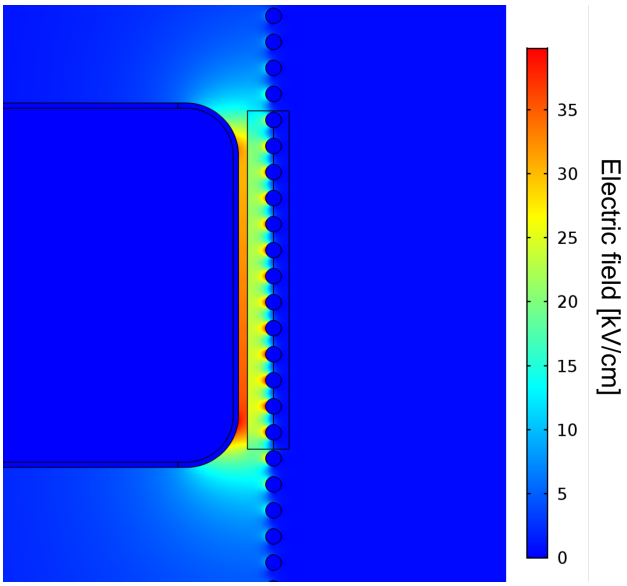

Figure 4.5: COMSOL electric field simulations at the interface between the beam plug and the TPC.

fixed resistor. This forms a resistor chain, generating the smooth voltage distribution that is required along the TPC.

Non-uniformities should be well understood, since their presence can lead to uncertainties when reconstructing the path of drifted electrons, leading to uncertainties in track reconstruction, vertex location and PID. The uniformity of the drift field is mostly defined by the shape of the field cage elements and their relative spacing. A large number of field cage elements improves drift field uniformity but can come at the expense of increasing cost, assembly time and chance of failures due to increasing complexity and number of components. The shape of the field cage elements is also important. The field cage element shape often depends on many external requirements such as necessary mechanical interfaces to support the weight of field cage and facilitating the required electrical connections to the resistor chain. Generally, field cage elements are made from easily procured structural shapes such as rods, tubes, roll formed profiles or extruded sections.

The ARIADNE field cage is formed from 79, 6mm diameter, CNC wire bent stainless steel rods. A solid cross section was chosen over tube to eliminate the possibility of a trapped volume inside the field cage. Tube sections require the drilling of vent holes throughout the structure which both adds cost and can introduces sharp edges around each drilled hole. For very large detectors, solid field cage elements can become extremely heavy and so this concession often becomes a necessity. Once formed into the required square shape, the ends of the field cage rings are welded together and polished smooth. The surface finish near the weld seams is indistinguishable from rest of the field cage ring. The four corners of each field cage ring are formed with a radius of 13 mm.

The field cage is designed to be slightly larger than the active area of the THGEM. This additional dead region in the periphery of the TPC provides a small volume in which any non-uniformity in the drift field are able to subside. A simulation of the electric field inside the active region is shown in Figure 4.6. This simulation was performed using the nominal field cage dimensions, and does not include any 'as-built' imperfections such as welding distortions or installation inaccuracies. In general, the field uniformity is better than 1 % inside the active volume of the TPC. Some local non-uniformities exist in the region of the beam plug, and also near gaps in certain field cage rings which have openings for the laser calibration system.

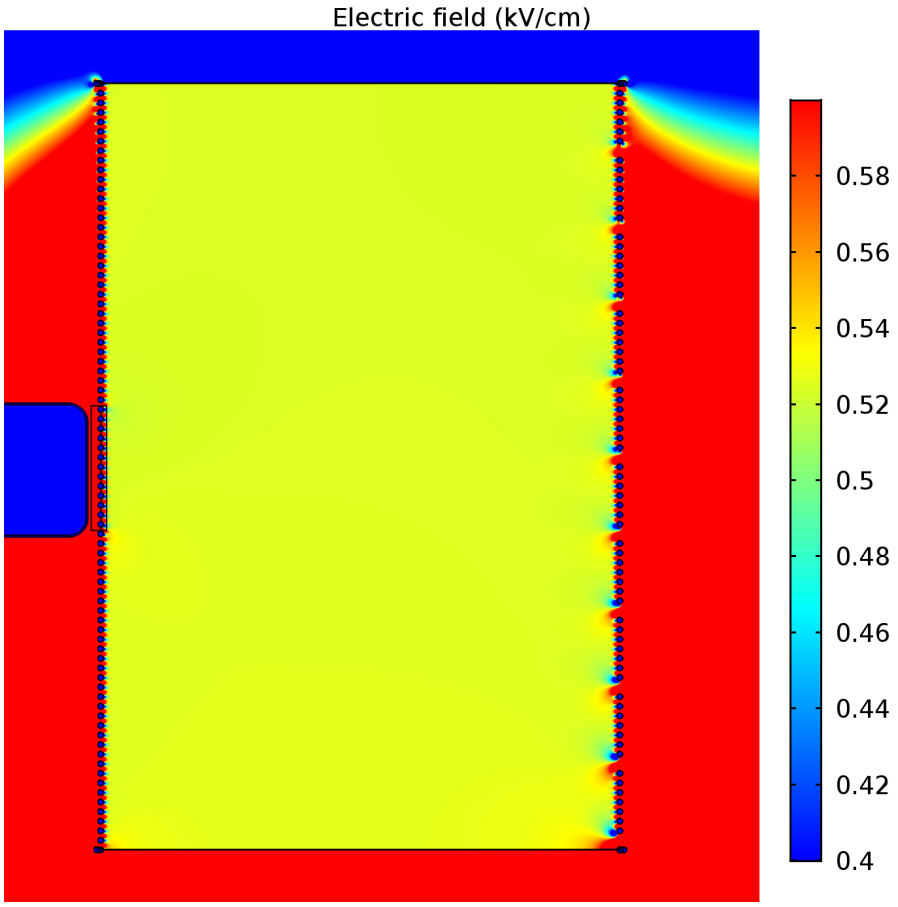

Figure 4.6: COMSOL simulation of drift field uniformity. The largest non-uniformities exist near those field cage rings which have gaps which are entrance points for the laser calibration system.

The effect of the beam plug on the electric field inside of the TPC is shown in Figure 4.7. This effect is $O(5\ \%)$ and is highly locailised and so is not expected to cause a large degradation to the performance of the drift field. The effect of the penetrations in the field cage for the laser calibration system is larger, $O(10\ \%)$. These non-uniformities are again highly localised.

The expected containment of the ARIADNE TPC for a range of particle species and momenta was studied using Geant4. This simulation was performed by generating a mix of particles species and momenta at the exit point of the beam window, and measuring the total energy deposition in the active volume of the ARIADNE detector. The active volume was surrounded by an secondary, effectively infinite volume of liquid Argon. Containment was defined as the total energy deposition in the ARIADNE active volume, relative to the total energy deposition in both the active volume and the

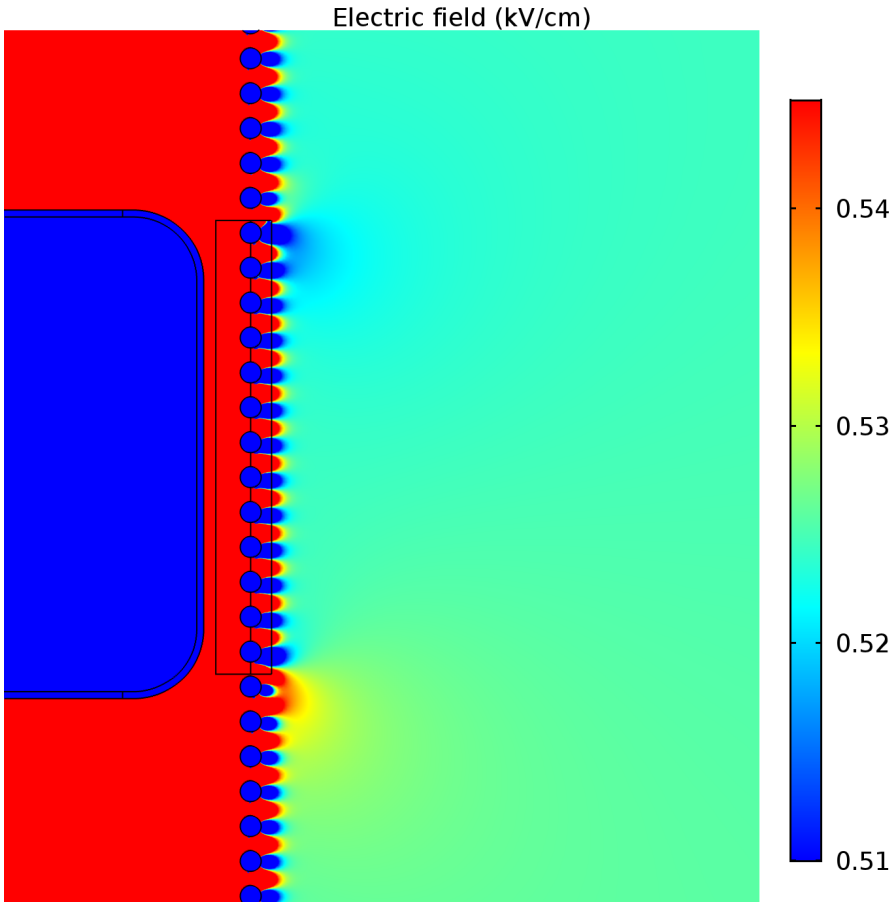

Figure 4.7: Zoomed in view of drift field non-uniformities induced by the beam plug.

secondary containing volume combined. The results of the study are shown in Figure 4.8. Several interesting trends are visible from the simulation:

- For protons, at low momenta, containment is close to 100%. Protons exhibit a much steeper decline of containment versus other species as momentum increases. This is due to the difference in energy deposition of protons compared to the other species simulated. Protons exhibit a characteristically sharp Bragg peak for stopping tracks. Compared to other species, a disproportionately large energy deposition occurs at the end of the track. As the simulated momenta increases, the end of this stopping track moves outside of the active volume of the TPC. Once the Bragg peak of the proton track leaves the active volume, a very steep drop of containment is seen.

- For anti-protons, an initial rise of containment can be seen, followed by a steady decline. The rise in containment can be explained by the nature of anti-proton interactions in Liquid Argon. Anti-proton annihilation in liquid Argon produces interaction products that travel in all directions, even backwards against the direction of travel of the incident anti-proton. At low momenta, the anti-protons interact quickly in the Liquid Argon and much of the energy of the resulting products is lost backwards, outside of the TPC. As momenta increases, containment reaches a maxima, when the anti-proton interaction happens close to the center of the TPC. This condition provides optimal containment of all of the interaction products, which travel in all directions. As momentum continues to increase, eventually the interaction preferentially occurs beyond the active volume of the TPC, resulting in a drop in containment.

- For the remaining species simulated, the containments trends largely are described with similar shapes. Muons exhibit the cleanest containment distribution, explained by their low rate of interaction with Liquid Argon. Muons generally produce few products of interaction and their energy loss is well explained as throughgoing minimally ionising particles. Electrons and pions both produce interaction products at higher rates than muons, which explains containment curves which exhibit more variation, especially at lower momenta.

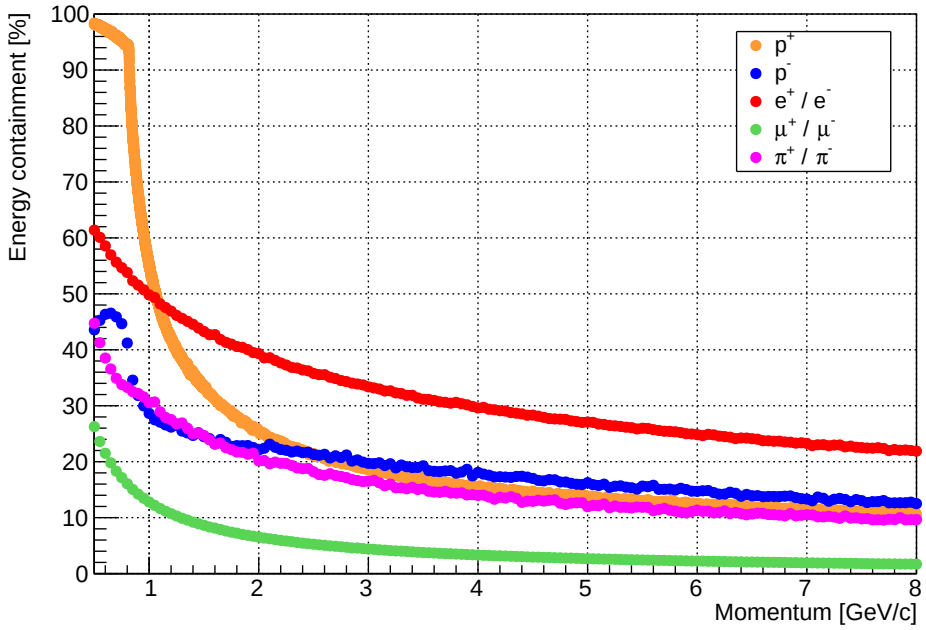

Figure 4.8: Simulated containment of the ARIADNE TPC. The species and momenta range simulated were chosen to be appropriate for the CERN T9 beamline, discussed later in Section 5.

4.4.1 Resistor chain PCBs

The resistor chain is built from eight PCBs, each of which has 11 connections to the field cage rings. The electrical connection to the field cage is made using fuse clips. These fuse clips are designed for 6mm diameter fuses, and mount very firmly onto the 6mm diameter field cage rings. A photograph of the resistor chain PCB can be seen in Figure 4.9, alongside a truncated schematic which shows the circuit which interconnects each field cage ring. Each leg of the resistor chain has milled slots which allow some flexibility. This flexibility is sufficient to allow for small variations in the field cage geometry due to contraction in cryogenics.

Two 100 MΩ resistors are connected in parallel between each field cage ring. This setup gives the total field cage a resistance in the region of 4 GΩ. When the cathode is nominally biased to 46 kV, the total current through the field cage is $O(10\mu\text{A})$. The two resistors connected in parallel provide slight redundancy in the case of resistor failure. If a single resistor fails, the resistance between the two field cage rings is doubled. This would produce a slice of the TPC with increased drift field, but the TPC would remain functional. Metal oxide varistors are also included between each field cage ring. These varistors act as an open circuit short when the ring to ring bias

is greater than 1800 volts. This value is much larger than the expected ring to ring voltage during normal operation, and is intended to act as a safety mechanism for the protection in the resistor chain in case of discharges. In case that a discharge of the field cage occurs, the open circuit varistor paths provide a safe route for current to flow, which would otherwise flow through the resistors of the resistor chain PCBs.

At the back of each PCB is a second PCB, which contains no active components. This daughter board contains flat copper traces, biased to the same potential as the associated field cage ring. This daughter board is designed to screen the sharp edges of the active components on the main resistor chain PCB. Without the daughter board, the sharp edges of the resistors may experience large electric fields and potentially emit electrons by corona discharge. The shielding daughter board greatly screens the electric field experienced by the components of the main PCB. The soldering on these PCBs is generally performed using high voltage soldering techniques, or ball soldering. Wherever possible, all solder joints are formed into rounded fillets or balls. This can be seen in Figure 4.9 as ball solder joints which connect the legs of the black varistors to the main resistor chain PCB.

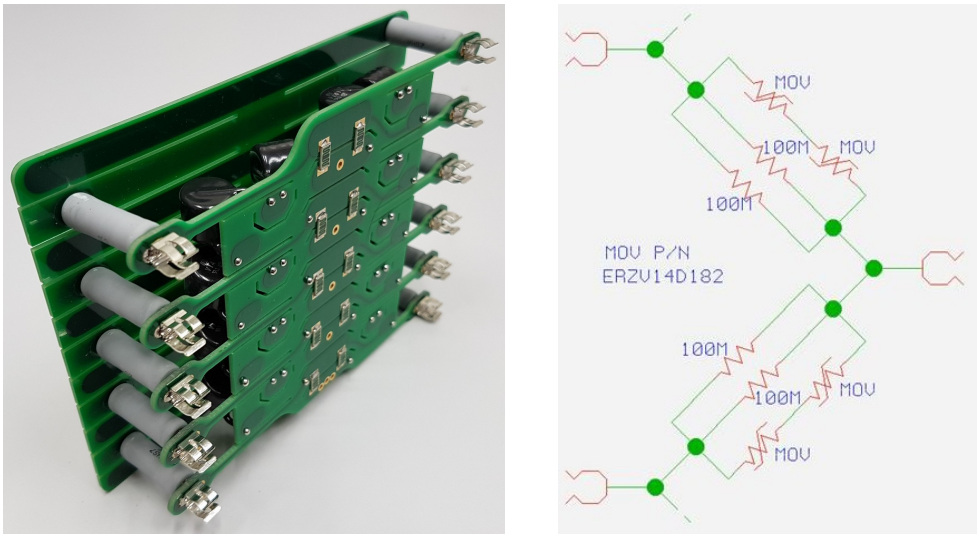

(a) (b)

Figure 4.9: Resistor chain PCBs. Fuse clips are used to make the connection to the field cage rings.

4.5 High voltage feedthroughs

4.5.1 General high voltage considerations

The dielectric strength of Liquid Argon has been studied in some detail [90, 91]. A value in the region of 38 - 40 kV/cm appears to be a safer lower limit, even in the case of bubble formation. The results of [90] showed that dielectric breakdown of Liquid Argon can be initiated by bubble formation. It may therefore be pragmatic to ensure that components which generate heat in a LArTPC should be kept far from the regions of the detector which need to sustain stable high voltage for long periods of time.

The exact breakdown voltage in Liquid Argon has, naturally, a strong dependence on geometry. The results of [91] showed the breakdown voltage of Liquid Argon depends on the surface area of the electrode which has an electric field which is above 80-90% of the maximum electric field. This is the so called stressed area. The results are consistent with a prediction [92] that the breakdown field is proportional to the -0.26th power of the area. For the same electrode shape, doubling the surface area reduces the electric field required for a discharge by roughly 80 %. The results of this study suggest that when designing high voltage components of a LArTPC, every effort should be made to minimise the surface area of the component that sustains a high electric field.

Although it has not yet been directly demonstrated in Liquid Argon, predictions of [92] also suggest that the breakdown field also depends on the physical volume around an electrode which is subject to a high electric field. The simple argument is that as this stressed volume increases, the probability of a flaw, such as an ion, wandering into the critical volume and initiating a breakdown, increases. One possible technique has been demonstrated which can help to reduce the possibility of dielectric breakdown in Liquid Argon [93]. It was shown that a thin dielectric coating, when applied to an electrode, can substantially increase the electric field strength that can be sustained without discharge.

Interpreting the above literature, it is possible to propose some simple guidelines for HV design. In the first instance, the shape of the electrode should be formed to reduce the maximum electric field on the surface of the electrode. This broadly reduces to using well rounded shapes such as spheres and toroids and avoiding sharp edges. The total surface area of the electrode

which sustains an electric field greater than 80-90% of the maximum field should be minimised. For parallel-plate type geometries this can be interpreted as reducing the physical size of the electrode. The dielectric strength of Liquid Argon has been shown to be proportional to the stressed area$^{-0.26}$. Changes to geometry which actually increase the maximum electric field on the surface may be favourable as long as the total stressed area is reduced by more than the 0.26^{th} power of the increase in electric field.

4.5.2 ARIADNE Cathode and HV feedthrough

At the base of the TPC is the ARIADNE cathode. This cathode is formed by a tensioned stainless steel mesh which is welded into a supporting frame. On one side of the cathode, a stainless steel toroid is welded, inside which the connection to the high voltage feedthrough is made. This torus has a large radius of curvature, slightly greater than 38 mm. This large radius helps reduce the local electric field on the surface of this connection. The shape of this toroid additionally shields the tip of the HVFT, which makes electrical connection inside of its circumference. The cathode bias is supplied by a Heinzinger PNChp -100 kV power supply.

The cathode of ARIADNE was designed to allow drift fields of up 1 kV/cm. This requirement dictates a maximum required cathode bias of -80 kV. The ARIADNE cathode was designed with a nominal capability of up to -100 kV to allow some margin of safety. During nominal operation, a drift field of 0.5 kV/cm is used. A photograph of the ARIADNE cathode is shown in Figure 4.11. A central stainless steel core is biased to the required cathode voltage. This stainless steel core is contained within a cryofitted UHMWPE sleeve. This sleeve forms the electrical insulation of the feedthrough and also creates a vacuum tight seal against the outer grounded stainless steel housing. The vacuum tightness of this assembly improves over time, since UHMWPE exhibits properties of cold flow. As the UHMWPE warms up and compresses tightly against the central core, the material is able to flow and fill any microscopic voids, ensuring a robust and extremely leak tight seal. The final assembly is leak tight better than 1E-8 mbar l/s, the limitation of leak testing equipment that was available. This outer stainless steel grounded housing provides substantial mechanical strength to the feedthrough.

A stainless steel torroid is welded to the detector side of the grounded

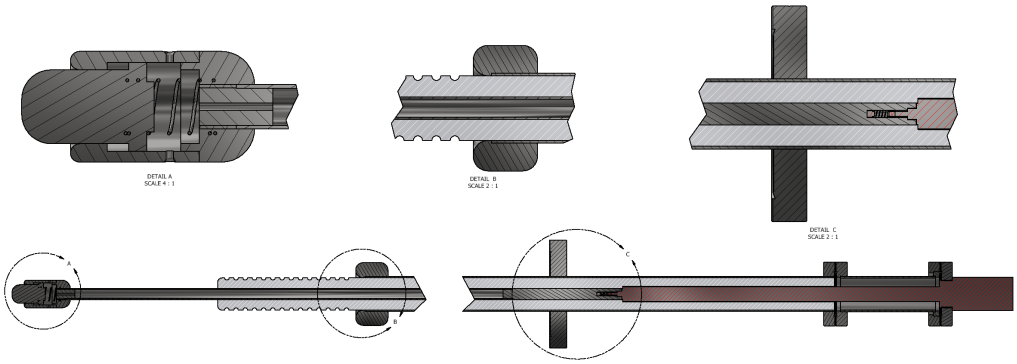

Figure 4.10: Cross section model of the ARIADNE high voltage feedthrough. The design of the spring loaded tip ensures a reliable electrical connection to the cathode. Grooves in the UHMWPE insulating jacket mitigate dielectric charging. A Conflat flange is integrated into the top end of the feedthrough, allowing the assembly to be connected to the flange of the detector.

Figure 4.11: Photograph of the completed ARIADNE high voltage feedthrough.

jacket, minimising the electric field at this interface. This interface requires significant attention since it is generally the location of highest field intensity. Many design variants exist, handling this interface in different ways. The LBNE [94] high voltage feedthrough features a flared conical end to the grounded jacket, providing a greatly smoothed electric field. A conflat flange is welded at the other end of the grounded jacket. This flange allows the HVFT to be mounted to the top flange of the detector. Figure 4.10 shows a cross section model of the ARIADNE HVFT. The spring loaded tip ensures a reliable electrical connection between the cathode and the HVFT, even in the case of cryogenic contractions.

COMSOL was used during the design stage of the high voltage feedthough to predict the performance. As can be seen in Figure 4.12a, the large diameter of the torroid located on the cathode of the TPC provides very effective field shaping. In this region, the highest field is 35 kV/cm, between the cathode toroid and the protection grid of the PMTs, which is grounded. A

much higher field, up to 80 kV/cm, is seen at the region where the grounded jacket of the HVFT terminates. This high field region is a common problem of feedthrough designs of this class, which use a torroidal termination at the end of the grounded jacket. The feedthrough has been successfully tested up to 80 kV/cm with no adverse issues and so the effect of this large field region is unclear. It is this large field region that is overcome by the flared grounded jacket of the LBNE style feedthroughs. As can be seen from the COMSOL simulations, the grooves in the end of the UHMWPE insulation have little effect on the electric field. The grooves serve a different purpose, to trap charge carriers. Both ionising radiation and the high electric field surrounding the cathode can create free electrons. These electrons accumulate on the surface of the insulating surfaces, an effect known as charging up. If the insulating surface is flat, these charge carriers can migrate along the surface. The accumulation of a sufficient quantity of charge carriers is believed to be a possible cause of discharges. The grooves in the UHMWPE insulation trap free charges, minimising the rate of surface charge accumulation.

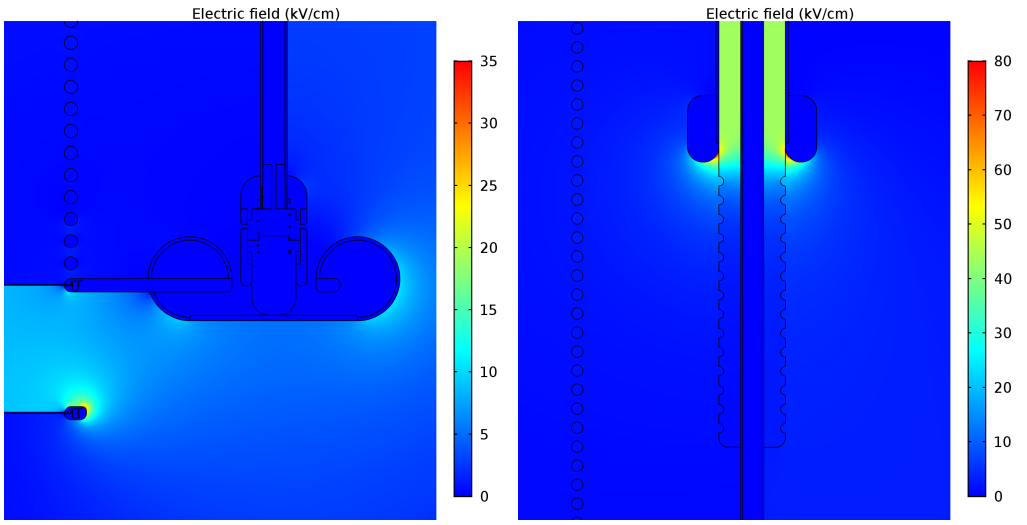

(a) (b)

Figure 4.12: COMSOL simulations of the electric field around the high voltage feedthrough. a) The electric field between the cathode and the PMT protection grid is approximately 35 kV/cm. b) Near the end of the grounded jacket of the high voltage feedthrough, a large local electric field exists. While not ideal, this feature was not found to have any noticeable adverse effects during operation.

4.5.3 20 kV feedthrough

The resistor chain of the TPC is terminated by a 20 kV feedthrough, connected to the extraction grid. This feedthrough is a commercial power feedthough, modified in length, such that the electrical connection is made in the liquid. The feedthrough has a threaded termination. A cable with a crimped loop termination is soldered to the extraction grid on one end, and secured to the 20 kV feedthrough using a nut on the other end. On the air side, this feedthrough is connected to a secondary high voltage power supply, which is used to regulate the bias applied to the extraction grid.

4.6 THGEM

The ARIADNE THGEM has typical dimensions, 1mm thick, containing a hexagonal array of through holes on a 800 micron pitch. Each hole has a diameter of 500 micron. Each hole additionally has a 50 micron dielectric rim etched back. This rim is believed to extend the breakdown voltage of the THGEM. Figure 4.13a shows a general view of the THGEM and Figure 4.13b shows a close up view of several holes. The individual layers of FR4 laminate are visible in each hole. The THGEM was manufactured by the CERN PCB workshop. Around the edge of the THGEM is a 5 mm wide guard ring. This guard ring contains no holes, and serves to ensure a more uniform electric field in the active region of the THGEM. In the case that the THGEM holes go all the way to the edge of the copper, the holes near the edge experience field distortions which produce gain variations compared to the bulk active area. The guard ring generally ensures that all of the holes in the active area have comparable electric field intensifies within them.

Electrical connection to the THGEM is made by two soldered coaxial cables. The central core of the cable is soldered to the THGEM plane and the coaxial shield is cut back around 5 cm to avoid presenting a discharge route. Once soldered, each cable is covered by a tightly fitting PTFE block, which provides electrical insulation. A photograph of the electrical connections to the THGEM can be seen in Figure 4.14. This PTFE block was found to be important for preventing discharges. Since the soldered connection to the THGEM is probably the closest point to the extraction grid below (The fillet of the solder is taller than the height of the copper THGEM plane), discharges were often localised to this connection when the PTFE block was not used.

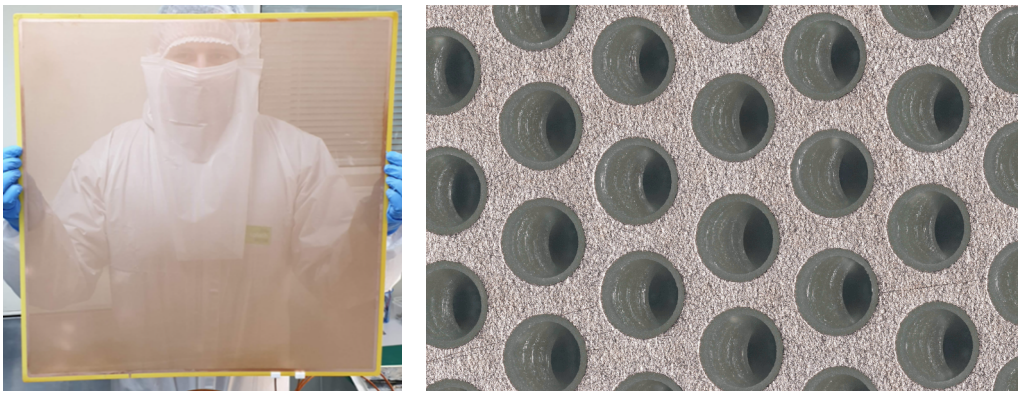

(a) (b)

Figure 4.13: The ARIADNE THGEM. a) A general overview of the THGEM. The active area is 53 cm × 53 cm. b) A close up view of individual holes in the THGEM. The individual FR4 laminate layers are visible inside each hole. The dielectric rim around each hole can also be seen.

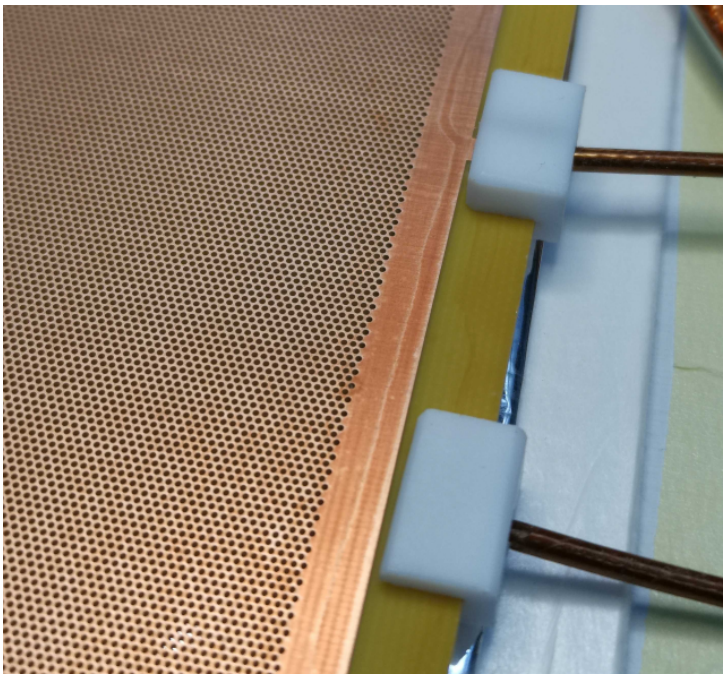

Figure 4.14: A close up view of the PTFE connector blocks, used to insulate the electrical connection to the THGEM. A cable is soldered to the THGEM, and then the PTFE blocks are installed with a light press fit, encapsulating the solder fillet.

4.7 Glass sheet / wavelength shifting

The light released from the THGEM in Argon is at 128 nm. For now, this light cannot be detected directly. TPB is used to wavelength shift the 128 nm light to 420 nm. 420 nm can be detected with good quantum efficiency by the EMCCD cameras. To perform this wavelength shifting, a 2.75mm thick borofloat glass sheet, with a finish of 60/40 scratch/dig is coated on the underside with TPB. The sheet is installed 1.8 mm above the THGEM. The distance between the THGEM and the TPB was found to have some influence on tracking resolution - this is discussed further in Section 9.1.3. The nominal coating thickness was 0.05 mg/cm^2.

The coating was performed by vacuum evaporation, using a custom-built vacuum evaporation chamber. The chamber uses five crucibles to increasing coating uniformity. A model of the vacuum evaporation chamber is shown in Figure 4.15. The chamber was evacuated to better than 1E-4 mbar before the coating process is started. Once a good vacuum is achieved, current is supplied to the crucibles, causing them to heat up. The current supplied to each crucible is gradually increased until the TPB within each crucible evaporates and coats the underside of the glass, which is suspended above. The coating thickness is controlled by adjusting both the ammount of TPB contained within each crucible and the distance between the crucibles and the glass sheet. A viewport on the side of the vacuum chamber provides access to visually inspect the coating process and to check that all of the crucibles have successfully evaporated the TPB. Once the coating is complete, the glass sheet is generally stored in the vacuum chamber for as long as possible. Once the detector is ready to close, the glass sheet is removed from the chamber and installed in the detector. This process attempts to minimise the amount of time which the TPB is exposed to ambient light, since TPB is known to deteriorate by exposure.

Figure 4.15: CAD model of the vacuum evaporation chamber used for TPB coating. The five crucibles are visible at the base of the chamber, as well as the viewport on the side of the chamber for optical inspection throughout the coating process.

4.8 EMCCD Cameras

The baseline design of ARIADNE includes four Andor iXon Ultra 888 EMCCD cameras for optical readout. In traditional CCD cameras, the sensitivity is eventually limited by the readout noise of each pixel. The cameras take advantage of thermoelectric cooling to lower the readout noise. To overcome the remaining readout noise, EMCCD cameras feature an internal gain stage, which amplifies the incident light signal. This amplification allows very faint signals to easily overcome the readout noise. The iXon Ultra 888 EMCCD cameras allow signal gains of up to 1000 in each pixel. The cameras have a read noise of approximately $100e^-$, introduced by analog to digital conversion and the frame readout process after exposure. This readout noise is approximately constant, independent of camera binning. Thus, provided photons are shared across multiple pixels, increasing pixel binning generally increases signal-to-noise.

The camera has a sensor size of 1024 $\times$ 1024 pixels, each 13 micron $\times$ 13 micron. During operation, the pixels of the camera may be binned together, increasing light collection at the cost of image resolution. Typically, the cameras are operated at either 4x4 or 8x8 binning. Considering each camera has a field of view of roughly 30 cm $\times$ 30 cm, 4x4 binning yields a resolution of just over 1 mm/pixel.

This resolution value was chosen based on previous experience [95] as well as considerations based on the expected transverse diffusion with the ARIADNE detector. As can be seen in Figure 2.10, the expected standard deviation transverse diffusion for a track which drifts the full length of the TPC is approximately 1.1 mm when operating at the nominal drift fields. Thus, the just over 1 mm/pixel nominal camera resolution was chosen to provide close to diffusion limited tracking.

When running at full resolution, the maximum readout rate is 26 frames per second. The readout rate increases with increasing binning since less pixels, and therefore less data, must be readout. At 4x4 binning, the maximum frame rate is increased to 92 frames per second.

The cameras have excellent quantum efficiency, better than 80 % between 410 nm and 780 nm. The quantum efficiency curve of the camera is shown in Figure 4.17. The camera has 16-bit digitisation and a pixel well depth of up to 80,000 electrons. The linearity of the camera is better than 99.9%

Figure 4.16: Four Andor iXon Ultra 888 EMCCD cameras, mounted onto the CCD leveling plate which is installed on the top flange of the detector.

across the entire pixel depth range.

Typically, a Spacecom VF50095M lens is used with each camera. This lens has a focal length of 50mm, and very high speed of f/0.95. All four cameras are mounted on a common reference surface, which has parallel machined flats in front of each camera, to which they are bolted securely. This ensures that the field of view of the four cameras is centered around a common axis. A light tight seal between the camera mounting plate and the detector flange is made using rubber bellows. These bellows can be easily lowered to gain quick access to the camera lenses to perform fine focus adjustments, without needing to dismount the whole camera from the mounting plate.

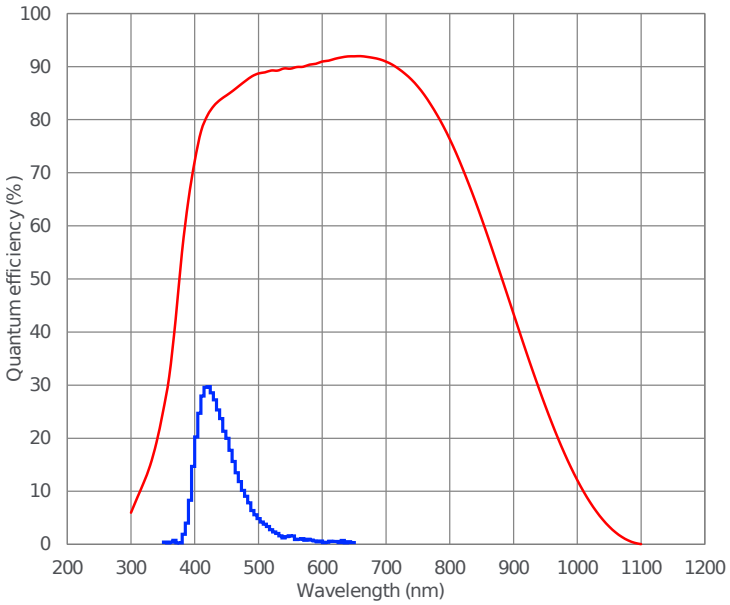

Figure 4.17: Quantum efficiency curve of the Andor iXon Ultra 888 EMCCD cameras, compared to the emission spectrum of TPB. TPB emission spectrum reproduced from [96].

4.9 PMTs and light collection

Apart from the four EMCCD cameras, the ARIADNE detector has four Hamamatsu R5912-02MOD PMTs, located underneath the TPC, for auxillary light collection. The R5912-02MOD PMT is a popular choice for many experiments [97–100]. More recent publications may refer to the R5912-20MOD PMT, but this is an identical device, just following a part number change by Hamamatsu. Figure 4.18 shows the four PMTs in the ARIADNE detector. Since the PMTs are not directly sensitive to 128 nm, they are coated with a 0.05 mg/cm^2 layer of TPB on the front face. This coating was deposited using vacuum evaporation, using the same method discussed in Section 4.7 for the coating of the wavelength shifting glass sheet.

To optimise light collection efficiency, the TPC is surrounded by four ESR Vikuiti reflector panels. The panels are coated with a thicker 0.22 mg/cm^2 layer of TPB. Two of the four reflector panels contain cnc knife cut holes, designed as entry and exit apertures for the laser calibration system. These holes allow the laser to traverse the TPC volume without contacting the reflector panels. It was unclear if the laser calibration system might cause damage to a reflector panel and so this was mostly a precautionary measure.

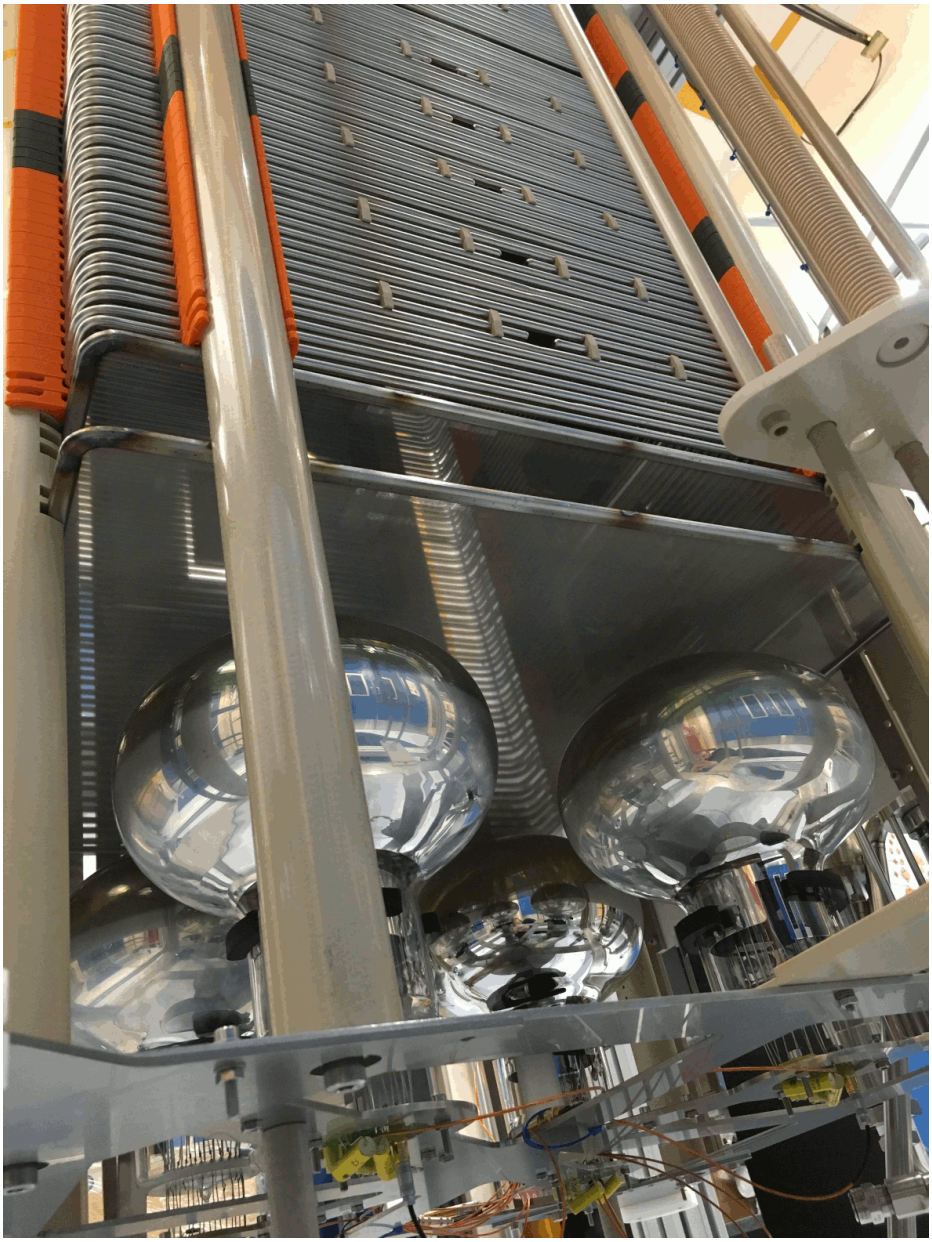

Figure 4.18: Photograph showing the four R5912-02MOD PMTs installed at the base of the ARIADNE TPC. The PMT protection grid is visible directly above the PMTs.

(a) (b)

Figure 4.19: ARIADNE reflector panels. a) the inside face of each reflector panel is coated with a 0.22 mg/cm^2 layer of TPB. b) The reflector panels installed onto the TPC. Holes in certain reflector panels are provided as access points for the laser calibration system. The UHMWPE block, that fills the interface between the beam plug and the TPC, is also visible.

4.10 Liquid Argon purification and recirculation

As we saw in Sections 2.4.1 and 2.5.3, Liquid argon purity is critical. The purity determines both the maximum drift distance in the TPC as well as the scintillation light yield. Control over electronegative impurities in particular is especially important. Electronegative impurities preferentially attach to drifting electrons, absorbing the detector signal. The purpose of the recirculation/filtration system in a liquid argon TPC is to remove those impurities which may degrade detector performance.

4.10.1 Liquid argon Purification cartridge

In the case of ARIADNE, an external purification system would greatly complicate cryostat design. It was decided that an internal system was a more practical option. An internal recirculation system promises minimal heat losses since the liquid argon is recirculated within a single cryostat. Obvious drawbacks however are the difficulty of accessing the system in case of any problems. The difficulty of access to the recirculation system for maintenance places tough constraints on the design. The system has to be designed for reliable, maintenance-free operation for extended periods of time. These constraints favour a design that is mechanically simple. Difficulty of access also means that before detector filling, the recirculation system must be fully regenerated. The filtration system cannot be accessed during operation and so its capacity must be sufficient to purify the detector volume without regeneration.

The purification rate of the system is defined by the volume flow rate of liquid argon through the purification cartridge, as well as the composition of the purification cartridge. A popular composition is a mixture of Engelhard CU-0226 S 14 $\times$ 20 mesh (Q-5) alongside 3 Å and 4 Å molecular sieves. The Q-5 mesh provides filtration of oxygen while the 3 Å and 4 Å molecular sieves provide filtration of H_2O. Limited data exists about the capacity of Q-5 in cryogenic liquid service. One measurement suggests a capacity of 0.49 gram of O_2 per kilogram of Q-5 [101]. This capacity is, at best, 25% of the room temperature capacity. As the oxygen retention of Q-5 mesh increases, efficiency decreases until eventually the mesh is saturated. For Q-5 mesh,

the filtration rate is proportional to the flow rate through the cartridge, at least for gas service. Once again, limited data exists for the efficiency of Q-5 as a function of cryogenic liquid flow rate, with most of the available test data presented as a function of gas flow rate at room temperature. The ARIADNE filtration system has a nominal flow rate of 300 L/h liquid through a $\approx$ 13.5 L filtration cartridge. [102]

Given the limited availability of test data for the performance of Q-5 in cryogenic liquid service, the volume of purification chemicals used in the ARIADNE purification system is heavily oversized. The purification system is never expected to be close to saturation and therefore should work close to peak efficiency for the entire purification cycle.

The following calculations were used to determine the volume and mixture of purification chemicals used in the ARIADNE recirculation system. We have, from [101], that the capacity of Q-5 at cryogenic temperatures is roughly 0.49 gram of O_2 per kilogram of Q-5. In order to determine the quantity of Q-5 required, we must determine the expected quantity of O_2 impurities that should be filtered. The ARIADNE detector is filled using N6.0 Argon, which has 99.9999 % minimum purity. In the worst case, the residual 0.0001 % Argon impurity could be completely O_2. The ARIADNE cryostat has a rated capacity of 1530 litres at 95% full. It is assumed that 2000 L of Liquid Argon is required for filling to account for any losses cooling down the cryostat. With a density of 1401 g/L, this corresponds to a requirement of roughly 2800 kg of Liquid Argon. Assuming N6.0 purity, this mass of liquid Argon could, in the worst case, introduce 3 grams of O_2 (0.0001 % $\times$ 2800 kg). Roughly 6 kilograms of Q-5 is required per 3 grams of O_2 impurity before saturation. Given that the efficiency of Q-5 reduces as it's capacity is taken up, it is preferred to use more Q-5 than strictly necessary. The ARIADNE internal filter cartridge uses roughly 10 kilograms of Q-5. These calculations predict that the internal filter cartridge should have sufficient capacity to purify a direct fill of N6.0 liquid Argon. A photograph from inside the internal purification cartridge can be seen in Figure 4.20. As an added precaution, and to reduce the burden on the internal filtration cartridge, the ARIADNE detector also has a large external filter which is used to pre-purify liquid Argon during filling. This external filter has a volume of 30 liters, of which roughly 25 liters is Q-5.

Recent catalyst developments have presented several alternatives to En-

Figure 4.20: A photograph inside of the internal purification cartridge. A mix of 3 Å and 4 Å molecular sieves can be seen as white pellets. Engelhard CU-0226 S 14 × 20 mesh (Q-5) mesh is seen in maroon.

gelhard Q-5. BASF Catalyst R3-11G, GetterMax 133 and GetterMax 233 have all been shown to have higher oxygen capacity than Q-5, at least at room temperature [103]. Another possibility may be to additionally consider the purification of Nitrogen. Nitrogen is a known quencher of light production in Liquid Argon for concentrations above roughly 1 ppm [23].

For measuring Liquid Argon purity inside the detector, two methods are commonplace. First, the slow component decay time of scintillation light can be studied. For the purest Liquid Argon, slow component decay times upwards of 1500 ns have been reported in the literature [104, 105]. Impurities within the Liquid Argon will quench the slow component decay time. Thus, by measuring the relative change of slow component decay time, the Liquid Argon purify can be inferred. A typically used model is

$$\tau = 300/O_2 \tag{4.1}$$

where τ is the electron lifetime in microsecond, and O_2 is the O_2 equivalent impurities in parts per billion. This method does have certain limitations. Specific impurities, such as nitrogen, can quench scintillation light production whilst not attaching to drifting electrons. Thus, this method should be used with caution when attempting to infer electron lifetime. Liquid Argon purity can naturally also be quantified by direct measurements of

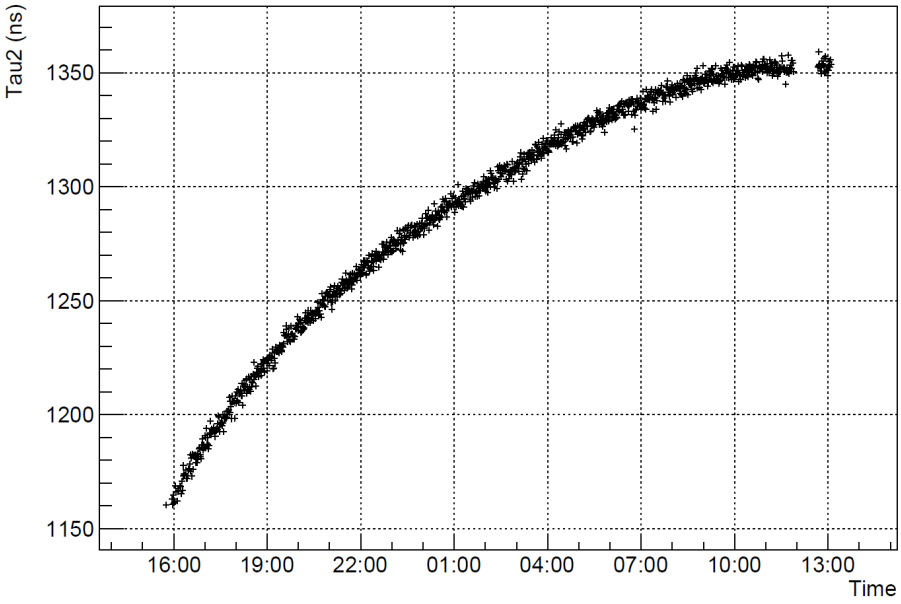

Figure 4.21: Liquid Argon slow component decay time as a function of time during the Liquid Argon purification process.

electron lifetime. By measuring the relative intensity of tracks in the TPC as a function of drift time, the quantity of electronegative impurities can be determined. Since the slow component measurement technique is more sensitive to light quenching impurities, and the electron lifetime measurement is more sensitive to electronegative impurities, both methods are highly complimentary. Figure 4.21 shows a plot of slow component decay time as a function of time during Liquid Argon purification.

It is significant to note here that the slow component decay did not continue to increase much beyond 1350 ns during continued recirculation. Despite this, electron lifetime was seen to continue to increase. Presumably, trace quantities of Nitrogen remain in the Liquid Argon, which are not filtered by the purification system. These Nitrogen impurities prevent further increase of the slow component decay time, but do not prevent the further increase of electron lifetime.

4.10.2 Liquid argon Recirculation

The ARIADNE detector performs liquid Argon recirculation using a custom built double bellow positive displacement pump. This pump is designed with a nominal flow rate of 300 L/h. However, the pump is typically operated at a reduced speed and stroke length to extend the service life of the bellows. A

diagram showing the general operating principle of the re-circulation system is shown in Figure 4.22.

The air side bellow of the ARIADNE pump system is driven by a custom designed linear motion assembly. The assembly is designed with minimal footprint on the ARIADNE flange so as to not interfere with neighboring feedthroughs and ports. A CAD drawing of the pump drive system is shown in Figure 4.23.

The system was designed to be easy to operate while retaining flexibility. It should be possible to quickly change certain pumping parameters such as stroke length and pumping speed without an extensive understanding of the system. The mechanical design of the system can be split up into several components. First is the supporting frame. This frame is formed from three standard linear shafts from Misumi. These shafts provide generous mechanical strength to the assembly but also double up as the linear motion solution. Three IGUS maintenance-free linear bearings run along the outer diameter of these shafts. The combined used of these shafts for structural as well as linear motion helps maintain the small footprint of the assembly. The three linear bushings are bolted to the plate which will perform the reciprocating motion. This plate is connected to the top of the bellow using three stainless steel shafts. By moving this plate, the bellow can be compressed or extended and thus the pump can be operated. The motion of this plate is driven by a 16 mm diameter, 50 mm pitch ballscrew. The high pitch of this ballscrew enables a fast pumping speed. The axial force generated by this ballscrew during pumping can be significant. These axial loads are far in excess of the loads that the bearings in the driving motor are capable of handling directly. Most motors are generally only rated for very modest axial loads so it is a good practice to handle these forces before the motor. The ballscrew used in the assembly has a stepped and threaded end. The end of the ballscrew is retained into a fixed end support in a secondary fixed plate, above the reciprocating plate. This fixed plate takes up all of the axial load of the ballscrew so that the motor bearings are protected.

A fixed mounting bracket is provided at the top of the assembly for mounting a NEMA34 frame size motor. Originally a stepper mounted was mounted here but this motor was later replaced with a Clearpath integrated servo motor. The motor shaft is coupled to the ballscrew using a stainless

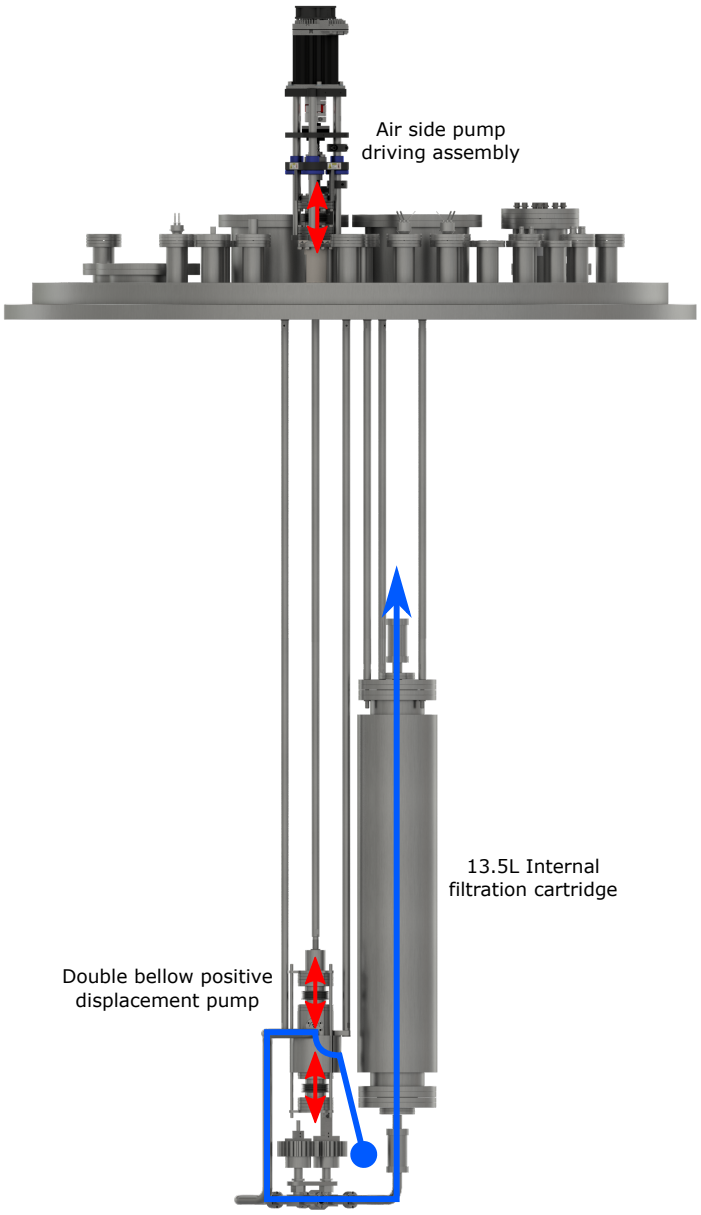

Figure 4.22: Recirculation system operating principle. A more detailed description of the air side assembly is given in Figure 4.23. Liquid Argon is drawn up from the base of the cryostat, and pumped through the internal purification cartridge. The purified Argon is returned to the cryostat volume near the top of the detector, far from the intake.

steel jaw coupling.

When compared to a stepper motor, the Clearpath integrated servo motor is a formidable upgrade. While the economical stepper motor definitely has its place for inexpensive or non-critical motion control applications, several shortcomings are imposing. Firstly, the basic stepper motor has very limited positional feedback. It is possible that a stepper motor can lose steps if a specific movement requires more torque than the stepper motor can deliver. In order to try and mitigate the possibility of losing steps is it common that an oversized stepper motor is used. This can lead to excessive power consumption and noise. Stepper motors can also produce substantial amounts of heat when powered at their rated motor power.

Clearpath integrated servo motors integrate a brushless DC motor with a high resolution encoder. This encoder constantly monitors the position of the motor shaft and provides high resolution, high speed feedback about the angle of the motor shaft. A digital servo drive is integrated directly into the motor. This servo drive provides commands to the BLDC motor and monitors encoder feedback to ensure that the motion is performing as expected. This feedback loop allows for very reliable motion control.

Clearpath servo motors are provided in several configurations. Each configuration is tailored towards several ways that a user may wish to provide commands to the motor. ClearPath-SD motors offer a simple step and direction interface. The user should send pulses to the step pin of the motor to turn the shaft a single step in the direction set by the voltage applied to the direction pin. These step and direction pulses can be easily generated using an Arduino, Raspberry Pi or FPGA. This control scheme makes operation of a ClearPath-SD series motor very similar to the operation of a stepper motors. In most cases a ClearPath-SD motor would be a drop in replacement for a stepper motor.

ClearPath-SC motors are designed for software control. This motor configuration comes with a complete C++ motion control library, compatible with Windows and Linux. Up to 16 Clearpath motors can be controlled with a single USB port. ClearPath-SC motors are ideal for applications that require tight synchronization of several axes or for applications that require integration of motor control into other processing software. Consider the example of calibration of a sensor using a telescope. Control of the ClearPath-SC motor could be integrated together with DAQ to enable

sensor scans and calibration using a single C++ script. The integration of motor control and DAQ together in applications such as this can greatly improve process reliability.

All Clearpath motors have a third control method. A micro-usb connection at the rear of the motor housing is provided which enables both motor control and monitor monitoring. A windows program is available which provides a GUI capable of powerful motor control options while providing live motor monitoring. Figure 4.24 shows a screenshot of the ARIADNE pump motor being controlled using this software. By providing a Teamviewer connection on the windows PC that is connected to the motor, remote control and monitoring of the motor was easily made possible. The clearpath software provides comprehensive feedback about all motor parameters including position, torque and motor temperature. A user can quickly confirm that the motor is performing the required motion profile and that the torque output of the motor is as expected. In the case of the ARIADNE detector the torque output of the motor provides a measure of the pumping force that is being exerted. By monitoring for changes in pumping force over time it is possible to monitor for wear of the pump or of the bellows. Unexpected changes in torque output of the motor over time may give advanced warning of mechanical problems in the system. The Clearpath motors were found to be very reliable and are thoroughly recommended for dependable motion control applications.

4.11 Cryogenics

Once the cryostat is full with liquid Argon, heat inputs through the cryostat and top flange will slowly boil the liquid Argon. Without intervention, the liquid Argon will be boiled off and the gas phase pressure of the detector will rise. In order to counteract the heat losses of the cryostat, a cryocooler is installed into the top flange. This cryocooler extracts heat from the gas phase of the detector and deposits the heat into an external water chiller. The cryocooler itself has no option to control its own cooling power output. Instead, to avoid over condensation of liquid Argon, the cold head is wrapped with a flexible Kapton heater. By providing extra heat input to the kapton heater, the total cooling power of the cryocooler system is controlled. This is comparable to maintaining the speed limit in your car by applying full

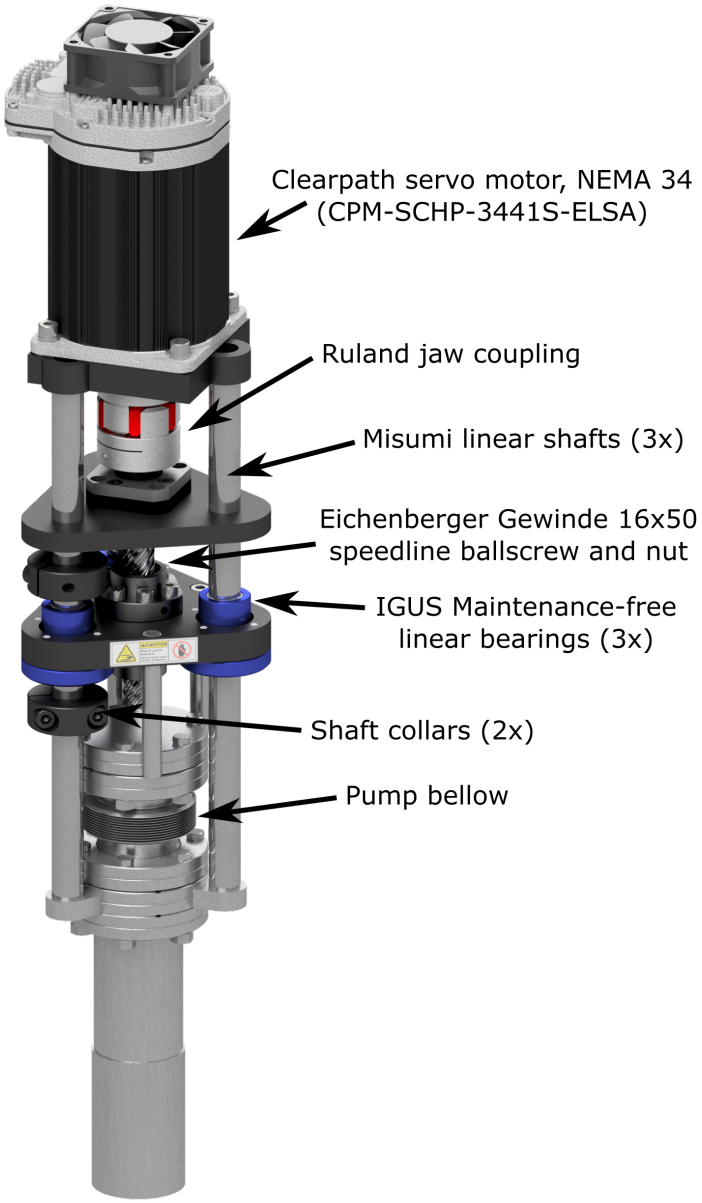

Figure 4.23: Air side pump motor driving system. A Clearpath servo motor provides robust motion control.

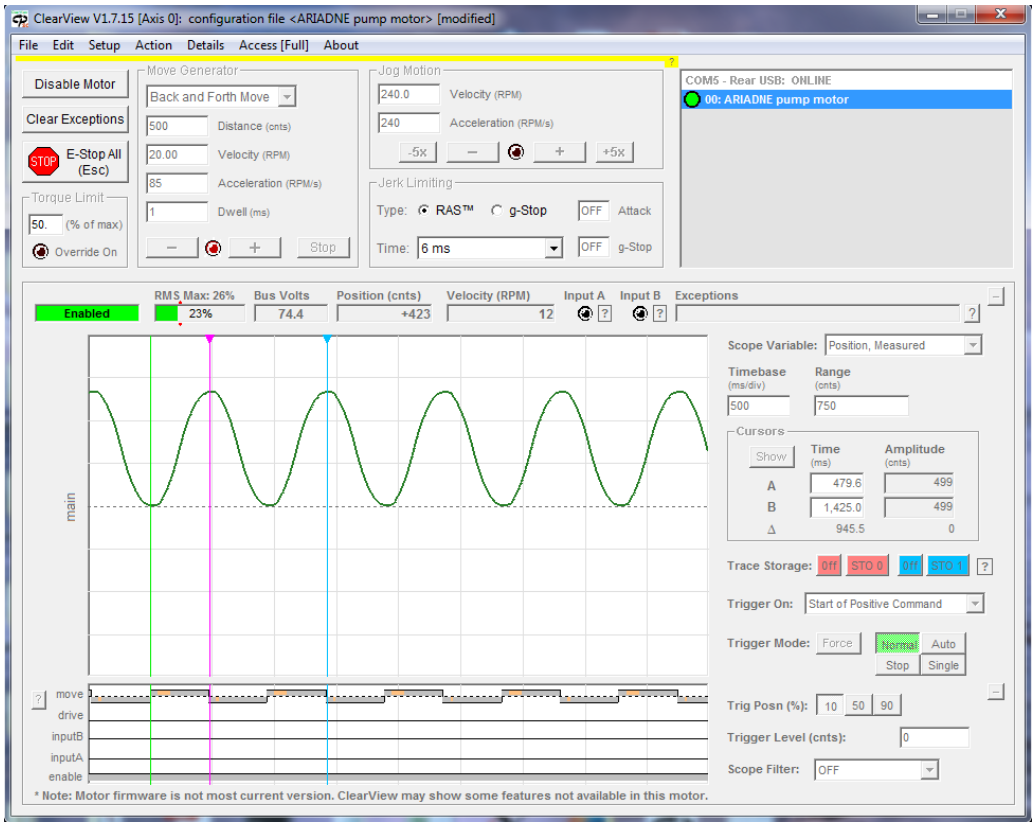

Figure 4.24: Screenshot taken from the clearview software. Using this software, motor control parameters such as maximum torque and speed can be configured. The oscilloscope view provides live feedback about the motor status, including position feedback and torque usage.

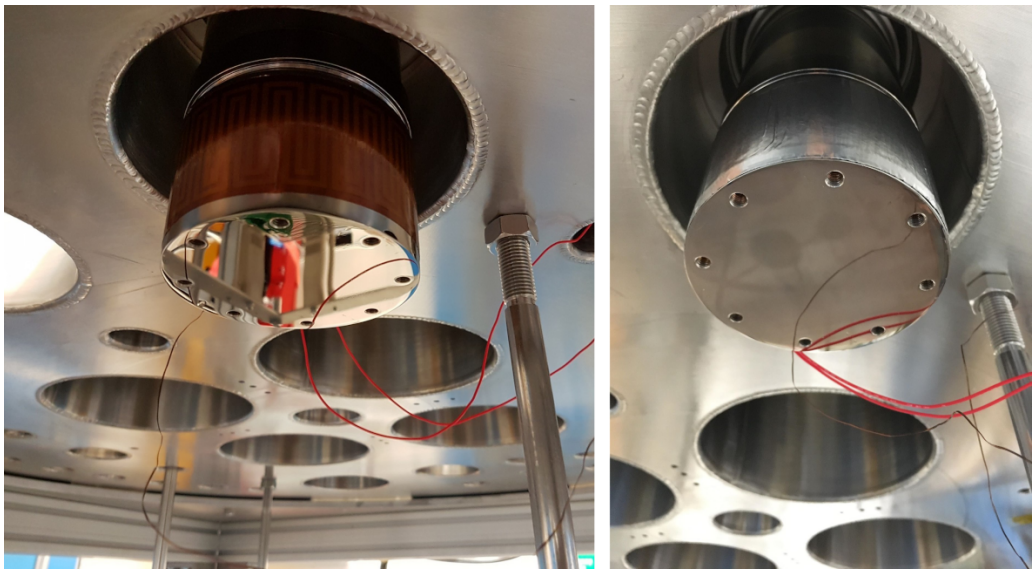

Figure 4.25: Photograph of the cryocooler head inside the detector volume. On the left, the kapton heater is visible, which is wrapped around the cryocooler head. The heater provides heat input to the system, regulating the cooling power of the cryocooler. On the right, the heater has been wrapped with cryogenically serviceable aluminum tape, to provide extra mechanical support to the kapton heater connection.

throttle while simultaneously holding the brakes. This control loop appears to be an extravagant waste of energy but was found to be very reliable.

The cryocooler has been successfully used for operation of the ARIADNE detector at a stable pressure for extended periods of time. By fine control of the heat input provided to the cold head the pressure in the detector was controllable to the millibar level. It is important to ensure that the cryocooler has a reliable supply of both electricity and cooling water. In the case of loss of electrical or cooling power the cryocooler will shut down for self-preservation. This can result in a short period of instability of the liquid Argon level until the cryocooler is reactivated and thermal equilibrium can be restored. This may induce a longer period of detector instability if the THGEM becomes wet due to an unstable Liquid Argon level.

4.12 Detector monitoring and slow control

In order to monitor the detector during operation, a suite of sensors and monitoring systems are installed. Three internal thermocouples, placed at the bottom, middle, and top of the TPC provide feedback of the Liquid

Argon level during filling and emptying. In principle these thermocouples could be used to monitor temperature gradients in the TPC but since they were not calibrated this study has not yet been performed. An additional internal thermocouple is mounted to the underside of the top flange using kapton tape with a matching thermocouple mounted externally on the top of the flange. This thermocouple pair is mainly used to estimate the heat losses that should be present through the flange. A final external thermocouple is attached arbitrarily to the cryostat outer wall. Trends in this thermocouples temperature can be used to infer the condition of the vacuum jacket of the cryostat.

Two internal webcams provide feedback on the Liquid Argon level close to the THGEM as well as provide a view of the internal recirculation system. The first webcam is used to ensure that the Liquid level is roughly parallel to the THGEM. The second webcam provides video feedback of Liquid Argon recirculation which is used to confirm that the Liquid Argon pump is functioning well. These internal webcams require light to operate so a selection of individually controllable LEDs are installed around the top of the TPC. These LEDs provide both blue and red illumination to all key parts of the detector which can be seen by the webcams.

Pressure monitoring is performed using two pressure sensors. One pressure sensor is better suited to monitor overpressure, whilst the other is only used when evacuating the cryostat, and provides accurate pressure readings down to 1E-9 mbar.

Chapter 5

The ARIADNE detector exposed to the CERN T9 beamline

The performance of the ARIADNE detector using EMCCD cameras was tested at the CERN T9 beamline in March/April 2018. The T9 beamline is a mixed charge particle testbeam, providing a mixture of electrons, muons, pions, kaons and protons in a momentum range between 0.5 - 8 GeV/c. Before the experiment was deployed to the beamline, Geant4 beamline simulations were performed. These are discussed in Section 5.1. A gallery of events and discussion of detector operation at the beamline is presented in Section 5.2.

5.1 Beamline simulation

The goal of the T9 beamline simulation was to provide a better understanding of the particle flux that could be expected at the reference focus of the beamline. Available documentation for the T9 beamline [106] only provides composition of the beam at the production target, not at the reference focus. Certain, short lived, particles such as as pions, may decay in the beamline and not reach the experimental area. The beamline simulation allowed us to quantify these effects, to make more informed decisions about which momentum range should be scanned during data taking. Figure 5.1 shows a photograph of a section of the beamline, immediately upstream of the experimental area. In this photograph we can identify two quadrupole magnets

in blue, a dipole magnet in green, and a short gap in the beamline which can be used for installing time of flight systems. Two large concrete/iron shielding elements are visible in red, both of which are found after dipole magnets. These shielded elements absorb particles which are not successfully transported by the dipole magnets, shielding the experimental area.

The beamline simulation was constructed completely from Geant4 primitives. More complete packages for beamline simulation do exist, such as G4Beamline, but these packages are more tailored towards beamline design, rather than using the beamline to produce a particle sample to be delivered to a simulated detector. The geometry of the beamline was constructed using publicly available CAD models of the beamline. Figure 5.2 shows a schematic of the T9 beamline, and two screenshots of the simulated geometry. In the simulated geometry we can identify the quadrupole magnets as blue and the dipole magnets as green. The concrete shielding of the beamline is visible in white. The ARIADNE detector is seen on the far right, sitting at the reference focus of the beamline.

The magnet parameters of the beamline were initially approximately using publicly available values of the current delivered to each magnet. These values were then fine tuned until the transport properties of the beamline were in rough agreement with the simulations that were performed by CERN during the beam commissioning [107]. Figure 5.3 shows the simulated beam profiles as a function of position along the beamline, for both horizontal and vertical planes.

The simulations provided guidance for detector placement in the experimental area. From the simulations, it was found that the detector need not be positioned extremely precisely in the experimental area, since the beam is mostly coherent over a few meters at the reference focus. For computational reasons, the initial products of the beamline at the north multitarget were assumed, distributed according to simulations produced by CERN. This assumption however misses one detail about beamline operation. During the interaction of the PS beam with the north multitarget, a large quantity of muons, distributed over a wide momentum range, are produced. These muons easily pass through the beamline shielding and produce a background of events in the detector. These muons are often called beam halo muons. Had the interaction of the PS beam on the north multitarget been simulated, the beamline simulation may have provided information about the

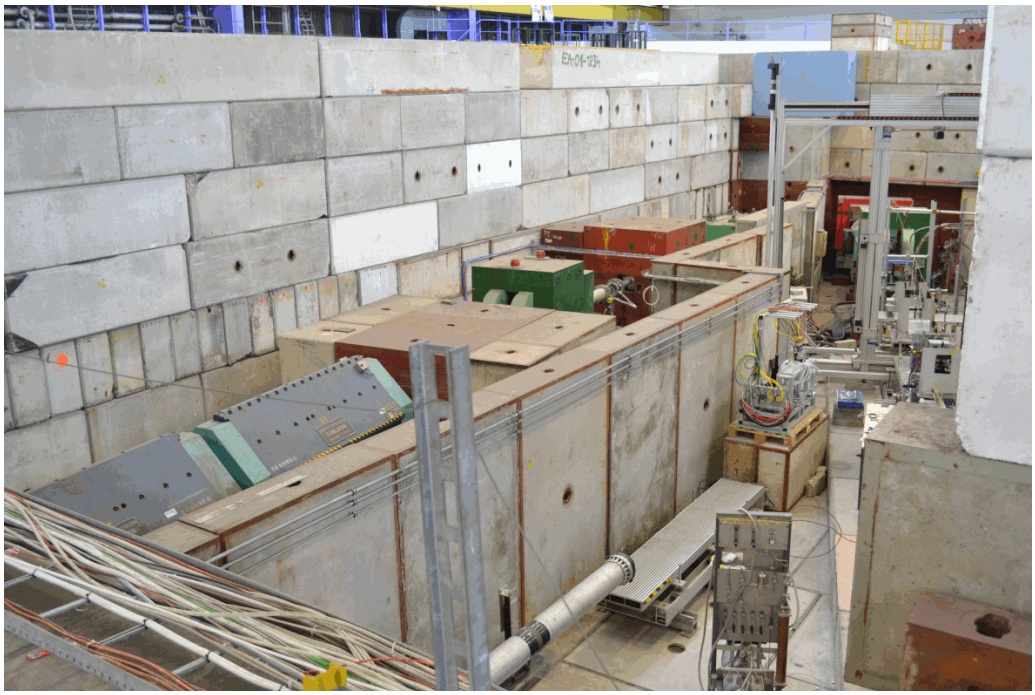

Figure 5.1: Photograph of the T9 beamline, upstream of the experimental area. Dipole magnets can be seen in Green, and quadrupole magnets in blue. A gap in the beamline is visible, allowing time of flight systems to be installed.

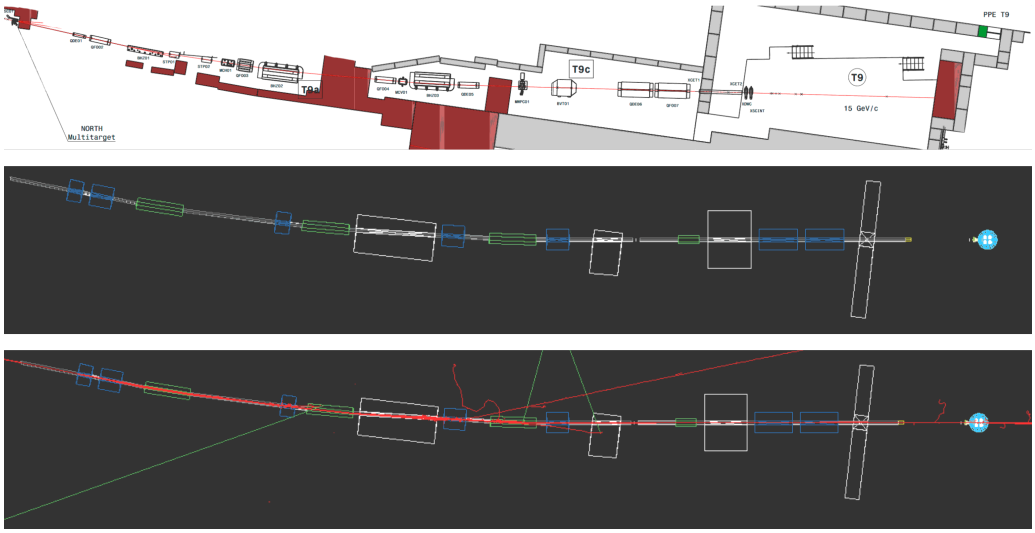

Figure 5.2: A comparison of the simulated T9 beamline geometry to an overhead schematic of the T9 beamline. All beamline magnets are included, as well as all important elements of concrete shielding, which are typically found immediately after a dipole magnet. In the bottom most image, a simulated beam spill is visible.

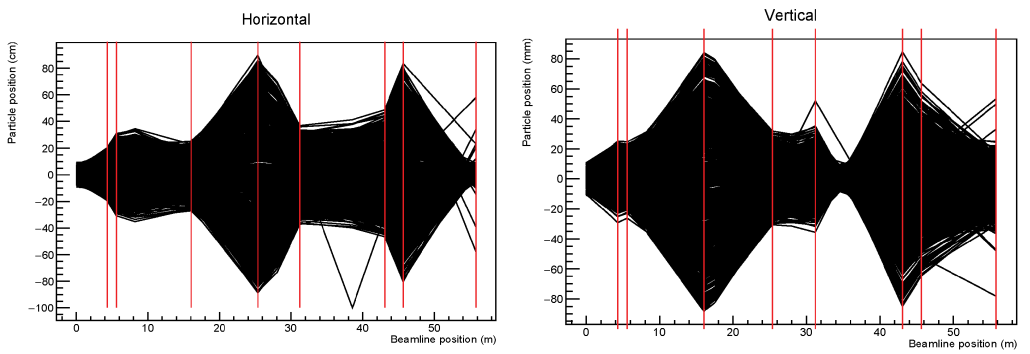

Figure 5.3: Simulated T9 beam profiles in both horizontal and vertical planes. Red lines mark the positions of quadrupole magnets, and finally the reference focus of the beam. The beam profiles are in reasonable agreement with simulations performed during commissioning of the beamline, available elsewhere [106].

rate of halo muons in the ARIADNE detector, before deployment. These halo muons served as an irreducible background during data taking, greatly complicating subsequent analysis. This point illustrates the peril of making assumptions to simplify simulations.

5.2 Beamline deployment

Once at CERN, the ARIADNE detector was craned into the experimental area. The detector was placed at the reference focus of the beam, and the height of the detector was adjusted such that the beam window was at the height of the beamline. For filling, the detector was connected to provided venting lines, which vented any excess Argon outside of the east area building. Once full, a short period of recirculation and purification was performed before the beamline became available.

From the T9 control center, a user of the beamline has access to adjust magnets currents for each of the different magnets in the beamline. A table of predefined operating currents is provided for each beamline momentum setting, but the user is free to tweak these values to tune the beamline performance. By adjusting the dipole magnet currents, the momentum acceptance of the beamline can be changed. By adjusting the quadrupole magnet settings, the focus of the beam can be adjusted within the experimental area. The beam can be scanned in the vertical and horizontal planes to ensure

good alignment with the beam window.

The user also has access to collimator controls, which allows for fine control over the beam flux. The collimators are two sets of movable jaws, in two planes perpendicular to the beam axis. Closing the collimators causes the jaws to impinge into the beam profile, reducing the rate of particles reaching the experimental area. Generally, the collimators were tuned to provide approximately 20 particles per spill, to minimise pileup. Each spill of the beamline has a duration of 350 ms, during which particles are provided uniformly, within a time tolerance of nanoseconds. The EMCCD cameras were found to operate best at a rate close to 50 Hz, and an exposure time of 400 microseconds. 20 particles provided during a 350 millisecond beam window, translates to one particle roughly every 17.5 milliseconds. This rate is in line with the maximum 50 Hz readout rate of the cameras, and the chance of pileup of beamline particles was expected to be minimal. As was earlier discussed, each beamline spill also provided an irreducible background of halo muons. Thus, each event window generally contained one or fewer beamline particles, plus this halo muon background.

Due to ongoing building works in the experimental area, a scaffolding was constructed around and above the detector, providing protection from works overhead. Figure 5.4 shows several photographs of the ARIADNE experiment at the T9 beamline.

Typically, the ARIADNE detector was operated with a drift field of 960 V/cm. Given the strict timelines of beamline operation, limited time for purification was available. The larger drift field helped to compensate for the less than nominal electron lifetime. An electrical fault with the THGEM feedthrough meant that the maximum bias that could be applied to the THGEM was 2.7 kV. Later testing in Liverpool found that during manufacture, the ceramic insulation of the feedthrough had been damaged during the welding process. This damage reduced the insulating capability of the feedthrough, limiting the maximum bias that was possible. At the lower THGEM bias of 2.7 kV, light production from the THGEM is quite heavily suppressed. Figure 5.5 shows a calibration performed of the THGEM at Liverpool, with a full functional feedthrough. From the Figure, a clear suppression of light production is seen at 2.7 kV. If operated at the nominal bias of 3.2 kV, at least double the light output could be expected.

Despite this large reduction in light production, data taking was still

possible with a reasonable level of signal to noise. Over the 18 days of beam time, a total of 800,000 events were collected, mostly below 2 GeV/c. Figure 5.7 shows two selected events from the data taken at T9. Analysis is ongoing with data taken from the beamline.

As well as beamline events, several interesting cosmic events were also seen during operation at CERN. Figure 5.8 shows an event display of a cosmic air shower. After inspecting the data that was taken, it was clear that excellent (x, y) resolution was possible. Yet, operation at the T9 beamline highlighted a key challenge of optical readout using EMCCDs, namely z dimension reconstruction. The general principle of 3D reconstruction was that the EMCCD readout channel should be combined with a faster readout channel, such as a PMT, to recover z position information about the track. By performing pulse shape analysis, it is possible to determine both the depth and extent of an event in the z-axis. The topmost part of the track can be identified by measuring the time delay between the S1 and S2 signals on the PMT. The total extent of the track in z can be determined by measuring the total time duration of the S2 pulse. The general principle of this reconstruction method is shown in Figure 5.6. The S2 signal is seen to be distinct from the S1 signal, which allows the depth of the event in the TPC to be determined. The duration and intensity of the S2 profile allows information about the event in the z dimension to be inferred.

Although this method had proven to be quite robust for simple through-going cosmic muons, the beamline environment was much more challenging. Considering an isolated electromagnetic shower; the task of assigning segments of a PMT S2 pulse to individual branches of the shower is mostly intractable. This challenge was compounded by the highly active environment of the beamline. The halo muons from the PS beamline accompanied each beam spill, essentially guaranteeing pileup within any event window. Figure 5.9 shows an event display containing the typical level of halo muon contamination. Following return from the beamline, substantial R&D effort began to tackle this limitation. This R&D effort culminated in the development of a novel optical readout technology, which enables full (x, y, z) reconstruction using a camera. This development is presented in Chapter 6.

Figure 5.4: Photographs taken during the deployment of the ARIADNE detector to the CERN T9 beamline. Top left: ARIADNE is unloaded after transportation. Top right: The ARIADNE detector is craned into the experimental area. Bottom left: The ARIADNE detector in the experimental area, taken during initial detector setup. Bottom right: The ARIADNE detector surrounded by protective scaffolding, shielding the detector from works overhead.

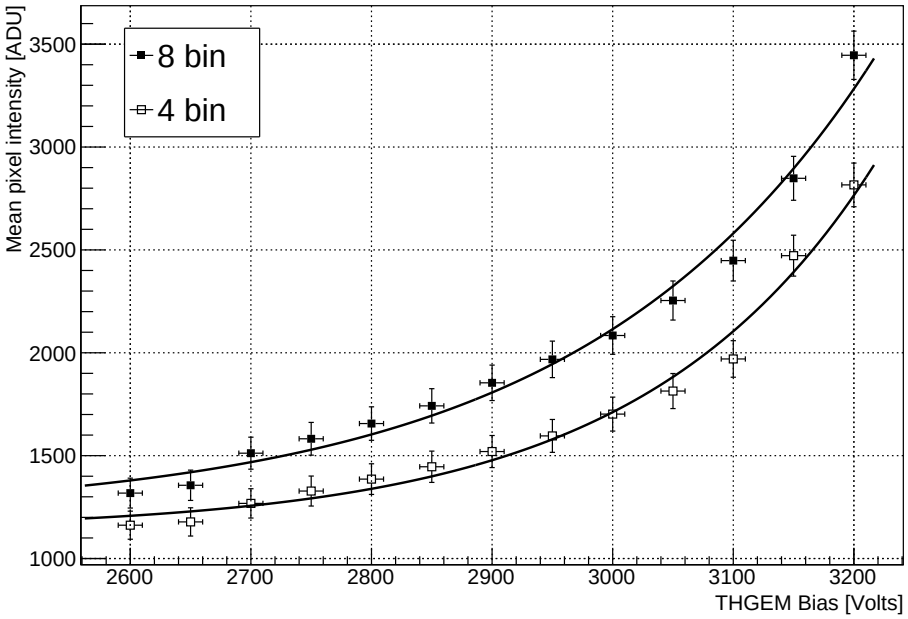

Figure 5.5: Measurement of light production from the ARIADNE THGEM in Liverpool, following repairs to the THGEM high voltage feedthrough. From these measurements, it is clear to see the suppressed light production that would have been present during T9 beamline operation, where the maximum THGEM bias was limited to 2.7 kV.

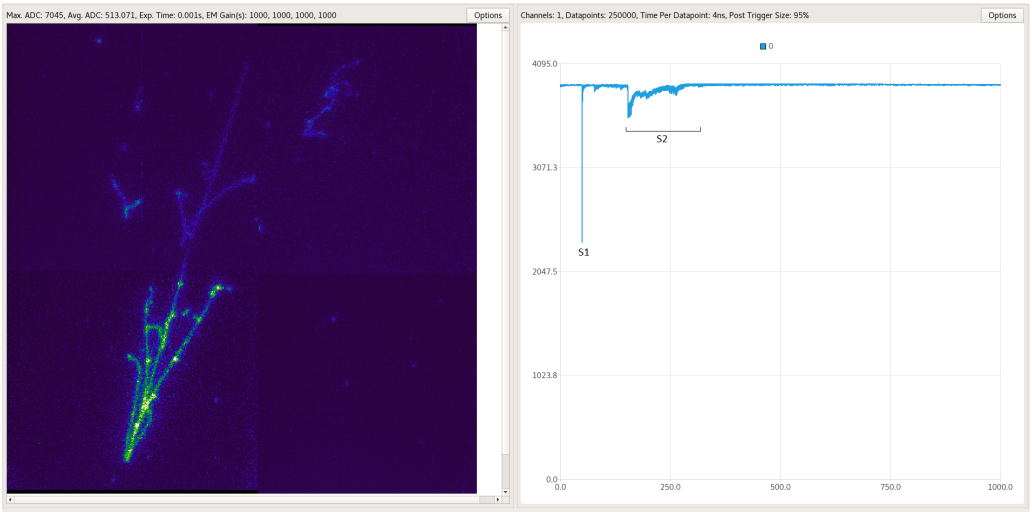

Figure 5.6: Demonstration the 3D reconstruction principle possible by the combination of an EMCCD image with a PMT signal. From the PMT response on the right of the Figure, we can see that the S1 and S2 signals are disconnected. From the time delay between these two signals, we can infer the depth of the event in the TPC. The duration of the S2 pulse, as well as it's intensity profile, allows coarse 3D reconstruction of the event in the z direction.

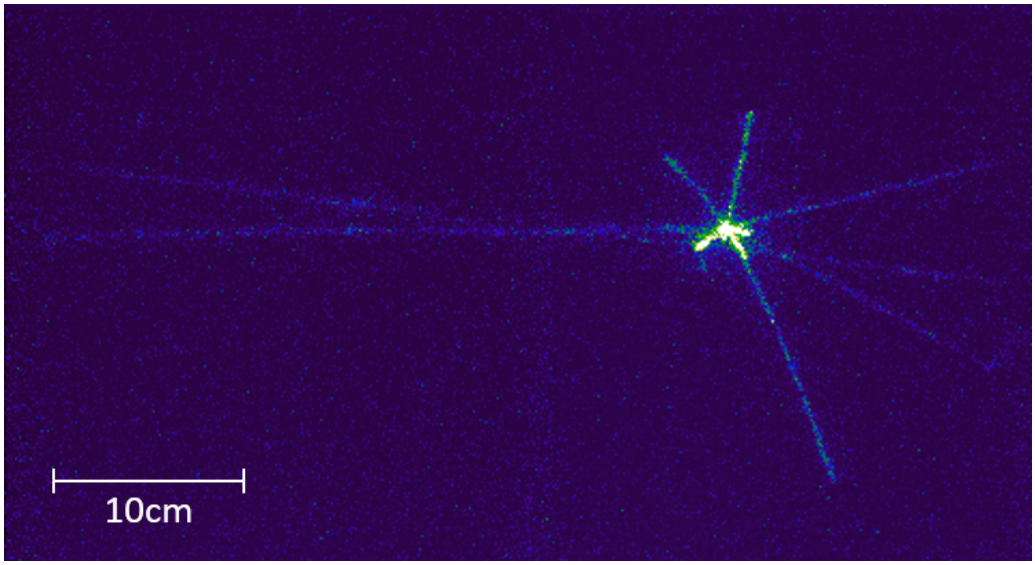

(a) 3.0 GeV/c anti-proton candidate

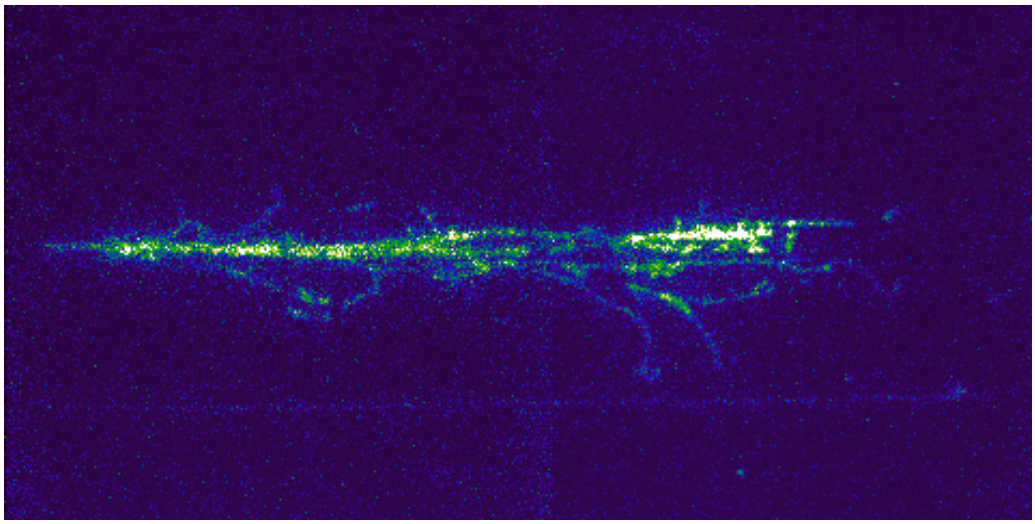

(b) 5.0 GeV/c electromagnetic shower

Figure 5.7: Two sample events taken during beamline operation.

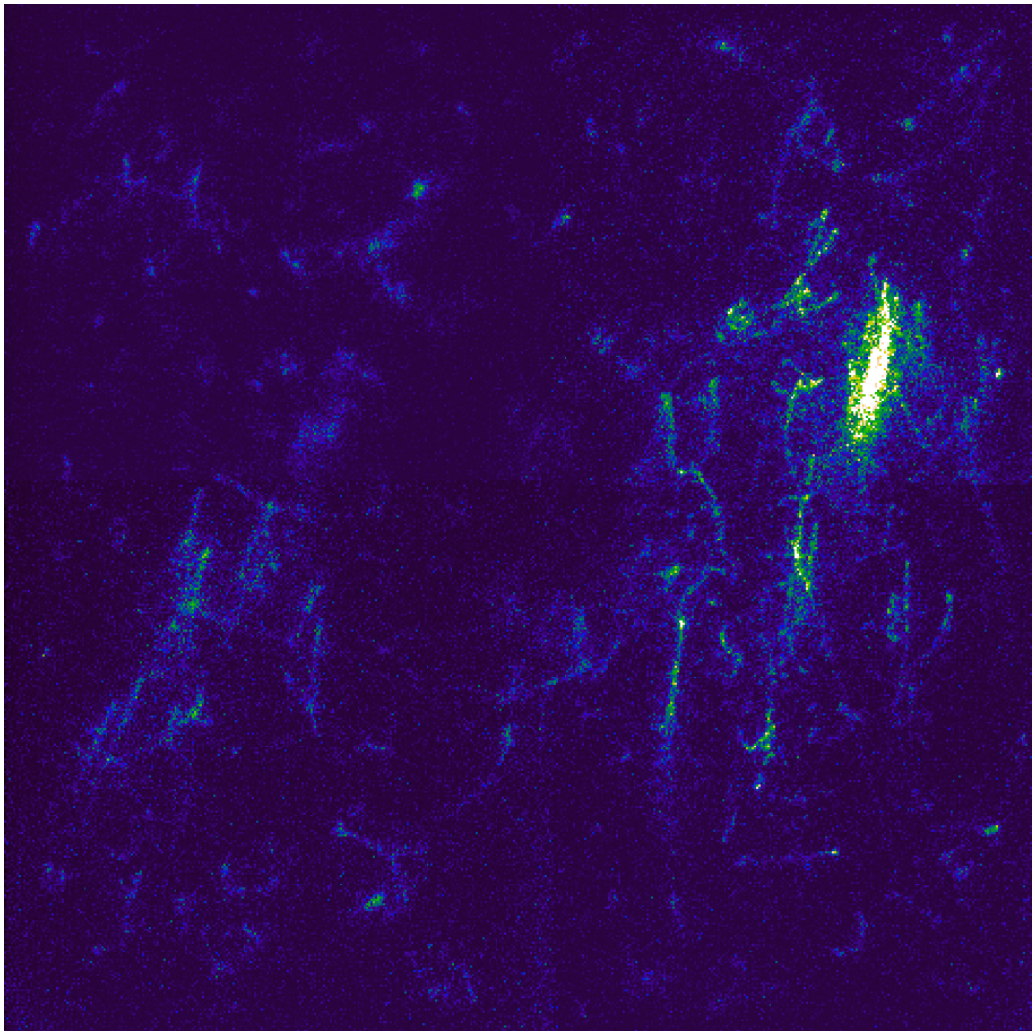

Figure 5.8: A cosmic air shower seen during operation at the T9 beamline.

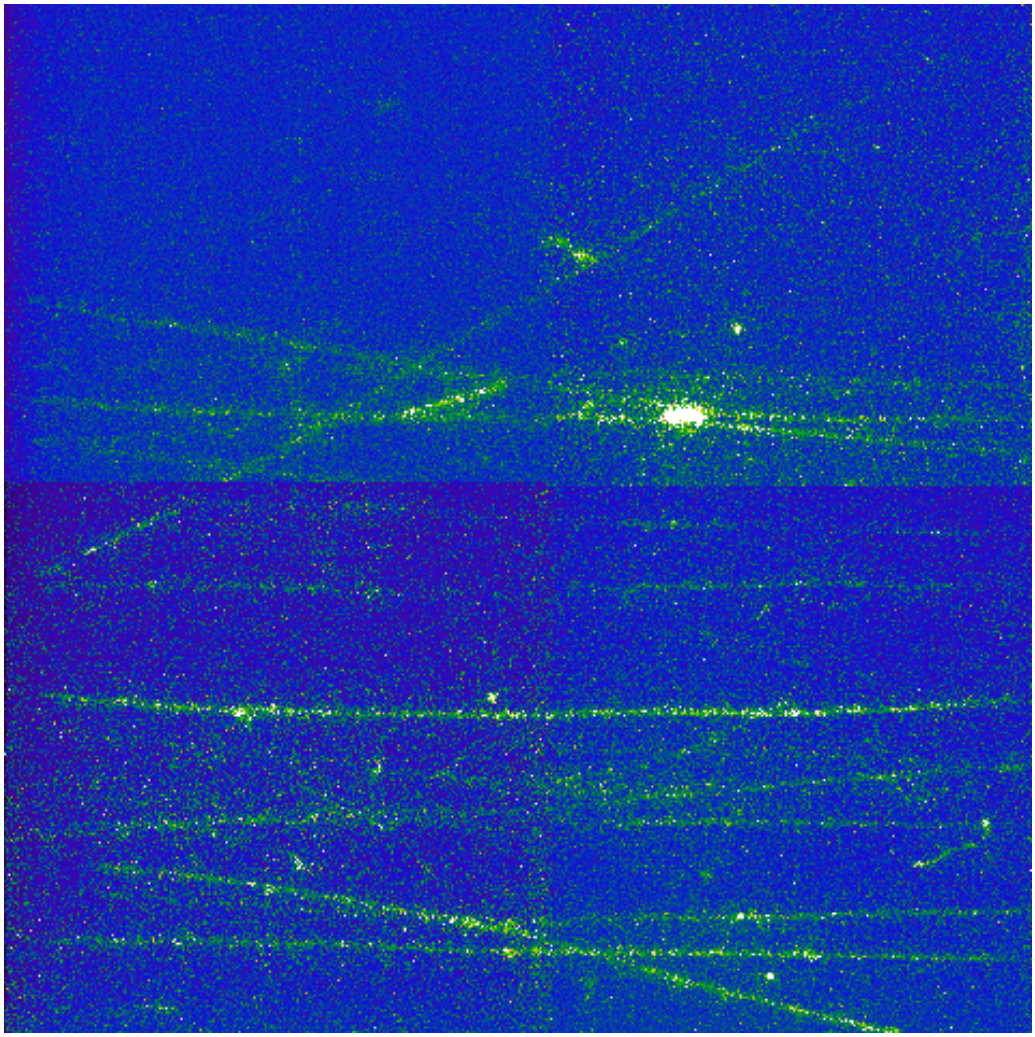

Figure 5.9: An example event display, which shows the typical level of beam halo muon contamination in any event window. This halo muon contamination makes disentangling beamline events from background a challenge.

Chapter 6

Development of Timepix 3 based camera readout

Results from the T9 beamlined showed that excellent (x, y) resolution was possible with optical readout. The z dimension however, remained a challenge. Moreover, the frame based readout can also be limiting. EMCCD cameras operate by integrating light over a predefined exposure time. Given the drift velocity of electrons in LAr is $\approx 1.6\text{mm}/\mu\text{s}$ at 0.5 kV/cm, an exposure time of less than ≈ 500 ns would be required for z position resolution on the millimeter scale. This infers a frame rate of 2 MHz, unattainable using today's commercial EMCCD or CMOS camera technologies. Moreover, even if this frame rate was possible, the ensuing data rate would be practically unmanageable. Early on during R&D efforts, it became clear that high resolution z position tracking would require a new approach. Such an approach was developed using a camera based on the Timepix 3 (TPX3) ASIC. The crucial benefit of this ASIC is the escape from frame-based readout.

6.1 The Timepix3 ASIC

Timepix 3 (TPX3) [108] is a general purpose ASIC, designed to provide simultaneous intensity and timing information for detected signals. Each pixel of TPX3 contains an individually customisable pre-amplifier and digitiser. The general operating principle of the TPX3 ASIC is described as follows

1. Signal arrives at a pixel of TPX3

2. The pre-amplifer in the pixel integrates the signal that is received. If

this charge signal goes above a predefined pixel threshold, then the readout process begins. If the signal does not exceed the pixel threshold then the pixel is not readout (it is zero-supressed).

3. The time at which the pre-amplifier signal crosses the pixel threshold is known as the Time of Arrival (ToA). This value has 1.6 ns resolution, limited by the 640 MHz fast time of arrival clock within the TPX3 ASIC.

4. The pre-amplifer signal begins to decay. The time duration between the pre-amplifier signal rising over the pixel threshold and decaying below the pixel threshold is known as Time over Threshold (ToT). This value is proportional to the intensity of the signal and is stored with 10-bit resolution.

5. A packet of data containing ToA, ToT and pixel address information is created and readout from the ASIC. The pixel address is a 16-bit value which encodes the pixel's (x, y) location on the ASIC. This readout step incurs a 475 ns pixel dead time.

6. After the 475 ns dead time, the pixel is ready for the next event.

The TPX3 ASIC is a general purpose readout chip, designed to be suitable for a wide variety of applications. Thus, a wide selection of parameters are available through which the response of the ASIC can be customised. For best performance, these parameters should be reasonably well tuned to the specific application. The effect of some of these parameters is illustrated on Figure 6.1. One important settings is the pixel Krummenacher current. This current dictates the decay time of the pre-amplifier. A high current allows a fast pre-amplifier decay and visa versa. If the pre-amplifier decay time is too short, the full 10-bit ToT range may not be used. Conversely, if the decay time is too long, hits may saturate the 10-bit range and calorimetric information may be lost. During operation, this value was tuned to try and best use the 10-bit ToT range. Other parameters, such as rise time of the pre-amplifier, can also be customised. Ideally, the rise time should be as fast as possible. If the rise time is slow, the time at which the pre-amplifier signal crosses the pixel threshold can be different from the time at which the signal hit the pixel. This effect is known as time walk. The drawback of a fast pre-amplifier rise time is increased heat output and power draw

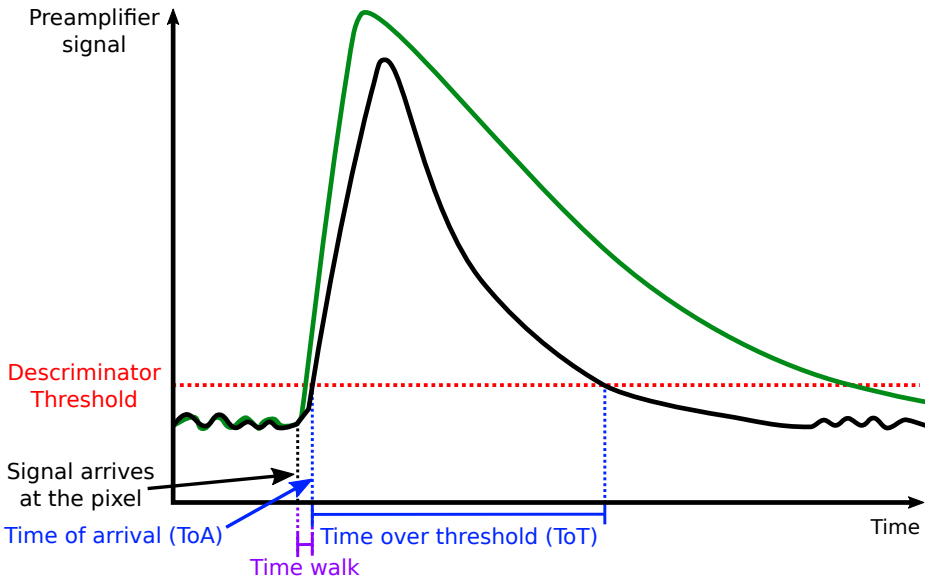

Figure 6.1: Illustrative example of the Timepix 3 ASIC pixel preamplifer response. Upon receiving a charge signal, the preamplifer in each pixel will rise, followed by a decay time. Time of arrival is defined as the time at which the pre-amplifer signal first crosses the pixel threshold, on the rising edge. Time over threshold is the time duration for which the pre-amplifer remains above the pixel threshold. The green and black curves illustrate different pixel responses that are possible using different pixel configurations, see the main text for details.

of the ASIC. Figure 6.1 shows the effect of these settings on a conceptual pre-amplifier signal. The green curve has a faster pre-amplifier rise time, but a slower decay time. The extension of ToT is visible, as well as a reduction in time walk. The effects of increased heat dissipation of the ASIC are probably more of a concern when cooling of the ASIC is difficult. For this application, the ASIC is easily accessible for cooling and so the increased heat output of the ASIC is not an issue.

6.1.1 Detecting optical photons using Timepix 3

Timepix 3, until very recently, has generally been used for the detection of charged particles which pass through a sensor bonded to the ASIC. The possibility of detecting photons using TPX3 was recently made possible following development of a novel sensor, specifically optimised for the detection of optical photons [109–111]. The design of the sensor is described in detail elsewhere [109], but we will briefly review some important aspects. The sensor is a p-on-n type silicon sensor, 300 μm thick. The difficulty of using a

silicon silicon sensor to detect optical photons is their relatively low energy. To uniformly apply bias to a silicon sensor, the front of the sensor is generally doped until it becomes sufficiently conductive. The sensor can then be biased from both the front and the back, generating a more uniform drift field within the silicon. For detecting optical photons, this doping layer must be very thin, such that the relatively low energy optical photons can reliably penetrate and reach the sensitive bulk silicon. The sensor uses a 50 nm thick passivation layer, allowing efficient penetration for photons between 370 nm - 1050 nm. The sensor is additionally coated with an anti-reflecting coating, which improves transmission efficiency. The final coated sensor has better than 80% quantum efficiency in the range 400 nm - 950 nm.

The next challenge is how to use this sensor to detect the photons which are produced by the THGEM in the ARIADNE detector. The Timepix 3 ASIC is designed for a minimum working threshold of $500e^-$, at 6 standard deviations [112]. The noise in each pixel is generally $90e^-$ RMS or less. A single photon arriving on the sensor will simply be drowned in this readout noise. Instead, the TPX3 camera is better suited for detecting bursts of 1000 photons or more per pixel. Thus, to detect single photons, a photon gain stage is mandatory before the camera. This photon gain is provided by an image intensifier. Section 6.3 provides a detailed discussion of image intensifiers. Figure 6.2 shows a model of the TPX3Cam camera, combined with an intensifier and lens. TPX3Cam is a commercially available product, which combines a TPX3 ASIC with a light sensitive silicon sensor and SPIDR readout board. The user simply needs to provide power and an Ethernet connection to control the device and receive data.

Figure 6.2: CAD model of TPX3Cam, connected to a Photonis cricket image intensifier and lens. TPX3Cam provides the union of the TPX3 ASIC bonded to the light sensitive silicon sensor. The chip is readout using a SPIDR readout board, which is also integrated within the TPX3Cam enclosure.

6.2 DAQ and readout

The TPX3 ASIC generally operates using what is known as 'data-driven' readout. Each pixel is read out independently. Once a 'hit' is received in a pixel, data about the pixels (x, y) location and the hit ToA and ToT is collated and set off chip in a data packet. The data driven readout concept, in the context of this application, is shown in Figure 6.3.

An interface to the TPX3 ASIC is provided by the SPIDR readout board [113]. During operation, a continuous stream of data is received from the camera. This stream contains a mixture of data packets, including pixel hits and additional timing information packets. Since the readout of TPX3 is not triggered, the SPIDR readout board provides an optional interface for trigger-like operation. An external signal may be sent to the SPIDR board which, when received, inserts an additional external timestamp packet into the data stream. This packet encodes the time at which the signal was received, with a resolution of 200 ps. In the case of optical TPC readout, this external timestamp can be used to identify the t_0 time in the TPC from primary scintillation, using an internal PMT.

The internal pixel time counter of the TPX3 ASIC has 14-bit range. Since the pixel clock of the TPX3 ASIC runs at 40 MHz, this internal counter will overflow after roughly 410 μs. In case that two hits are received exactly 410 μs apart, they will have the same time of arrival timestamp. This introduces an ambiguity about if the pixels were both hit simultaneously, or an integer multiple of 410 μs apart in time. For many applications, this ambiguity is not acceptable. Thus, the SPIDR readout board implements several additional counters to extend the ambiguity-free operating time range of the ASIC. A 16-bit counter records the number of times the pixel clock of TPX3 ASIC overflows. Thus, the ambiguity-free timestamp range is extended to roughly 410 μs $\times$ 2^{16} = 27 seconds. The TPX3 ASIC has a larger, global, 48-bit counter. This counter has an ambiguity-free range of 1/(40 Megahertz) $\times$ 2^{48} = 81 days. Every second, SPIDR reads this 48-bit counter and places two packets encoding this information into the data stream. This is called the 1 Hz heartbeat. Combining the 1 Hz heartbeat, 16-bit SPIDR time and 14-bit pixel time gives ambiguity-free operation for up to 81 days with 1.6 ns resolution. Figure 6.3 shows the specification of the data packets which are received from the SPIDR readout board.

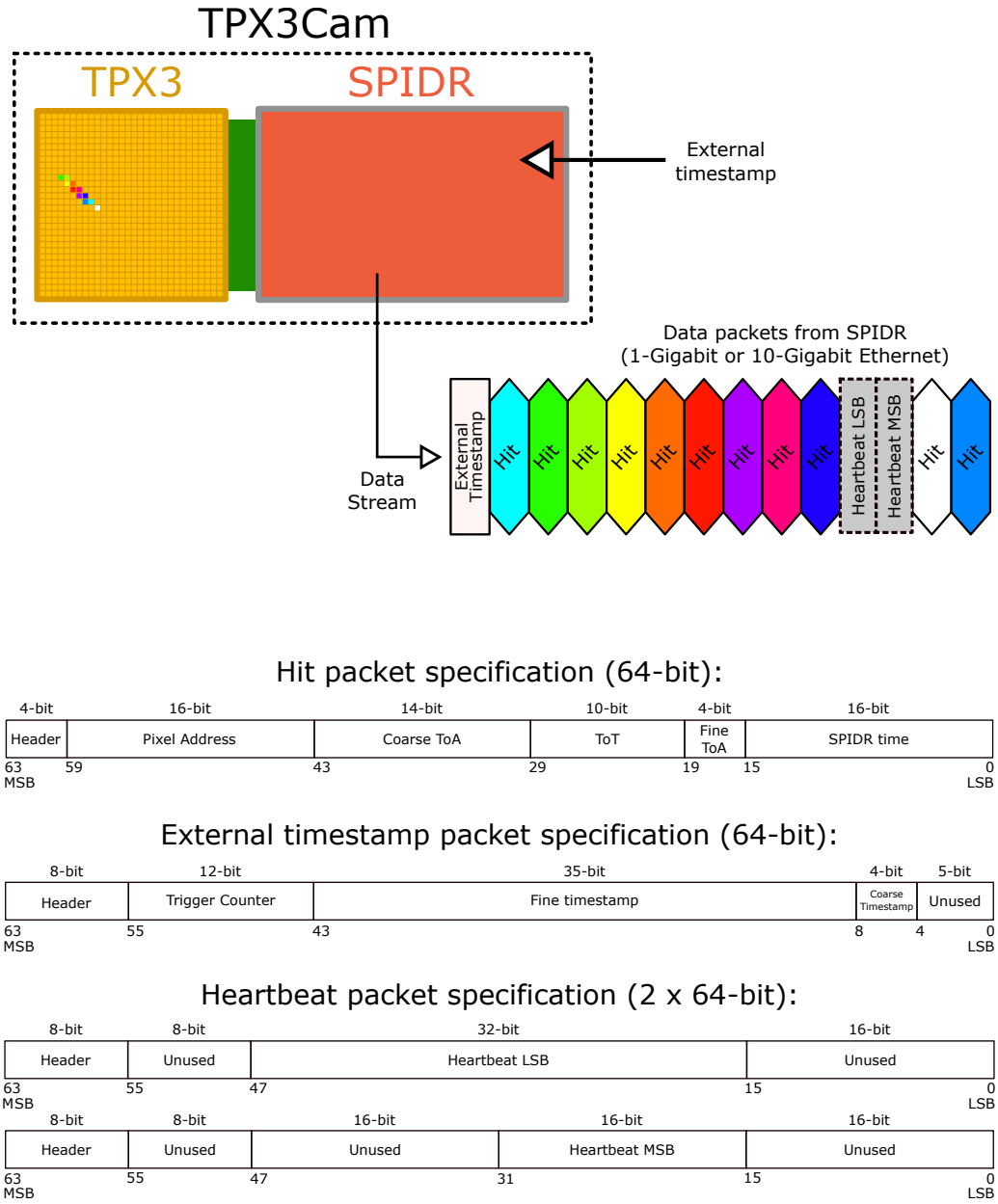

Figure 6.3: General overview of the operation of the SPIDR readout board, in the context of TPX3Cam. The SPIDR readout board generates a stream of data packets, which encode all information taking during operation. See the text for a detailed explanation of each of the possible packet types. This data stream is written to disk over a gigabit Ethernet connection or fiber link, if higher data rates are required. The data packets are parsed and decoded in offline analysis, where the events can be reconstructed.

Data driven readout provides very efficient data compression when the pixel occupancy is low. When each pixel is read out independently, each packet from the camera must encode the pixels' (x, y) location with a 16-bit address. When the pixel occupancy becomes very high (greater than 50%), it is more efficient to simply read every pixel and not require this 16-bit pixel address. Given the low occupancy of an optical TPC, data driven readout is surely the more efficient solution.

As well as data driven readout, the data from the camera can be manipulated to provide frame based like readout. The SoPhy software, provided with TPX3Cam, manipulates the data stream from the camera to present entire frames of data at once. This allows the camera to be operated more like a CCD camera. This type of operation is ideal for diagnostics tasks such as lens focusing. The lens focus can be adjusted in realtime while watching the image on the SoPhy software, until it is set correctly. The SoPhy software is also ideal for tuning the operating settings for the camera. Chip parameters of the TPX3 ASIC can be adjusted in real time in the software, and the effect of the changes observed in real time. Typically, the camera is first connected and operated using SoPhy. The ideal settings are found using SoPhy, and then these settings are transferred to a text file. This text file is parsed by the command line DAQ, which then operates the camera in data driven mode for actual data taking. This type of operation was found to be quite user friendly and intuitive.

6.3 Image intensifiers

As was discussed earlier, to achieve single photon sensitivity, a photon gain stage is mandatory to overcome the approximately 500 e^- readout noise of each pixel of TPX3. This photon gain is provided using an image intensifier. Image intensifiers take advantage of a multi-stage process, producing a gain of up to 1E6 photons/photon. First, incident photons are converted to an electron on a photocathode. This electron is then accelerated into one or more micochannel plates (MCPs), which provide electron gains up to 1E6. Finally, the resulting electron cloud leaving the MCP is accelerated into a phosphor screen, producing an amplified light signal. Each of these three stages is individually customisable to meet the specific needs of the application. Important aspects when configuring each stage of an image

intensifier will be discussed in the following sections.

6.3.1 Photocathode

The photocathode of an image intensifier defines the spectral sensitivity of the device. The performance of a photocathode can broadly be quantified with two quantities; Detective quantum efficiency and dark count.

Quantum efficiency (QE) measures the probability that an incoming photon is converted to an electron. Naturally, the ideal photocathode would have maximal quantum efficiency over the working wavelength range. Once the incident photon is converted to an electron on the photocathode, it is accelerated towards the MCPs. However, this electron is not necessarily always collected by the microchannel plates. Detective quantum efficiency (DQE), instead measures the efficiency of the image intensifier, including any efficiency losses when collecting photoelectrons into the microchannel plates. It is typical for an image intensifier to be specified in terms DQE rather than QE, although these two values do remain closely linked. A more detailed discussion of the differences between DQE and QE is given in subsection 6.3.2, as well as a look at some modern techniques to maximise DQE.

Another key figure of merit for a photocathode is dark count. Periodically, a photocathode may randomly emit an electron. The mechanism for this emission is beyond the scope of this discussion but more details are available from [114]. The dark count of a photocathode is defined by the rate of this spurious electron emission. Ideally, the dark count would be zero. The dark count of a photocathode tends to be quite closely tied to the spectral sensitivity of the photocathode. Photocathodes which maintain sensitivity towards the infrared spectrum tend to have high dark count rates (tens of kilohertz), due to increased sensitivity to thermal photons. Photocathodes which are only sensitive in the UV range, such as caesium iodide, can have dark count rates in the single hertz range.

6.3.2 Microchannel plates (MCPs)

A microchannel plate [115] is a thin disc or rectangular shaped component, made from a highly resistive material. A microchannel plate contains a densely packed array of through holes, or channels. A bias is applied across

the microchannel plate. The diameter of these channels is very small, typically tens of microns or less. The channels are tilted at a slight angle relative to the surface of the microchannel plate. This slight angle means that an electron which enters the MCP will impact with the wall of the channel. If the electron impacts the wall of the channel with sufficient energy, secondary electron emission is possible. If this electron emission process results in the emission of two or more electrons, thus resulting in an electron gain. These secondary electrons can in turn go on to impact the walls of the channel and produce further electrons. The resulting electron avalanche produces the gain of the MCP.

Customisation of the microchannel plate is possible by altering parameters such as the the shape of the MCP, the diameter of the microchannels and the resistivity of the MCP substrate. Manufacturing considerations place limitations on how densely the individual microchannels can be packed. An open area ratio (OAR) of roughly 60 % is typically achieved. In the basic configuration, this means that 60 % of electrons emitted from the photocathode of the intensifier will enter a channel of the MCP whereas the remaining 40 % will impact the flat face of the MCP and be lost. Thus, for a basic image intensifier configuration, DQE is typically close to 60 % of the photocathode quantum efficiency. For certain applications, such as photon counting, this 40 % loss of electrons is very undesirable. Recent developments have resulted in new methods which can improve the collection efficiency of MCPs [116]. These techniques generally involve coating the front face of the MCP with a substance which is capable of secondary electron emission. If a photo-electron misses the entrance of a channel and instead impacts the coated front face of the MCP, electrons are emitted from the face. These electrons then have another chance to be drawn into a channel. This additional coating improves the collection efficiency of the MCP to essentially 100%. The drawback of this coating is that the process of secondary emission takes a small amount of time and therefore slightly degrades the timing resolution of the MCP. The impact of timing resolution is generally sub-nanosecond and so for many applications this degradation is not observable. Therefore, such a coating to improve DQE can be extremely favorable. Given the 1.6 ns timing resolution of TPX3, MCPs with such a coating can only be beneficial. The degradation of MCP timing that results from the coating is completely lost within the timing resolution of the TPX3

ASIC.

The gain of the image intensifier is defined by both the bias voltage applied across the microchannel plates, as well as the number of microchannel plates used. For single photon detection, two MCPs, arranged in a chevron configuration, are typically used. The chevron configuration helps to reduce the backflow of ions from the second MCP to the first, extending the life of the MCPs.

6.3.3 Phosphor screen and relay optics

The final step in the image intensifier chain is converting electrons back to photons. This is generally achieved using a scintillator or phosphor screen. The choice of screen is customisable, defining both the wavelength of the emitted photons and the timing resolution of the scintillation process. Different phosphor screens are available with different scintillation efficiencies as well as rise times and decay times. Broadly speaking, phosphors with a long decay time are more efficient at producing photons and thus can yield brighter images. For this work, the phosphor screen should have a timing resolution compatible with the 1.6 ns resolution of the TPX3 ASIC. The most easily available commercial option is a phosphor screen known as P47. This phosphor has a rise time of 7 ns [117], mostly compatible with the 1.6 ns timing resolution of TPX3, although a slight degradation of timing performance may be possible. Practically, for the application of optical TPC readout, 7 ns timing resolution is comfortably sufficient. The light output spectrum of the P47 phosphor is peaked at 430 nm, with a tail out to around 650 nm. This output spectrum is a good match to the quantum efficiency of the light sensitive silicon sensor that is bonded to the TPX3 ASIC.

6.3.4 Photonis Cricket

For all work later discussed in this Thesis, Photonis Cricket [118] image intensifiers were used. These intensifiers incorporate an image intensifier tube into an aluminium housing which itself incorporates C-mount threads on both the front rear faces of the device. This allows a lens to be easily attached to the front of the intensifier, and the intensifier itself to be easily attached to the front of TPX3Cam. A relay lens mounted inside of the Photonis cricket image intensifier takes care of focusing the output light from

the phosphor screen of the intensifier onto the silicon sensor of TPX3Cam. A focus wheel is provided, allowing fine adjustment of the focal point of the relay optics.

The Photonis cricket intensifier has a built in power supply with over current protection. In case that the intensifier is exposed to bright light, the voltage across the MCPs is reduced to protect both the MCP and the phosphor screen. The cricket is powered using a basic, low voltage, micro-usb cable. The internal power supply converts the usb voltage into the high voltage required by the intensifier. The cricket additionally has a LEMO connector, which can be used to regulate the gain of the intensifier by applying an external voltage. When no voltage is applied to this connector, the gain of the MCP is maximum. Up to 5V can be applied to this connector, reducing the gain of the intensifier by at least 100 times. For this work, the intensifier was always used at maximum gain. The Photonis Cricket was found to be very user friendly and provided essentially plug and play capability.

Chapter 7

Performance of optical TPX3 readout in 100 mbar CF4 gas

This section is an expanded discussion surrounding the work published in [119].

After returning from CERN, the ARIADNE detector was unavailable due to a period of maintenance and upgrade. The first attempt at Timepix based optical readout was therefore performed using a smaller secondary TPC. The ARIADNE demonstrator is a 40 liter TPC, which has in the past been used for tests using CCD and EMCCD cameras [95, 120]. The smaller size of the demonstrator TPC makes it more practical for certain R&D activities; The smaller detector volume makes exchanging gas mixtures possible in a much shorter time frame.

7.0.1 Intensifier configuration

A Photonis cricket intensifier was used for these tests. The intensifier had a Photonis Hi-QE Red photocathode. This photocathode has a quantum efficiency of $\approx 20\%$ at 620 nm, the peak scintillation wavelength of CF4 of 620 nm. One drawback of the Hi-QE Red photocathode is the relatively high dark count. The dark count rate of the photocathode is in the range 30-60 kHz. The intensifier has two MCPs, arranged in a chevron configuration with a total electron gain of 85 000 and an output brightness of 1.8 cd/m^2. The output screen is a P47 phosphor. Figure 7.1 shows a photograph of the camera, with the image intensifier and lens attached. A lens cap is installed

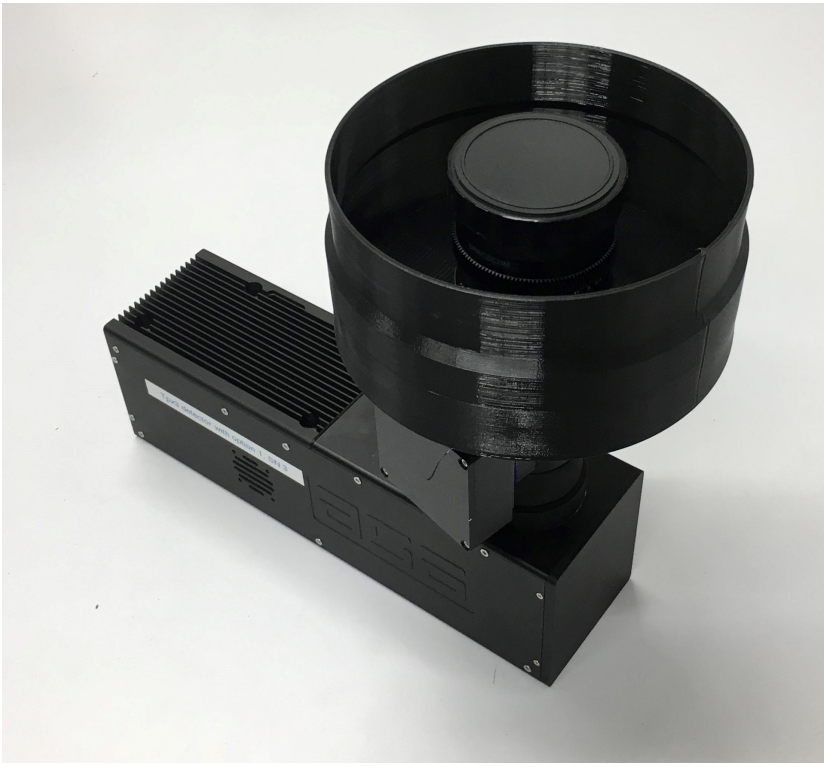

Figure 7.1: The camera used during these tests. TPX3Cam, is seen at the bottom, with a Photonis cricket intensifier mounted to its front face. A 50mm focal length lens is installed in front of the intensifier. A 3D printed light tight bellow is installed around the lens, which provides a light tight connection between the camera and the detector.

to protect the photocathode of the intensifier. A 3D printed bellow is also installed around the intensifier. This bellow is secured to the TPC, and creates a light tight seal between the camera and the TPC.

7.0.2 Detector setup

For these gas tests, the demonstrator was prepared with two THGEMs, stacked one on top of the other. Care was taken to align the holes of the top THGEM with the holes in the bottom THGEM, to optimise transfer efficiency between the THGEMs. The THGEMs have identical specifications to the larger THGEM of ARIADNE, except for smaller x and y dimensions. The THGEMs both have 500 μm diameter holes, arranged on a hexagonal array with 800 μm pitch.

An Americium-241 alpha source was suspended inside of the TPC, connected to a rotary feedthrough. This alpha source was used to generate alpha

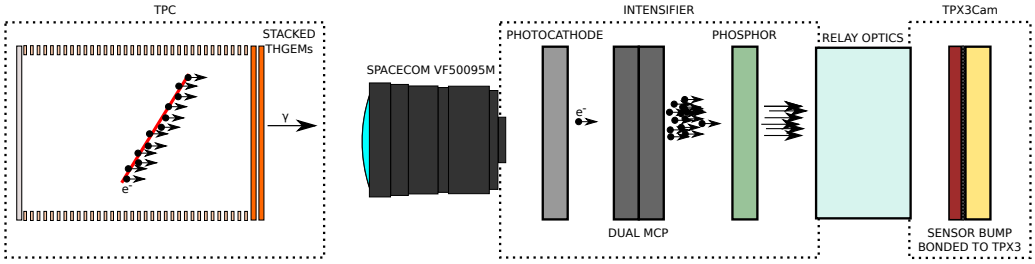

Figure 7.2: Detection principle using an intensified TPX3Cam to detect light produced from a THGEM. This detection principle is generic, beyond the scope of this individual detector setup. The same principle would also apply for optical readout of a dual-phase liquid Argon TPC.

tracks within the TPC, with a known energy of 5.5 MeV. The source was collimated to reduce the observed rate to roughly 1 kHz. For all measurements, the detector was filled with 100 mbar CF4. The cathode was biased to -3 kV and the extraction grid was biased to -1 kV, producing a drift field of 100 V/cm. Equal bias was always applied across both THGEMs, such that they should have similar gain. The TPX3Cam was configured such that the pixel threshold was substantially above the noise floor of the chip, approximately 1000 e^- relative to a noise floor of 500 e^-. This threshold means that when the intensifier is switched off, zero hits are seen from the camera. The exact value for the pixel threshold was not found to be especially critical.

A Hamamatsu R5912-20 PMT is installed at the base of the demonstrator TPC. In principle, this PMT may be used to detect the primary scintillation light of the alpha tracks in the TPC, and define t_0. This information is needed to define an absolute z coordinate of events within the TPC. Detection of S1 light using TPX3Cam may, in principle, be possible, but this has yet to be extensively studied. For this work, information from the PMT was not used. Instead, we focus the discussion only on the data provided by TPX3Cam. For the event displays shown in this Chapter, relative z information is presented, with the topmost part of the track being defined as $z = 0$. This allows for a more dedicated discussion of the raw data provided by the camera, rather than introducing systematics of separate detector components.

The detection principle is shown in Figure 7.2. The experimental setup is shown diagrammatically in Figure 7.3, and a photograph of the setup is shown in Figure 7.4.

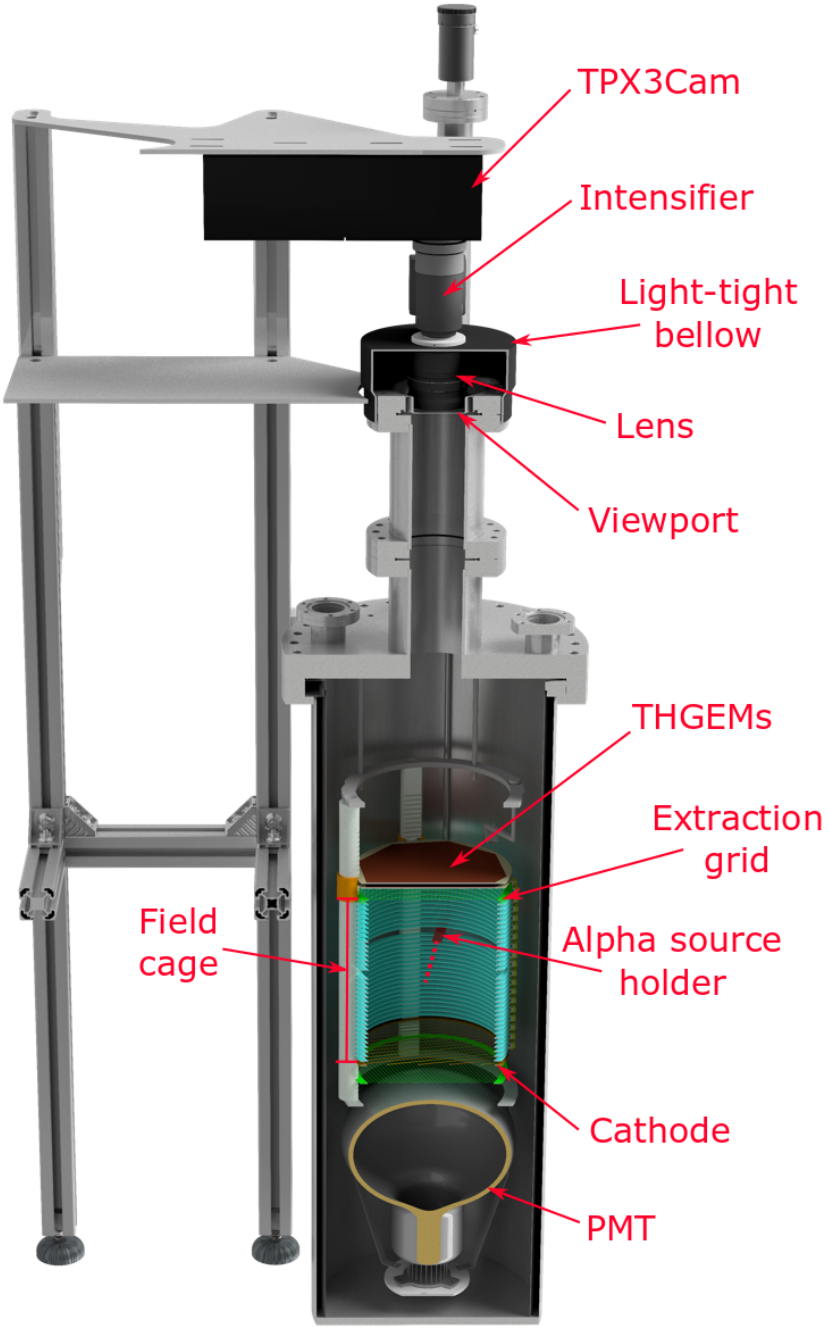

Figure 7.3: Detector setup for these tests. The intensifier TPX3Cam is mounted externally, looking down through an optical viewport into the detector volume.

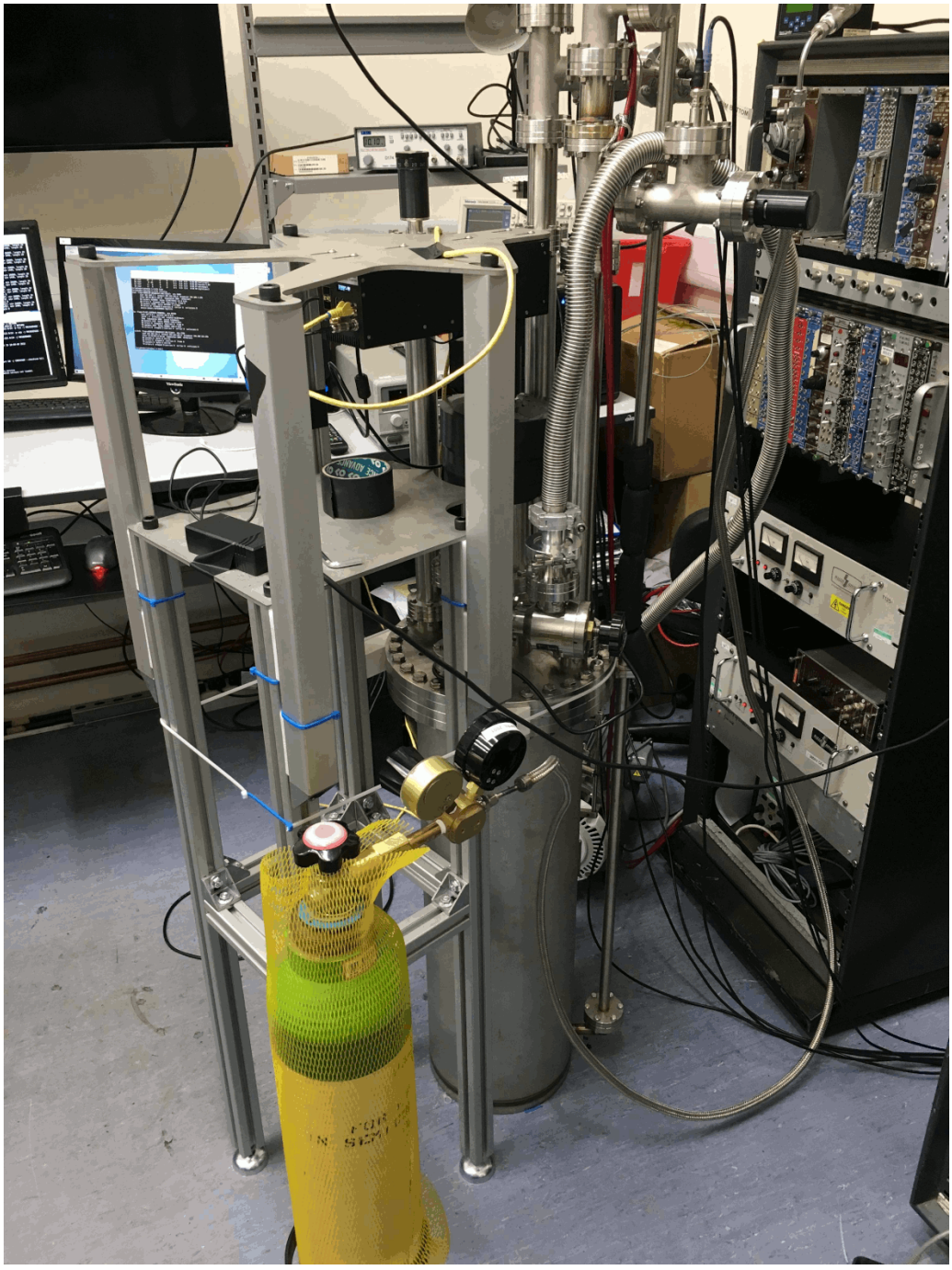

Figure 7.4: A photograph of the experimental setup. The single Ethernet cable connection to the camera was found to be very user friendly.

7.0.3 Results

As discussed in 6.2, we can consider two types of data readout. Firstly, there is readout using SoPhy. SoPhy manipulates the data stream from TPX3Cam, emulating a camera with a traditional frame based readout. By integrating all hits within a specified time window, a single image is produced with a simulated exposure time. This type of readout is ideal for basic diagnostic tasks, such as focusing the lens of the camera. This software was used to initially asses the sensitivity of the camera to the light produced in the TPC, and get a rough feel for the performance of the device. Figures 7.5 and 7.6 shows event displays taken using SoPhy, for two different exposure settings. Two separate views are seen, one is time over threshold (intensity) and the other is time of arrival. From these initial observations in SoPhy, it was possible to draw several initial conclusions. First, each track is seen to have a clear Bragg peak. This give a promising outlook for the calorimetric performance of the camera. Secondly, each alpha track is clearly resolved from one another in time, shown by each track having a different colour in ToA mode. Moreover, when we adjust the colour scale to focus on a single alpha track, changing timing information along the length of the track is visible. Since the drift velocity in a TPC is know, this timing information along the length of the track can be used to perform a full 3D track reconstruction in (x,y,z). Considering the extremely fast drift velocity of 10 cm/μs in 100 mbar CF4, compared to 0.16 cm/μs in Liquid Argon, this was a critical success. It was clear early on during experimentation in SoPhy that the timing resolution of the camera was more than sufficient for the application of optical TPC readout.

In the event displays, a halo of hits can be seen around each image. This halo is caused by the field of view of the camera being wider than required. Reflections from the stainless steel nipple, leading up from the THGEM to the camera, are seen by the camera. This lens gives the camera a larger field of view than is required for these measurements. These reflections would not be present when using properly configured optics. These tests were deliberately performed with this excessive field of view, using the Spacecom VF50095M lens, so that results may be easily interpreted in the context of ARIADNE, where this lens is used by the EMCCD cameras.

Once the camera had been reasonably configured using SoPhy, data was taken using the data driven command line DAQ. This results in the creation

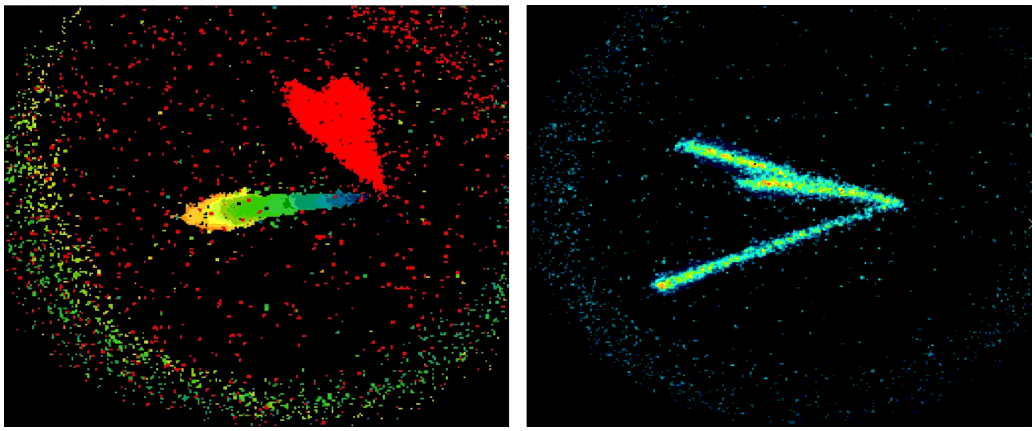

Figure 7.5: 1 millisecond exposure taken using SoPhy. On the right, the data is visualised in Time over Threshold. We see three alpha tracks, each with a visible Bragg peak. On the left, the data is visualised as time of arrival. The colour scale has been manipulated to show the time profile of a single alpha track. Reflections from the stainless steel nipple, leading up from the THGEM to the camera, are seen as a halo of hits around the image.

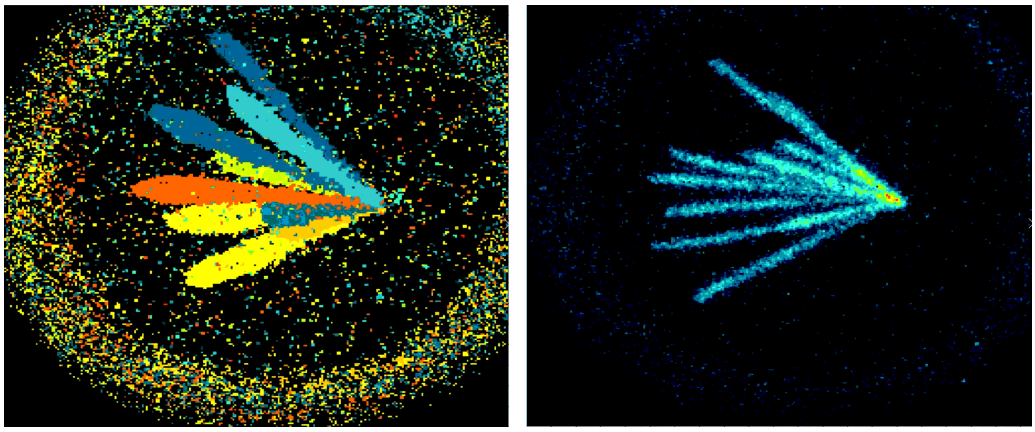

Figure 7.6: 10 millisecond exposure taken using SoPhy. On the right, the data is visualised in Time over Threshold. On the left, the data is visualised as time of arrival. The 1.6 nanosecond timing resolution of the TPX3 ASIC easily allows each alpha track to be resolved from one another. There are not enough colours to display all of the timing information that is available in the left image. Reflections from the stainless steel nipple, leading up from the THGEM to the camera, are seen as a halo of hits around the image.

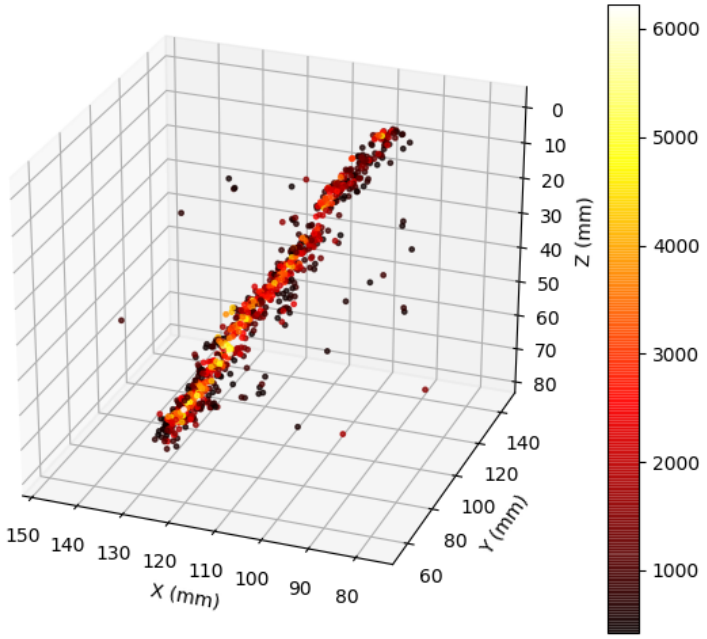

Figure 7.7: 3D event display of a single alpha track seen within the TPC. Millimeter scale resolution is realised in all axes.

of a binary file, which contains the stream of data packets from the camera. Interpretation of these hits in 3D is relatively straightforward; Conversion of (x, y) pixel number to a physical distance is trivial using the known field of view of the camera. ToA may be converted to a physical z position by using the known drift velocity in the TPC. Thus, 3D reconstruction is possible using only simple multiplicative factors applied to each axis. This reconstruction method is certainly more straightforward than techniques that are required for the reconstruction of plane view based readout approaches. Additionally, the pixel based nature of this readout approach eliminates any ambiguities that may be possible with plane based readout approaches. Figure 7.7 shows a single alpha track that has been reconstructed in 3D.

When the alpha source is removed from the TPC, cosmic events are still expected within the TPC. When set to a long exposure, these cosmics illuminated the active THGEM. Figure 7.8 shows the cosmic illuminated THGEM. Given the low pressure gas in the TPC, the energy deposition of the MIPs is very low. Thus, the total light output of the detector for these cosmic events is also very low. Observation of these cosmics is promising in regards to the sensitivity of the camera. A selection of interesting cosmic events were also plotted in 3D, shown in Figure 7.9.

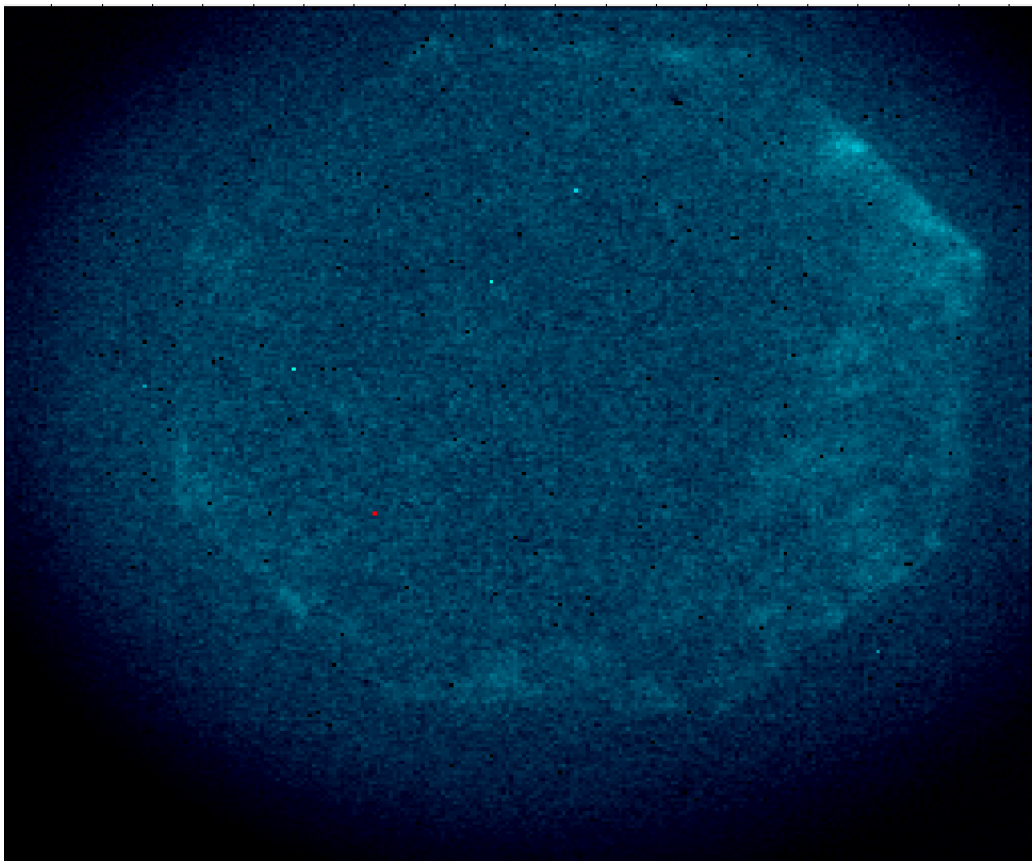

Figure 7.8: With alpha source removed, the camera is set to integrate all hits over a long exposure time. Cosmic particles passing through the detector illuminate the octagonal active area of the THGEM.

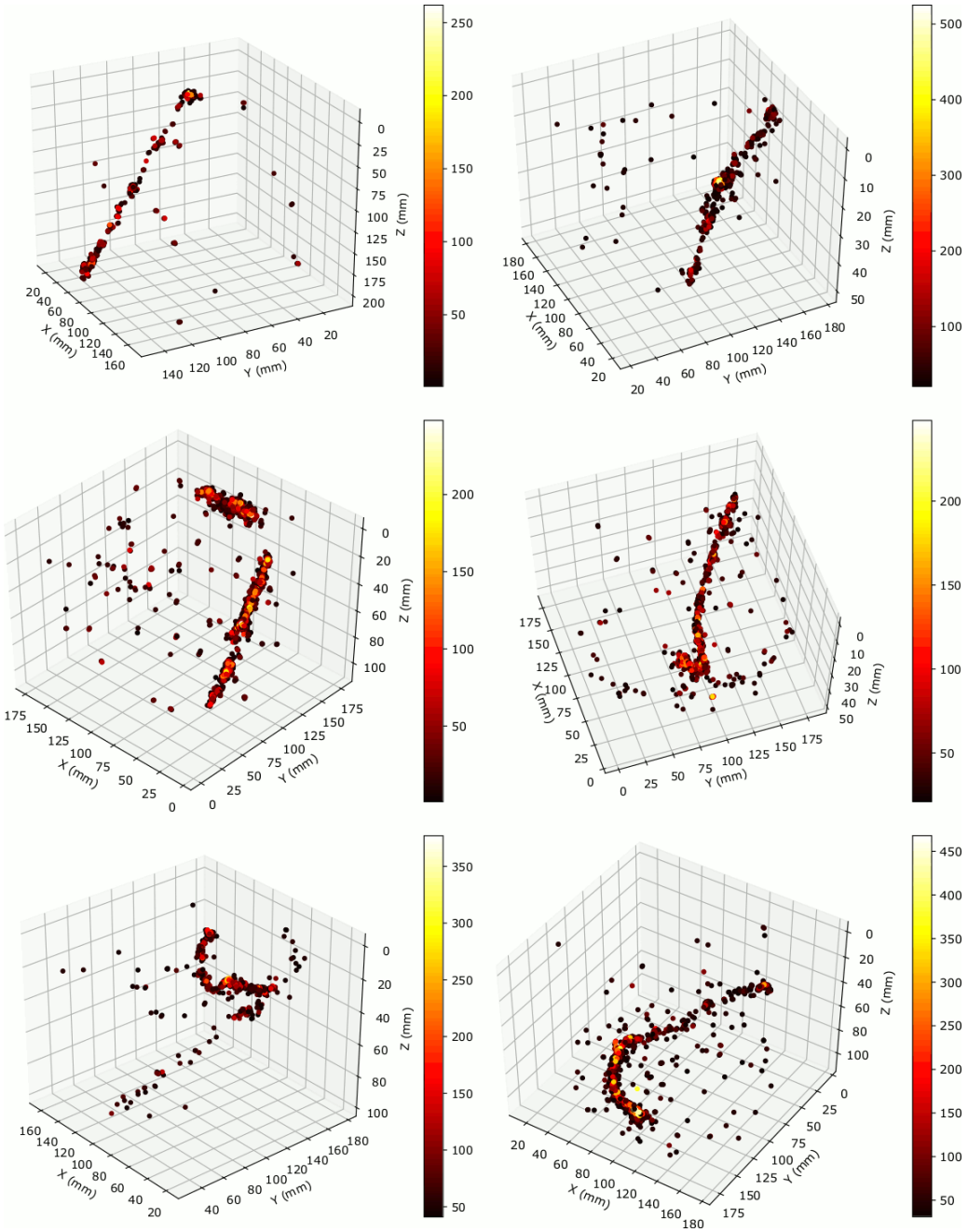

Figure 7.9: Gallery of individual cosmic events seen in the detector.

7.0.4 THGEM Bias scan

The response of the camera to changing THGEM bias was studied. For a single THGEM, the light production in a THGEM can be decomposed into a linear and exponential components. With inccreasing bias across the THGEM, the light production of the THGEM also increases. This means that more photons should reach the camera. This should, in turn, lead to an increasing number of hits seen by the camera. If we plot the camera hit rate versus THGEM bias, we can measure light production. Figure 7.10 shows the hit rate of the camera as a function of THGEM bias. In this Figure, a single exponential function has been used to fit the data. The theoretical model predicted in Section 3 does not fit the data well. This is most likely due to this setup having a double THGEM setup, whereas the proposed function is only appropriate for a single THGEM. Nevertheless, a single exponential function provides a decent description of the data.

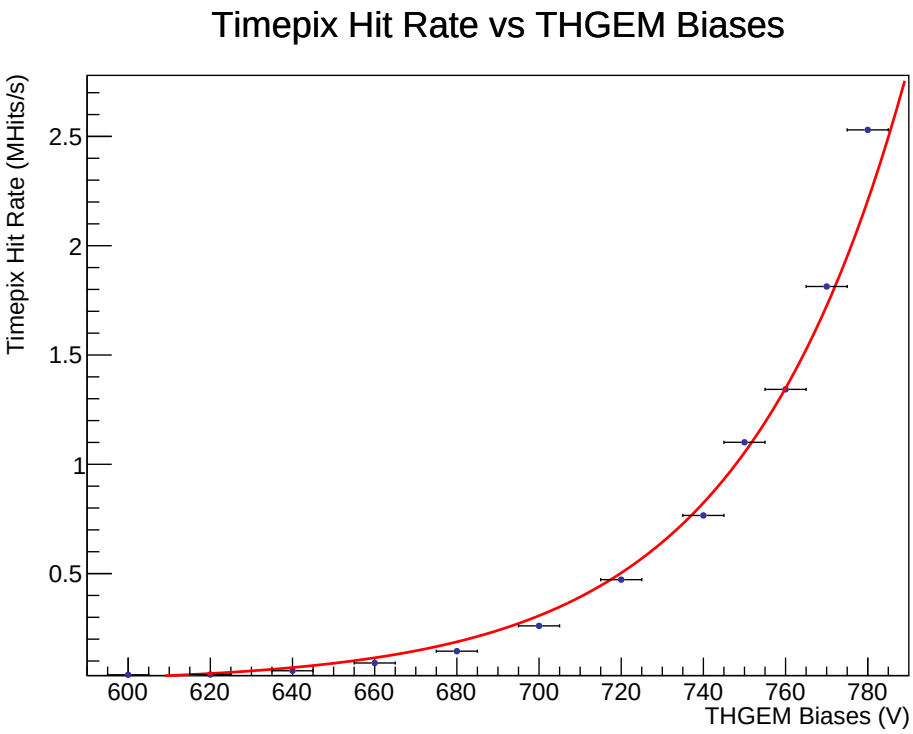

Figure 7.10: Measurement of total light production from both THGEMs as a function of bias. A single exponential provides a reasonable description of the data. See the text for a more detailed discussion.

7.0.5 Calorimetry

More detailed studies regarding the calorimetric performance of the camera have also been performed. First, we measure the total energy deposition of the alpha particles. For the whole dataset, we begin by finding the highest intensity hit. Then, we integrate all hits around this brightest hit, forwards and backwards by the length of the TPC. This generally selects the Bragg peak of the alpha tracks, then integrates all hits from the alpha track, plus a small amount of dark count. Eventually, once all alpha tracks have been integrated, the algorithm will also form clusters from only dark count hits. Thus, we place a cut on clusters containing more than 160 hits, to select only those clusters which are likely alpha particles. Next, we sum the total time over threshold of each hit within the cluster. This sum should be a measure of the total energy deposition of the alpha particle. Figure 7.11 shows the produced distribution. The distribution is well described by a single Gaussian, corresponding to the alpha energy of 5.5 MeV. The energy resolution, σE/E, is measured as 16 %.

Next, we will study the Bragg peak of the alpha tracks. To do this, we make the same selection of clusters as described above. Next, a straight line is fitted to each track in the $y-z$ plane. To make a common distribution of energy deposition versus length along the track, the alphas much be given a common origin. The z coordinate of each cluster is adjusted until all of the alpha sources converge on a common origin, which would be the alpha source in the TPC. The reconstructed distribution of a small sample of alphas around the common origin is shown in Figure 7.12. From this, we are able to construct the angular distribution of the source. Figure 7.13 shows the measured distribution. The distribution has a net downwards distribution in the $y-z$ plane, with a mean of 42 degrees. This is as expected, since the alpha source holder is designed to point the alpha source down 45 degrees into the TPC.

Now that all alpha track clusters have a common origin, we can measure the energy deposition of the clusters as a function of distance from this origin. This should form the Bragg peak of the tracks. Figure 7.14 shows the results of this distribution. A clear peak in the distribution is visible. Since the alpha tracks are produced at an angle of 45 degrees down into the TPC, it is possible that an impurity effect in the TPC could be suppressing this peak. This effect would preferentially reduce the relative height of the

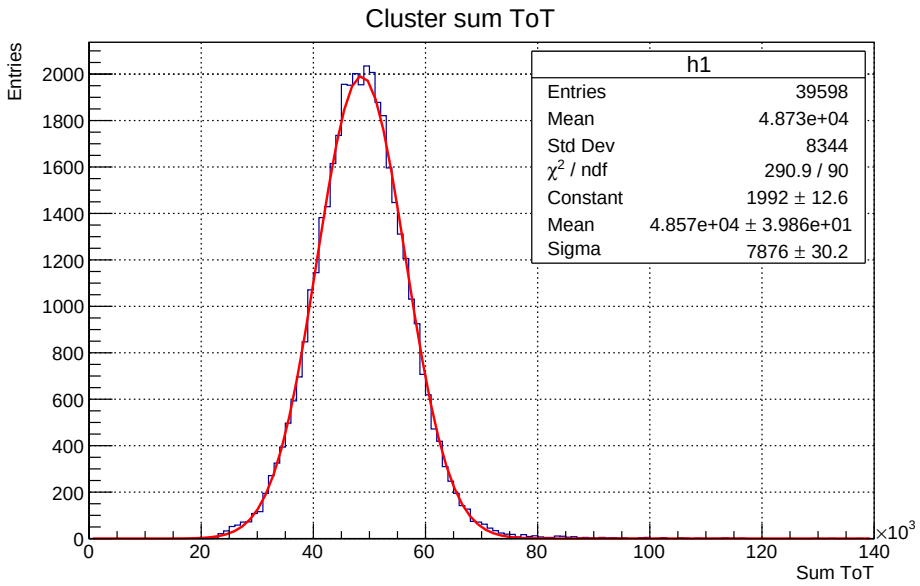

Figure 7.11: Distribution of total energy deposition from a sample of Americium-241 alpha particles. A clear peak is seen corresponding to the alpha energy of 5.5 MeV.

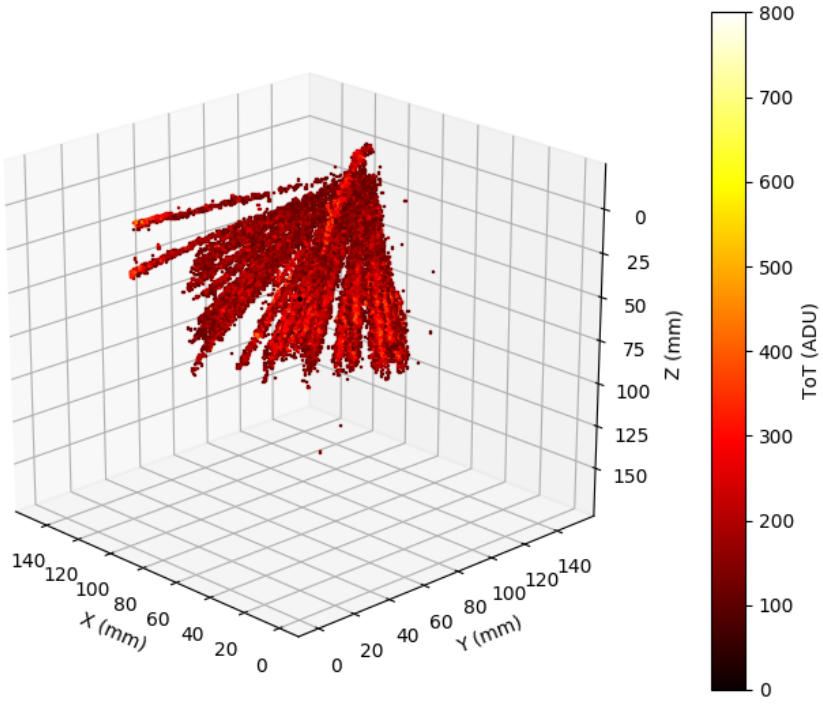

Figure 7.12: Event display showing the distribution of alpha particles from the source.

peak, since electrons from the Bragg peak of the track have to drift further in the TPC. Future work will attempt to quantify this impurity effect. If this impurity effect is present and corrected for, the alpha energy resolution shown in Figure 7.11 may also be improved.

7.0.6 Discussion

The initial performance of TPX3Cam in these gas tests was very promising. The most critical benefit is that full (x, y, z, E) tracking is now possible using a single device. Alongside this however, TPX3 also delivered many additional benefits. The native 3D data format provided to be very convenient. The simplicity of 3D reconstruction using a single multiplicative factor on each axis greatly simplified analysis efforts. Moreover, the zero suppressed nature of the data provided very clean events in 3D. This raw data format was ideal for analysis tasks such as straight line fitting and clustering. In the past, using EMCCDs, initial pre-filtering was required to remove background pixels from the raw data, which inevitably introduced inefficiencies.

The zero-suppressed nature of the raw data was additionally found to produce very low data rates from the camera. Each hit from the camera is defined using 64 bits. The alpha tracks are generally formed by 1000 hits or less. Thus, each track is fully defined with $O(10$ kilobytes). Given the source rate of 1 kHz, the total hit rate from the camera is roughly 1 Mhits/s. This is far from the maximum bandwidth of 80 MHits/s that is possible using the SPIDR readout board. It was clear that the camera would have no readout difficulty, even in high pileup environments.

The triggerless nature of the readout was also a novel component of this camera. The decoupling of the camera from the trigger system meant that any inefficiencies in trigger selection can not introduce bias into the raw data. The camera streams all data from the TPC, and comparison of the data to the trigger timestamps is done offline in analysis. In case that a trigger bias does exist, this can be understood and corrected offline. The triggering configuration never effects the raw data stream from the camera, and thus the raw data can never become unintentionally biased.

Before these tests were performed, it was unclear if the timing resolution of the TPX3 ASIC would be sufficient for high resolution z axis reconstruction in gas TPCs, where the drift velocity is much faster than Liquid Argon.

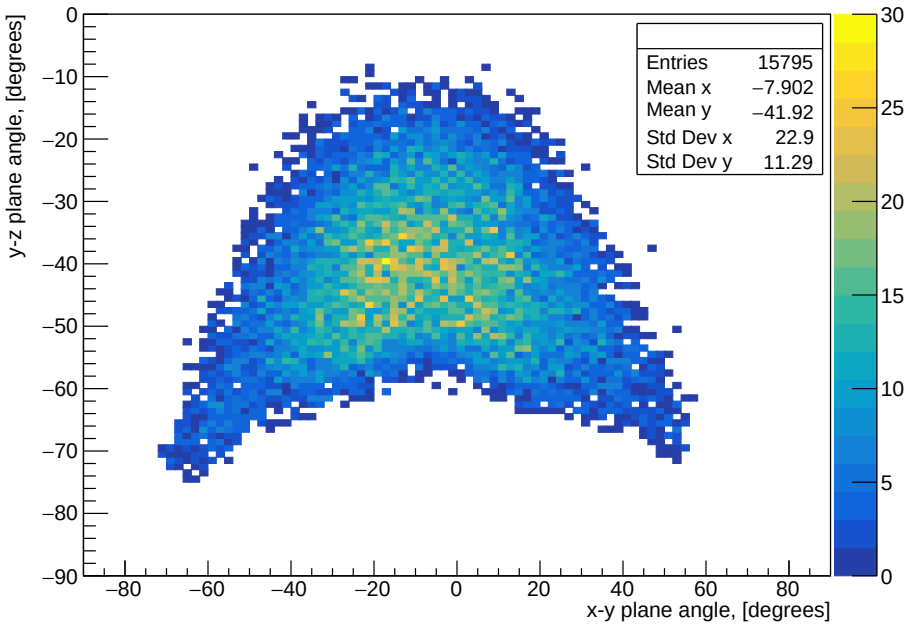

Figure 7.13: Angular distribution of alpha particles from the alpha source. The distribution has a net downwards angle in the $y - z$ plane, which is in agreement with the fact that the source was intentionally angled approximately 45 degrees down in the TPC.

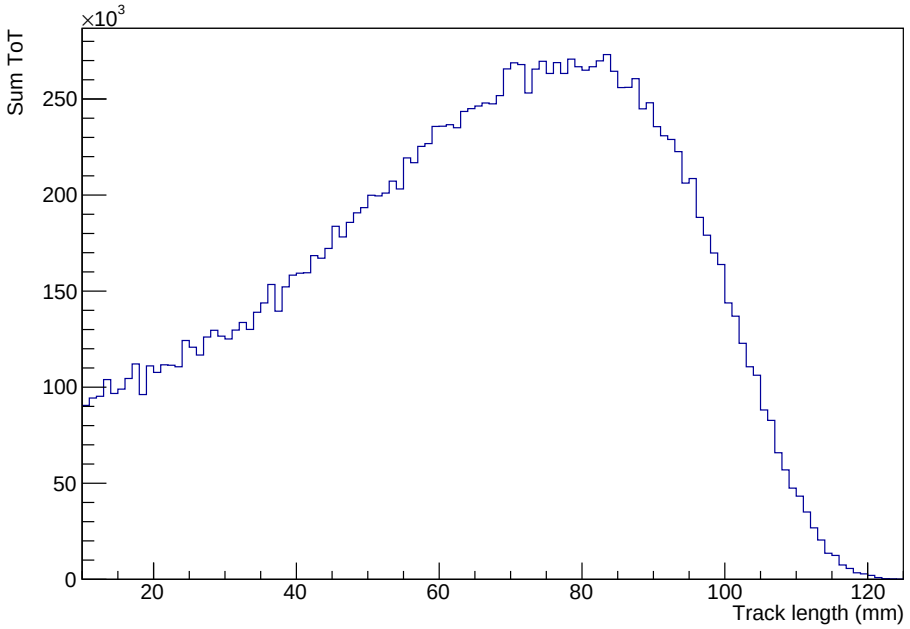

Figure 7.14: Energy deposition as a function of track length for the alpha particles. A clear Bragg peak is formed in the distribution.

In fact, this work found that the timing resolution was easily sufficient for millimeter scale resolution in the z axis. It may be conceivable to read-out high pressure gas TPCs using this technology, provided sufficient light production is possible.

Chapter 8

Performance of optical TPX3 readout in Liquid Argon

Following the successful demonstration in gas, a TPX3 camera was installed onto the ARIADNE detector to perform a Liquid Argon demonstration. For this demonstration, a Photonis cricket image intensifier was used, as described in Section 6.3.4. The intensifier has a Photonis Hi-QE Green photocathode, with a quantum efficiency of 30 % at 430 nm, the peak emission wavelength of TPB. The dark count rate of this photocathode is 50 Hz, orders of magnitude less than that of the photocathode used in the gas demonstration. For these measurements, a trigger timestamp, generated by the internal PMTs, was supplied to the camera. This allowed the absolute z position of the tracks in the TPC to be determined by measuring the time difference between S1 and S2 signals. Figure 8.1 shows the camera installed onto the ARIADNE detector.

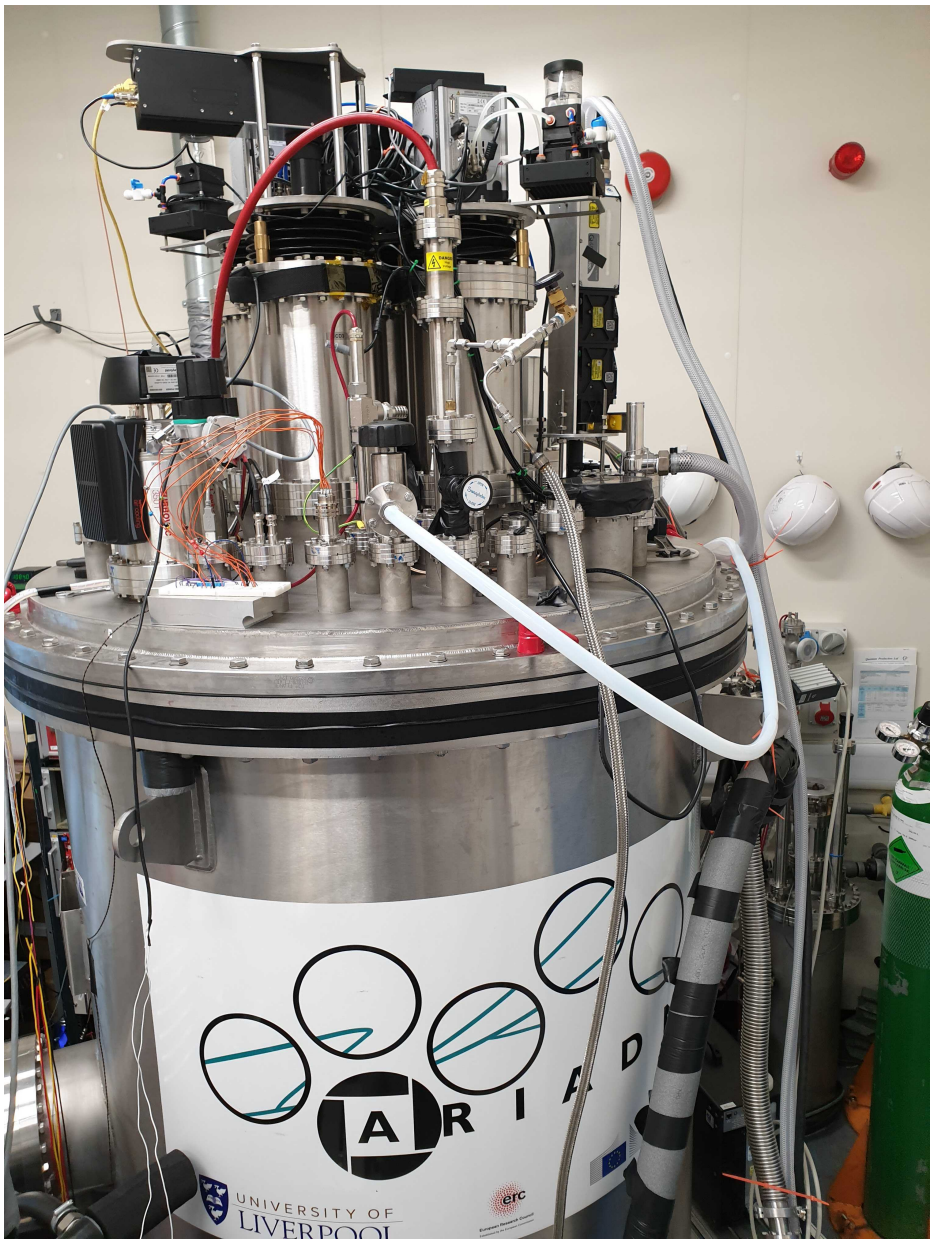

Figure 8.1: Photograph of TPX3Cam installed on the top flange of the ARIADNE detector. The external nature of the EMCCD cameras allowed for easy interchange. The camera looks down through the viewports, and has a field of view that covers slightly more than a quarter of the total ARIADNE THGEM.

8.1 Gallery

The performance of the camera was first assessed using the diagnostic software SoPhy. Figures 8.2 and 8.3 show several screenshots taking using the SoPhy software, in both time over threshold and time of arrival modes. The brightness of the cosmic muons is seen to decrease with depth in the TPC, due to losses to electronegative impurities. In fact, a detailed measurement of this effect allows for a determination of electron lifetime. This is discussed further in Section 8.3. Several point-like events are visible in the galleries, which are background Gamma interactions, believed to be caused by ^{39}Ar.

Data was also taken using the full Timepix3 DAQ, which provides simultaneous ToT and ToA. Figures 8.4 through 8.6 present a gallery of sample events, reconstructed in 3D. The absolute z position of each event was determined by comparison with the PMT trigger timestamp, t_0. By measuring the delay in time between the PMT t_0 timestamp and the time of arrival timestamp of the muon track signals, the z depth of the track in the TPC may be determined. This time difference is converted to a physical distance using the known drift velocity in the TPC. (x, y) pixel number was converted to mm using the known field of view of the camera, as determined from the earlier gas tests. The z position was converted from the time to distance using the known drift velocity in the TPC. The first four events show cosmic muons with a range of different delta rays. The last two events are two stopping muon candidates. In both stopping muon events, a Bragg peak at the end of the stopping muon track is visible, along with the produced Michel Electron.

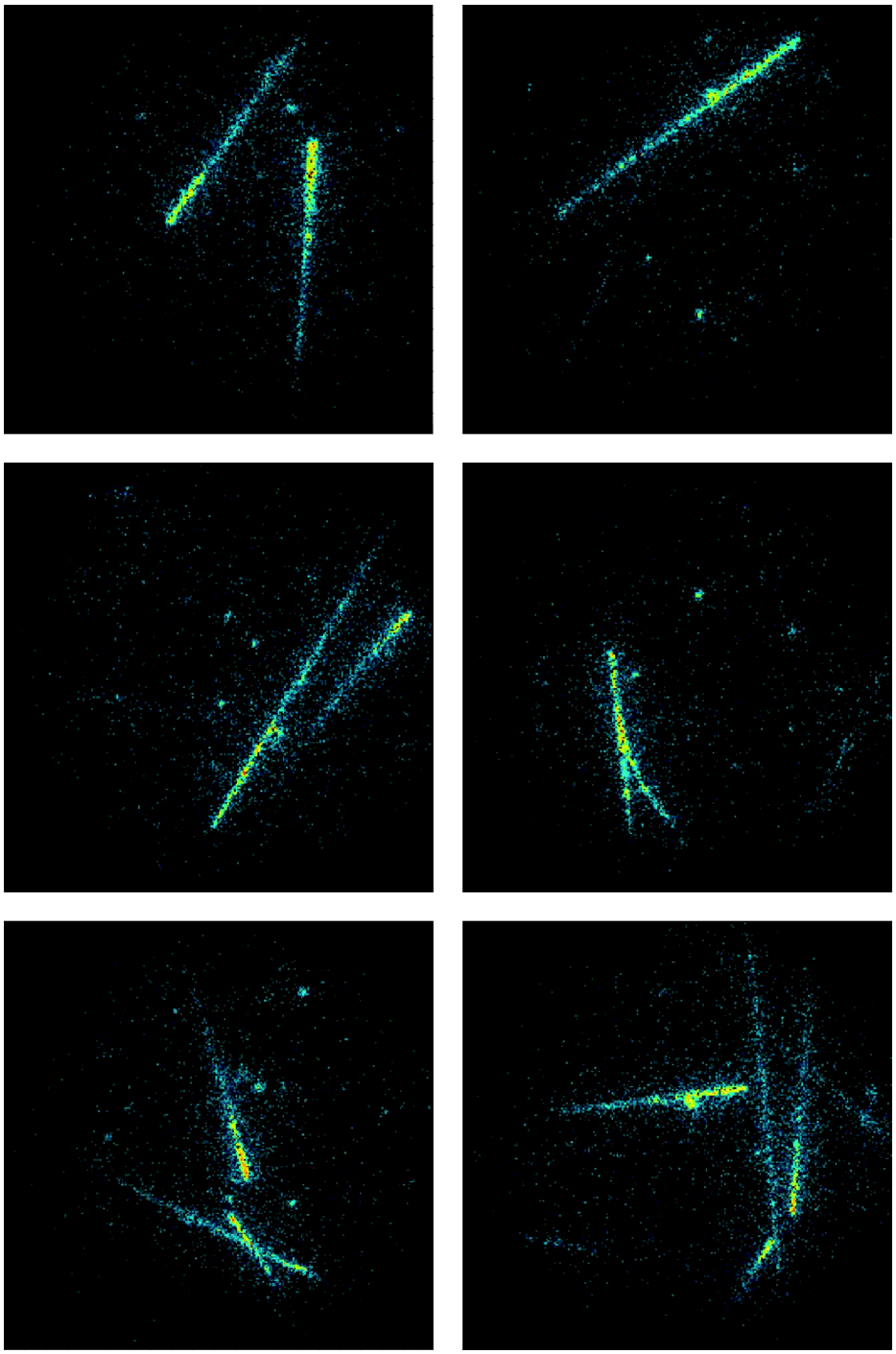

Figure 8.2: Selection of sample events taken using the SoPhy software in time over threshold mode. In the event displays, cosmic muons are seen passing through the detector. The brightness of the track is seen to decrease with depth in the TPC, an effect caused by losses of drifting electrons to impurities. Also seen in the images are bright, point-like events. These are background gammas, possibly from the decay of ^{39}Ar.

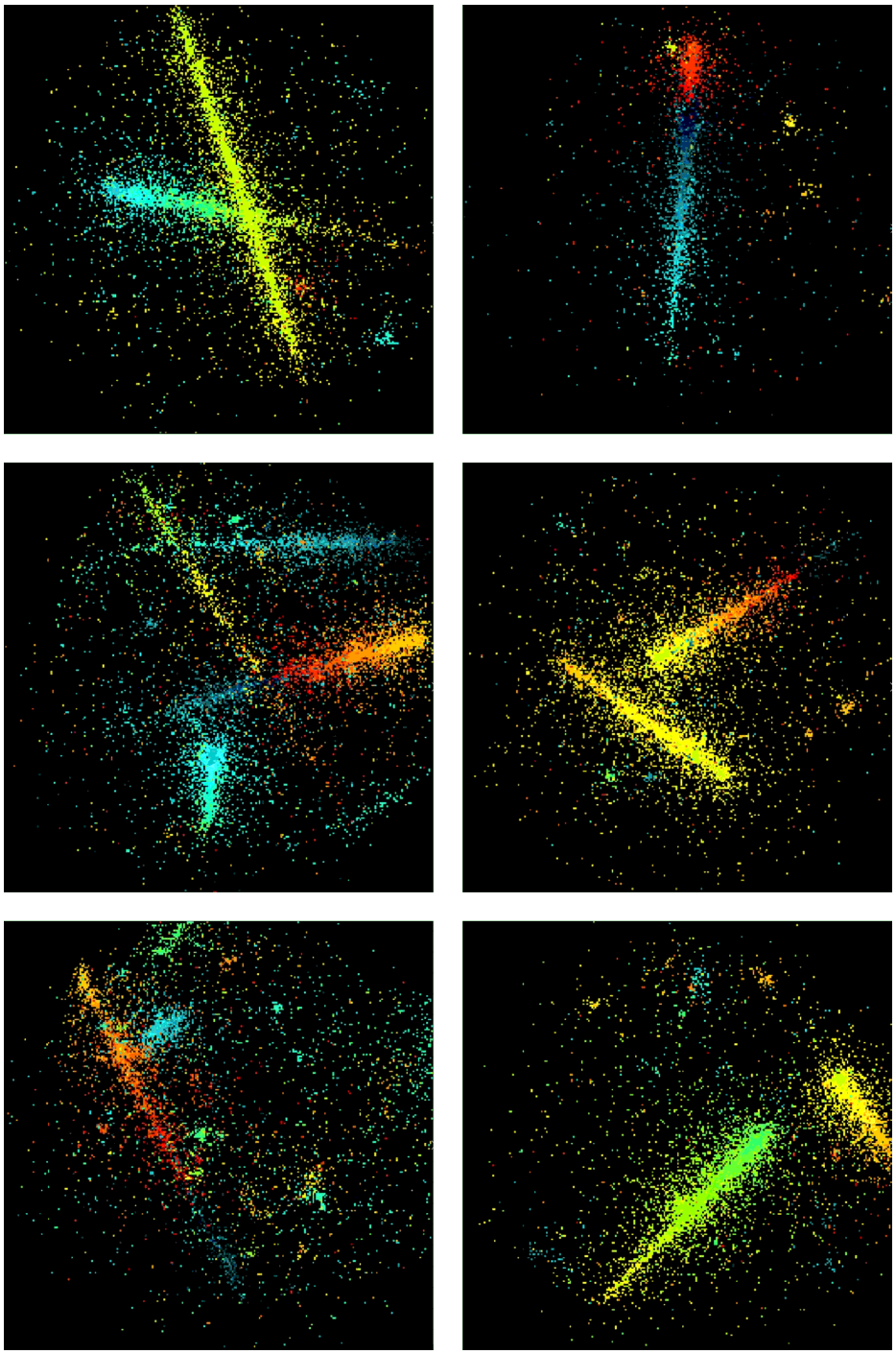

Figure 8.3: Selection of sample events taken using the SoPhy software in time of arrival mode. For events which contain multiple muons, we can see that each event is easily distinguishable in time from one another. Some muons are also seen to have a varying colour scheme along their length. From this, we can accurately calculate the z position of each hit along the track within the TPC and perform full 3D reconstruction.

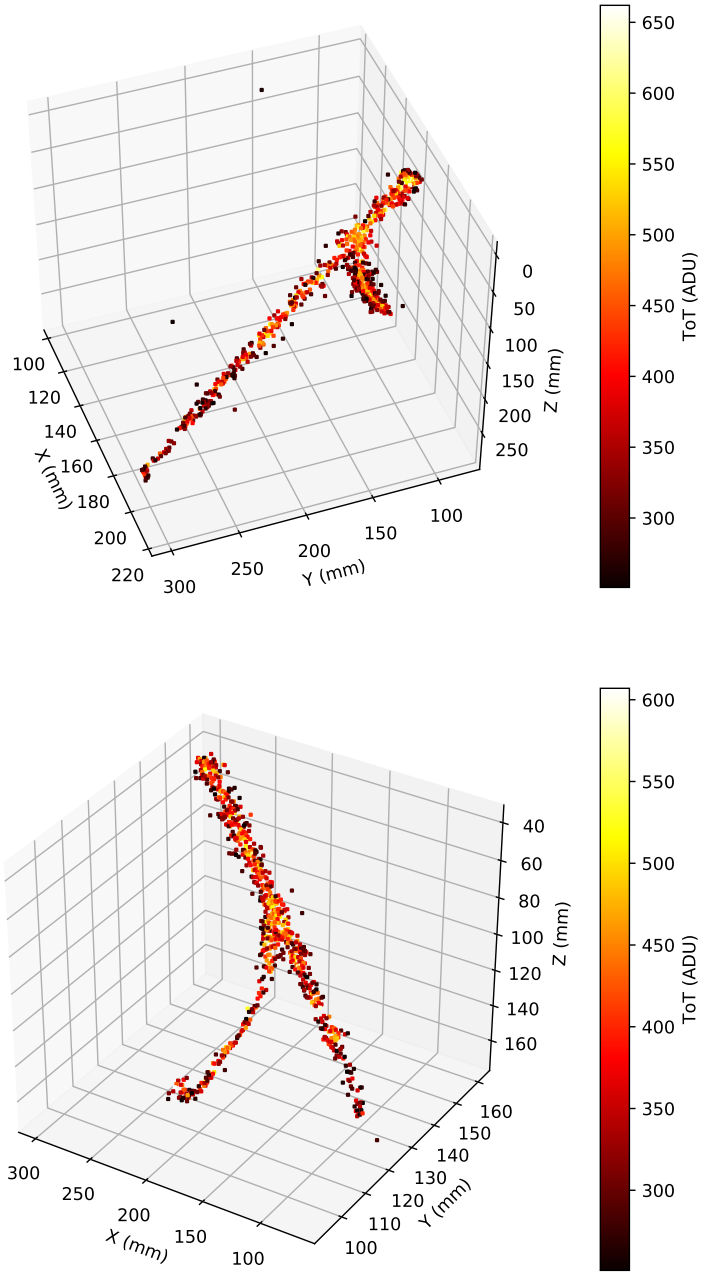

Figure 8.4: Gallery of two events, both containing delta rays.

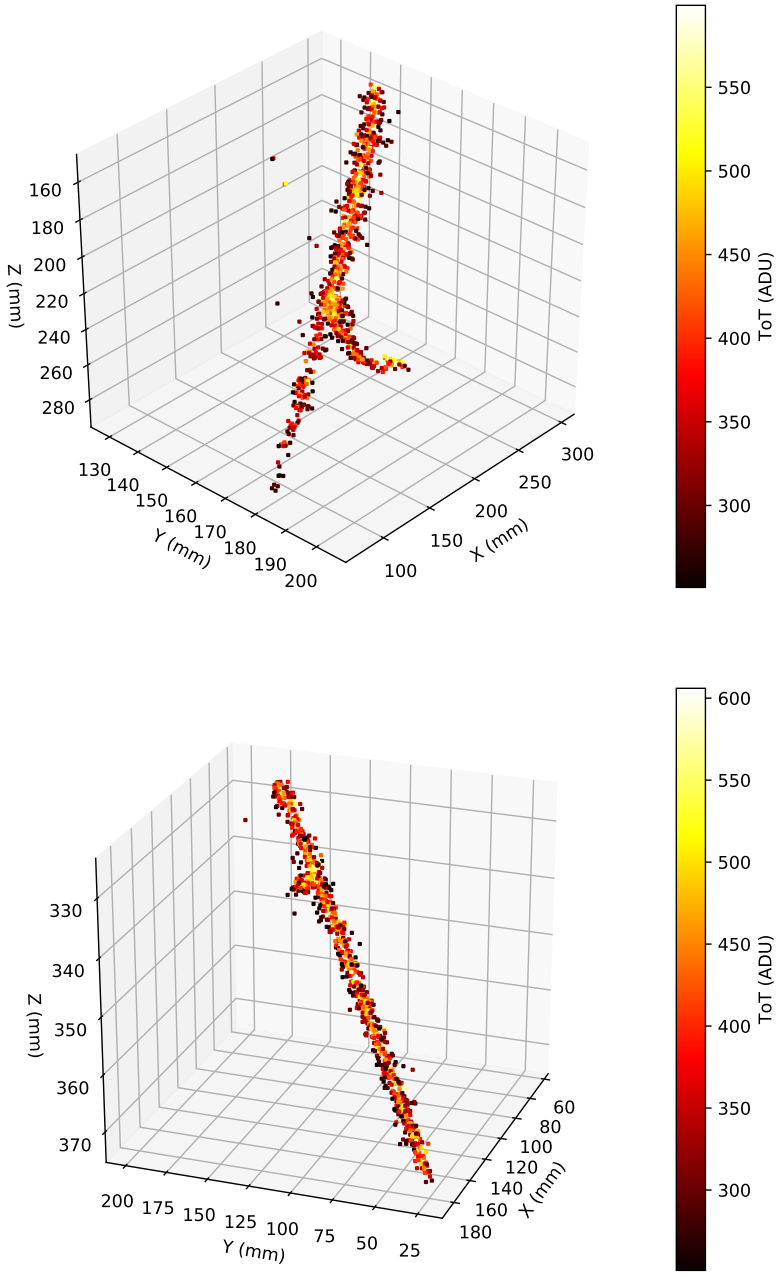

Figure 8.5: Gallery of two more events, both containing delta rays.

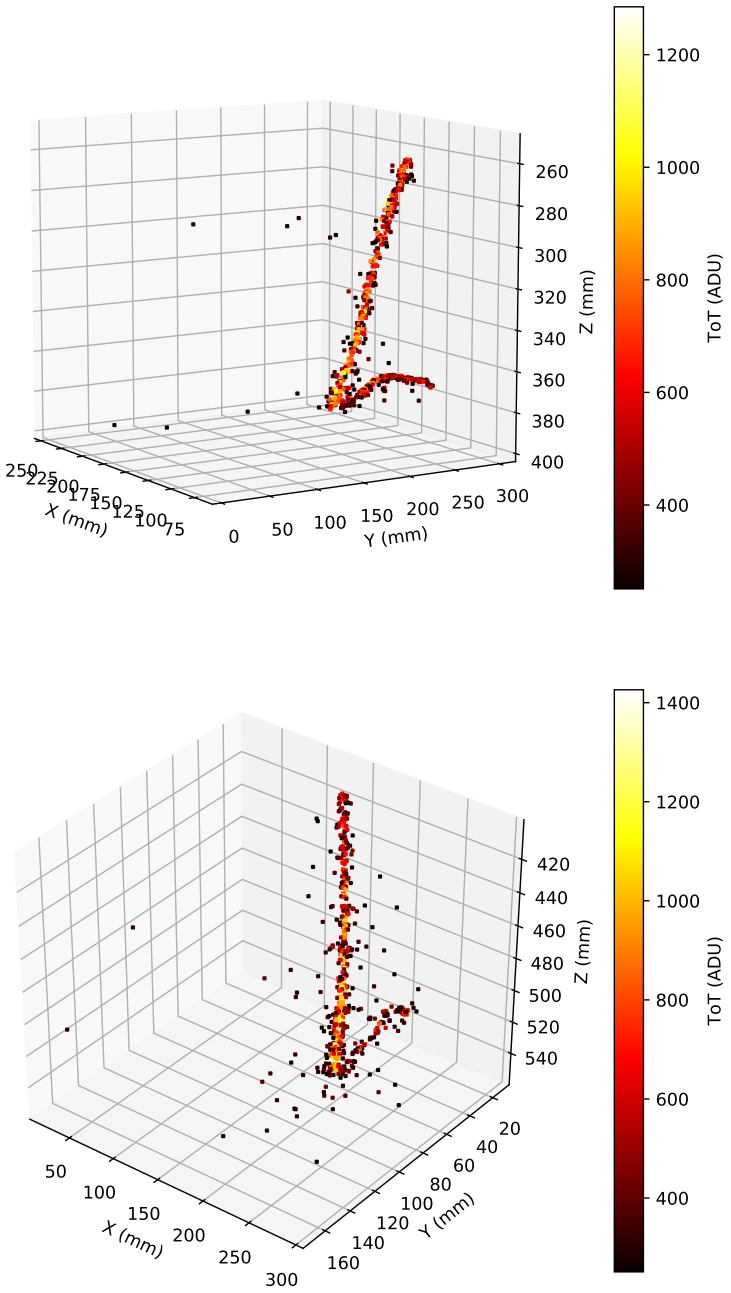

Figure 8.6: Gallery of two stopping muon candidates. These events are seen to have a Bragg peak, followed by the production of a candidate Michel electron. The topmost event is investigated in more detail in Section 8.4.

8.2 Measurement of THGEM light production

As discussed in Chapter 3, light production in a THGEM is expected to be broadly formed from two components. First, a linear regime is expected from proportional electroluminescence at lower biases. Once the field across the THGEM becomes large enough, the electrons may be sufficiently accelerated to ionise Argon atoms. Beyond this point, the light production becomes exponentially enhanced.

The light production of the ARIADNE THGEM was measured using the TPX3Cam system. A short (5 minute) dataset was taken at several THGEM biases. From each dataset, we count the total number of hits seen by the camera, and calculate the mean hit rate of the dataset. As light production increases, the hit rate is expected to also increase. The THGEM bias was scanned from 600 volts up to 2800 volts, in 200 volt increments. An additional data point was taken at 2900 volts, before the THGEM began to discharge. Figure 8.7 shows the results of the study.

The light sensitivity of the system was found to be excellent. Even at a THGEM bias of 800 volts, where the light production should be no more than a few tens of photons per incident electron, a clear signal was detected above the background dark count rate of the photocathode. The theoretical function of THGEM light production proposed in Chapter 3 was used to fit the experimental data. The parameters of the model have been refitted.

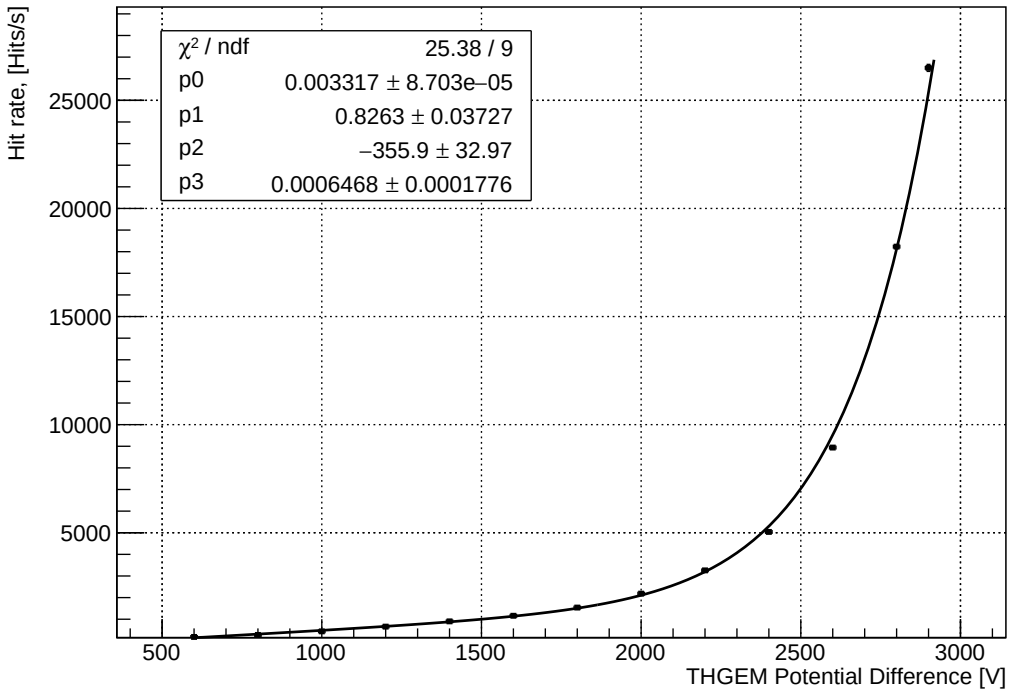

Figure 8.7: Measured light production of the ARIADNE THGEM as a function of bias. The data is well described by a function of the form $p_1 x(1 + p_3 \exp(p_0 x)) + p_2$.

8.3 Measuring electron lifetime

As electron drift time increases, the probability that the electron may encounter an impurity and be captured also increases. This results in the intensity of MIPs being observed to reduce with increasing depth in the TPC. Since throughgoing MIPs should have a generally uniform energy deposition along their path length, they can be used as kind of a standard candle. By measuring the track intensity versus depth in the TPC, the electron lifetime may be determined.

In this study, a selection was made on MIPs which pass through the THGEM. For these MIPs, we measure the track intensity as a function of drift time, or depth in the TPC. This process is repeated for many MIPs until an average distribution is formed. An exponential is fitted to this distribution to determine electron lifetime. The method for event selection is as follows;

1. Raw data is composed of both hits from TPX3Cam and trigger timestamp signals from the PMT. Trigger timestamp signals are assumed to correspond to S1 (t_0).

2. For each PMT trigger timestamp t_0, collect all hits between t_0 and $t_0 + 550$ μs (maximum ARIADNE drift length).

3. Cut those events which contain less than 1000 hits. This cut broadly selects track-like events.

4. Perform a robust linear fit [1] in both x-z and y-z planes. The R-Squared value must be > 0.8 in both planes. Combine these two 2D linear fits to determine the 3D entry/exit points of the track in the TPC.

5. Make a selection of only those tracks which pass through the THGEM.

6. For all hits in the run, fill a histogram of hit intensity (ToT) versus drift time ($t_0 - \text{ToA}$).

This process was performed for two different datasets, taken five days apart, during the liquid argon purification process. Figure 8.8 shows the measured electron lifetime in the earlier dataset while Figure 8.9 shows the

[1] `https://www.gnu.org/software/gsl/doc/html/lls.html#robust-linear-regression`

electron lifetime measured in the later dataset. The loss of drifting electrons to impurities is expected to be distributed according to $Q/Q_0 = exp(-t/\tau)$, where t is the drift time and τ is the electron lifetime. Thus, the electron lifetime is given by the negative reciprocal of the slope of the fitted function, which is of the form $Aexp(kx)$. From the first dataset, we measure an electron lifetime of approximately 135 μs, whereas in the later dataset an electron lifetime of approximately 320 μs is measured. It is clear that the recirculation process was improving the Liquid Argon purity.

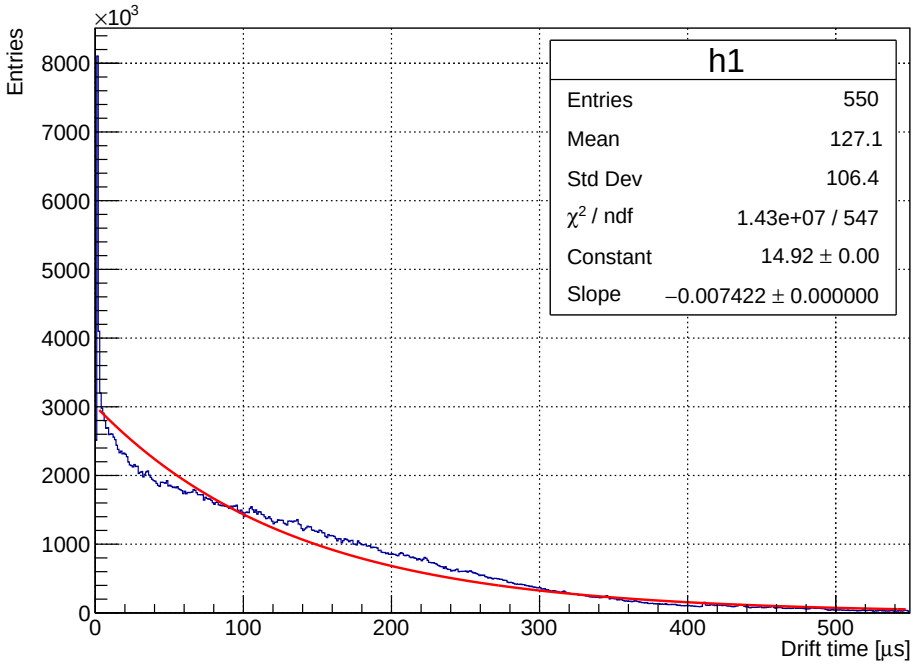

Figure 8.8: Measured muon intensity as a function of drift time for an earlier data set, taken five days before Figure 8.9. The calculated electron lifetime is approximately 135 μs.

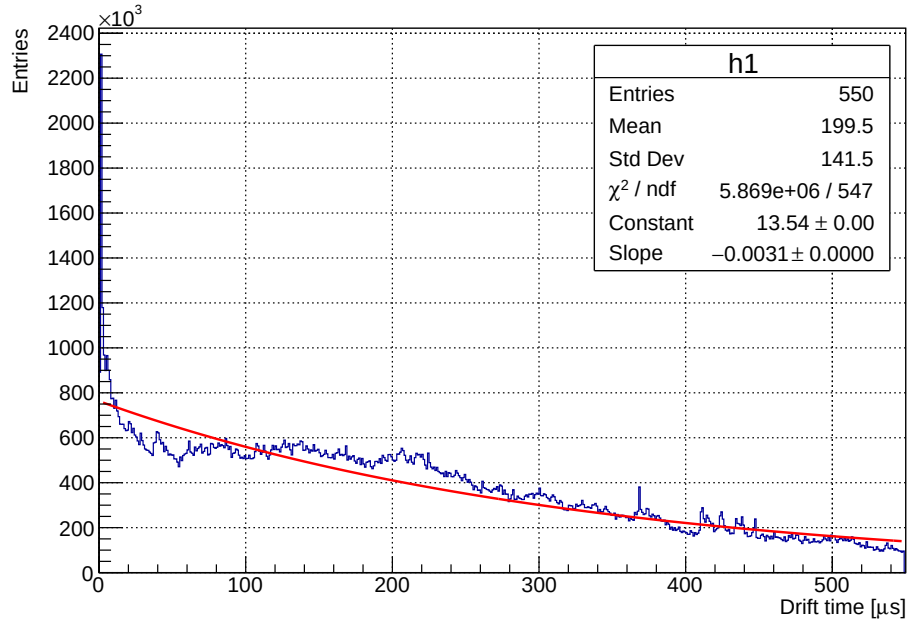

Figure 8.9: Measured muon intensity as a function of drift time for the later data set, taken five days after Figure 8.8. The calculated electron lifetime is approximately 320 μs.

8.4 Energy deposition of throughgoing MIPs

The energy loss of throughgoing MIPs can be measured in several ways. Typical methods involve measuring the mean energy loss and the most probable energy loss. The distribution formed from taking a sample of the energy loss along many single segments of a minimum ionising track should generally be distributed according to a Landau distribution. From this distribution we could measure two quantities. First, we could measure the mean energy loss, below a certain cutoff energy. Or, we could fit a Landau function to the distribution and measure the most probable value (MPV) of this distribution. Both methods have their own merits and caveats, but here we will focus on the later technique. The MPV energy loss for highly energetic muons is approximately 1.6 MeV/cm [121]. Using a short (1 hour) sample of cosmic data in ARIADNE, we can measure the energy deposition of throughgoing cosmic muons. For this analysis, event selection is as follows;

1. Raw data is composed of both hits from TPX3Cam and trigger timestamp signals from the PMT. Trigger timestamp signals are assumed to correspond to S1 (t_0).

2. For each PMT trigger timestamp t_0, collect all hits between t_0 and $t_0 + 550$ μs (maximum ARIADNE drift length). Hits with ToT < 20 ADU are cut.

3. Cut those events which contain less than 1000 hits. This cut broadly selects track-like events.

4. A purity correction of $\tau = 320$ μs is applied to the data. This is done by adjusting the ToT value of hits according to their drift length by $Q/Q_0 = \exp(-t/\tau)$ where Q is the measured ToT value, Q_0 is the corrected ToT value, t is the drift time and τ is the electron lifetime.

5. Perform a robust linear fit [2] in both x-z and y-z planes. The R-Squared value must be > 0.8 in both planes. Combine these two 2D linear fits to determine the 3D entry/exit points of the track in the TPC.

6. Cut hits that are further than 20mm from the fitted 3D line.

[2] `https://www.gnu.org/software/gsl/doc/html/lls.html#robust-linear-regression`

7. For all remaining hits, find the closest point on the fitted line to the hit.

8. Calculate the distance from the track starting point to the closest point on the fitted line.

9. Fill a histogram bin with the ToT value of this hit. The bin number to be filled is the distance from the start of the track to the calculated closest point on the fitted line. The resulting histogram is a histogram of energy deposition as a function of track length.

10. Taking each bin of the previous histogram, plot a histogram of energy deposition per 1 mm step in track length. This is a histogram of energy deposition per 1 mm step size in the TPC, and should be distributed according to a Landau distribution for a MIP.

Figures 8.10 and 8.11 show two sample distributions from the data set, with the associated Landau fit.

By taking the mean MPV values for these fitted distributions across the dataset, we are able to build an energy calibration. Figure 8.12 shows the average MPV from well fitted tracks. By using the previously found $\langle -\frac{dE}{dX} \rangle_{\text{MPV}}$ of 1.6 MeV/cm through a 1 mm thickness of Liquid Argon, we can approximate a very coarse energy calibration of 3470 $\pm$ 680 ADU/MeV. A slice width of 1 mm was chosen to maximise the number of available entries for fitting MPV distributions, examples of which are seen in Figures 8.10 and 8.11. The slice width of 1 mm takes maximal advantage of the 1 mm/pixel tracking resolution in the detector. This calibration will easily be improved in future work, using longer datasets with improved electron lifetime.

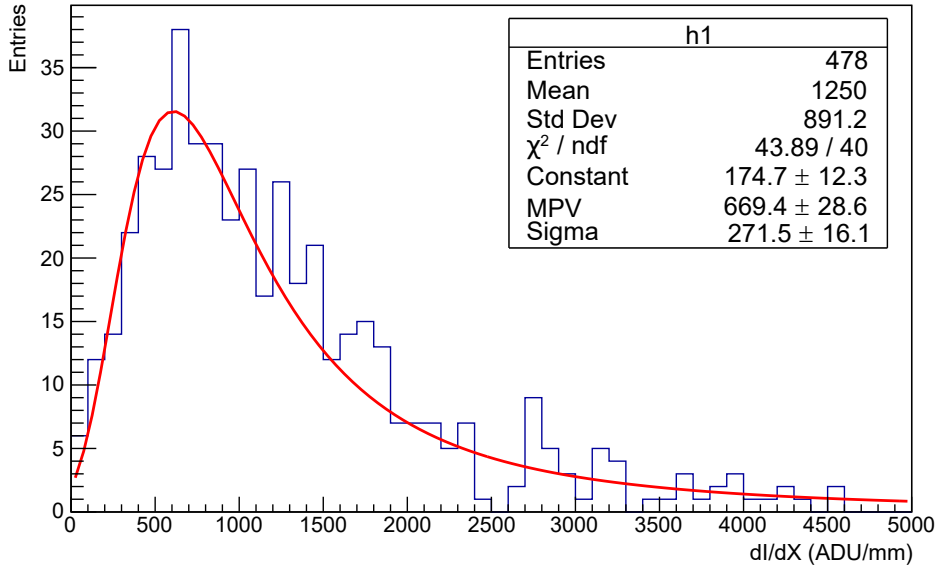

Figure 8.10: Sample distribution of summed hit intensities for 1 mm slices of a cosmic muon track. The distribution has been fitted with a Landau function. See the text for a more detailed description of the distribution building algorithm.

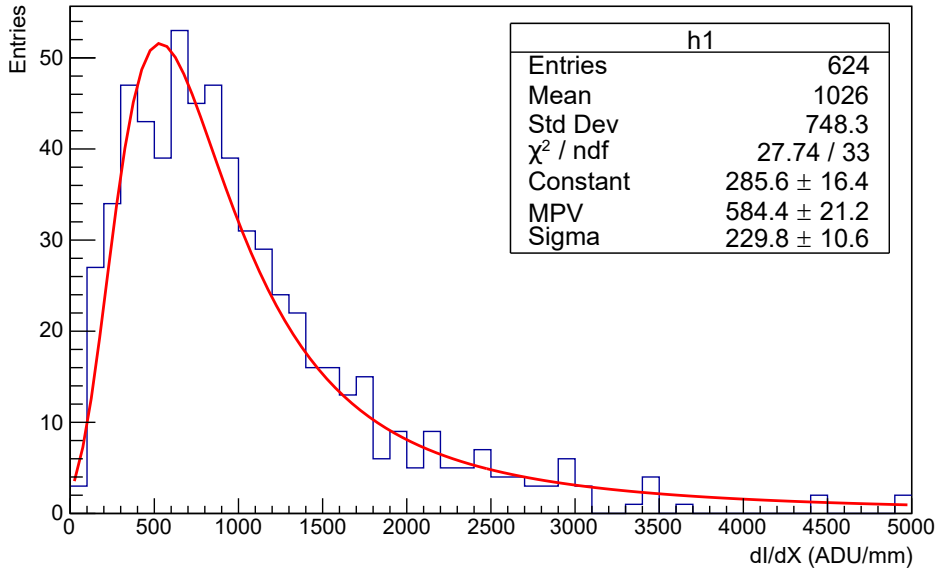

Figure 8.11: Sample distribution of summed hit intensities for 1 mm slices of a cosmic muon track. The distribution has been fitted with a Landau function. See the text for a more detailed description of the distribution building algorithm.

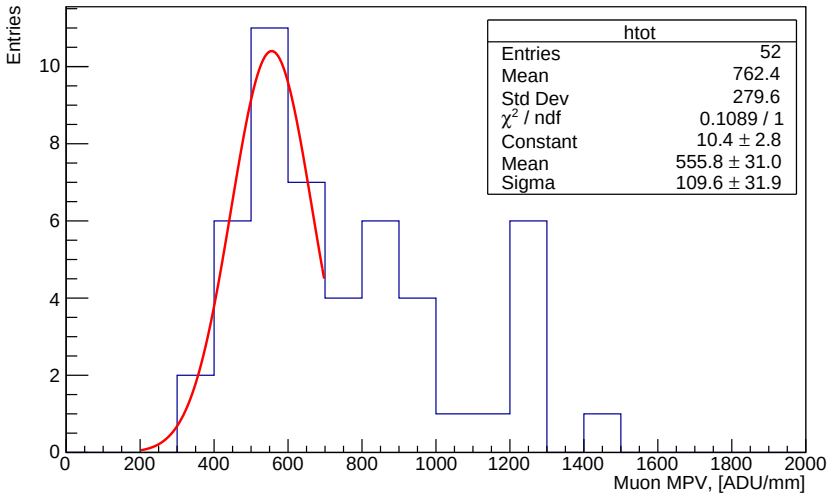

Figure 8.12: Distribution of MPV values for well fitted cosmic muon samples in the short dataset taken during purification. A Gaussian function has been fitted to the peak of the distribution, which corresponds to the expected muon MPV energy loss of 1.6 MeV/cm.

A stopping muon candidate

A preliminary study was also performed on a single stopping muon candidate, shown in Figure 8.6. For this event, we plot the intensity of the track as a function of track length. Figure 8.14 shows the intensity profile of the stopping muon. By using the previous calculated energy calibration, we can plot this with units of energy. The large error bars are the result of the relatively coarse energy calibration discussed earlier, combined with uncertainties arising from electron lifetime corrections. Future work with improved electron lifetimes and longer data samples will allow more precise measurement of stopping muon energy distributions.

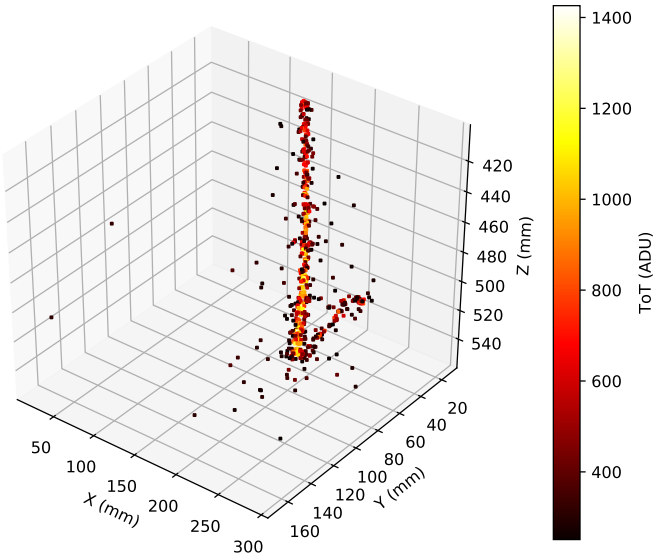

Figure 8.13: Event display of the stopping muon candidate discussed in this Section.

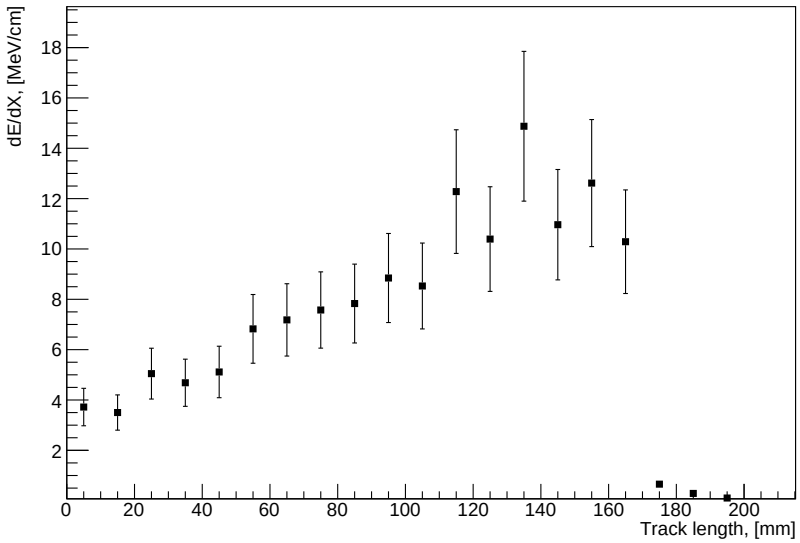

Figure 8.14: Energy profile of a stopping muon event. Studies will be performed in the future using a larger sample of events.

8.5 Position resolution

8.5.1 x, y direction

From the earlier reconstructed cosmic muons, the spatial resolution of the Timepix 3 camera can be measured. For each muon which has been successfully fitted with a straight line, we measure the (x, y) distance of each hit from the closest point on the line. By plotting a distribution of this distance, we can estimate the position resolution in the (x, y) plane. Figure 8.15 shows this distribution. In general, we can describe the distribution as having two components. In the center of the track is a a narrow peak, well described by a single Gaussian, with a standard deviation of σ_{xy} =3 mm. Either side of this central peak is a tailing distribution of hits, which are not well described by the same distribution of the core of the track. These tails are believed to be caused by the wavelength shifting stage. The small gap between the THGEM and the TPB wavelength shifting glass allows for the light produced in the THGEM holes to diffuse. Given that these tails do not seem to disturb the distribution of the central core of the track, it is unlikely that this feature degrades position resolution. However, from a data quality point of view, these hits are not ideal. Future work will investigate ways to mitigate this effect, either by reducing the distance between the TPB and the THGEM, or by eliminating TPB entirely (see Section 9.1.3). Since the hits that result from the TPB are low intensity, it is very easy to apply a cut to time over threshold to remove them. Figure 8.16 shows the x, y distribution of a track which has a cut applied for hits below 300 ADU. Once this cut is applied, a very clean distribution is seen, well described by a single Gaussian with a standard deviation of σ_{xy} =2.2 mm. This measured standard deviation includes the effects of electron diffusion, as well as detector readout contributions. As can be seen in Figure 2.10, the expected electron diffusion contribution is 1.1 mm. Convolving this with the pixel resolution of 1.1mm/pixel predicts a tracking resolution of $\sqrt{1.1^2 + 1.1^2} = 1.6$ mm. A remaining contribution of $\sigma = 1.5$ mm is seen in the distribution. Track broadening due to the TPB wavelength shifting stage is expected contribute to this extra broadening. as well as effects of multiple coulomb scattering that are included when performing a linear fit across the entire track length.

We can attempt to disentangle the effects of multiple coulomb scattering by repeating this study using multiple shorter track segments, rather than

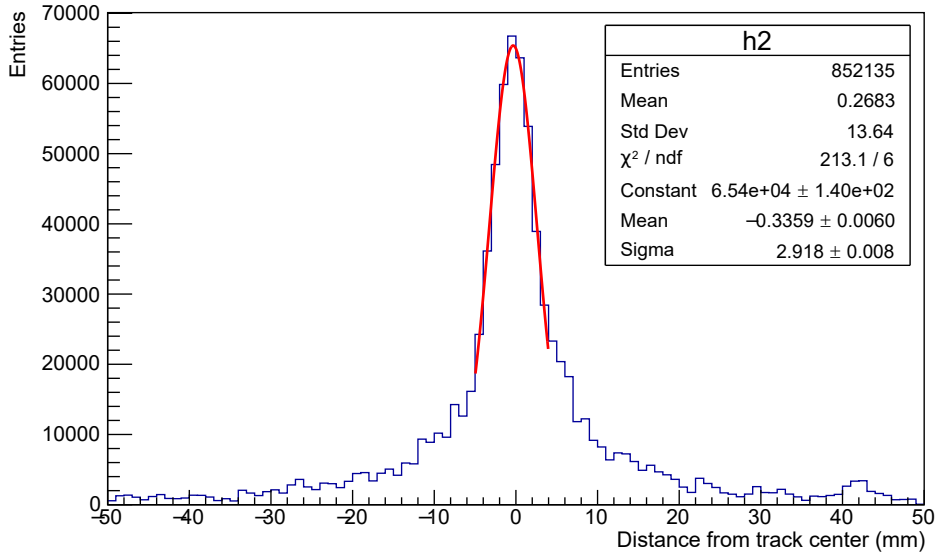

Figure 8.15: Distribution of $x - y$ pixel hits from the track center. A well defined central core of the track is seen. Tails either side of the distribution are due to a track broadening effect of TPB.

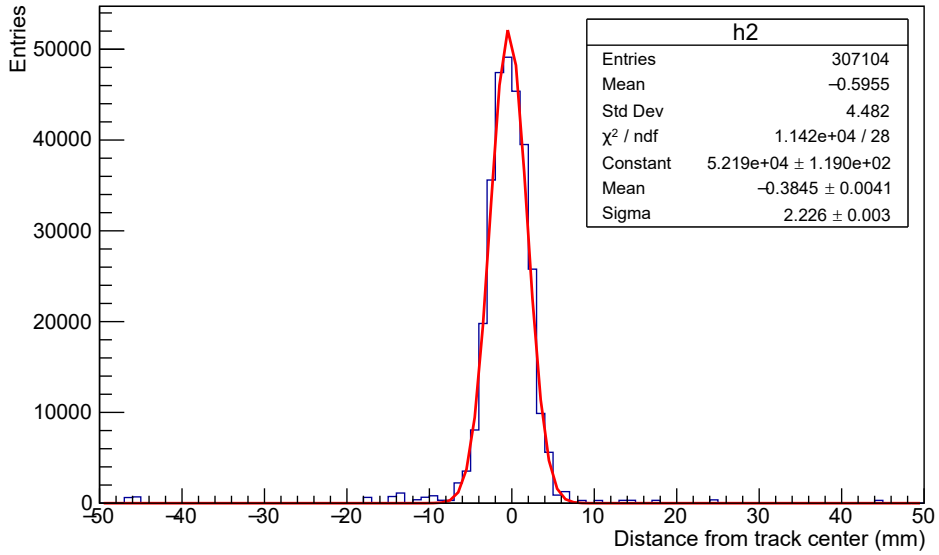

Figure 8.16: Distribution of $x - y$ pixel hits from the track center, with a cut applied to remove all hits with an intensity below 300 ADU. This cut cleanly removes the low intensity hits that result from the TPB broadening. A well defined central core of the track is all that remains.

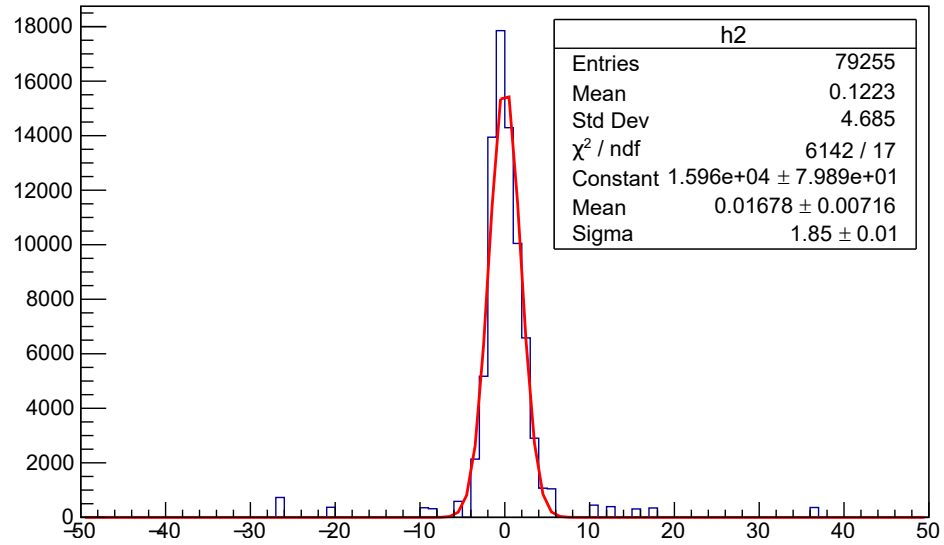

Figure 8.17: Distribution of $x - y$ pixel hits around the multiple fitted 1 cm track segments, with a cut applied to remove all hits with an intensity below 300 ADU.

the full track. This study was repeated, splitting the track into 1 cm segments along the axis found by the original straight line fit over the whole track. These 1 cm track segments are refitted, and the (x, y) distribution of hits around each of these track segments is found. Figure 8.17 plots the result of this study. The standard deviation of the resulting distribution has been seen to be reduced to σ_{xy} =1.85 mm. This resolution is comparable to the value predicted by the convolution of diffusion and detector pixel resolution effects ($\sqrt{1.1^2 + 1.1^2} = 1.6$ mm).

8.5.2 z direction

In the z direction, we will discuss the resolution in units of time. For clean throughgoing MIPs, Figures 8.18 and 8.19 present the timing distribution of hits, relative to the track center. Both are well described by a single Gaussian, with a standard deviation of approximately 1 μs. These results can be interpreted in mm using a conversion of 1.648 mm/μs. Applying a ToT cut to remove the effect of the TPB broadening, as was done in the x, y plane, does not make any noticeable change to the resolution in the z axis. This is to be expected, since the TPB broadening effect should only be a spatial effect in the x, y plane, and not affect timing, which ultimately dictates the z position resolution. It is worthwhile to note that z position resolution should not change with varying field of view of the camera. If a larger detector area is covered per camera, the x, y resolution will be reduced. However, the z resolution is dictated by the timing resolution of the TPX3 ASIC and should remain excellent.

8.6 Discussion

Performance of the TPX3 based cameras in Liquid Argon was generally found to be excellent. The timestamping capability of TPX3Cam was found to provide extremely precise z axis resolution. Now, a single camera is capable of performing readout of all (x, y, z, E). When compared to the EMCCD cameras, TPX3Cam combined with an intensifier seemed to offer comparable or even greater sensitivity.

Correlation of the camera with a PMT using the external timestamping signal feature was tested thoroughly. The connection appeared robust, with no obvious timing problems being seen. The effect of track broadening by TPB was closely studied. Once suitable cuts are selected, it seems that this effect had a negligible impact on tracking resolution. In the future, options will be explored to reduce or even eliminate this TPB component.

At the time of writing, the ARIADNE detector continues to be purified. Currently, the electron lifetime is in the region of 350 microseconds. Once a suitable electron lifetime is achieved, perhaps closer to several milliseconds, more detailed analyses will be performed. Longer datasets will be taken with improved electron lifetime, providing greater statistics while simultaneously reducing the magnitude of systematic uncertainties introduced by purity

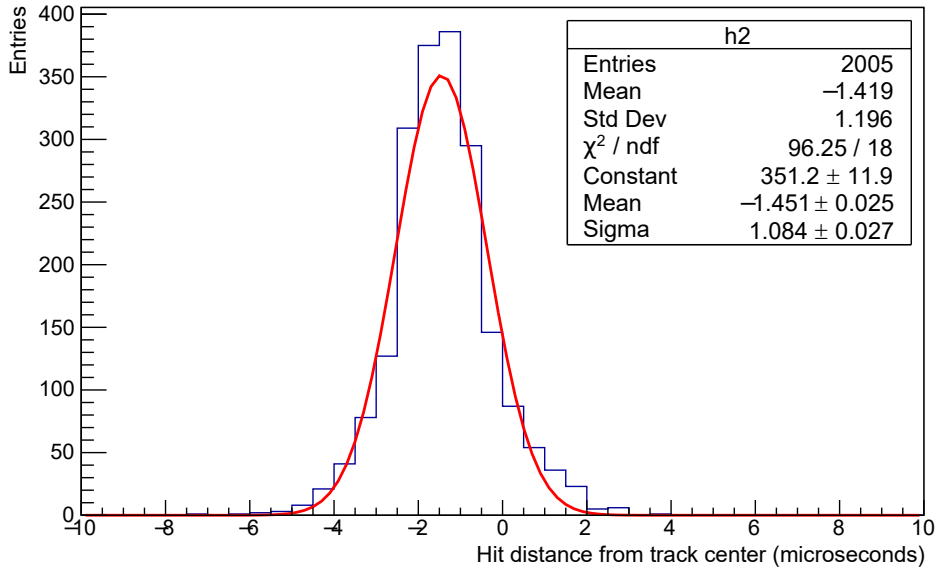

Figure 8.18: Distribution of hit timings in the z axis, relative to the center of the fitted track. The distribution is well described by a Gaussian, with a standard deviation of only 1 microsecond.

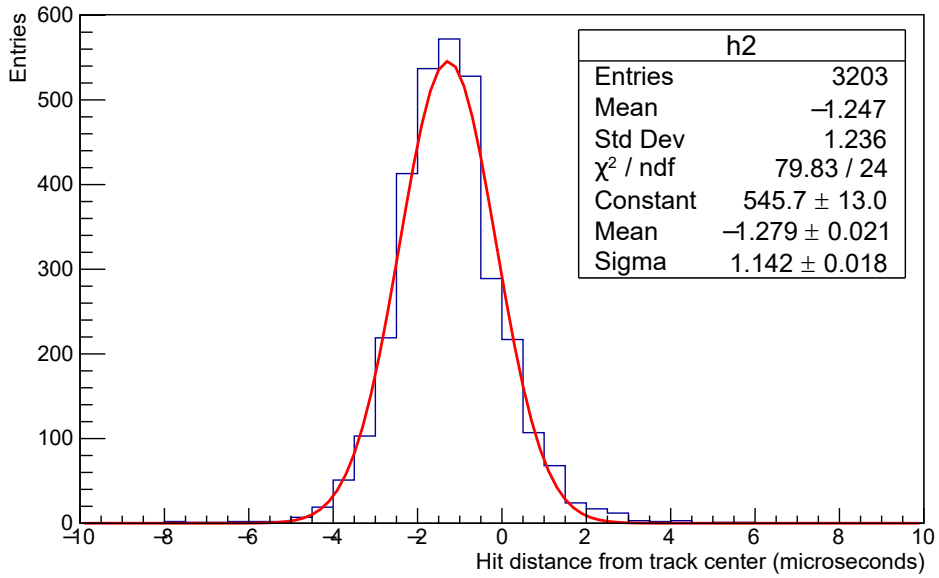

Figure 8.19: Distribution of hit timings in the z axis for a second example track, relative to the center of the fitted track. The distribution is also well described by a Gaussian.

corrections. This should allow for a much more robust energy calibration of the system. It is expected that a more complete sample of stopping muons will also be obtained, allowing more detailed studies to be performed. The intensity profile of stopping muons can be analysed in much greater detail, and perhaps the energy distribution of the resulting Michel electrons can also be measured.

Chapter 9

Future developments

9.1 Technological advances

Several profitable technological developments may be realised in the near future. Three flavours of improvements are particularly interesting. Developments of new versions of the Timepix ASIC should provide compelling cost reductions and performance improvements. Improvements in image intensifier photocathode quantum efficiency presents the opportunity for improved light collection. Recent image intensifier advancements have also presented an intriguing opportunity for potential direct imaging of VUV scintillation light, without use of a wavelength shifter. Finally, some interesting possibilities are emerging for THGEM designs which have been tailored for electroluminescence light production.

9.1.1 Timepix 4

The Medipix4 Collaboration is currently developing the Timepix4 (TPX4) ASIC [122]. The exact specification of TPX4 is not yet formally defined although the main design goals are a larger ASIC (close to 512 $\times$ 512 pixels) and improved resolution of both ToT and ToA. Given that the 1.6 ns timing resolution of TPX3 was already ample for optical readout of both gas and liquid TPCs, the improvements to ToA resolution are not especially interesting. The improvement of ToT resolution should enhance calorimetric performance. The improved 12-bit resolution of TPX4 is now only marginally less than the 14-bit resolution proposed by two-phase charge readout technologies. The larger size of the TPX4 ASIC means that a larger detector

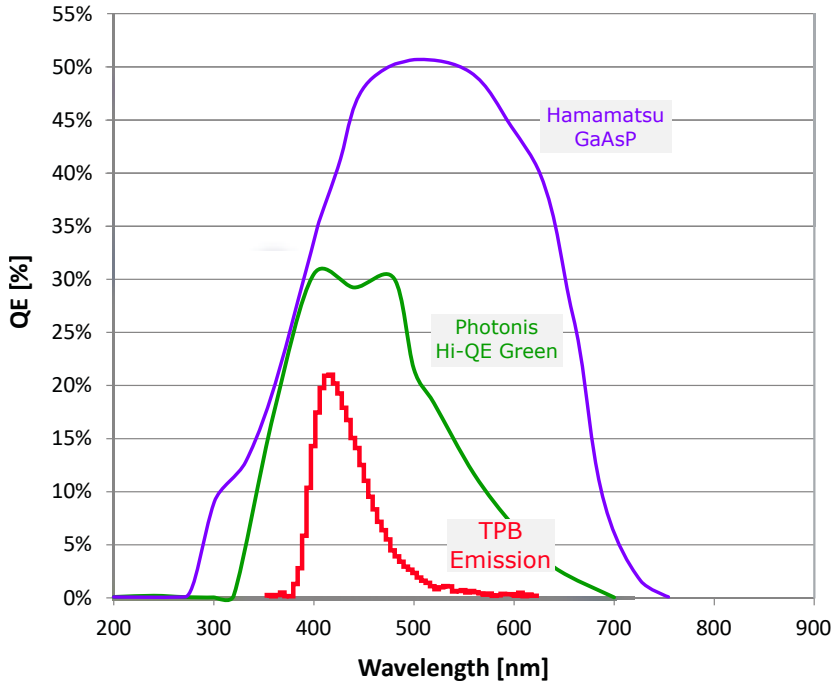

Figure 9.1: Comparison of commercially available photocathode options. Photonis Hi-QE green was used for the liquid Argon demonstration in this Thesis. Improved light collection is immediately possible using Hamamatsu GaAsP photocathodes.

area can be covered using a single camera. Since each camera requires an image intensifier, this reduction to the number of required cameras is doubly favourable in terms of cost savings. Additional requirements such as optical feedthroughs, ethernet connections for DAQ, etc are also reduced.

9.1.2 Image intensifier developments

Modern image intensifier developments that are significant for optical readout generally concern the photocathode. A Gallium arsenide phosphide (GaAsP) photocathode can offer significantly improved quantum efficiency compared to the Hi-QE green photocathode for the detection of light emitted by TPB. Figure 9.1 compares the quantum efficiency of a GaAsP photocathode to Hi-QE green. The GaAsP photocathode has slightly higher QE than Hi-QE Green at the peak wavelength of TPB emission (430 nm), but also has substantially higher QE throughout the tail of the TPB emission spectrum. Integrated over the entire emission spectrum, a GaAsP photocathode will collect approximately 50% more light.

9.1.3 Direct VUV imaging

An exciting possibility may result in the elimination of the TPB wavelength shifter all together. Certain photocathodes exhibit good quantum efficiency in the VUV, making direct detection of the VUV scintillation light from Argon (or Xenon) a possibility. Although TPB is frequently used, it is not without problems. The coating process requires careful consideration to ensure that the coating has both a well defined thickness that this thickness is uniform over the whole surface. It is conceivable that variations in TPB coating thickness would induce variations in detector response. Additionally, TPB coatings have been shown to degrade under UV exposure [123]. Losses can be as high as 40 % with a single day of exposure to ambient light. Considerations to protect TPB coatings from ambient light can result in added expense and complication. TPB has been shown to have a clear aging effect when exposed to ambient light [124]. Beyond these initial manufacturing concerns, TPB may also result in subtle yet important changes to detector performance. Considering its widespread application, the emission time spectrum of TPB has not been studied in much detail. Recent studies have discovered the existence of a long lived triplet states in TPB [125]. The existence of these states has been suggested as an explanation for often observed 'intermediate' decay components, which have no basis in the known emission spectrum of pure Argon. This highlights the care that must be taken when introducing an additional step in a detection process. Unless a complete and thorough understanding of the process is known, subtleties can present themselves. Given this, perhaps the elimination of the TPB wavelength shifting step is pragmatic.

Direct VUV optical readout requires both an image intensifier that is sensitive to 128nm as well as suitable optics. Cesium iodode (CsI) coated MCPs have historically been produced with quantum efficiencies generally in the region of 20 % to 30 % [126–131]. The performance of CsI photocathodes has been found to be stable over at least six years of operation [132]. Photek Limited, a manufacturer of image intensifiers based in the UK, has recently developed CsI coated MCPs with detection efficiencies in the range of 20 % to 35 % at 128 nm, measured behind a magnesium fluoride input window.

In order to be transparent to 128 nm photons, an intensifier should use an input window made from Magnesium Fluoride (MgF2). The transmission of MgF2 at 128 nm is around 65 %, and close to 90 % at 178 nm.

An MgF2 imaging lens is required on the detector side, focusing the VUV photons onto the input window of the intensifier. This lens should have around 65 % transparency at 128 nm, reducing detection efficiency from 20-35 % to 13-23 %. Although this detection efficiency, at first glace, seems inferior to the roughly 30 % DQE currently achieved with Hi-QE green photocathode, the elimination of the TPB wavelength shifting step should realise substantial improvements in light collection efficiency. We can express the total light collection efficiency of the optical readout setup as

$$\eta = \eta_{\mathrm{WLS}} \Omega \lambda_{\mathrm{DQE}} \tag{9.1}$$

where η_{WLS} represents the efficiency of the wavelength shifting process, Ω represents the solid angle from the TPB to the lens and λ_{DQE} represents the detective efficiency of readout device (either optical or VUV). Given that the solid angle is the same for both optical or VUV readout, we can express the relative detection efficiency between the two approaches as

$$\frac{\eta_{\mathrm{VUV}}}{\eta_{\mathrm{Optical}}} = \frac{\lambda_{\mathrm{VUV}}}{\eta_{\mathrm{WLS}} \lambda_{\mathrm{Optical}}} \tag{9.2}$$

We know that $\lambda_{\mathrm{Optical}}$ is 30% for the Photonis cricket and we will assume λ_{VUV} of 18%, based from the average of photocathodes that were produced by Photek, discussed earlier. Thus,

$$\frac{\eta_{\mathrm{VUV}}}{\eta_{\mathrm{Optical}}} = \frac{0.6}{\eta_{\mathrm{WLS}}} \tag{9.3}$$

Thus, η_{VUV} is greater than η_{Optical} for any η_{WLS} less than 60%. Even if we assume that all light production happens at the top of the THGEM hole, and that any light produced that hits the TPB is converted to useful light, η_{WLS} reaches a theoretical maximum of 50%, given that half of the light produced in any hole goes downwards, away from the TPB. Thus, direct VUV imaging seems promising for improved detection efficiency.

In reality, η_{WLS} is not going to be 50%. A more realistic value may be predicted by assuming all light production happens in the middle of the hole thickness, which yields η_{WLS} of only 6%.

Separating the imaging lens and intensifier input window allows some flexibility for lens R&D. Different lenses can be exchanged without disturb-

ing the vacuum of the intensifier. Once lens design is finalised it is conceivable to seal the intensifier tube using the lens as the input window, recovering some efficiency. The rest of the configuration of the image intensifier remains unchanged. A P47 phosphor screen allows the intensifer to still output the light signal at a wavelength that is compatible with the spectral sensitivity of TPX3Cam - no additional R&D work is required on the air side.

Since VUV photons do not travel through air, the imaging lens and input window must be installed in the Argon volume. This is possible by integrating the intensifier into a vacuum flange. Such an integration is commonplace so should not pose a technical challenge. The final assembly has the phosphor screen output on the air side which can be easily coupled to the camera. In order to maintain flexibility to remove the intensifier and lens, the system could be mounted to a detector using a gate valve setup as shown in Figure 9.2.

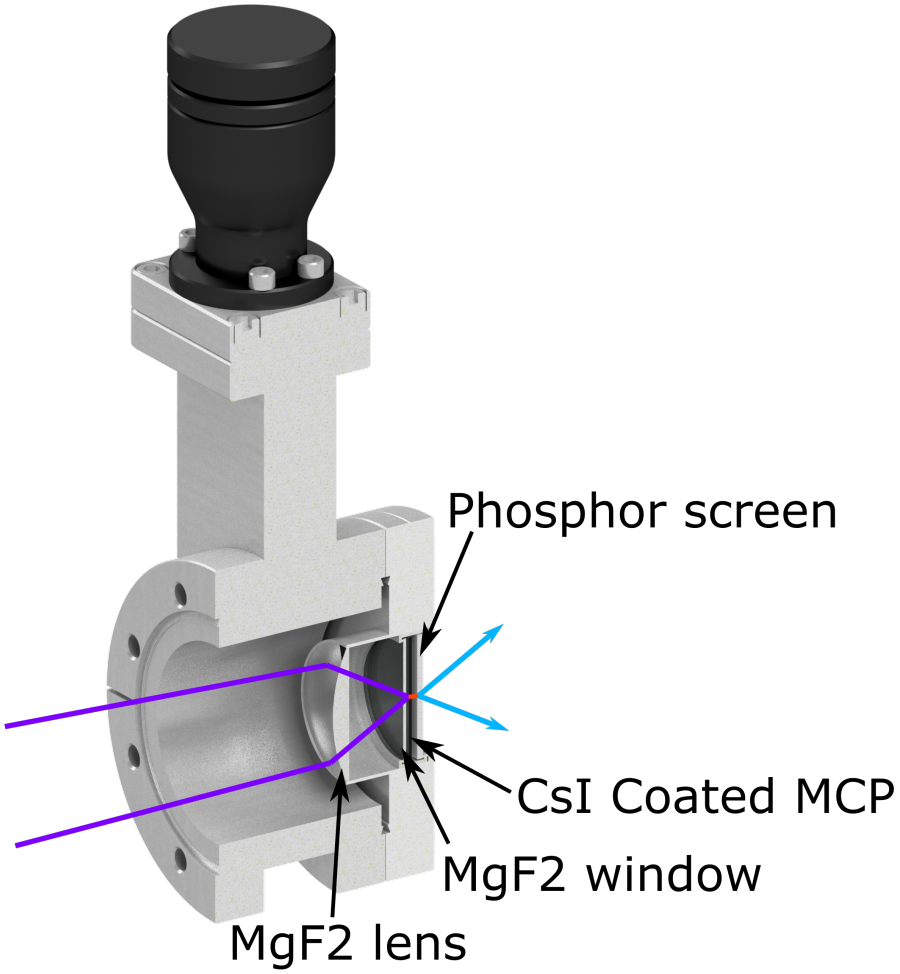

Figure 9.2: Conceptual direct VUV imaging setup. The device is mounted onto a gate valve so that it may still be removed from the detector without disturbing the cryogenic volume.

9.2 Imaging larger areas

The performance of the Timepix camera was tested using a 15mm focal length lens, which provided a much larger field of view. This lens, however, has a much lower speed than the 50mm lens typically used, with f/1.4 compared to f/0.95. The field of view can be calculated as

$$\text{Field of view} = 2\text{atan}\left(\frac{h}{2f}\right) \tag{9.4}$$

where h is the height of the sensor (14 mm for TPX3) and f is the focal length of the lens. When using a 15 mm focal length lens, the resulting field of view is 50 degrees. When installed on ARIADNE, at a distance of 1100 mm from the THGEM, the resulting field of view is approximately 1m $\times$ 1m. Given that the timepix3 sensor has 256 $\times$ 256 pixels, the inferred resolution is 4 mm/pixel.

As seen earlier in Equation 3.2, the lower speed of f/1.4 of the 15 mm lens translates to a smaller effective lens diameter. This in turn reduces optical acceptance. A 15 mm lens with f/0.95 would have an effective diameter of approximately 15.8 mm, which translates to a solid angle of 1.62E-4 Steradian when 1100 mm from the THGEM. A lens with f/1.4 has an effective diameter of 10.7 mm, reducing the solid angle to 7.45E-5 Steradian.

Due to optical limits of the viewports on the ARIADNE detector, the camera is only able to view a THGEM area of 30 cm$\times$30 cm, but this test provided initial feedback on the sensitivity of the device with a larger field of view. Figure 9.3 shows a integrated image taken using SoPhy. The white spot in the center of the image is a micro-discharge that occurred on the THGEM during the long integrated exposure time. The edges of the active area of the THGEM can be seen, as well as the circular aperture of the stainless steel nipple. Figure 9.3 also shows an event display from SoPhy of a single event in Time over threshold mode. A long cosmic is seen passing across the THGEM.

Figure 9.4 shows a 3D reconstruction of a cosmic muon in the TPC. Future work will perform more detailed studied into the performance of optical readout when imaging larger detector areas.

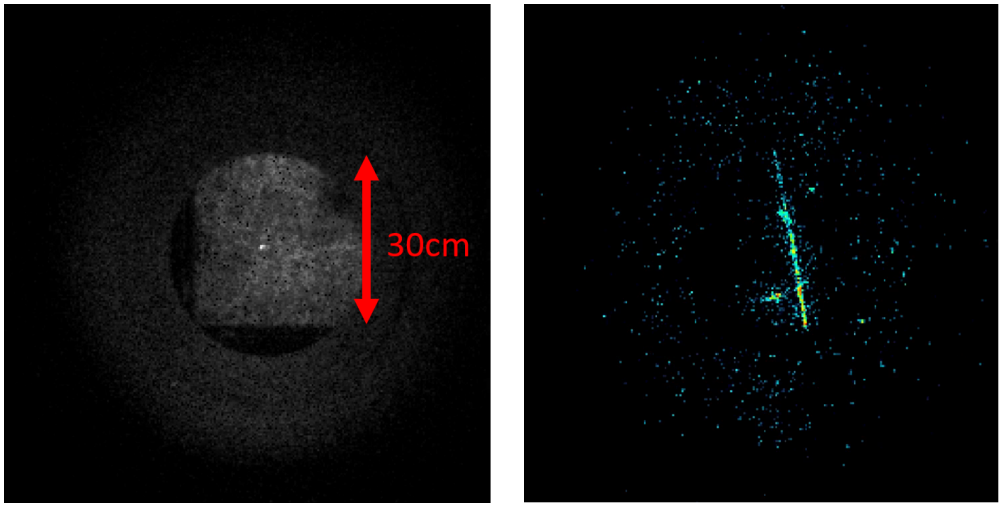

Figure 9.3: Left: Field of view seen when using the 15mm focal length lens. The 30cm × 30cm area that is visible of the THGEM only takes up roughly 1/3 of the total sensor area. The total view of view is approximately 1m × 1m. The resolution is 4mm per pixel in x and y. Right: A single cosmic muon seen in Time over threshold mode. The muon passes across most of the 30 cm length of the THGEM that is visible.

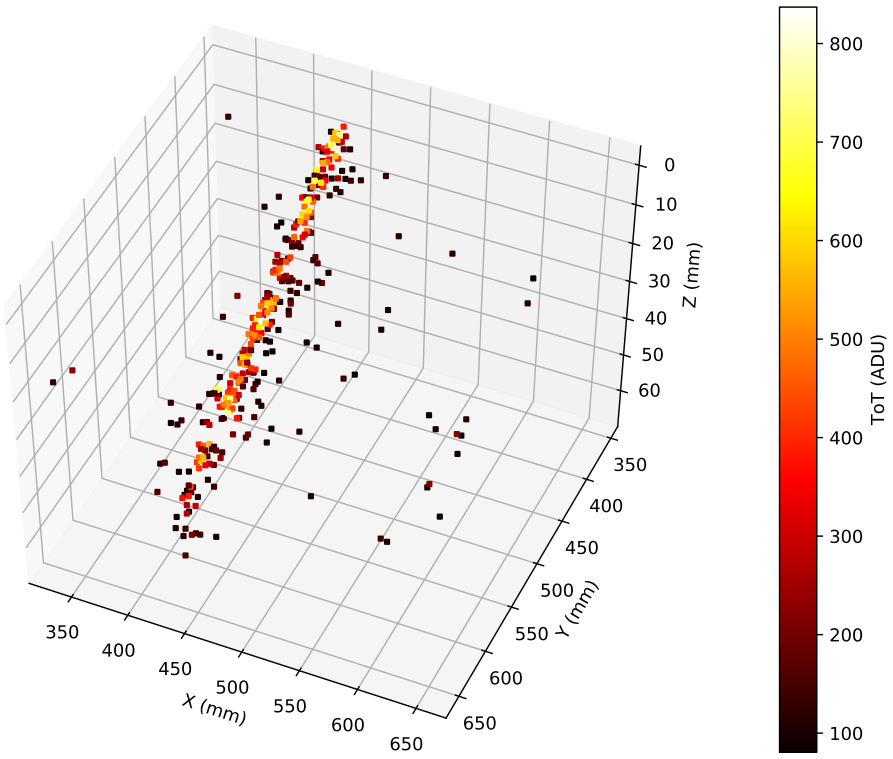

Figure 9.4: 3D reconstruction of a single sample event using the 15mm focal length lens. The resolution is 4mm/pixel in x and y axes. Future work will continue to explore the performance of the camera when imaging larger detector areas.

Chapter 10

Conclusion

In Chapter 1, the current state of neutrino physics is briefly discussed, providing a motivation for the construction and use of Liquid Argon TPCs as a tool for future discoveries. In Chapter 2, the operation aspects of dual-phase Liquid Argon TPCs are discussed in detail.

In Chapter 3, the concept of optical readout of a dual-phase Liquid Argon TPC is introduced. A model of THGEM light production is presented. The rate of light production in a THGEM is compared to that of charge production.

Chapter 4 introduces the ARIADNE detector. The ARIADNE detector is discussed from design phase, through to construction and finally operation ongoing at the time of writing. Key design aspects are explained in detail and possible future improvements are also discussed. The design and manufacture of the ARIADNE 100 kV high voltage feedthrough is explained.

In Chapter 5, the deployment of the ARIADNE detector to the CERN T9 beamline is presented. Results from beamline operation highlighted the excellent sensitivity of EMCCD cameras, as well as excellent x, y resolution. Subsequent analysis of the data taken at the beamline showed that z dimension reconstruction using EMCCDs can be challenging. This limitation motivated R&D activities, culminating in the development of a novel camera technology. This new camera technology was introduced and characterised in Chapters 6, 7 and 8. Full (x, y, z, E) readout is now possible using a single device.

Many benefits were found during testing;

- Externally mounted cameras provided easy access for upgrade, repair and calibration throughout the life of an experiment.

- Sensitivity to the linear electroluminescence light produced by the THGEM was demonstrated. Operation of the THGEM at low field may help to ease problems related to ion backflow.

- Millimeter scale resolution in x, y and z axes was demonstrated.

- The zero-suppressed and natively 3D data format allows for simple data manipulation during analysis. 3D reconstruction of events is trivial. In Chapter 7, the readout of a gas TPC with a high event rate (1 kHz) was demonstrated. This demonstrates the flexibility of the technology for applications beyond dual-phase Liquid Argon TPCs.

Future developments are certain to continue to improve the performance of optical readout. In particular, development of direct VUV imaging technologies are particularly exciting, discussed in Section 9.1.3. In future work, the potential application of optical readout in the context of future kiloton scale LArTPCs will be explored. In Section 9.2, we saw that preliminary testing using a 1m $\times$ 1m field of view, on initial impressions, seems to retain good sensitivity.

In the future, the Timepix 4 ASIC with its larger sensor size may allow the readout of increased readout areas, closer to 1.5m $\times$ 1.5m per camera. Future work will investigate the applicability of optical readout to larger detector areas. Considering the proposed 720 m^2 readout area per DUNE module, a 1.5m $\times$ 1.5m field of view per camera could allow detector readout using only 320 cameras with 2-3 millimeter scale resolution in all axes.

Bibliography

[1] DUNE Collaboration et al. "Long-Baseline Neutrino Facility (LBNF) and Deep Underground Neutrino Experiment (DUNE) Conceptual Design Report Volume 2: The Physics Program for DUNE at LBNF". In: 2 (Dec. 2015). arXiv: 1512.06148. URL: http://arxiv.org/abs/1512.06148.

[2] Adam Roberts et al. "ARIADNE, a Photographic Two-Phase LAr TPC". In: *Proceedings of The European Physical Society Conference on High Energy Physics — PoS(EPS-HEP2017)*. Trieste, Italy: Sissa Medialab, Jan. 2018, p. 802. DOI: 10.22323/1.314.0802. URL: https://pos.sissa.it/314/802.

[3] Simeon Bird et al. "Did LIGO Detect Dark Matter?" In: *Physical Review Letters* 116.20 (May 2016), p. 201301. ISSN: 0031-9007. DOI: 10.1103/PhysRevLett.116.201301. arXiv: arXiv:1603.00464v2. URL: https://link.aps.org/doi/10.1103/PhysRevLett.116.201301.

[4] Carlo Giunti and Chung W. Kim. *Fundamentals of Neutrino Physics and Astrophysics*. Oxford University Press, Mar. 2007. ISBN: 9780198508717. DOI: 10.1093/acprof:oso/9780198508717.001.0001. URL: http://www.oxfordscholarship.com/view/10.1093/acprof:oso/9780198508717.001.0001/acprof-9780198508717.

[5] M. Tanabashi et al. "Review of Particle Physics". In: *Physical Review D* 98.3 (2018), p. 30001. ISSN: 24700029. DOI: 10.1103/PhysRevD.98.030001. URL: https://doi.org/10.1103/PhysRevD.98.030001.

[6] F. P. An et al. "Search for a Light Sterile Neutrino at Daya Bay". In: *Journal of Physics: Conference Series* 888.1 (July 2014), pp. 1–7. ISSN: 17426596. DOI: 10.1103/PhysRevLett.113.141802. arXiv:

1407.7259. URL: http://arxiv.org/abs/1407.7259%20http://dx.doi.org/10.1103/PhysRevLett.113.141802.

[7] M. A. Acero. "Measurement of the neutrino oscillation parameters by NOvA". In: *Journal of Physics: Conference Series* 1219.1 (May 2019), p. 012021. ISSN: 1742-6588. DOI: 10.1088/1742-6596/1219/1/012021. URL: https://iopscience.iop.org/article/10.1088/1742-6596/1219/1/012021.

[8] K. Abe et al. "Measurement of neutrino and antineutrino oscillations by the T2K experiment including a new additional sample of nu_e interactions at the far detector". In: *Physical Review D* 96.9 (July 2017), pp. 1–50. ISSN: 24700029. DOI: 10.1103/PhysRevD.96.092006. arXiv: 1707.01048. URL: http://dx.doi.org/10.1103/PhysRevD.96.092006.

[9] K. Abe et al. "Updated T2K measurements of muon neutrino and antineutrino disappearance using 1.5e21 protons on target". In: *Physical Review D* 96.1 (Apr. 2017), pp. 1–8. ISSN: 24700029. DOI: 10.1103/PhysRevD.96.011102. arXiv: 1704.06409. URL: http://dx.doi.org/10.1103/PhysRevD.96.011102.

[10] Super-Kamiokande Collaboration et al. "Atmospheric Neutrino Oscillation Analysis With Improved Event Reconstruction in Super-Kamiokande IV". In: *Progress of Theoretical and Experimental Physics* 2019.5 (Jan. 2019), pp. 1–42. ISSN: 20503911. DOI: 10.1093/ptep/ptz015. arXiv: 1901.03230. URL: http://dx.doi.org/10.1093/ptep/ptz015.

[11] Paul Langacker. "Grand unified theories and proton decay". In: *Physics Reports* 72.4 (June 1981), pp. 185–385. ISSN: 03701573. DOI: 10.1016/0370-1573(81)90059-4. URL: https://linkinghub.elsevier.com/retrieve/pii/0370157381900594.

[12] Goran Senjanovic. "Proton decay and grand unification". In: *AIP Conference Proceedings* 1200 (Dec. 2009), pp. 131–141. ISSN: 0094243X. DOI: 10.1063/1.3327552. arXiv: 0912.5375. URL: http://dx.doi.org/10.1063/1.3327552.

[13] The Super-Kamiokande Collaboration et al. "Search for Proton Decay into Muon plus Neutral Kaon in Super-Kamiokande I, II, and III". In: (May 2012), pp. 1–15. DOI: 10.1103/PhysRevD.86.012006. arXiv: 1205.6538. URL: http://dx.doi.org/10.1103/PhysRevD.86.012006.

[14] The Super-Kamiokande Collaboration et al. "Search for Proton Decay via p nu K+ using 260 kiloton year data of Super-Kamiokande". In: *Physical Review D* 90.7 (Aug. 2014), p. 072005. ISSN: 1550-7998. DOI: 10.1103/PhysRevD.90.072005. arXiv: 1408.1195. URL: https://link.aps.org/doi/10.1103/PhysRevD.90.072005.

[15] V. Alan Kostelecký and Matthew Mewes. "Neutrinos with Lorentz-violating operators of arbitrary dimension". In: *Physical Review D - Particles, Fields, Gravitation and Cosmology* 85.9 (2012), pp. 1–35. ISSN: 15507998. DOI: 10.1103/PhysRevD.85.096005. arXiv: 1112.6395.

[16] C. E. Aalseth et al. "DarkSide-20k: A 20 tonne two-phase LAr TPC for direct dark matter detection at LNGS". In: *European Physical Journal Plus* 133.3 (2018). ISSN: 21905444. DOI: 10.1140/epjp/i2018-11973-4. arXiv: arXiv:1707.08145v1.

[17] J. Calvo et al. "Commissioning of the ArDM experiment at the Canfranc underground laboratory: first steps towards a tonne-scale liquid argon time projection chamber for Dark Matter searches". In: *Journal of Cosmology and Astroparticle Physics* 2017.03 (Mar. 2017), pp. 003–003. ISSN: 1475-7516. DOI: 10.1088/1475-7516/2017/03/003. URL: http://stacks.iop.org/1475-7516/2017/i=03/a=003?key=crossref.866228893f85dbc8e67d1c4d8c018448.

[18] André Rubbia. "ArDM: a ton-scale liquid Argon experiment for direct detection of Dark Matter in the Universe". In: *Journal of Physics: Conference Series* 39.1 (May 2006), pp. 129–132. ISSN: 1742-6588. DOI: 10.1088/1742-6596/39/1/028. URL: http://stacks.iop.org/1742-6596/39/i=1/a=028?key=crossref.dd9b7c9c6dae25c6813dd731d3cb135c.

[19] A. Marchionni et al. "ArDM: A ton-scale LAr detector for direct Dark Matter searches". In: *Journal of Physics: Conference Series* 308.1 (2011). ISSN: 17426596. DOI: 10.1088/1742-6596/308/1/012006.

[20] R. Acciarri et al. “The WArP Experiment”. In: *Journal of Physics: Conference Series* 308.1 (2011). ISSN: 17426596. DOI: 10.1088/1742-6596/308/1/012005.

[21] C. Amsler. “Search for WIMPs in liquid argon”. In: (May 2011), p. 13. arXiv: 1105.4524. URL: http://arxiv.org/abs/1105.4524.

[22] Marc Schumann. “Dark Matter Search with liquid Noble Gases”. In: (June 2012). arXiv: 1206.2169. URL: http://arxiv.org/abs/1206.2169.

[23] B. J. Mount et al. “LUX-ZEPLIN (LZ) Technical Design Report”. In: (Mar. 2017). arXiv: 1703.09144. URL: http://arxiv.org/abs/1703.09144.

[24] C. Rubbia. “The Liquid Argon Time Projection Chamber: A New Concept for Neutrino Detectors”. In: *CERN-EP/77-08* (1977).

[25] T. Heindl et al. “Table-top setup for investigating the scintillation properties of liquid argon”. In: *Journal of Instrumentation* 6.02 (Feb. 2011), P02011–P02011. ISSN: 1748-0221. DOI: 10.1088/1748-0221/6/02/P02011. URL: http://stacks.iop.org/1748-0221/6/i=02/a=P02011?key=crossref.8c7308d67c4adb8426ffba2b2ae6399a.

[26] R. Saldanha et al. “Cosmogenic production of $ˆ{39}$Ar and $ˆ{37}$Ar in argon”. In: (2019). arXiv: 1902.09072. URL: http://arxiv.org/abs/1902.09072.

[27] R. M. Sternheimer, S. M. Seltzer, and M. J. Berger. “Density effect for the ionization loss of charged particles in various substances”. In: *Physical Review B* 26.11 (Dec. 1982), pp. 6067–6076. ISSN: 0163-1829. DOI: 10.1103/PhysRevB.26.6067. URL: https://link.aps.org/doi/10.1103/PhysRevB.26.6067.

[28] Gerald R. Lynch and Orin I. Dahl. “Approximations to multiple Coulomb scattering”. In: *Nuclear Inst. and Methods in Physics Research, B* 58.1 (1991), pp. 6–10. ISSN: 0168583X. DOI: 10.1016/0168-583X(91)95671-Y.

[29] M. Antonello et al. “Muon momentum measurement in ICARUS-T600 LAr-TPC via multiple scattering in few-GeV range”. In: *Journal of Instrumentation* 12.4 (2017). ISSN: 17480221. DOI: 10.1088/1748-0221/12/04/P04010.

[30] P. Abratenko et al. "Determination of muon momentum in the MicroBooNE LArTPC using an improved model of multiple Coulomb scattering". In: *Journal of Instrumentation* 12.10 (2017). ISSN: 17480221. DOI: 10.1088/1748-0221/12/10/P10010. arXiv: arXiv:1703.06187v3.

[31] T. Takahashi et al. "The W-value of liquid argon". In: *Physics Letters A* 44.2 (May 1973), pp. 123–124. ISSN: 03759601. DOI: 10.1016/0375-9601(73)90814-1. URL: https://linkinghub.elsevier.com/retrieve/pii/0375960173908141.

[32] H Tawara et al. "Measurements of the W values in argon, nitrogen, and methane for 0.93 to 5.3 MeV alpha particles". In: *Nuclear Inst. and Methods in Physics Research, B* 29.3 (Dec. 1987), pp. 447–455. ISSN: 0168583X. DOI: 10.1016/0168-583X(87)90055-3. URL: https://linkinghub.elsevier.com/retrieve/pii/0168583X87900553.

[33] T. Doke et al. "Estimation of Fano factors in liquid argon, krypton, xenon and xenon-doped liquid argon". In: *Nuclear Instruments and Methods* 134.2 (Apr. 1976), pp. 353–357. ISSN: 0029554X. DOI: 10.1016/0029-554X(76)90292-5. URL: https://linkinghub.elsevier.com/retrieve/pii/0029554X76902925.

[34] S. Amoruso et al. "Study of electron recombination in liquid argon with the ICARUS TPC". In: *Nuclear Instruments and Methods in Physics Research, Section A: Accelerators, Spectrometers, Detectors and Associated Equipment* 523.3 (2004), pp. 275–286. ISSN: 01689002. DOI: 10.1016/j.nima.2003.11.423.

[35] R. Acciarri et al. "A study of electron recombination using highly ionizing particles in the ArgoNeuT Liquid Argon TPC". In: *Journal of Instrumentation* 8.8 (2013). ISSN: 17480221. DOI: 10.1088/1748-0221/8/08/P08005. arXiv: arXiv:1306.1712v1.

[36] L. Onsager. "Initial recombination of ions". In: *Physical Review* 54.8 (1938), pp. 554–557. ISSN: 0031899X. DOI: 10.1103/PhysRev.54.554.

[37] Ulrich Sowada, John M. Warman, and Matthijs P. De Haas. "Hot-electron thermalization in solid and liquid argon, krypton, and xenon". In: *Physical Review B* 25.5 (1982), pp. 3434–3437. ISSN: 01631829. DOI: 10.1103/PhysRevB.25.3434.

[38] Mariusz Wojcik and M. Tachiya. "Electron thermalization and electron-ion recombination in liquid argon". In: *Chemical Physics Letters* 379.1-2 (2003), pp. 20–27. ISSN: 00092614. DOI: 10.1016/j.cplett.2003.08.006.

[39] O. K. Rice. "The Thermodynamic Properties of Liquid Argon". In: *The Journal of Chemical Physics* 14.5 (May 1946), pp. 324–338. ISSN: 0021-9606. DOI: 10.1063/1.1724140. URL: http://aip.scitation.org/doi/10.1063/1.1724140.

[40] R. T. Scalettar et al. "Critical test of geminate recombination in liquid argon". In: *Physical Review A* 25.4 (Apr. 1982), pp. 2419–2422. ISSN: 0556-2791. DOI: 10.1103/PhysRevA.25.2419. URL: https://link.aps.org/doi/10.1103/PhysRevA.25.2419.

[41] George Jaffé. "Zur Theorie der Ionisation in Kolonnen". In: *Annalen der Physik* 347.12 (1913), pp. 303–344. ISSN: 00033804. DOI: 10.1002/andp.19133471205. URL: http://doi.wiley.com/10.1002/andp.19133471205.

[42] H. A. Kramers. "On a modification of jaffé's theory of column-ionization". In: *Physica* 18.10 (1952), pp. 665–675. ISSN: 00318914. DOI: 10.1016/S0031-8914(52)80255-1.

[43] D. A. Imel J. Thomas. "Recombination of electron-ion pairs in liquid argon and liquid xenon". In: *Physical Review A* 36.2 (1987), pp. 614–616. ISSN: 1050-2947. DOI: 10.1103/PhysRevA.36.614.

[44] Yichen Li et al. "Measurement of Longitudinal Electron Diffusion in Liquid Argon". In: Yichen Li (2015). DOI: 10.1016/j.nima.2016.01.094. arXiv: 1508.07059. URL: http://dx.doi.org/10.1016/j.nima.2016.01.094.

[45] T. Heindl et al. "The scintillation of liquid argon". In: *Epl* 91.6 (2010), pp. 14–17. ISSN: 02955075. DOI: 10.1209/0295-5075/91/62002.

[46] S Kubota, M. Hishida, and J. Raun. "Evidence for a triplet state of the self-trapped exciton states in liquid argon, krypton and xenon". In: *Journal of Physics C: Solid State Physics* 11.12 (1978), pp. 2645–2651. ISSN: 00223719. DOI: 10.1088/0022-3719/11/12/024.

[47] Robert S. Mulliken. "Potential curves of diatomic rare-gas molecules and their ions, with particular reference to Xe2". In: *The Journal of Chemical Physics* 52.10 (1970), pp. 5170–5180. ISSN: 00219606. DOI: 10.1063/1.1672756.

[48] C.K. Rhodes. *Excimer Lasers*. Springer Science & Business Media, 2013, p. 12.

[49] Masakatsu Umehara. "Theory for self-trapped holes in rare-gas solids. I. Formalism and result for solid argon". In: *Physical Review B* 33.6 (1986), pp. 4237–4244. ISSN: 01631829. DOI: 10.1103/PhysRevB.33.4237.

[50] D. C. Lorents. "The physics of electron beam excited rare gases at high densities". In: *Physica B+C* 82.1 (1976), pp. 19–26. ISSN: 03784363. DOI: 10.1016/0378-4363(76)90265-5.

[51] Masayo Suzuki, Jian zhi Ruan(Gen), and Shinzou Kubota. "Time dependence of the recombination luminescence from high-pressure argon, krypton and xenon excited by alpha particles". In: *Nuclear Instruments and Methods* 192.2-3 (1982), pp. 565–574. ISSN: 0029554X. DOI: 10.1016/0029-554X(82)90874-6.

[52] Marlo Martin. "Exciton self-trapping in rare-gas crystals". In: *The Journal of Chemical Physics* 54.8 (Apr. 1971), pp. 3289–3299. ISSN: 00219606. DOI: 10.1063/1.1675342. URL: http://aip.scitation.org/doi/10.1063/1.1675342.

[53] A. Bondar et al. "Study of infrared scintillations in gaseous and liquid argon - Part I: methodology and time measurements". In: *Journal of Instrumentation* 7.6 (Apr. 2012). ISSN: 17480221. DOI: 10.1088/1748-0221/7/06/P06015. arXiv: 1204.0180. URL: http://dx.doi.org/10.1088/1748-0221/7/06/P06015.

[54] A. Bondar et al. "Study of infrared scintillations in gaseous and liquid argon - Part II: light yield and possible applications". In: *Journal of Instrumentation* 7.06 (Apr. 2012), P06015–P06015. ISSN: 1748-0221. DOI: 10.1088/1748-0221/7/06/P06014. arXiv: 1204.0580. URL: http://dx.doi.org/10.1088/1748-0221/7/06/P06014.

[55] K. Mavrokoridis et al. "Argon purification studies and a novel liquid argon re-circulation system". In: *Journal of Instrumentation* 6.8 (2011). ISSN: 17480221. DOI: 10.1088/1748-0221/6/08/P08003. arXiv: arXiv:1106.5226v1.

[56] R. Acciarri et al. "Effects of Nitrogen and Oxygen contamination in liquid Argon". In: *Nuclear Physics B - Proceedings Supplements* 197.1 (2009), pp. 70–73. ISSN: 09205632. DOI: 10.1016/j.nuclphysbps.2009.10.037.

[57] Christie Chiu. *Liquid Argon scintillation light quenching due to Nitrogen impurities : measurements performed for the MicroBooNE vertical slice test*. Tech. rep. Batavia, IL (United States): Fermi National Accelerator Laboratory (FNAL), Jan. 2013. DOI: 10.2172/1155184. URL: http://www.osti.gov/servlets/purl/1155184/.

[58] B. J.P. Jones et al. "The effects of dissolved methane upon liquid argon scintillation light". In: *Journal of Instrumentation* 8.12 (2013). ISSN: 17480221. DOI: 10.1088/1748-0221/8/12/P12015.

[59] Adolph Fick. "V. On liquid diffusion". In: *The London, Edinburgh, and Dublin Philosophical Magazine and Journal of Science* 10.63 (July 1855), pp. 30–39. ISSN: 1941-5982. DOI: 10.1080/14786445508641925. URL: https://www.tandfonline.com/doi/full/10.1080/14786445508641925.

[60] Adolf Fick. "Ueber Diffusion". In: *Annalen der Physik und Chemie* 170.1 (1855), pp. 59–86. ISSN: 00033804. DOI: 10.1002/andp.18551700105. URL: http://doi.wiley.com/10.1002/andp.18551700105.

[61] W. Walkowiak. "Drift velocity of free electrons in liquid argon". In: *Nuclear Instruments and Methods in Physics Research, Section A: Accelerators, Spectrometers, Detectors and Associated Equipment* 449.1 (2000), pp. 288–294. ISSN: 01689002. DOI: 10.1016/S0168-9002(99)01301-7.

[62] S. Amoruso et al. "Analysis of the liquid argon purity in the ICARUS T600 TPC". In: *Nuclear Instruments and Methods in Physics Research, Section A: Accelerators, Spectrometers, Detectors and Associated Equipment* 516.1 (2004), pp. 68–79. ISSN: 01689002. DOI: 10.1016/j.nima.2003.07.043.

[63] A. Herzenberg. "Attachment of Slow Electrons to Oxygen Molecules". In: *The Journal of Chemical Physics* 51.11 (Dec. 1969), pp. 4942–4950. ISSN: 0021-9606. DOI: 10.1063/1.1671887. URL: http://aip.scitation.org/doi/10.1063/1.1671887.

[64] George Bakale, Ulrich Sowada, and Werner F. Schmidt. "Effect of an electric field on electron attachment to sulfur hexafluoride, nitrous oxide, and molecular oxygen in liquid argon and xenon". In: *The Journal of Physical Chemistry* 80.23 (2005), pp. 2556–2559. ISSN: 0022-3654. DOI: 10.1021/j100564a006.

[65] A. Bettini et al. "A study of the factors affecting the electron lifetime in ultra-pure liquid argon". In: *Nuclear Instruments and Methods in Physics Research Section A: Accelerators, Spectrometers, Detectors and Associated Equipment* 305.1 (July 1991), pp. 177–186. ISSN: 01689002. DOI: 10.1016/0168-9002(91)90532-U. URL: https://linkinghub.elsevier.com/retrieve/pii/016890029190532U.

[66] S. van der Laan, R. E. M. Neubert, and H. A. J. Meijer. "A single gas chromatograph for accurate atmospheric mixing ratio measurements of CO2, CH4, N2O, SF6 and CO". In: *Atmospheric Measurement Techniques Discussions* 2.3 (May 2009), pp. 1321–1349. ISSN: 1867-8610. DOI: 10.5194/amtd-2-1321-2009. URL: http://www.atmos-meas-tech-discuss.net/2/1321/2009/.

[67] Yichen Li et al. "A 20-Liter Test Stand with Gas Purification for Liquid Argon Research". In: Yichen Li (2016). DOI: 10.1088/1748-0221/11/06/T06001. arXiv: arXiv:1602.01884v2. URL: https://arxiv.org/abs/1602.01884.

[68] M. Adamowski et al. "The liquid argon purity demonstrator". In: *Journal of Instrumentation* 9.7 (2014). ISSN: 17480221. DOI: 10.1088/1748-0221/9/07/P07005.

[69] R. Andrews et al. "A system to test the effect of materials on electron drift lifetime in liquid argon and the effect of water". In: *Nuclear Instruments and Methods in Physics Research Section A: Accelerators, Spectrometers, Detectors and Associated Equipment* 608.2 (Sept. 2009), pp. 251–258. ISSN: 01689002. DOI: 10.1016/j.nima.2009.07.024. URL: https://linkinghub.elsevier.com/retrieve/pii/S0168900209014624.

[70] B Baibussinov et al. "Free electron lifetime achievements in Liquid Argon Imaging TPC". In: *Jinst* 5 (Oct. 2009), P03005. ISSN: 17480221. DOI: 10.1088/1748-0221/5/03/P03005. arXiv: 0910.5087. URL: http://dx.doi.org/10.1088/1748-0221/5/03/P03005.

[71] J. Asaadi et al. "A pixelated charge readout for Liquid Argon Time Projection Chambers". In: *Journal of Instrumentation* 13.02 (Feb. 2018), pp. C02008–C02008. ISSN: 1748-0221. DOI: 10.1088/1748-0221/13/02/C02008. arXiv: arXiv:1801.08884v1. URL: http://stacks.iop.org/1748-0221/13/i=02/a=C02008?key=crossref.17f0d52079ce024fa11ea9b0d83f7c84.

[72] S. Amerio et al. "Design, construction and tests of the ICARUS T600 detector". In: *Nuclear Instruments and Methods in Physics Research Section A: Accelerators, Spectrometers, Detectors and Associated Equipment* 527.3 (July 2004), pp. 329–410. ISSN: 01689002. DOI: 10.1016/j.nima.2004.02.044. URL: https://linkinghub.elsevier.com/retrieve/pii/S0168900204004966.

[73] R. Acciarri et al. "Design and construction of the MicroBooNE detector". In: *Journal of Instrumentation* 12.2 (Dec. 2017). ISSN: 17480221. DOI: 10.1088/1748-0221/12/02/P02017. arXiv: 1612.05824. URL: http://dx.doi.org/10.1088/1748-0221/12/02/P02017.

[74] R. Acciarri et al. "A Proposal for a Three Detector Short-Baseline Neutrino Oscillation Program in the Fermilab Booster Neutrino Beam". In: (Mar. 2015). arXiv: 1503.01520. URL: http://arxiv.org/abs/1503.01520.

[75] B. Abi et al. "The Single-Phase ProtoDUNE Technical Design Report". In: (June 2017). arXiv: 1706.07081. URL: http://arxiv.org/abs/1706.07081.

[76] A. Bondar et al. "Electron emission properties of two-phase argon and argon-nitrogen avalanche detectors". In: *Journal of Instrumentation* 4.09 (Sept. 2009), P09013–P09013. ISSN: 1748-0221. DOI: 10.1088/1748-0221/4/09/P09013. URL: http://stacks.iop.org/1748-0221/4/i=09/a=P09013?key=crossref.e226346bd9965b4a9f065cfd285a7e24.

[77] A.F. Borghesani et al. "Electron transmission through the Ar liquid-vapor interface". In: *Physics Letters A* 149.9 (Oct. 1990), pp. 481–484. ISSN: 03759601. DOI: 10.1016/0375-9601(90)90221-9. URL: https://linkinghub.elsevier.com/retrieve/pii/0375960190902219.

[78] E M Gushchin, A A Kruglov, and I M Obodovskii. "Emission of "hot" electrons from liquid and solid argon and xenon". In: *Sov. Phys. JETP* 55 (1982), p. 860.

[79] R CHECHIK et al. "Thick GEM-like hole multipliers: properties and possible applications". In: *Nuclear Instruments and Methods in Physics Research Section A: Accelerators, Spectrometers, Detectors and Associated Equipment* 535.1-2 (Dec. 2004), pp. 303–308. ISSN: 01689002. DOI: 10.1016/S0168-9002(04)01666-3. URL: https://linkinghub.elsevier.com/retrieve/pii/S0168900204016663.

[80] A. Breskin et al. "A concise review on THGEM detectors". In: *Nuclear Instruments and Methods in Physics Research Section A: Accelerators, Spectrometers, Detectors and Associated Equipment* 598.1 (Jan. 2009), pp. 107–111. ISSN: 01689002. DOI: 10.1016/j.nima.2008.08.062. URL: https://linkinghub.elsevier.com/retrieve/pii/S0168900208012047.

[81] F Sauli. "GEM: A new concept for electron amplification in gas detectors". In: *Nuclear Instruments and Methods in Physics Research Section A: Accelerators, Spectrometers, Detectors and Associated Equipment* 386.2-3 (Feb. 1997), pp. 531–534. ISSN: 01689002. DOI: 10.1016/S0168-9002(96)01172-2. URL: https://linkinghub.elsevier.com/retrieve/pii/S0168900296011722.

[82] L. Arazi et al. "Liquid Hole Multipliers: Bubble-assisted electroluminescence in liquid xenon". In: *Journal of Instrumentation* 10.8 (2015). ISSN: 17480221. DOI: 10.1088/1748-0221/10/08/P08015.

[83] "Recent advances in bubble-assisted Liquid Hole-Multipliers in liquid xenon". In: *Journal of Instrumentation* 13.12 (2018). ISSN: 1748-0221. DOI: 10.1088/1748-0221/13/12/P12008.

[84] DUNE Collaboration et al. "The DUNE Far Detector Interim Design Report, Volume 3: Dual-Phase Module". In: 3 (2018). arXiv: 1807.10340. URL: http://arxiv.org/abs/1807.10340.

[85] T H Dey and T J Lewis. "Ion mobility and liquid motion in liquefied argon". In: *Journal of Physics D: Applied Physics* 1.8 (Aug. 1968), p. 309. ISSN: 00223727. DOI: 10.1088/0022-3727/1/8/309. URL: http://stacks.iop.org/0022-3727/1/i=8/a=309?key=crossref.12e45c7a66da8f931afed77df39e0595.

[86] A Buzulutskov et al. "Revealing neutral bremsstrahlung in two-phase argon electroluminescence". In: *Astroparticle Physics* 103 (Mar. 2018), pp. 29–40. ISSN: 09276505. DOI: 10.1016/j.astropartphys.2018.06.005. arXiv: 1803.05329. URL: http://dx.doi.org/10.1016/j.astropartphys.2018.06.005.

[87] A Bondar et al. "Neutral bremsstrahlung in two-phase argon electroluminescence: further studies and possible applications". In: *Nuclear Instruments and Methods in Physics Research Section A: Accelerators, Spectrometers, Detectors and Associated Equipment* (May 2019), p. 162432. ISSN: 01689002. DOI: 10.1016/j.nima.2019.162432. arXiv: 1905.05502. URL: http://arxiv.org/abs/1905.05502.

[88] S F Biagi. "Monte Carlo simulation of electron drift and diffusion in counting gases under the influence of electric and magnetic fields". In: *Nuclear Instruments and Methods in Physics Research, Section A: Accelerators, Spectrometers, Detectors and Associated Equipment* 421.1-2 (1999), pp. 234–240. ISSN: 01689002. DOI: 10.1016/S0168-9002(98)01233-9.

[89] R Veenhof. "Garfield, a drift chamber simulation program". In: *Conf. Proc.* C9306149.November (1993), pp. 66–71.

[90] F. Bay et al. "Evidence of electric breakdown induced by bubbles in liquid argon". In: January (2014), pp. 8–9. arXiv: 1401.2777. URL: http://arxiv.org/abs/1401.2777.

[91] R. Acciarri et al. "Liquid argon dielectric breakdown studies with the MicroBooNE purification system". In: *Journal of Instrumentation* 9.11 (2014), pp. 0–13. ISSN: 17480221. DOI: 10.1088/1748-0221/9/11/P11001. arXiv: arXiv:1408.0264v1.

[92] J. Gerhold, M. Hubmann, and E. Telser. "Gap size effect on liquid helium breakdown". In: *Cryogenics* 34.7 (1994), pp. 579–586. ISSN: 00112275. DOI: 10.1016/0011-2275(94)90183-X.

[93] M. Auger et al. "A method to suppress dielectric breakdowns in liquid argon ionization detectors for cathode to ground distances of several millimeters". In: *Journal of Instrumentation* 9.7 (2014). ISSN: 17480221. DOI: 10.1088/1748-0221/9/07/P07023. arXiv: arXiv:1406.3929v1.

[94] B. Rebel et al. "High voltage in noble liquids for high energy physics". In: *Journal of Instrumentation* 9.8 (2014). ISSN: 17480221. DOI: 10.1088/1748-0221/9/08/T08004. arXiv: arXiv:1403.3613v2.

[95] K. Mavrokoridis et al. "First Demonstration of Imaging Cosmic Muons in a Two-Phase Liquid Argon TPC using an EMCCD Camera and a THGEM". In: *Journal of Instrumentation* 10.10 (July 2015), P10004–P10004. ISSN: 1748-0221. DOI: 10.1088/1748-0221/10/10/P10004. arXiv: 1507.06586.

[96] V. M. Gehman et al. "Fluorescence Efficiency and Visible Re-emission Spectrum of Tetraphenyl Butadiene Films at Extreme Ultraviolet Wavelengths". In: *Nuclear Instruments and Methods in Physics Research, Section A: Accelerators, Spectrometers, Detectors and Associated Equipment* 654.1 (Apr. 2011), pp. 116–121. ISSN: 01689002. DOI: 10.1016/j.nima.2011.06.088. arXiv: 1104.3259. URL: http://dx.doi.org/10.1016/j.nima.2011.06.088.

[97] T. Caldwell, S. Seibert, and S. Jaditz. "Characterization of the R5912-02 MOD photomultiplier tube at cryogenic temperatures". In: *Journal of Instrumentation* 8.9 (2013). ISSN: 17480221. DOI: 10.1088/1748-0221/8/09/C09004.

[98] T. Briese et al. "Testing of cryogenic photomultiplier tubes for the MicroBooNE experiment". In: *Journal of Instrumentation* 8.7 (2013). ISSN: 17480221. DOI: 10.1088/1748-0221/8/07/T07005. arXiv: arXiv:1304.0821v4.

[99] Tanner Kaptanoglu. "Characterization of the Hamamatsu 8" R5912-MOD Photomultiplier tube". In: *Nuclear Instruments and Methods in Physics Research, Section A: Accelerators, Spectrometers, Detectors and Associated Equipment* 889 (2018), pp. 69–77. ISSN: 01689002. DOI: 10.1016/j.nima.2018.01.086. arXiv: arXiv:1710.03334v1.

[100] D. Belver et al. "Cryogenic R5912-20Mod photomultiplier tube characterization for the ProtoDUNE dual phase detector". In: *Journal of Instrumentation* 13.10 (2018). ISSN: 17480221. DOI: 10.1088/1748-0221/13/10/T10006. arXiv: arXiv:1806.04571v4.

[101] M. Adamowski et al. "The liquid argon purity demonstrator". In: *Journal of Instrumentation* 9.7 (2014). ISSN: 17480221. DOI: 10.1088/1748-0221/9/07/P07005. arXiv: arXiv:1403.7236v1.

[102] Mitchell Soderberg. "MicroBooNE: A New Liquid Argon Time Projection Chamber Experiment". In: *AIP Conference Proceedings* 1189 (Oct. 2009), pp. 83–87. ISSN: 0094243X. DOI: 10.1063/1.3274193. arXiv: 0910.3497.

[103] B.J.P. Jones et al. "Summary of the second workshop on liquid argon time projection chamber research and development in the United States". In: *Journal of Instrumentation* 10.07 (2015), T07006–T07006. ISSN: 1748-0221. DOI: 10.1088/1748-0221/10/07/T07006.

[104] M.J. Carvalho and G. Klein. "Luminescence decay in condensed argon under high energy excitation". In: *Journal of Luminescence* 18-19.PART 1 (Jan. 1979), pp. 487–490. ISSN: 00222313. DOI: 10.1016/0022-2313(79)90167-4. URL: https://linkinghub.elsevier.com/retrieve/pii/0022231379901674.

[105] Akira Hitachi et al. "Effect of ionization density on the time dependence of luminescence from liquid argon and xenon". In: *Physical Review B* 27.9 (1983), pp. 5279–5285. ISSN: 01631829. DOI: 10.1103/PhysRevB.27.5279.

[106] *Cern east area documentation*. URL: http://sba.web.cern.ch/sba/BeamsAndAreas/East/East.htm.

[107] L. Durieu, M. Martini, and A. S. Müller. "Optics studies for the T9 beam line in the CERN PS East Area secondary beam facility". In: *Proceedings of the IEEE Particle Accelerator Conference* 2 (2001), pp. 1547–1549.

[108] T. Poikela et al. "Timepix3: A 65K channel hybrid pixel readout chip with simultaneous ToA/ToT and sparse readout". In: *Journal of Instrumentation* 9.5 (2014). ISSN: 17480221. DOI: 10.1088/1748-0221/9/05/C05013.

[109] M. Fisher-Levine and A. Nomerotski. "TimepixCam: A fast optical imager with time-stamping". In: *Journal of Instrumentation* 11.3 (2016). ISSN: 17480221. DOI: 10.1088/1748-0221/11/03/C03016.

[110] Andrei Nomerotski et al. "Characterization of TimepixCam, a fast imager for the time-stamping of optical photons". In: *Journal of Instrumentation* 12.1 (2017). ISSN: 17480221. DOI: 10.1088/1748-0221/12/01/C01017.

[111] Andrei Nomerotski. "Imaging and time stamping of photons with nanosecond resolution in Timepix based optical cameras". In: *Nuclear Instruments and Methods in Physics Research, Section A: Accelerators, Spectrometers, Detectors and Associated Equipment* 937 (2019), pp. 26–30. ISSN: 01689002. DOI: 10.1016/j.nima.2019.05.034. arXiv: arXiv:1902.01357v3.

[112] M De Gaspari et al. "Design of the analog front-end for the Timepix3 and Smallpix hybrid pixel detectors in 130 nm CMOS technology". In: *Journal of Instrumentation* 9.01 (Jan. 2014), pp. C01037–C01037. ISSN: 1748-0221. DOI: 10.1088/1748-0221/9/01/C01037. URL: http://stacks.iop.org/1748-0221/9/i=01/a=C01037?key=crossref.76466b2e78780b9f274e9e85a6250254.

[113] B. Van Der Heijden et al. "SPIDR, a general-purpose readout system for pixel ASICs". In: *Journal of Instrumentation* 12.2 (2017). ISSN: 17480221. DOI: 10.1088/1748-0221/12/02/C02040.

[114] Hamamatsu Photonics K K. "4: CHARACTERISTICS OF Characteristics of Photocathodes". In: *Hamamatsu PMT Handbook* (2007).

[115] Joseph Ladislas Wiza. "TP209_MCP_Reprint.pdf". In: *Nuclear Instruments and Methods* 162 (1979), pp. 587–601. URL: https://www.photonis.com/uploads/literature/library/TP209_MCP_Reprint.pdf.

[116] D. A. Orlov et al. "High collection efficiency MCPs for photon counting detectors". In: *Journal of Instrumentation* 13.1 (2018). ISSN: 17480221. DOI: 10.1088/1748-0221/13/01/C01047.

[117] B. Winter et al. "A fast microchannel plate-scintillator detector for velocity map imaging and imaging mass spectrometry". In: *Review*

of Scientific Instruments 85.2 (2014). ISSN: 00346748. DOI: 10.1063/1.4866647.

[118] *Photonis Cricket image intensifier*. URL: https://www.photonis.com/product/cricket (visited on 09/23/2019).

[119] A. Roberts et al. "First demonstration of 3D optical readout of a TPC using a single photon sensitive Timepix3 based camera". In: (2018). arXiv: 1810.09955. URL: http://arxiv.org/abs/1810.09955.

[120] K. Mavrokoridis et al. "Optical readout of a two phase liquid argon TPC using CCD camera and THGEMs". In: *Journal of Instrumentation* 9.2 (2014). ISSN: 17480221. DOI: 10.1088/1748-0221/9/02/P02006. arXiv: arXiv:1401.0525v2.

[121] Microboone. "Detector calibration using through going and stopping muons in the MicroBooNE LArTPC". In: *MICROBOONE-NOTE-1048-PUB* (2018), pp. 1–24.

[122] M. Campbell et al. "Towards a new generation of pixel detector readout chips". In: *Journal of Instrumentation* 11.1 (2016). ISSN: 17480221. DOI: 10.1088/1748-0221/11/01/C01007.

[123] C. S. Chiu et al. "Environmental effects on TPB wavelength-shifting coatings". In: *Journal of Instrumentation* 7.7 (2012). ISSN: 17480221. DOI: 10.1088/1748-0221/7/07/P07007. arXiv: arXiv:1204.5762v1.

[124] R. Acciarri et al. "Aging studies on thin tetra-phenyl butadiene films". In: *Journal of Instrumentation* 8.10 (Oct. 2013), pp. C10002–C10002. ISSN: 1748-0221. DOI: 10.1088/1748-0221/8/10/C10002. URL: http://stacks.iop.org/1748-0221/8/i=10/a=C10002?key=crossref.969f6c6b901f0085be50d45e4d30f617.

[125] E. Segreto. "Evidence of delayed light emission of tetraphenyl-butadiene excited by liquid-argon scintillation light". In: *Physical Review C* 91.3 (Mar. 2015), p. 035503. ISSN: 0556-2813. DOI: 10.1103/PhysRevC.91.035503. URL: https://link.aps.org/doi/10.1103/PhysRevC.91.035503.

[126] M. A. Barstow, G. W. Fraser, and S. R. Milward. "Imaging Microchannel Plate Detectors For XUV Sky Survey Experiments". In: *X-Ray Instrumentation in Astronomy* 0597.July 1986 (2013), p. 352. DOI: 10.1117/12.966601.

[127] A.S. Tremsin. "The dependence of quantum efficiency of alkali halide photocathodes on the radiation incidence angle". In: *Proc. SPIE* 3765 (1999), pp. 1–11. ISSN: 0277786X. DOI: 10.1117/12.366524. URL: http://dx.doi.org/10.1117/12.366524.

[128] D. G. Simons et al. "UV and XUV quantum detection efficiencies of CsI-coated microchannel plates". In: *Nuclear Inst. and Methods in Physics Research, A* 261.3 (1987), pp. 579–586. ISSN: 01689002. DOI: 10.1016/0168-9002(87)90371-8.

[129] Anton S Tremsin and Oswald H W Siegmund. "visible light rejection of alkali halide". In: *UV, Optical, and IR Space Telescopes and Instruments*. Vol. 4013. July 2000. 2003, pp. 411–420. DOI: 10.1117/12.394023.

[130] Zhe Liu et al. "The properties of opaque CsI photocathode". In: November 2018. 2018, p. 55. DOI: 10.1117/12.2505107.

[131] Ryoji Enomoto, Takayuki Sumiyoshi, and Yoshio Fujita. "Test of various photocathodes". In: *Nuclear Inst. and Methods in Physics Research, A* 343.1 (1994), pp. 117–120. ISSN: 01689002. DOI: 10.1016/0168-9002(94)90540-1.

[132] M. Alexeev et al. "Long term experience with CsI photocathodes in gas photon detectors". In: *Journal of Instrumentation* 9.1 (2014). ISSN: 17480221. DOI: 10.1088/1748-0221/9/01/P01006.

Appendices

Appendix A

Determination of D_T

From [44] we have that

$$D_L = \left(\frac{a_0 + a_1E + a_2E^{3/2} + a_3E^{5/2}}{1 + (a_1/a_0)E + a_4E^2 + a_5E^3}\right)\left(\frac{b_0 + b_1E + b_2E^2}{1 + (b_1/b_0)E + b_3E^2}\right)\left(\frac{T}{T_1}\right)\left(\frac{T}{T_0}\right)^{-3/2} \tag{A.1}$$

and that

$$\frac{D_L}{D_T} = 1 + \frac{E}{\mu}\frac{\partial \mu}{\partial E} \tag{A.2}$$

Thus,

$$D_T = \frac{D_L}{1 + \frac{E}{\mu}\frac{\partial}{\partial E}(\mu)} \tag{A.3}$$

$$D_T = \frac{\left(\frac{a_0+a_1E+a_2E^{3/2}+a_3E^{5/2}}{1+(a_1/a_0)E+a_4E^2+a_5E^3}\right)\left(\frac{b_0+b_1E+b_2E^2}{1+(b_1/b_0)E+b_3E^2}\right)\left(\frac{T}{T_1}\right)\left(\frac{T}{T_0}\right)^{-3/2}}{1 + \frac{E}{\mu}\frac{\partial}{\partial E}\left(\frac{a_0+a_1E+a_2E^{3/2}+a_3E^{5/2}}{1+(a_1/a_0)E+a_4E^2+a_5E^3}\right)} \tag{A.4}$$

$$D_T = \frac{\left(\frac{a_0+a_1E+a_2E^{3/2}+a_3E^{5/2}}{1+(a_1/a_0)E+a_4E^2+a_5E^3}\right)\left(\frac{b_0+b_1E+b_2E^2}{1+(b_1/b_0)E+b_3E^2}\right)\left(\frac{T}{T_1}\right)\left(\frac{T}{T_0}\right)^{-3/2}}{1 + \frac{E}{\mu}\left(\frac{(5/2)a_3E^{3/2}+\frac{3a_2\sqrt{E}}{2}+a_1}{a_5E^3+a_4E^2+\frac{a_1E}{a_0}+1} + \frac{\left(a_3E^{5/2}+a_2E^{3/2}+a_1E+a_0\right)\left(3a_5E^2+2a_4E+\frac{a_1}{a_0}\right)}{\left(a_5E^3+a_4E^2+\frac{a_1E}{a_0}+1\right)^2}\right)} \tag{A.5}$$